Transition Metal-Based Electrocatalysts for Highly Selective CO$_2$ Reduction

Chaochen Xu

A thesis submitted for the degree of Doctor of Philosophy at
The University of Adelaide

November 2020

Contents

Abstract

The electrochemical CO_2 reduction reaction (CRR) can combine carbon cycling with renewable energy to convert CO_2 into high-value carbonaceous feedstocks. However, this process suffers from kinetically sluggish because of the complicated electron transfer and high energy barriers involved. Well-designed transition metal materials as promising electrocatalysts show remarkable catalytic activities for the CRR. Therefore, this Thesis is to study the catalytic activity and selectivity on these transition metal catalysts, and a fundamental understanding of the catalytic mechanism is given through a series of experimental and computational results using advanced synthesis methods, electrochemical measurements, material characterization including microscopy and spectroscopy, synchrotron-based X-ray spectroscopy, in situ spectroscopy, and density functional theory (DFT) calculations. The scope of this Thesis is narrowed to nanoscale and sub-nanoscale engineered 3d-block transition metal (mainly, Fe, Co, Ni, Cu) catalysts for the CRR process.

In this Thesis, the first section introduces research progress including catalytic performance and mechanisms on sub-nanoscale 3d-block transition metal catalysts for the CRR. The second section consists of published and submitted works: (1) The first project starts with the investigation of the CRR on Ni catalysts. We engineered and alloyed Ni with Cu to obtain ultrasmall graphene-encapsulated Ni-Cu bimetallic catalysts. The Cu-lean catalyst exhibited significant activity and selectivity, and the highest Faradaic efficiency (FE) toward CO was 90% at -1.0 V vs. RHE. By coupling synchrotron-based X-ray absorption and *in situ*

Raman spectroscopy studies, we found that there is a negative correlation with the Cu content in Ni-Cu catalyst and CO selectivity due to redistribution of the 3d electrons from Ni and Cu. (2) Because of the high catalytic activity was received on ultrasmall Ni-Cu particles, the second project aims to fabricate sub-nanoscale transition metal catalysts for the CRR. We synthesized atomically dispersed Fe immobilized within N-doped carbon nanosheets. The optimal Fe catalyst achieved FE of 90% toward CO at -0.58 V vs. RHE. A series of controlled tests revealed that there is a synergistic effect between the Fe sites and the pyrrolic-N-framework which promotes the catalytic activity of CO evolution. (3) The third work is based on the previous Fe catalyst and investigates the unique single-atom Cu catalyst (Cu-N_4-NG). The chemical structure and coordination environment of Cu-N_4-NG were identified using synchrotron-based characterization. Compared to a traditional bulk Cu catalyst, Cu-N_4-NG performed a FE of 80.6% towards CO at -1.0 V vs. RHE. The experimental results revealed that the presence of Cu-N_4 moieties largely promotes CO_2 activation and water dissociation, showing CO_2 reduction is kinetically preferred on Cu-N_4-NG. Also, the computational investigation suggested a thermodynamic explanation that CO_2 reduction is less hindered on Cu-N_4-NG compared to hydrogen evolution. (4) Although high FEs were obtained on single-atom transition metal catalyst shown in the previous two works, the two catalysts were not strictly single-atom catalysts with a uniform structure of M-N_4, some coordination defects existed. Thus, graphene-supported metal phthalocyanine catalysts with M-N_4 structure were reported in the fourth work, which achieved almost 100% CO_2 conversion to CO on graphene-supported cobalt phthalocyanine. Further experimental studies showed that the phthalocyanines with graphene were significantly activated than the pure ones. A series of control tests uncovered that the graphene substrate facilitates electron transfer between the catalyst and CO_2 molecules, which increased CO selectivity.

Declaration

I certify that this work contains no material which has been accepted for the award of any other degree or diploma in my name, in any university or other tertiary institution and, to the best of my knowledge and belief, contains no material previously published or written by another person, except where due reference has been made in the text. In addition, I certify that no part of this work will, in the future, be used in a submission in my name, for any other degree or diploma in any university or other tertiary institution without the prior approval of the University of Adelaide and where applicable, any partner institution responsible for the joint-award of this degree.

I acknowledge that copyright of published works contained within this thesis resides with the copyright holder(s) of those works.

I also give permission for the digital version of my thesis to be made available on the web, via the University's digital research repository, the Library Search and also through web search engines, unless permission has been granted by the University to restrict access for a period of time.

Signed:

Date: November 10, 2020

Acknowledgements

Chapter 1

Introduction

1.1 Research background

Currently, society is being heavily dependent on using traditional energy resources and is suffering environmental problems caused by the consumption of fossil fuels. [1, 2] The electrochemical CO_2 reduction reaction (CRR) as a cutting-edge technique for energy conversion can combine carbon capture storage (CCS) with renewable energy utilization to convert CO_2 into useful chemical feedstocks at ambient conditions. [1,3] However, this heterogeneous process is kinetically sluggish due to multiple electron transfer steps and high energy barriers involved. Also, the CRR suffers from low selectivity leading to insufficient conversion for a certain product. [4] Therefore, highly selective electrocatalysts are desired to reduce energy barriers and facilitate CO_2 reduction. Recent studies of candidate screening for the CRR focus on transition metal electrocatalysts (*e.g.* Fe, Co, Ni, Cu). [5–10] As a result of complicated 3d-block electronic structures, the transition metal group exhibits unique catalytic behaviors in CO_2 reduction. [8, 11–13] Therefore, nanoscale and sub-nanoscale engineered 3d-block transition metal electrocatalysts provide a promising solution for the CRR applications involving CO_2 capture and renewable energy utilization.

1.2 Research objectives

The objectives of this thesis are to develop the heterogeneous 3d-block transition metal electrocatalysts for highly selective CO_2 reduction and comprehensively understand the catalytic mechanism. Specifically, the objectives include as follows:

Improve catalytic performance. This objective involves the improvement of Faradaic efficiency and overpotential. The Faradaic efficiency (FE) describes the efficiency with which electrons are transferred in the CRR. The higher FE received indicates high catalytic selectivity. And the overpotential describes the difference between experimental potential and theoretical potential. A low overpotential is preferred due to the less-hindered reaction occurs on the catalyst. For these, the

electrocatalysts with high Faradaic efficiency at low overpotential are in demand.

Understand catalytic mechanisms. This objective is to comprehend and unravel the catalytic mechanism for the CRR. The mechanism study brings more insights into understanding the reason why the presence of catalysts can largely facilitate reaction selectivity (*i.e.* FE) and reduce the energy barrier (*i.e.* overpotential). A throughout understanding of the mechanism can guide to optimize catalyst design.

1.3   Thesis outline

This Thesis highlights the development of nanoscale and sub-nanoscale engineered 3d transition metals (*i.e.* Fe, Co, Ni, Cu) as heterogeneous electrocatalysts for CO_2 reduction at ambient conditions. The Thesis starts with **Chapter 1**, Introduction, to introduce research background, research objectives, and thesis outline. In **Chapter 2**, Literature Review, a review paper is given to introduce the current research progress of sub-nanoscale 3d transition metal electrocatalysts for CO_2 reduction. **Chapter 3** presents electrochemical and spectroscopic studies of Ni-Cu bimetallic catalysts for the CRR. This chapter is slightly different from the following chapters due to the development of the catalyst is under nanoscale engineering rather than sub-nanoscale engineering. The related literature review of nanoscale-engineered Cu-based bimetallic catalysts for the CRR is shown in **Appendix A** as a supplementary review. As the improvement of the synthesis method, the atom-level Fe catalyst was successfully obtained in **Chapter 4**. A high FE for CO was received. A synergistic effect between the Fe center and its surrounding pyrrolic-N-C framework was identified that facilitates CO_2 reduction toward CO. **Chapter 5** is the study of single-atom Cu catalysts for the CRR. Compared to the previous Fe catalyst, the Cu catalyst has a similar chemical structure determined by synchrotron-based X-ray absorption spectroscopy but a different catalytic mechanism for the CRR. In CO_2 reduction, the Cu-N_4 moiety

improved the CO_2 activation step, the graphene layer served as a place for water dissociation which provides protons for CO_2 reduction. Also, computational results confirmed that the CO_2 reduction was less hindered thermodynamically on single-atom Cu catalysts compared to the bulk Cu. Although single-atom catalysts have been reported in Chapters 4 and 5, their chemical structures were not strictly M-N_4 throughout the catalysts because of the difficulty in synthesis. So, the catalysts with the ideal M-N_4 structure were reported in **Chapter 6**. Graphene-supported metal phthalocyanines (MPc, M = Fe, Co, Ni) were investigated for the CRR, which showed that the highest CO selectivity (almost 100%) was received on graphene-supported cobalt phthalocyanine. A series of experiments were carried out and demonstrated that there was a synergistic effect between the metal phthalocyanine molecule and the graphene substrate via strong π-π stacking, leading to high CRR performance received on graphene-supported MPc rather than pristine MPc. In the end, **Chapter 7**, conclusions are given to summarize the works completed during PhD candidature, and perspectives are proposed for the further study of electrocatalytic CO_2 reduction. The full publication list during PhD candidature is shown in **Appendix B**.

References

[1] Chi Chen, Juliet F Khosrowabadi Kotyk, and Stafford W Sheehan. Progress toward commercial application of electrochemical carbon dioxide reduction. *Chem*, 4(11):2571–2586, 2018.

[2] Michele Aresta, Angela Dibenedetto, and Antonella Angelini. Catalysis for the valorization of exhaust carbon: from CO_2 to chemicals, materials, and fuels. Technological use of CO_2. *Chemical Reviews*, 114(3):1709–1742, 2014.

[3] Dong Dong Zhu, Jin Long Liu, and Shi Zhang Qiao. Recent advances in inorganic heterogeneous electrocatalysts for reduction of carbon dioxide. *Advanced Materials*, 28(18):3423–3452, 2016.

[4] Zhenyu Sun, Tao Ma, Hengcong Tao, Qun Fan, and Buxing Han. Fundamentals and challenges of electrochemical CO_2 reduction using two-dimensional materials. *Chem*, 3(4):560–587, 2017.

[5] Yuanjun Chen, Shufang Ji, Chen Chen, Qing Peng, Dingsheng Wang, and Yadong Li. Single-atom catalysts: synthetic strategies and electrochemical applications. *Joule*, 2(7):1242–1264, 2018.

[6] Bingzhang Lu, Qiming Liu, and Shaowei Chen. Electrocatalysis of single atom sites: Impacts of atomic coordination. *ACS Catalysis*, 10(14):7584–7618, 2020.

[7] Aiqin Wang, Jun Li, and Tao Zhang. Heterogeneous single-atom catalysis. *Nature Reviews Chemistry*, 2(6):65–81, 2018.

[8] Liming Wang, Wenlong Chen, Doudou Zhang, Yaping Du, Rose Amal, Shizhang Qiao, Jianbo Wu, and Zongyou Yin. Surface strategies for catalytic CO_2 reduction: from two-dimensional materials to nanoclusters to single atoms. *Chemical Society Reviews*, 48(21):5310–5349, 2019.

[9] Chengzhou Zhu, Shaofang Fu, Qiurong Shi, Dan Du, and Yuehe Lin. Single-atom electrocatalysts. *Angewandte Chemie International Edition*, 56(45):13944–13960, 2017.

[10] Robert Francke, Benjamin Schille, and Michael Roemelt. Homogeneously catalyzed electroreduction of carbon dioxide—methods, mechanisms, and catalysts. *Chemical Reviews*, 118(9):4631–4701, 2018.

[11] Minhan Li, Haifeng Wang, Wei Luo, Peter C Sherrell, Jun Chen, and Jianping Yang. Heterogeneous single-atom catalysts for electrochemical CO_2 reduction reaction. *Advanced Materials*, 32(34):2001848, 2020.

[12] Ana Sofia Varela, Wen Ju, Alexander Bagger, Patricio Franco, Jan Rossmeisl, and Peter Strasser. Electrochemical reduction of CO_2 on metal-nitrogen-doped carbon catalysts. *ACS Catalysis*, 9(8):7270–7284, 2019.

[13] Yong Wang, Jun Mao, Xianguang Meng, Liang Yu, Dehui Deng, and Xinhe Bao. Catalysis with two-dimensional materials confining single atoms: concept, design, and applications. *Chemical Reviews*, 119(3):1806–1854, 2018.

Chapter 2

Literature Review: Recent Progress of 3d Transition Metal Single-Atom Catalysts for Electrochemical CO$_2$ Reduction

Recent studies on the electrochemical CO_2 reduction reaction (CRR) have shown that the single-atom catalysts (SACs) largely improve the catalytic activity and selectivity. However, there are few review reports on the related SACs for the CRR. Herein, we highlighted recent graphene-supported 3d-block transition metal SACs for the CRR. The first section briefly introduced two effective methods of material characterization, which were used for the determination of the existence of SACs. The followed section reported the representative SACs categorized into four subgroups that are (1) Ni, (2) Fe, (3) Co, and (4) Cu, Mn, and Zn, orderly. Also, we proposed suggestions for the future development of SACs for the CRR.

This Chapter is presented as a review paper by Chaochen Xu, Anthony Vasileff, Yao Zheng, and Shi-Zhang Qiao: Recent progress of 3d transition metal single-atom catalysts for electrochemical CO_2 reduction.

Statement of Authorship

Title of Paper	Recent Progress of 3d Transition Metal Single-Atom Catalysts for Electrochemical CO_2 Reduction
Publication Status	☐ Published ☐ Accepted for Publication ☑ Submitted for Publication ☐ Unpublished and Unsubmitted work written in manuscript style
Publication Details	Chaochen Xu, Anthony Vasileff, Yao Zheng, Shi-Zhang Qiao. *Advanced Materials Interfaces,* 2020.

Principal Author

Name of Principal Author (Candidate)	Chaochen Xu
Contribution to the Paper	Proposed ideas, collected references, wrote the manuscript.
Overall percentage (%)	70
Certification:	This paper reports on original research I conducted during the period of my Higher Degree by Research candidature and is not subject to any obligations or contractual agreements with a third party that would constrain its inclusion in this thesis. I am the primary author of this paper.
Signature		Date	

Co-Author Contributions

By signing the Statement of Authorship, each author certifies that:

     i.   the candidate's stated contribution to the publication is accurate (as detailed above);

    ii.   permission is granted for the candidate in include the publication in the thesis; and

   iii.   the sum of all co-author contributions is equal to 100% less the candidate's stated contribution.

Name of Co-Author	Anthony Vasileff
Contribution to the Paper	Discussed this review paper, wrote a few sections, revised the manuscript
Signature		Date	

Name of Co-Author	Yao Zheng
Contribution to the Paper	Discussed the concepts, supervised the research project, and revised the manuscript.
Signature		Date	

Name of Co-Author	Shi-Zhang Qiao
Contribution to the Paper	Discussed concepts, supervised research project and revised the manuscript.
Signature		Date	

Name of Co-Author	Shi-Zhang Qiao
Contribution to the Paper	Discussed concepts, supervised research project and revised the manuscript.
Signature		Date	

Recent Progress of 3d Transition Metal Single-Atom Catalysts for Electrochemical CO₂ Reduction

Chaochen Xu, Anthony Vasileff, Yao Zheng, and Shi-Zhang Qiao*

C. Xu, Dr. A. Vasileff, Dr. Y. Zheng, Prof. S.-Z. Qiao
Centre for Materials in Energy and Catalysis
School of Chemical Engineering and Advanced Materials
The University of Adelaide
Adelaide, SA 5005, Australia
E-mail: s.qiao@adelaide.edu.au

ABSTRACT: Recent studies have shown that single-atom catalysts (SACs) have significantly better catalytic activity and selectivity for the electrochemical CO_2 reduction reaction (CRR) compared to their bulk metal and nanostructured counterparts. However, there are few relevant articles reviewing SACs for the CRR, despite their importance in the field. Herein, the scope of this review is the recent development of single-atom 3d-block transition metal catalysts (metal = Mn, Fe, Co, Ni, Cu, Zn) and their application as electrocatalysts for the CRR. We summarize the recent representative works by metal. Results show that (1) Ni and Fe SACs exhibit superior catalytic performance for CO evolution; (2) Co, Mn, Zn SACs are less reported due to their relative inertness for the CRR; (3) Cu SACs have ordinary catalytic activity for the CRR, however, C2 products are observed in a few reports. Point (3) is attractive to the prospective study of CO_2 to highly reduced products. Finally, we briefly propose some suggestions for the future development of SACs for the CRR.

Keywords: CO_2 conversion; electrocatalytic CO_2 reduction; single-atom catalyst; 3d transition metal

1. Introduction

The electrochemical CO_2 reduction reaction (CRR) is a promising renewable energy conversion technology which can effectively convert CO_2 to useful chemical feedstocks.[1-3] This process is thermodynamically feasible but suffers from sluggish kinetics and poor product selectivity. To solve this issue, well-designed catalysts are needed to improve catalytic activity and selectivity.[4, 5] Current research in this field mainly focuses on engineering nanoparticle catalysts to obtain favorable CRR performance.[6, 7] However, two issues with the use of nanostructured catalysts for the CRR have been raised: (1) low catalytic selectivity, and (2) low atomic utilization. The CRR involves multiple-electron transfer processes and every catalyst has different adsorption characteristics for reaction intermediates. Consequently, the CRR can proceed through multiple reaction pathways, resulting in various reduction products and poor overall selectivity.[8] For a catalytic process on a bulk or nanostructured catalyst, the adsorbed intermediate is adsorbed and reacts on the surface atoms/active sites only. However, the unexposed active sites underneath the surface are unable to directly interact with CO_2 and/or adsorbed intermediates, leading to significantly reduced atomic utilization.[7]

Recent studies have employed single-atom catalysts (SACs) for the CRR to address the above two issues.[7, 9, 10] These atomically dispersed catalysts can increase the total number of exposed active sites. To avoid aggregation of the metal centers into nanoparticles and thus reducing atom utilization, these atomically dispersed catalysts are generally stabilized by anchoring the metal atoms in a two-dimensional framework such as a carbon matrix.[7, 11] Specifically, the metal atom (M) is generally coordinated with adjacent non-metal atoms, such as nitrogen, to form M-N structures. These M-N structures have unique electronic configurations that are different from the M-M bonds in the bulk metals. This particular electronic distribution changes the adsorption characteristics of the metal sites for CO_2 and reaction intermediates.[11] Normally, the atomically dispersed metal atoms in SACs are fully exposed and participate in the catalytic

process at a sub-nanoscale level. Further, for the same metal content, the number of active sites in SACs is considerably higher than that in nanoparticles, which leads to an improvement of catalytic performance.[11] SAC catalysts for the CRR have recently been summarized in review papers, classified by synthesis method, chemical structures, and coordination environment.[10, 12] The metal center type is also a factor that can affect the catalytic process as the electronic structure is different for each metal. However, relevant reviews regarding the effects of the metal center in SAC catalysts toward CRR performance have not been comprehensively reported.

Herein, we highlighted recent graphene-supported 3d-block transition metal SACs for the CRR. The representative SACs are categorized into four groups: (1) Ni, (2) Fe, (3) Co, and (4) Cu, Mn, and Zn. We focus on their reported catalytic activities and discuss the effect of the metal center on the catalytic mechanism. Details of the reported catalytic performance, such as Faradaic efficiencies (FEs) and experimental conditions, are listed in **Table 1-4**. As concluding remarks, we provide some perspective on the challenges associated with the future development of SACs for the CRR.

2. Single-Atom Ni Catalysts

Single-atom Ni catalysts are the most reported 3d-block transition metal SACs for the CRR because of their extremely high catalytic performance (**Table 1**). Jiang *et al.* reported Ni atoms coordinated in a graphene shell as active centers for the CRR, exhibiting FEs over 90% at currents up to 60 mA per mg of catalyst. Theoretical simulations showed that compared to bulk Ni catalysts, the single-atom Ni sites have unique electronic structures that can enhance the conversion of CO_2 toward CO and can simultaneously suppress hydrogen evolution.[13] They further studied single-atom Ni in graphene nanosheets with four different types of Ni atomic configurations as shown in **Figure 1**a.[14] Density functional theory (DFT) calculations indicated that bulk Ni(111) has the highest barrier to *CO desorption. By comparison, nitrogen-

coordinated Ni (Ni-N) with double vacancies has the lowest barrier which facilitated CO formation during the CRR (**Figure 1b**). Further, the competing hydrogen evolution reaction was negligible on this single-atom Ni catalyst due to large limiting potentials for the HER (**Figure 1c**). As a result, a FE toward CO of 95% was achieved on the Ni-N graphene sample. Similarly, Ju *et al.* observed a FE for CO of 85% (at -0.78 V *vs.* RHE) on a nitrogen-doped porous carbon which contained active Ni-N_x moieties.[15] Li *et al*. reported an exclusive single-atom Ni, coordinated by four N atoms (Ni-N_4), using topochemical transformation. On this catalyst, a maximum FE of 99% toward CO was observed in the potential range of -0.5 to -0.9 V *vs.* RHE. Compared to the pristine graphene substrate, DFT calculations found that the CRR process is less hindered thermodynamically than the hydrogen evolution process on the Ni-N_4 catalyst.[16] Using a different synthesis method, Bi *et al.* reported an unsaturated Ni-N_3 structure derived from a ZIF-8 MOF.[17] [18] The low-coordinated Ni sites on the surface resulted in strong binding of activated CO_2 molecules, yielding a CO production of 71.9 % at -0.78 V *vs.* RHE. Similarly, Yan *et al.* also synthesized a ZIF-8-derived single-atom Ni with unsaturated coordination for the CRR. The measured FEs for CO were 92.0 ~ 98.0 % over a wide potential range from -0.53 to -1.03 V *vs.* RHE.[19] Cheng *et al.* dispersed Ni atoms on N-doped carbon nanotubes instead of on graphene sheets, and a high FE for CO of 91.3 % at -0.7 V *vs.* RHE was obtained.[20] Yang *et al.* reported atomically dispersed Ni(I) catalysts which exhibited stability over 100-h for CO evolution at -0.72 V *vs.* RHE.[21] In addition, they proposed a pathway for the reaction of CO_2 over their catalyst. As shown in **Figure 1d**, a CO_2 molecule is first adsorbed at the Ni atom site. The CO_2 molecule then accepts an electron from Ni to form activated *CO_2, which results in electron delocalization on the Ni. The subsequent reaction steps progress on the Ni site and CO is finally desorbed. Large-scale application of single-atom Ni catalysts for the CRR was demonstrated by Zheng *et al*. They prepared single-atom Ni catalysts at the gram-scale through a one-batch synthesis method and the catalyst was able to

operate at a current density of 100 mA cm^{-2} with nearly 100 % CO_2 conversion to CO.[22] This study provides an outlook for the application of SACs in industrial-scale CRR.

3. Single-Atom Fe Catalysts

Fe SACs are the second most reported 3d metal SACs in recent studies due to their comparable catalytic activities to Ni SACs (**Table 2**). Ju *et al.* experimentally determined that atomically dispersed Fe was active for CO_2 reduction to CO, with a FE for CO of roughly 60% at -0.5 V *vs.* RHE.[15] Zhang *et al.* later synthesized single-atom Fe catalysts coordinated with an additional axial ligand, *i.e.* Fe-N$_5$, which achieved near total selectivity for CO (FE ~97%) at -0.46 V *vs.* RHE (**Figure 2a**). They postulate that the d electrons of Fe transfer to the p$_{x,y}$ orbitals of the pyrrolic-N. This electronic effect weakens the π back-donation between Fe-CO which results in weaker adsorption of CO at the Fe-N$_5$ site and subsequently enhances CO kinetics.[23] Another work found that atomically dispersed Fe could maintain a high oxidation state (+3) during CO_2 reduction, which facilitated CO_2 adsorption and weakened CO absorption compared to Fe^{2+} sites. Due to this optimized adsorption of reactants and intermediates in this system, CO_2 could rapidly react and form *CO intermediates, and then be effectively desorbed from the surface as CO (**Figure 2b**).[24] Xu *et al.* investigated the synergistic effect between single-atom Fe and adjacent N species for CO_2 adsorption and reduction.[25] As shown in **Figure 2c**, the FE toward CO for three different samples was clearly correlated with the N species composition. Specifically, the catalysts with a higher content of pyrrolic-N species showed a positive correlation with the FE for CO. However, there was no such relationship for the set Fe nanoparticle (Fe-NP) samples (**Figure 2d**). These experimental results demonstrated that the role of the Fe centers was mainly to provide protons for the CRR via water dissociation, while the negatively charged pyrrolic-N sites provided sites for CO_2 adsorption.

4. Single-Atom Co Catalysts

Compared to Ni and Fe SACs, relatively fewer studies have been devoted to Co SAC catalysts for the CRR. This may be due to their low selectivity reported for C1 products (**Table 3**). However, some representative works using Co SACs exhibited unique structures and performances. In particular, a Co SAC with $Co-N_5$ configuration was first reported by Pan *et al*. In this material, the additional N coordination was assigned to the N atoms located in the N-doped carbon spheres. Compared to CoPc, the $Co-N_5$ sites acted as active centers for CO_2 activation and showed nearly 100 % FE for CO (**Figure 3a**). It was also found the FEs for CO decreased with decreasing coordination number of the $Co-N_x$ moiety (**Figure 3b**).[26] Interestingly, Wang *et al*. found the opposite trend whereby Co SACs with a lower coordination number better facilitated the CRR (**Figure 3c**), which is consistent with previous findings for Ni SACs.[27] From a series of ZIF-derived Co SACs with different coordination numbers, the highest FE for CO was observed on atomically dispersed Co with two-coordinating N atoms. Although unsaturated coordination of the metal center can improve CRR performance generally, the opposite was observed for ZIF-derived Co SACs reported by Geng *et al*. A well-coordinated Co_1-N_4 sample exhibited a high FE for CO of 80 % at -0.8 V *vs*. RHE, while an unsaturated $Co_1-N_{4-x}C_x$ sample exhibited a FE of less than 50 % (**Figure 3d**).[28] Further experiments showed that Co_1-N_4 exhibited stronger CO_2 binding strength compared to $Co_1-N_{4-x}C_x$. This indicates that the coordination environment contributes predominantly to strengthening the binding of CO_2, and ultimately changes the catalytic selectivity and activity.

5. Single-Atom Cu, Mn, and Zn Catalysts

Details of reported CRR performance on single-atom Cu, Mn, Zn catalysts are given in **Table 4**. Cu has been widely reported as a unique metal for the CRR because of its mild adsorption of intermediates and the ability to facilitate C-C coupling and produce C2 products.[4, 5, 29] However, atomically dispersed Cu has a distinct electronic structure which makes it

fundamentally different from bulk Cu catalysts. In a work by Jiao *et al.*, theoretical onset potentials were predicted using free energy diagrams on three different surfaces (**Figure 4a**).[30] Cu single atoms coordinated by graphitic carbon nitride (Cu-C_3N_4) were found to have lower onset potentials for CO_2 reduction products compared to Cu supported on nitrogen-doped graphene (Cu-NC) and Cu(111). Furthermore, in this work, the experimental results confirmed that Cu-C_3N_4 exhibits better catalytic activity with lower onset potential and more C2 products than Cu-NC.[30] Guan *et al.* found a relatively high selectivity toward CH_4 of 38.6% at -1.6 V *vs.* RHE on Cu SACs (**Figure 4b**). Compared to the examples above with relatively weak *CO binding, the Cu SACs likely had relatively strong adsorption of *CO to facilitate further reduction.[31] Unlike these two studies, Yang *et al.* studied a Cu catalyst that was highly selective towards CO and CH_3OH.[32] The isolated Cu atoms on carbon nanofibers achieved a maximum FE for CH_3OH of 44 % at -0.9 V *vs.* RHE, and the hydrogen evolution was completely suppressed (**Figure 4c**). As shown in **Figure 4d**, the proposed reaction pathway shows that *CO adsorbed on the Cu-N_4 site accepts an electron and proton to form *COH. The barrier for *COH reduction to *C is prohibitively high and *CHOH (and subsequently CH_3OH) is formed instead. Some of the single-atom Cu catalysts reported only catalyze CO_2 and H_2O to CO and H_2, without any further reduction products. For example, an unsaturated single-atom Cu catalyst (Cu-N_2/NG) exhibited a FE for CO of 81 % at -0.5 V *vs.* RHE (**Figure 4e**).[33] Karapinar *et al.* reported similar results with a single-atom $Cu_{0.5}$NC catalyst.[34] Therefore, Cu SACs are significantly different from the other transition metal SACs given their ability to produce a variety of both C1 and C2 products.

Mn and Zn SAC catalysts are rarely reported for the CRR. Recently, Zhang *et al.* reported a single-atom Mn for the CRR, exhibiting a maximum of FE of 97 % towards CO at -0.6 V *vs.* RHE. The experimental and theoretical results revealed that the Mn centers were the active sites.[35] A study of Zn SAC catalysts showed that CH_4 was the predominant CO_2 reduction

product obtained. Theoretical calculations suggested that the O atom in *OCHO, rather than the C atom, was preferentially adsorbed on the Zn active site. This blocked CO generation and aided the production of further reduction products, *i.e.* CH_4.[36]

6. Conclusions

In conclusion, SACs have shown great potential as selective catalysts for the CRR and exhibit varied catalytic performance depending on the metal center. Significantly high selectivity toward CO has mostly been achieved on Ni and Fe SACs. As summarized in **Figure 5a** and **b**, the average FE toward CO on Ni SACs is 93.9 %, which is higher than that on Fe SACs (85.6 %). However, the average overpotential of maximum CO selectivity on Fe SACs is only 450 mV, which is lower than that on Ni SACs (690 mV). Hence, both Ni and Fe SACs are promising candidates for large-scale CO_2 electrolysis due to their remarkable catalytic properties. For Co SACs, the major reduction product is also CO and while some examples are comparable to the Ni and Fe catalysts, the full set of CO selectivity reported is quite varied (**Figure 5c**). From **Figure 5d**, it is worthy to note that while single-atom Cu catalysts also have quite varied CO selectivity, Cu is a unique catalyst which can produce reduction products beyond CO. With relatively few reports of Cu SACs, there is much room for the development of these materials as selective catalysts for multi-carbon products. This can likely be achieved by various material engineering techniques like changing the Cu loading, introducing a secondary metal atom to form Cu-M dual active sites, changing the support structure, *etc*. We anticipate that the optimization of Cu SACs will show promising development for electrocatalytic CO_2 reduction. For other transition metal SAC candidates (*e.g.* Mn and Zn SACs), relatively fewer reports exist in the literature despite their promising early results. Therefore, it appears that these metals require greater attention in the search for more selective CRR catalysts. In particular, for Zn SACs, which have exhibited CO_2 reduction to CH_4, they represent a metal center beyond Cu

with the capability of further reduction of CO_2 past CO. This, therefore, provides the opportunity to widen the scope of CRR catalyst materials in a meaningful way.

Acknowledgements

Received: ((will be filled in by the editorial staff))
Revised: ((will be filled in by the editorial staff))
Published online: ((will be filled in by the editorial staff))

References

[1]   C. Chen, J. F. Khosrowabadi Kotyk, S. W. Sheehan, *Chem* **2018**, *4*, 2571-2586.

[2]   M. Aresta, A. Dibenedetto, A. Angelini, *Chem. Rev.* **2014**, *114*, 1709-1742.

[3]   E. E. Benson, C. P. Kubiak, A. J. Sathrum, J. M. Smieja, *Chem. Soc. Rev.* **2009**, *38*, 89-99.

[4]   S. Nitopi, E. Bertheussen, S. B. Scott, X. Liu, A. K. Engstfeld, S. Horch, B. Seger, I. E. L. Stephens, K. Chan, C. Hahn, J. K. Norskov, T. F. Jaramillo, I. Chorkendorff, *Chem. Rev.* **2019**, *119*, 7610-7672.

[5]   A. Vasileff, C. Xu, Y. Jiao, Y. Zheng, S.-Z. Qiao, *Chem* **2018**, *4*, 1809-1831.

[6]   R. Francke, B. Schille, M. Roemelt, *Chem. Rev.* **2018**, *118*, 4631-4701.

[7]   L. Wang, W. Chen, D. Zhang, Y. Du, R. Amal, S. Qiao, J. Wu, Z. Yin, *Chem. Soc. Rev.* **2019**, *48*, 5310-5349.

[8]   R. Kortlever, J. Shen, K. J. Schouten, F. Calle-Vallejo, M. T. Koper, *J Phys Chem Lett* **2015**, *6*, 4073-4082.

[9]   A. S. Varela, W. Ju, A. Bagger, P. Franco, J. Rossmeisl, P. Strasser, *ACS Catal.* **2019**, *9*, 7270-7284.

[10]   M. Li, H. Wang, W. Luo, P. C. Sherrell, J. Chen, J. Yang, *Adv. Mater.* **2020**, 2001848.

[11]   Y. Wang, J. Mao, X. Meng, L. Yu, D. Deng, X. Bao, *Chem. Rev.* **2019**, *119*, 1806-1854.

[12]   T. N. Nguyen, M. Salehi, Q. V. Le, A. Seifitokaldani, C. T. Dinh, *ACS Catal.* **2020**, *10*, 10068-10095.

[13] K. Jiang, S. Siahrostami, A. J. Akey, Y. Li, Z. Lu, J. Lattimer, Y. Hu, C. Stokes, M. Gangishetty, G. Chen, Y. Zhou, W. Hill, W.-B. Cai, D. Bell, K. Chan, J. K. Nørskov, Y. Cui, H. Wang, *Chem* **2017**, *3*, 950-960.

[14] K. Jiang, S. Siahrostami, T. Zheng, Y. Hu, S. Hwang, E. Stavitski, Y. Peng, J. Dynes, M. Gangisetty, D. Su, K. Attenkofer, H. Wang, *Energy Environ. Sci.* **2018**, *11*, 893-903.

[15] W. Ju, A. Bagger, G. P. Hao, A. S. Varela, I. Sinev, V. Bon, B. Roldan Cuenya, S. Kaskel, J. Rossmeisl, P. Strasser, *Nat. Commun.* **2017**, *8*, 944.

[16] X. Li, W. Bi, M. Chen, Y. Sun, H. Ju, W. Yan, J. Zhu, X. Wu, W. Chu, C. Wu, Y. Xie, *J. Am. Chem. Soc.* **2017**, *139*, 14889-14892.

[17] W. Bi, X. Li, R. You, M. Chen, R. Yuan, W. Huang, X. Wu, W. Chu, C. Wu, Y. Xie, *Adv. Mater.* **2018**, *30*, 1706617.

[18] C. Zhao, X. Dai, T. Yao, W. Chen, X. Wang, J. Wang, J. Yang, S. Wei, Y. Wu, Y. Li, *J. Am. Chem. Soc.* **2017**, *139*, 8078-8081.

[19] C. Yan, H. Li, Y. Ye, H. Wu, F. Cai, R. Si, J. Xiao, S. Miao, S. Xie, F. Yang, Y. Li, G. Wang, X. Bao, *Energy Environ. Sci.* **2018**, *11*, 1204-1210.

[20] Y. Cheng, S. Zhao, B. Johannessen, J. P. Veder, M. Saunders, M. R. Rowles, M. Cheng, C. Liu, M. F. Chisholm, R. De Marco, H. M. Cheng, S. Z. Yang, S. P. Jiang, *Adv. Mater.* **2018**, *30*, 1706287.

[21] H. B. Yang, S.-F. Hung, S. Liu, K. Yuan, S. Miao, L. Zhang, X. Huang, H.-Y. Wang, W. Cai, R. Chen, J. Gao, X. Yang, W. Chen, Y. Huang, H. M. Chen, C. M. Li, T. Zhang, B. Liu, *Nat. Energy* **2018**, *3*, 140-147.

[22] T. Zheng, K. Jiang, N. Ta, Y. Hu, J. Zeng, J. Liu, H. Wang, *Joule* **2019**, *3*, 265-278.

[23] H. Zhang, J. Li, S. Xi, Y. Du, X. Hai, J. Wang, H. Xu, G. Wu, J. Zhang, J. Lu, J. Wang, *Angew. Chem. Int. Ed.* **2019**, *58*, 14871-14876.

[24] J. Gu, C. S. Hsu, L. Bai, H. M. Chen, X. Hu, *Science* **2019**, *364*, 1091-1094.

[25] C. Xu, A. Vasileff, D. Wang, B. Jin, Y. Zheng, S.-Z. Qiao, *Nanoscale Horiz.* **2019**, *4*, 1411-1415.

[26] Y. Pan, R. Lin, Y. Chen, S. Liu, W. Zhu, X. Cao, W. Chen, K. Wu, W. C. Cheong, Y. Wang, L. Zheng, J. Luo, Y. Lin, Y. Liu, C. Liu, J. Li, Q. Lu, X. Chen, D. Wang, Q. Peng, C. Chen, Y. Li, *J. Am. Chem. Soc.* **2018**, *140*, 4218-4221.

[27]   X. Wang, Z. Chen, X. Zhao, T. Yao, W. Chen, R. You, C. Zhao, G. Wu, J. Wang, W. Huang, J. Yang, X. Hong, S. Wei, Y. Wu, Y. Li, *Angew. Chem. Int. Ed.* **2018**, *57*, 1944-1948.

[28]   Z. Geng, Y. Cao, W. Chen, X. Kong, Y. Liu, T. Yao, Y. Lin, *Appl. Catal. B* **2019**, *240*, 234-240.

[29]   Y. Zheng, A. Vasileff, X. Zhou, Y. Jiao, M. Jaroniec, S. Z. Qiao, *J. Am. Chem. Soc.* **2019**, *141*, 7646-7659.

[30]   Y. Jiao, Y. Zheng, P. Chen, M. Jaroniec, S. Z. Qiao, *J. Am. Chem. Soc.* **2017**, *139*, 18093-18100.

[31]   A. Guan, Z. Chen, Y. Quan, C. Peng, Z. Wang, T.-K. Sham, C. Yang, Y. Ji, L. Qian, X. Xu, G. Zheng, *ACS Energy Lett.* **2020**, *5*, 1044-1053.

[32]   H. Yang, Y. Wu, G. Li, Q. Lin, Q. Hu, Q. Zhang, J. Liu, C. He, *J. Am. Chem. Soc.* **2019**, *141*, 12717-12723.

[33]   W. Zheng, J. Yang, H. Chen, Y. Hou, Q. Wang, M. Gu, F. He, Y. Xia, Z. Xia, Z. Li, B. Yang, L. Lei, C. Yuan, Q. He, M. Qiu, X. Feng, *Adv. Funct. Mater.* **2019**, *30*, 1907658.

[34]   D. Karapinar, N. T. Huan, N. Ranjbar Sahraie, J. Li, D. Wakerley, N. Touati, S. Zanna, D. Taverna, L. H. Galvao Tizei, A. Zitolo, F. Jaouen, V. Mougel, M. Fontecave, *Angew. Chem. Int. Ed.* **2019**, *58*, 15098-15103.

[35]   B. Zhang, J. Zhang, J. Shi, D. Tan, L. Liu, F. Zhang, C. Lu, Z. Su, X. Tan, X. Cheng, B. Han, L. Zheng, J. Zhang, *Nat. Commun.* **2019**, *10*, 2980.

[36]   L. Han, S. Song, M. Liu, S. Yao, Z. Liang, H. Cheng, Z. Ren, W. Liu, R. Lin, G. Qi, X. Liu, Q. Wu, J. Luo, H. L. Xin, *J. Am. Chem. Soc.* **2020**, *142*, 12563-12567.

[37]   Y. Cheng, S. Zhao, H. Li, S. He, J.-P. Veder, B. Johannessen, J. Xiao, S. Lu, J. Pan, M. F. Chisholm, S.-Z. Yang, C. Liu, J. G. Chen, S. P. Jiang, *Appl. Catal. B* **2019**, *243*, 294-303.

[38]   Q. Fan, P. Hou, C. Choi, T. S. Wu, S. Hong, F. Li, Y. L. Soo, P. Kang, Y. Jung, Z. Sun, *Adv. Energy Mater.* **2019**, *10*, 1903068.

[39]   F. Li, S. Hong, T.-S. Wu, X. Li, J. Masa, Y.-L. Soo, Z. Sun, *ACS Appl. Energy Mater.* **2019**, *2*, 8836-8842.

[40]   S. Ma, P. Su, W. Huang, S. P. Jiang, S. Bai, J. Liu, *ChemCatChem* **2019**, *11*, 6092-6098.

[41]   K. Mou, Z. Chen, X. Zhang, M. Jiao, X. Zhang, X. Ge, W. Zhang, L. Liu, *Small* **2019**, *15*, 1903668.

[42] L. Takele Menisa, P. Cheng, C. Long, X. Qiu, Y. Zheng, J. Han, Y. Zhang, Y. Gao, Z. Tang, *Nanoscale* **2020**, *12*, 16617-16626.

[43] Y. N. Gong, L. Jiao, Y. Qian, C. Y. Pan, L. Zheng, X. Cai, B. Liu, S. H. Yu, H. L. Jiang, *Angew. Chem. Int. Ed.* **2020**, *59*, 2705-2709.

[44] Q. He, D. Liu, J. H. Lee, Y. Liu, Z. Xie, S. Hwang, S. Kattel, L. Song, J. G. Chen, *Angew. Chem. Int. Ed.* **2020**, *59*, 3033-3037.

[45] S. He, D. Ji, J. Zhang, P. Novello, X. Li, Q. Zhang, X. Zhang, J. Liu, *J. Phys. Chem. B* **2020**, *124*, 511-518.

[46] Y. Hou, Y.-L. Liang, P.-C. Shi, Y.-B. Huang, R. Cao, *Appl. Catal. B* **2020**, *271*, 118929.

[47] D. M. Koshy, S. Chen, D. U. Lee, M. B. Stevens, A. M. Abdellah, S. M. Dull, G. Chen, D. Nordlund, A. Gallo, C. Hahn, D. C. Higgins, Z. Bao, T. F. Jaramillo, *Angew. Chem. Int. Ed.* **2020**, *59*, 4043-4050.

[48] S. Liu, H. B. Yang, S. F. Hung, J. Ding, W. Cai, L. Liu, J. Gao, X. Li, X. Ren, Z. Kuang, Y. Huang, T. Zhang, B. Liu, *Angew. Chem. Int. Ed.* **2020**, *59*, 798-803.

[49] Z. Ma, X. Zhang, D. Wu, X. Han, L. Zhang, H. Wang, F. Xu, Z. Gao, K. Jiang, *J. Colloid Interface Sci.* **2020**, *570*, 31-40.

[50] X. Rong, H. J. Wang, X. L. Lu, R. Si, T. B. Lu, *Angew. Chem. Int. Ed.* **2020**, *59*, 1961-1965.

[51] C. Zhang, Z. Fu, Q. Zhao, Z. Du, R. Zhang, S. Li, *Electrochem. Commun.* **2020**, *116*, 106758.

[52] S. Zhao, T. Wang, G. Zhou, L. Zhang, C. Lin, J. P. Veder, B. Johannessen, M. Saunders, L. Yin, C. Liu, R. De Marco, S. Z. Yang, Q. Zhang, S. P. Jiang, *ChemNanoMat* **2020**, *6*, 1063-1074.

[53] R. Daiyan, X. Lu, X. Tan, X. Zhu, R. Chen, S. C. Smith, R. Amal, *ACS Appl. Energy Mater.* **2019**, *2*, 8002-8009.

[54] Y. Lu, H. Wang, P. Yu, Y. Yuan, R. Shahbazian-Yassar, Y. Sheng, S. Wu, W. Tu, G. Liu, M. Kraft, R. Xu, *Nano Energy* **2020**, *77*, 105158.

[55] F. Pan, H. Zhang, K. Liu, D. Cullen, K. More, M. Wang, Z. Feng, G. Wang, G. Wu, Y. Li, *ACS Catal.* **2018**, *8*, 3116-3122.

[56] C. Zhang, S. Yang, J. Wu, M. Liu, S. Yazdi, M. Ren, J. Sha, J. Zhong, K. Nie, A. S. Jalilov, Z. Li, H. Li, B. I. Yakobson, Q. Wu, E. Ringe, H. Xu, P. M. Ajayan, J. M. Tour, *Adv. Energy Mater.* **2018**, *8*, 1703487.

[57] Y. Chen, L. Zou, H. Liu, C. Chen, Q. Wang, M. Gu, B. Yang, Z. Zou, J. Fang, H. Yang, *J. Phys. Chem. C* **2019**, *123*, 16651-16659.

[58] X. Qin, S. Zhu, F. Xiao, L. Zhang, M. Shao, *ACS Energy Lett.* **2019**, *4*, 1778-1783.

[59] J. Tuo, Y. Zhu, L. Cheng, Y. Li, X. Yang, J. Shen, C. Li, *ChemSusChem* **2019**, *12*, 2644-2650.

[60] X. Li, S. Xi, L. Sun, S. Dou, Z. Huang, T. Su, X. Wang, *Adv. Sci.* **2020**, 2001545.

[61] F. Pan, B. Li, E. Sarnello, Y. Fei, Y. Gang, X. Xiang, Z. Du, P. Zhang, G. Wang, H. T. Nguyen, T. Li, Y. H. Hu, H. C. Zhou, Y. Li, *ACS Nano* **2020**, *14*, 5506-5516.

[62] S. Wu, X. Lv, D. Ping, G. Zhang, S. Wang, H. Wang, X. Yang, D. Guo, S. Fang, *Electrochim. Acta* **2020**, *340*, 135930.

[63] Y. Zhu, X. Li, X. Wang, K. Lv, G. Xiao, J. Feng, X. Jiang, M. Fang, Y. Zhu, *Chemistry Select* **2020**, *5*, 1282-1287.

[64] P. Hou, W. Song, X. Wang, Z. Hu, P. Kang, *Small* **2020**, *16*, 2001896.

[65] H. Yang, Q. Lin, Y. Wu, G. Li, Q. Hu, X. Chai, X. Ren, Q. Zhang, J. Liu, C. He, *Nano Energy* **2020**, *70*, 104454.

[66] R. Daiyan, R. Chen, P. Kumar, N. M. Bedford, J. Qu, J. M. Cairney, X. Lu, R. Amal, *ACS Appl. Mater. Interfaces* **2020**, *12*, 9307-9315.

[67] C. Xu, X. Zhi, A. Vasileff, D. Wang, B. Jin, Y. Jiao, Y. Zheng, S.-Z. Qiao, *Small Struct.* **2020**, *1*, 2000058.

[68] F. Yang, X. Mao, M. Ma, C. Jiang, P. Zhang, J. Wang, Q. Deng, Z. Zeng, S. Deng, *Carbon* **2020**, *168*, 528-535.

[69] F. Yang, P. Song, X. Liu, B. Mei, W. Xing, Z. Jiang, L. Gu, W. Xu, *Angew. Chem. Int. Ed.* **2018**, *57*, 12303-12307.
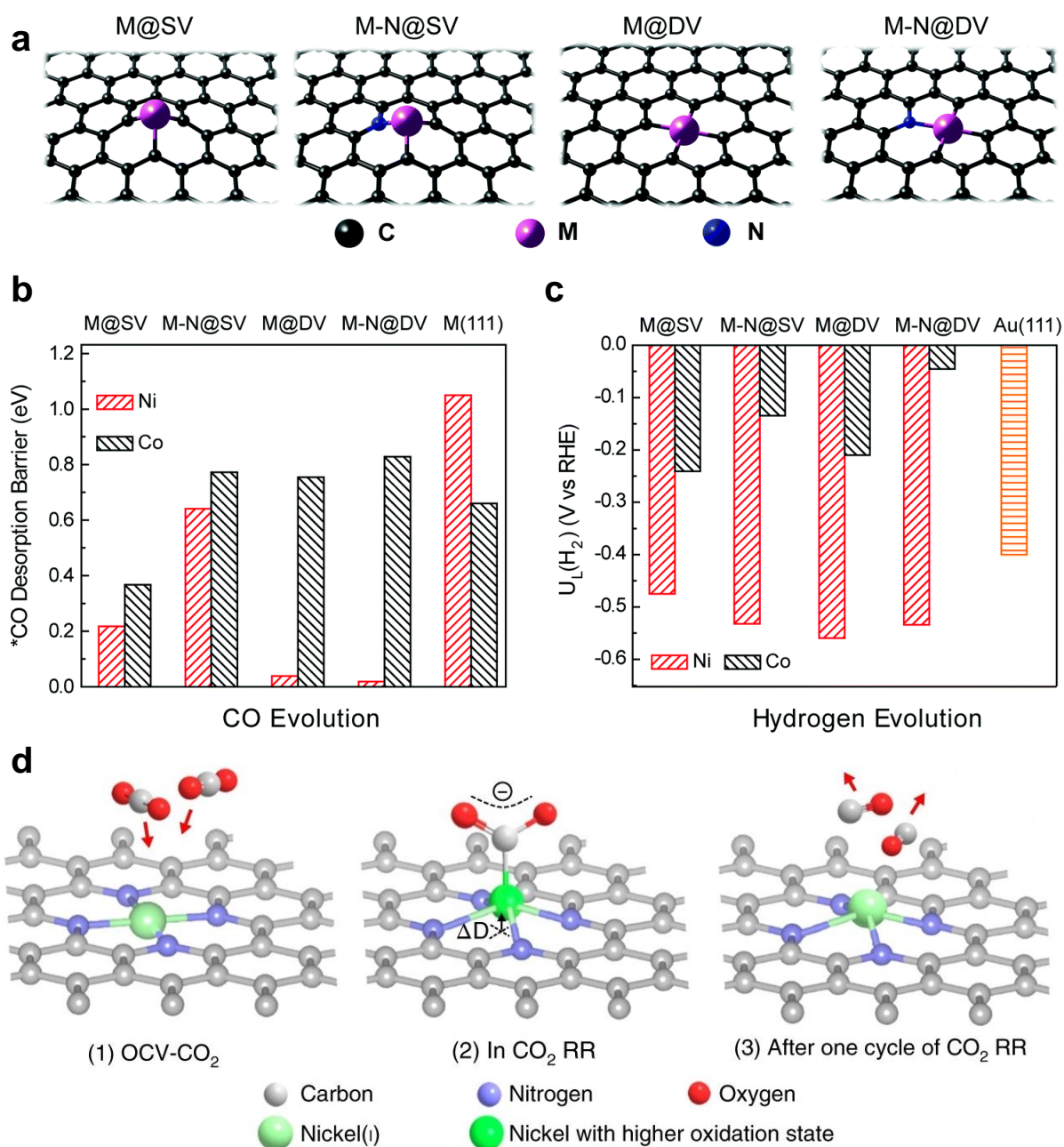
Figure 1 (a) Different atomic configurations in a graphene matrix for metal-carbon and/or metal-nitrogen-carbon coordination. (b) The desorption barrier for *CO and (c) the limiting potential diagram for the HER on model systems.[14] (d) Structural evolution of the active site in electrochemical CO_2 reduction: (1) The activation process for CO_2 molecules on the Ni(I) site at open-circuit voltage (OCV); (2) The CO_2 reduction process on the Ni site with higher oxidation state; and (3) The CO desorption process.[21] Reprinted and adapted with permission.
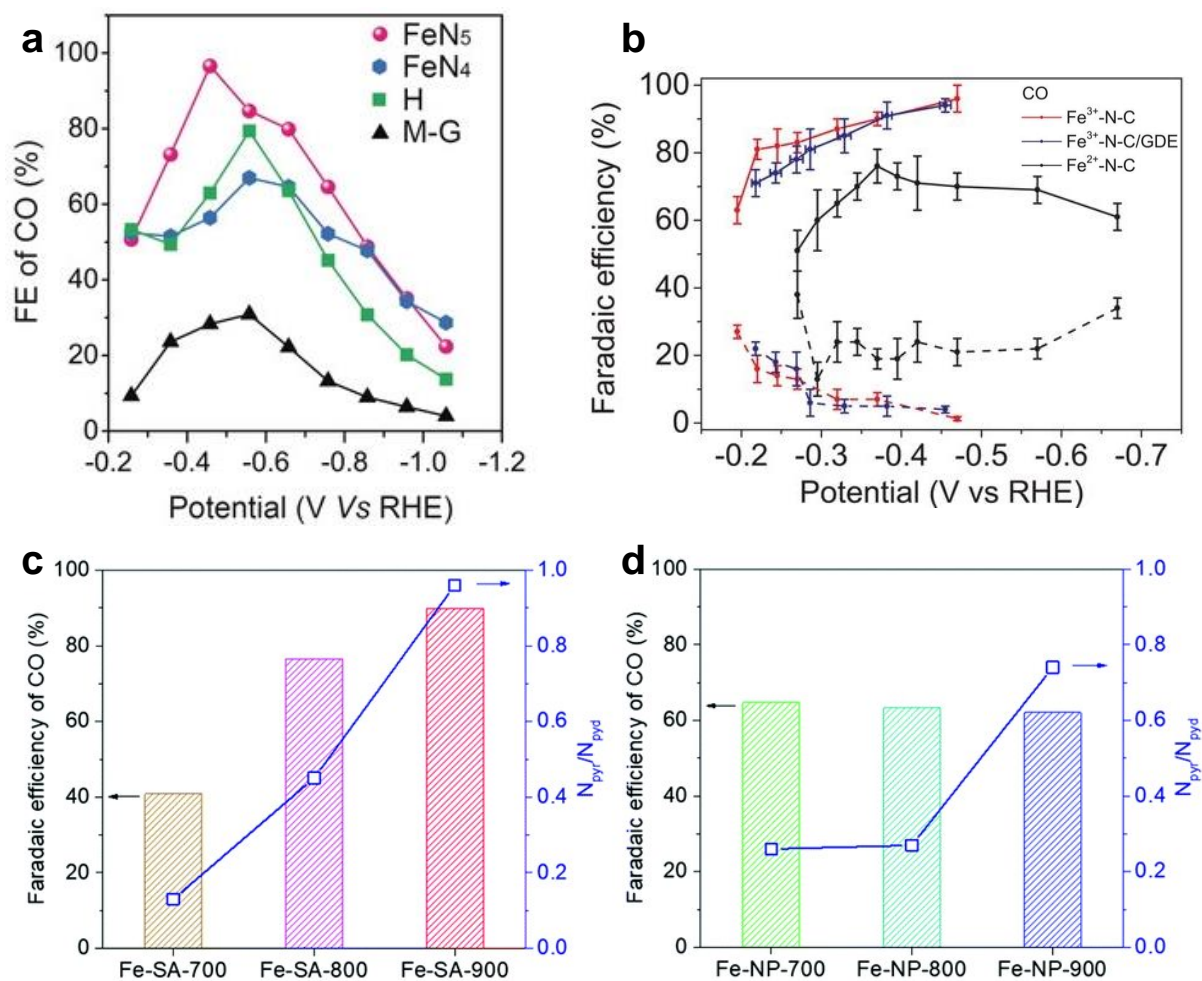
Figure 2 (a) Comparison of electrocatalytic activity of as-synthesized Fe catalysts.[23] (b) FE

for CO (solid lines) and H_2 (dashed lines) production on atomically dispersed Fe catalysts.[24]

The measured FEs of CO on (c) Fe-SA samples and (d) Fe-NP samples with the corresponding

ratios of pyrrolic-to-pyridinic-N species.[25] Reprinted and adapted with permission.
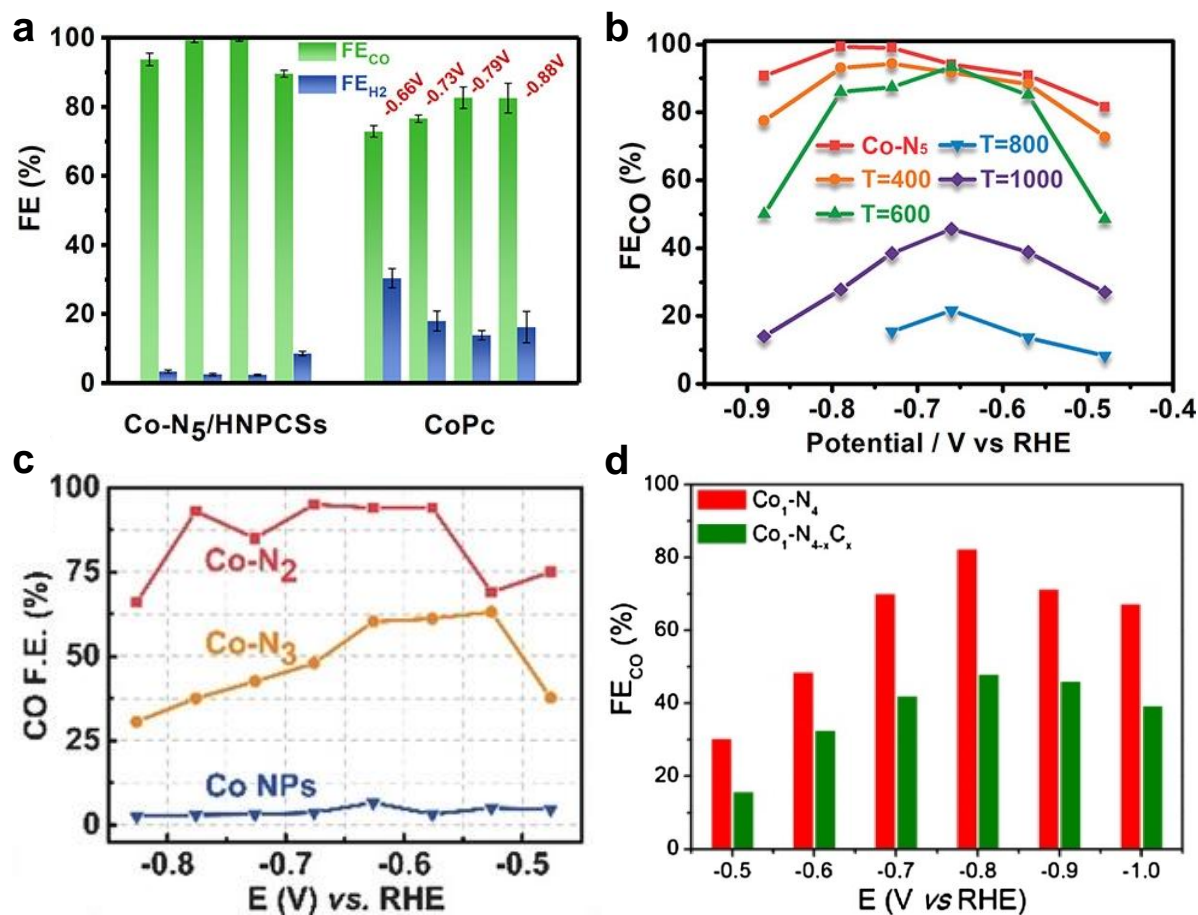
Figure 3 (a) FEs for CO and H_2 on Co-N$_5$/HNPCSs and CoPc.[26] (b) FEs for CO on CoN$_5$/HNPCSs synthesized at different annealing temperatures.[26] FEs for CO obtained at different applied potentials for (c) Co-N$_2$, Co-N$_3$, and Co NPs,[27] and (d) Co$_1$-N$_4$ and Co$_1$-N$_{4-x}$C$_x$.[28] Reprinted and adapted with permission.
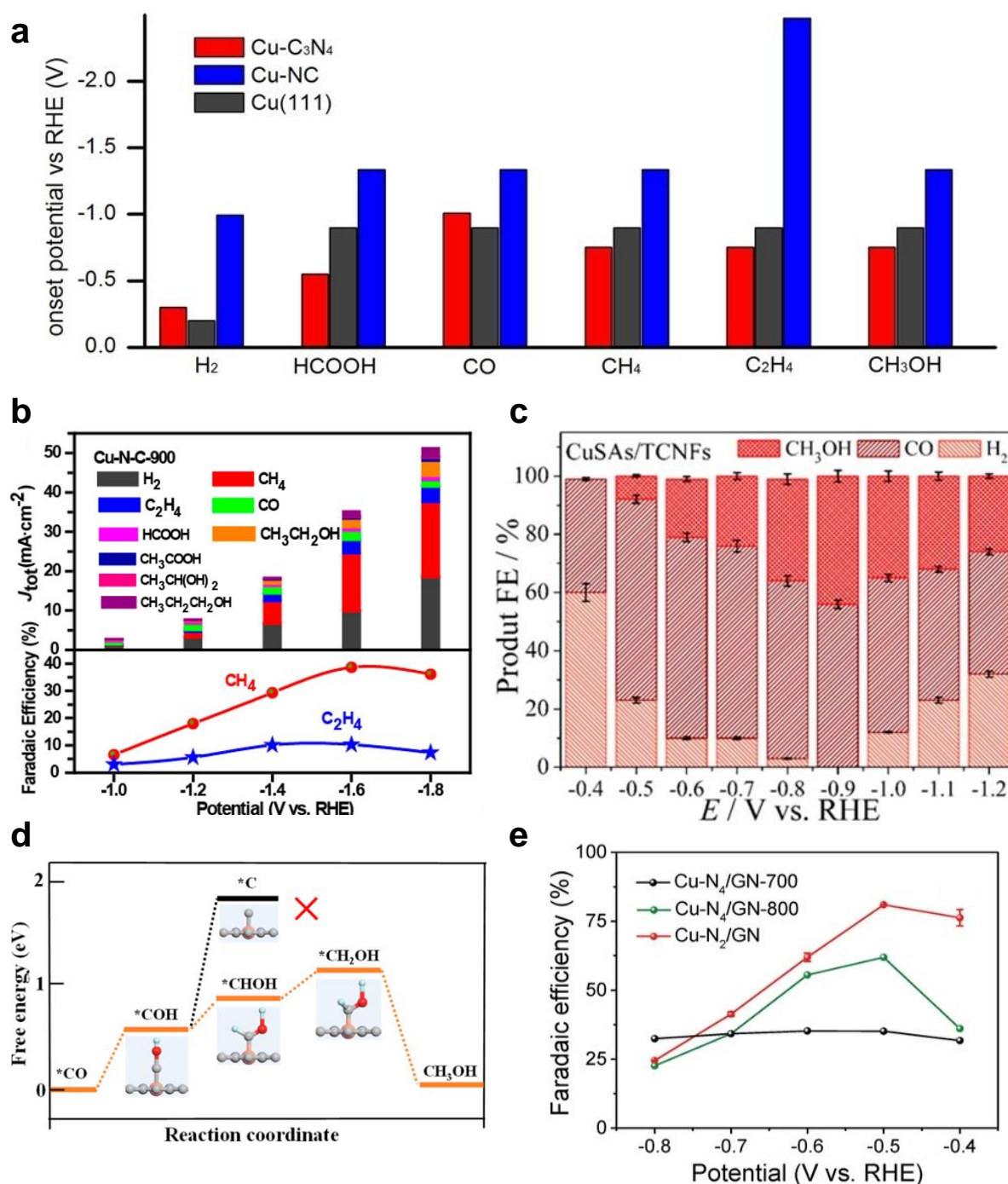
Figure 4 (a) Summary of onset potentials for various CRR products as predicted by the reaction free energy diagrams on three different surfaces.[30] (b) CO_2 electroreduction performance of the Cu-N-C-900 catalyst.[31] (c) FEs for CRR products on the CuSAs/TCNFs catalyst and (d) free energy diagram for the conversion of *CO to CH_3OH on the Cu-N_4 structure.[32] (e) FE for CO on Cu-N_4/GN-700, Cu-N_4/GN-800, and Cu-N_2/GN.[33] Reprinted and adapted with permission.
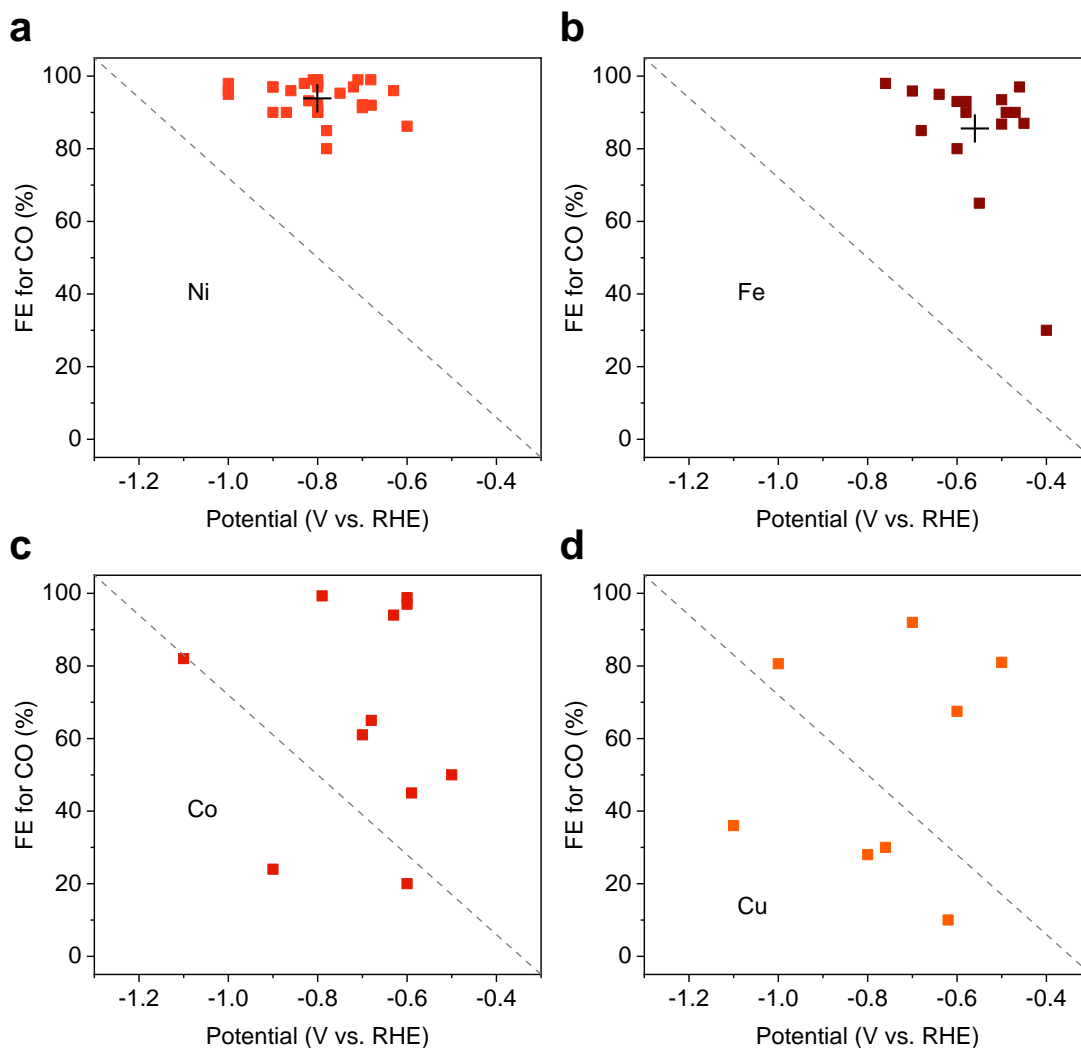
Figure 5 Reported FEs for CO on major single-atom M catalysts: a) Ni, b) Fe, c) Co, and d) Cu. The dashed lines indicate points located in the top-right region are generally favored due to both low applied potential and high CO selectivity. The average reported performance of single-atom Ni is FE_{CO} = 93.7% at -0.79 V *vs.* RHE (a) and of single-atom Fe is FE_{CO} = 85.6% at -0.56 V *vs.* RHE (b). Reprinted and adapted with permission. Data used in this figure is listed in Table 1-4.

Table 1. Reported FEs on single-atom Ni catalysts. Reprinted and adapted with permission.

Catalyst	KHCO$_3$ (M)	Potential (V *vs.* RHE)	FE for CO (%)	Ref.
NiN-GS	0.1	-0.82	93.2	[13]
Ni-N$_x$	0.1	-0.78	85	[15]
Ni-N$_4$	0.5	-0.81	99	[18]
Ni^{2+}@NG	0.5	-0.68	92	[17]
NiSA-N-CNTs	0.5	-0.70	91.3	[20]
Ni-NG	0.5	-0.87	90	[14]
C-Zn$_1$Ni$_4$ ZIF-8	0.5	-0.83	98.0	[19]
A-Ni-NSG	0.5	-0.72	97	[21]
Ni-N-MEGO	0.5	-0.7	92.1	[37]
NC-CNTs (Ni)	0.1	-0.8	90	[38]
Ni/NC	0.1	-0.8	92.3	[39]
Ni SAs/NCNTs	0.5	-0.9	97	[39]
Ni-N/C-1/4	0.5	-0.78	80	[40]
NiSA-NGA-900	0.5	-0.8	90.2	[41]
Ni-NCB	0.5	-0.681	99	[22]
Ni-N-C	0.1	-0.8	97	[42]
Ni$_{SA}$-N$_2$-C	0.5	-0.8	98	[43]
Ni-NC	0.5	-0.9	97	[44]
NiSA-NWC	0.1	-1.0[a]	95	[45]
Ni/NCTs	0.5	-1.0	98	[46]
Ni-PACN	0.1	-0.8	99	[47]
Ni-CNT-CC	0.5	-0.71	99	[48]
Ni-N-CNSs	0.5	-0.75	95.3	[49]
Ni-N$_3$-V SAC	0.5	-0.9	90	[50]
SA-Ni@NC	0.1	-0.6	86.2	[51]
NiSA-N-NG	0.5	-0.63	96	[52]
Ni@NC-900	0.1	-1.0	96	[53]
NiSA/N-C	0.1	-0.86	96	[54]

[a] -1.6 V *vs.* Ag/AgCl (Potentials measured against the Ag/AgCl electrode)

Table 2. Reported FEs on single-atom Fe catalysts. Reprinted and adapted with permission.

Catalyst	KHCO$_3$ (M)	Potential (V *vs.* RHE)	FE for CO (%)	Ref.
Fe-N$_x$	0.1	-0.55	65	[15]
Fe^{3+}@NG	0.5	-0.68	85	[17]
Fe-NG	0.5	-0.40	30	[14]
Fe-N-C	0.1	-0.5	86.8	[42]
Fe-N-C	0.1	-0.58	93	[55]
Fe/NG-750	0.1	-0.6	80	[56]
Fe-N-PC	0.5	-0.49	90	[57]
Fe^{3+}-N-C	0.5	-0.47	90	[24]
Fe-N-C	0.5	-0.5	93.5	[58]
MPPCN-750	0.5	-0.7	95.9	[59]
Fe-SA-900	0.1	-0.58	90	[25]
FeN$_5$	0.1	-0.46	97	[23]
FeN$_4$/C	0.1	-0.6	93	[60]
Fe-N/CNT@GNR	0.1	-0.76	98	[61]
Fe-N-C-0.5	0.5	-0.64	95	[62]
Fe-SA/NCS-700	0.5	-0.45	87	[63]

Table 3. Reported FEs on single-atom Co catalysts. Reprinted and adapted with permission.

| Catalyst	KHCO$_3$ (M)	Potential (V *vs.* RHE)	FE for CO (%)	Ref.
Co-N$_x$	0.1	-0.60	20	[15]
Co^{2+}@NG	0.5	-0.68	65	[17]
Co-N-C	0.1	-0.5	50	[42]
Co-NC	0.5	-0.90	24	[44]
Co-N-C	0.1	-0.59	45	[55]
Co-N$_5$/HNPCSs	0.2[b]	-0.79	99.3	[26]
Co-N$_2$	0.5	-0.63	94	[27]
Co$_1$-N$_4$	0.1	-1.1	82	[28]
Co-Tpy-C	0.5	-0.6	98.8	[64]
CoSA/HCNFs	0.1	-0.6	97	[65]
Co@CoNC-1000	0.1	-0.7	61	[66]

[b] NaHCO$_3$ was used as an electrolyte.

**Table 4.** Reported FEs on single-atom Cu, Mn, and Zn catalysts. Reprinted and adapted with permission.

| Catalyst	KHCO$_3$ (M)	Potential (V *vs.* RHE)	FE for CO (%)	Ref.
Cu-N$_x$	0.1	-0.76	30	[15]
Cu-NG	0.5	-0.62	10	[14]
Cu-N-C	0.1	-0.8	28	[42]
Cu-C$_3$N$_4$	0.1	-1.1	36	[30]
CuSAs/TCNFs	0.1	-0.9	CH$_3$OH: 44 CO: 56	[32]
Cu-N$_2$/GN	0.1	-0.5	81	[33]
Cu-SA-NG	0.1	-1.0	80.6	[67]
Cu-N-C-900	0.1	-1.6	CH$_4$: 38.6	[31]
Cu SAs/NC	0.1	-0.7	92	[68]
Cu$_{0.5}$NC	0.1[c]	-0.6	67.5	[34]
Mn-N$_x$	0.1	-0.55	40	[15]
Mn-NG	0.5	-0.52	17.5	[14]
(Cl, N)-Mn/G	0.5	-0.60	97	[35]
ZnN$_x$/C	0.5	-0.43	95	[69]
SA-Zn/MNC	1.0	-1.1[d]	CH$_4$: 85	[36]

[c] NaHCO$_3$ was used as an electrolyte.

[d] -1.8 V *vs.* SCE (Potentials measured against the saturated calomel electrode)
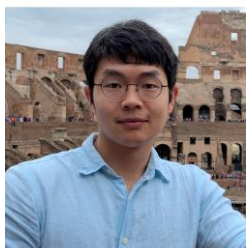
Chaochen Xu received his BEng at Beijing University of Chemical Technology in 2013 and MEng at the University of Adelaide in 2016. He is currently a PhD candidate at the University of Adelaide under the supervision of Prof. Shi-Zhang Qiao. His research interests include electrochemical and mechanistic studies of electrocatalytic CO_2 reduction under ambient conditions.
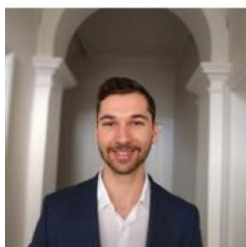
Anthony Vasileff received his PhD degree in Chemical Engineering at the University of Adelaide in 2020 under the supervision of Prof. Shi-Zhang Qiao. His current research interests include mechanistic studies to determine factors affecting product selectivity for electrochemical CO_2 reduction on a range of catalyst materials and the scale up of CO_2 conversion technologies.
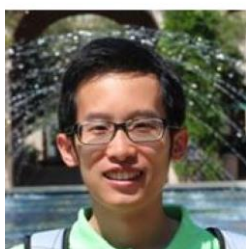

Yao Zheng received his PhD degree in 2014 from the University of Queensland, Australia. Currently, he is a Senior Lecturer at the University of Adelaide. His current research focuses on fundamental studies of some key electrocatalysis processes by combining experiments and theoretical computations, and the development of advanced electrocatalysts for energy conversion processes.

Shi-Zhang Qiao received his PhD degree in Chemical Engineering from the Hong Kong University of Science and Technology in 2000, and is currently a Chair Professor and ARC Australian Laureate Fellow at the School of Chemical Engineering and Advanced Materials of the University of Adelaide, Australia. His research interests include synthesis and characterization of nanostructured materials as well as their applications in catalysis, energy storage, and conversion (fuel cell, batteries, electrocatalysis, and photocatalysis).
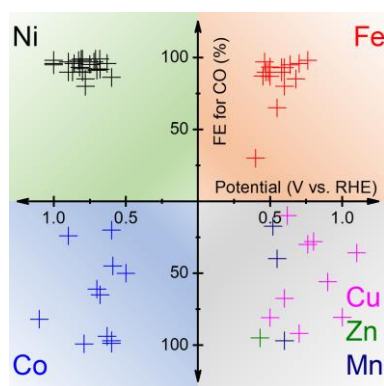
This review highlights graphene-supported 3d-block transition metal single-atom catalysts (SACs) used for the electrochemical CO_2 reduction reaction (CRR). The Faradaic efficiency (FE) for CO on SACs and corresponding applied potentials are illustrated in the scatter figure (X: Applied potential, Y: FE for CO). Specifically, higher FEs for CO were observed on Ni and Fe SACs under a moderate potential range. There are not sufficient reports of Co, Cu, Zn, and Mn SACs for the CRR, indicating a scattered distribution. Interestingly, a few studies reported that Cu SACs can potentially facilitate the CRR toward C2 products.

Chapter 3

Graphene-Encapsulated Nickel-Copper Bimetallic Nanoparticle Catalysts for Electrochemical Reduction of CO_2 to CO

Herein, we successfully designed and synthesized graphene-encapsulated $NiCu_x$ bimetallic nanoparticle catalysts ($NiCu_x$, x = 0.25, 0.5, and 1). The $NiCu_{0.25}$ exhibits a high Faradaic efficiency (FE) of 88.5% for CRR to CO at -1.0 V vs. RHE (reversible hydrogen electrode). The combination of X-ray absorption and in-situ Raman spectroscopy results explain that the increase of the Cu component in the catalyst enhances the electron donation from the metals and leads to a decrease in the 3d electron density of the catalyst, which further weakens the adsorption interaction of the catalyst for the reaction intermediates and reduces the catalytic selectivity. Thus, the Cu-lean catalyst, $NiCu_{0.25}$, shows the highest CO selectivity amongst the $NiCu_x$ alloys.

This Chapter is presented as a research paper by Chaochen Xu, Anthony Vasileff, Bo Jin, Dan Wang, Haolan Xu, Yao Zheng, and Shi-Zhang Qiao: Graphene-encapsulated nickel-copper bimetallic nanoparticle catalysts for electrochemical reduction of CO_2 to CO.

Statement of Authorship

Title of Paper	Graphene-Encapsulated Nickel-Copper Bimetallic Nanoparticle Catalysts for Electrochemical Reduction of CO_2 to CO
Publication Status	☑ Published ☐ Accepted for Publication ☐ Submitted for Publication ☐ Unpublished and Unsubmitted work written in manuscript style
Publication Details	Chaochen Xu, Anthony Vasileff, Bo Jin, Dan Wang, Haolan Xu, Yao Zheng, Shi-Zhang Qiao. *Chemical Communications*, 2020, 56, 11275-11278

Principal Author

Name of Principal Author (Candidate)	Chaochen Xu
Contribution to the Paper	Proposed ideas, performed experiments, carried out data processing and interpretation, wrote the manuscript.
Overall percentage (%)	70
Certification:	This paper reports on original research I conducted during the period of my Higher Degree by Research candidature and is not subject to any obligations or contractual agreements with a third party that would constrain its inclusion in this thesis. I am the primary author of this paper.
Signature	Date 12 Aug 2020

Co-Author Contributions

By signing the Statement of Authorship, each author certifies that:

i.   the candidate's stated contribution to the publication is accurate (as detailed above);

ii. permission is granted for the candidate in include the publication in the thesis; and

iii. the sum of all co-author contributions is equal to 100% less the candidate's stated contribution.

Name of Co-Author	Anthony Vasileff
Contribution to the Paper	Assisted in experiments and revised the manuscript.
Signature	Date 12 Aug 2020

Name of Co-Author	Bo Jin
Contribution to the Paper	Supervised the research project and revised the manuscript.
Signature	Date 12/08/2020

Name of Co-Author	Dan Wang
Contribution to the Paper	Supervised the research project and revised the manuscript.
Signature	Date 12/08/2020

Name of Co-Author	Haolan Xu
Contribution to the Paper	Conducted XPS measurements.
Signature	Date 12/08/2020

Name of Co-Author	Yao Zheng
Contribution to the Paper	Discussed experimental results and findings, supervised the research project, and revised the
Signature	Date 12/08/2020

Name of Co-Author	Shi-Zhang Qiao
Contribution to the Paper	Discussed experimental results and findings, supervised research project and revised the manuscript.
Signature	Date 12/08/2020

Graphene-encapsulated nickel–copper bimetallic nanoparticle catalysts for electrochemical reduction of CO$_2$ to CO†

Chaochen Xu, [ID] [a] Anthony Vasileff, [ID] [a] Bo Jin, [a] Dan Wang, [ID] [b] Haolan Xu, [ID] [c] Yao Zheng [ID] *[a] and Shi-Zhang Qiao [ID] *[a]

Highly selective CO$_2$ electroreduction to CO ($\sim$90% faradaic efficiency) was achieved on NiCu$_{0.25}$ bimetallic nanoparticle catalysts. By combining Synchrotron based X-ray absorption and *in situ* Raman spectroscopy studies, we found that there is a negative correlation between the Cu content in NiCu$_x$ and CO selectivity due to redistribution of the 3d electrons.

Electrochemical CO$_2$ reduction reaction (CRR) is a state-of-the-art technology that combines CO$_2$ capture with renewable energy to produce useful feedstocks.[1] Well-engineered electrocatalysts can make this process happen more efficiently. Currently, most CRR catalysts are limited to Cu metal and its derivatives because Cu is a unique element with a moderate adsorption capacity of CO$_2$.[2]

3d-block transition metals such as Group VIII$_B$ metals: Fe, Co, Ni have a similar electron configuration composed of fully-filled 4s orbital and unsaturated 3d orbitals (*i.e.* 3d$^{6-8}$4s^2). These metals feature diverse electronic structure, are low cost, and have controllable morphology/composition. However, compared with Cu catalysts, their CRR properties are scarcely reported.[3,4] With careful engineering, the well-developed VIII$_B$ metal catalysts can also be used for highly selective CRR, which could largely expand the range of potential catalysts and reduce costs. Bimetallic alloys have shown superior performance for CRR than single metal catalysts because introducing a secondary metal can provide dual active sites and reconstruct the local electron distribution, which optimizes catalytic activity and selectivity.[5] Few Group VIII$_B$ metal–Cu alloys have been reported for the CRR and it is still unknown whether these

alloys can be candidates for the CRR. Therefore, we engineered Ni and alloyed Ni with Cu as an example to provide experimental results to understand these VIII$_B$ metal–Cu bimetallic catalysts for the CRR.

Herein, we successfully designed and synthesized graphene-encapsulated NiCu$_x$ bimetallic nanoparticle catalysts (NiCu$_x$, x = 0.25, 0.5, and 1). The NiCu$_{0.25}$ exhibits a high faradaic efficiency (FE) of 88.5% for CRR to CO at -1.0 V *vs.* RHE (reversible hydrogen electrode). The combination of X-ray absorption and *in situ* Raman spectroscopy results explain that the increase of the Cu component in the catalyst enhances the electron donation from the metals and leads to a decrease in the 3d electron density of the catalyst, which further weakens the adsorption interaction of the catalyst for the reaction intermediates and reduces the catalytic selectivity. Thus, the Cu-lean catalyst, NiCu$_{0.25}$, shows the highest CO selectivity amongst the NiCu$_x$ alloys.

The NiCu$_x$ alloys were prepared from the annealing of Ni–Cu co-precipitates. Briefly, certain amounts of Ni and Cu ions were chelated by ethylenediaminetetraacetic acid (EDTA) to form bimetallic complexes, which was followed by an annealing treatment at 550 °C under an Ar atmosphere (see the ESI† for experimental details). The transmission electron microscopy (TEM) image shows that well-dispersed NiCu$_{0.25}$ nanoparticles are encapsulated by ultrathin layers of graphene (Fig. 1a). The Raman spectra also support the existence of graphene layers, which are evidenced by the characteristic D- and G-band peaks (Fig. S1, ESI†).[6] The graphene encapsulation prevents particle aggregation and results in forming small particles with an average size of 12.5 nm (Fig. S2, ESI†). Scanning electron microscopy (SEM) imaging with energy dispersive spectroscopy (EDS) analysis was also carried out, and the results are consistent with the TEM findings (Fig. S3, ESI†). The high-angle annular dark-field scanning transmission electron microscopy (HAADF-STEM) imaging with EDS mapping was used to confirm that Ni and Cu were distributed ubiquitously throughout the nanoparticles of NiCu$_{0.25}$, and that there was no evidence of a bimetallic core–shell structure (Fig. 1b and Fig. S4, ESI†). The

[a] *Centre for Materials in Energy and Catalysis, School of Chemical Engineering and Advanced Materials, The University of Adelaide, Adelaide, SA 5005, Australia. E-mail: s.qiao@adelaide.edu.au, yao.zheng01@adelaide.edu.au*

[b] *Institute of Process Engineering, Chinese Academy of Sciences, Beijing, 100190, China*

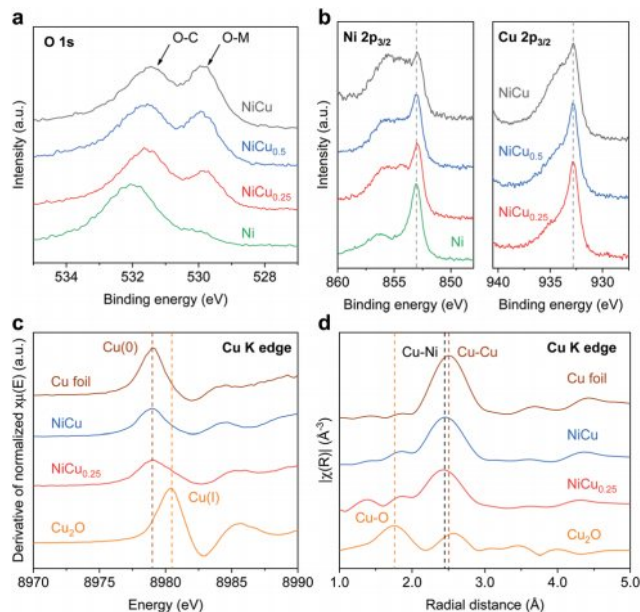[c] *Future Industries Institute, University of South Australia, SA 5095, Australia*
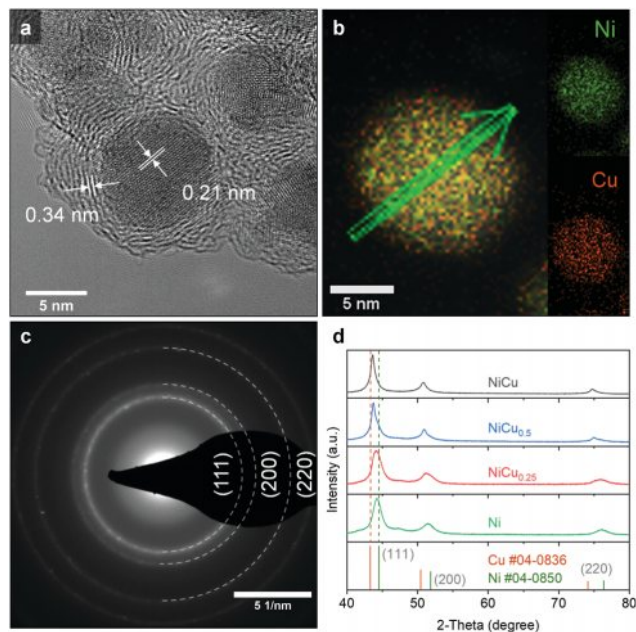
Fig. 1 (a) TEM image of NiCu$_{0.25}$ with measured lattice spacings. (b) HAADF-STEM image of NiCu$_{0.25}$ with EDS mappings. The line scan collected along the arrow direction. (c) SAED pattern of NiCu$_{0.25}$. (d) Powder XRD patterns of different samples.

Fig. 2 (a) O 1s and (b) Ni 2p$_{3/2}$ and Cu 2p$_{3/2}$ XPS spectra for different samples. The dashed lines indicate the binding energy of the dominant 2p$_{3/2}$ peak. (c) The first derivative of the normalized Cu K-edge XANES spectra for different samples. The dashed lines show the Cu absorption edges of Cu foil and Cu$_2$O, representing Cu(0) and Cu(I), respectively. (d) Cu K-edge EXAFS spectra in R-space of different samples.

Ni–Cu atomic ratios in the NiCu$_x$ alloys were also measured and agree with the proposed ratios (Table S1, ESI†). In addition, there were no atomically dispersed Ni and/or Cu species in NiCu$_x$ alloys (Fig. S5, ESI†). A selected area electron diffraction (SAED) pattern is shown in Fig. 1c. Specifically, the crystal structure was investigated by powder X-ray diffraction (XRD), in which all patterns are well-indexed between the metallic Cu (PDF#04-0836) and Ni (PDF#04-0850) phases in Fig. 1d. The interplanar spacing for the (111) plane of NiCu$_{0.25}$ is consistent with the d-spacing of 0.34 nm shown in Fig. 1a. Compared to the pure Ni catalyst, the diffraction peaks gradually shift to lower angles with increasing Cu content in the NiCu$_x$. This indicates that the metallic Cu phase displaces the Ni-dominated phase in the NiCu$_x$.

The X-ray photoelectron spectroscopy (XPS) survey spectra clearly identify distinct signals from C, N, O, Ni, and Cu (Fig. S6 and Table S2, ESI†). The high-resolution C 1s and N 1s signals confirm the presence of N-doped graphene, and the absence of metal carbides and nitrides (Fig. S7 and S8, ESI†). In Fig. 2a, the O 1s spectra of the NiCu$_x$ alloys exhibit two typical peaks: the peak at 531.5 eV is assigned to the O–C in N-doped graphene; the other peak at 530.0 eV is contributed by metal oxides (O–M).[7,8] In comparison to the O–C peak, the intensity of the O–M peak rises with increasing Cu content. This result demonstrates that the introduction of Cu enhances metal oxidation, and the degree of oxidation becomes stronger as the Cu content increases. In Fig. 2b, both the Ni 2p$_{3/2}$ and Cu 2p$_{3/2}$ spectra show that Ni and Cu in the NiCu$_x$ are prominently in the metallic state, respectively. And shoulder peaks referring to metal oxidation were also observed, which are consistent with the O 1s XPS results.[9–11] Therefore, the investigation indicates

that the existence of Cu causes Ni and Cu oxidation in the NiCu$_x$, and the degree of oxidation increases with Cu content. By contrast, without the addition of Cu, Ni remains in a metallic state. This phenomenon is likely because there are more Ni–Cu phase boundaries in the Cu-rich NiCu$_x$, and the bimetallic interface exhibits high reactivity during the synthesis process and leads to partial oxidation of the metals.[12–14]

To further confirm the Cu oxidation state and coordination environment, the Cu K-edge X-ray absorption near-edge structure (XANES) and extended X-ray absorption fine structure (EXAFS) were examined. From the XANES spectra shown in Fig. 2c, the absorption edges of NiCu$_{0.25}$ and NiCu appear at the same position as that of the Cu foil (8979.0 eV). This is consistent with the results in Fig. 2b (right), that is, Cu in the NiCu$_x$ is mainly in the metallic state. The information of the first-shell Cu coordination environment was derived from the EXAFS spectra shown in Fig. 2d, the Cu–Ni radial distances of NiCu$_{0.25}$ (2.42 Å) and NiCu (2.45 Å) are close but shorter than Cu–Cu in Cu foil (2.52 Å) because of the presence of strain in the bimetallic alloys.[15] Moreover, there are no obvious Cu–O bonds found in the spectra. This further confirms that Cu is predominantly in the metallic state in the bimetallic catalysts.

To explore how changes of metal composition in bimetallic catalysts affect the catalytic activity, the NiCu$_x$ and Ni were tested for CRR in CO$_2$-saturated 0.1 M KHCO$_3$ electrolyte (Fig. S9, ESI†). The gas products were identified through online gas chromatography, and only hydrogen, CO, and negligible methane were detected. No liquid products were detected by nuclear magnetic resonance spectroscopy. According to the measured FE distribution (Fig. S10, ESI†), a clear selectivity trend can be seen in
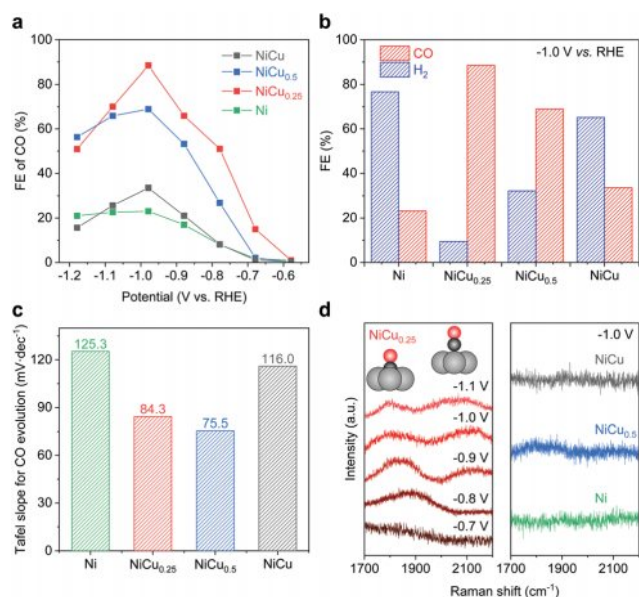
Fig. 3 CO_2 electroreduction in CO_2-saturated 0.1 M $KHCO_3$ electrolyte. (a) The measured FEs of CO. (b) The distributions of FEs under a potential of −1.0 V vs. RHE. (c) Comparison of Tafel slopes for CO evolution. (d) In situ Raman results. Left: Potential-dependent spectra of NiCu$_{0.25}$. The molecular adsorption models from left to right are *CO (bridge) and *CO (atop) on the catalytic sites. Right: The spectra for the other catalysts under a potential of −1.0 V vs. RHE. All potentials are given vs. RHE.

Fig. 3a. In detail, CO was firstly observed at the onset potential of ca. −0.7 V vs. RHE. With negatively increasing potential, the measured FE of CO rose to a maximum at a turning point of −1.0 V vs. RHE and then dropped. The highest FE of CO was achieved on NiCu$_{0.25}$, which reached 88.5% (Fig. S11, ESI†). As shown in Fig. 3b, the catalytic performance demonstrates two key findings that are (1) hydrogen evolution is a predominant reaction on the Ni catalyst, with FE as high as about 80%; (2) by the introduction of Cu, the NiCu$_x$ simultaneously exhibits suppression of hydrogen formation and promotion of CO_2 reduction toward CO. However, the FEs of CO decrease from 88.5% to 33.5% as the Cu content in the catalysts increases (Fig. 3b). The kinetic study indicates that the CO_2 activation steps on NiCu$_{0.25}$ and NiCu$_{0.5}$ are less hindered, and their Tafel slopes are obviously smaller than those of the Ni and Cu-rich NiCu (Fig. 3c and Fig. S12, ESI†).[16,17] Therefore, the electrochemical evaluation implies that the addition of Cu favors CO_2 reduction, but more Cu content cannot further facilitate the reduction reaction to CO, which indicates that the CO selectivity is inversely related to the Cu content in the NiCu$_x$. Additionally, the single metal Cu catalyst exhibited a preference of H_2 evolution with a small amount of hydrocarbons (Fig. S13, ESI†).

In situ Raman spectroscopy was used to uncover the intermediates adsorbed on the active sites of the catalysts and better understanding the inhibition of CO selectivity as Cu increases. The Raman spectra are divided into two regions corresponding to different adsorption types of CO: *CO$_{bridge}$ (1700–2000 cm^{-1}) and *CO$_{atop}$ (2000–2200 cm^{-1}).[18,19] The peak shift is attributed to the electrochemical vibrational Stark effect.[20] As can be seen in Fig. 3d (left), *CO$_{bridge}$ is first observed at −0.8 V vs. RHE. As the reduction potential increases, *CO$_{atop}$ then appears.

However, Fig. 3d (right) shows that *CO peaks were not detected on Ni and NiCu at the turning potential of −1.0 V vs. RHE, except for NiCu$_{0.5}$ where a slight *CO$_{bridge}$ peak was found. For the catalytic process with higher CO selectivity, more *CO intermediates are generated at the active sites of the catalyst during the reaction. According to the reported reaction pathways, *CO is produced through two reaction steps on the active site: the first step is $* + CO_2 + H^+ + e^- = *COOH$; the second step is that the generated *COOH continues to couple with a proton and an electron at the active site to obtain *CO, i.e. $*COOH + H^+ + e^- = *CO + H_2O$.[16] Namely, the stronger the adsorption of the catalyst for *COOH, the easier it is for *COOH to remain on the active site to participate in the reaction, which can promote the formation of *CO from CO_2. Otherwise, weak adsorption of *COOH by the catalyst will prevent further reduction to *CO. Therefore, a catalyst with stronger adsorption of *COOH is favorable. In Fig. 3d, the most noticeable *CO peaks were detected on NiCu$_{0.25}$, which achieved the highest CO selectivity. At the same potential, a weak peak was detected on NiCu$_{0.5}$, which had ordinary CO selectivity; while there were no peaks found on NiCu, which displayed the worst catalytic performance. From this, we deduce that by changing the Cu content in the NiCu$_x$ (i.e. changing electronic structure), the adsorption of *COOH by the catalyst can be tuned and further affect the final selectivity.

For transition metal catalysts, the electronic structure of the metal d electrons can be used to describe the intermediate adsorption on the catalyst, thereby establishing a structure–activity relationship.[21,22] Soft X-ray absorption spectroscopy was used to investigate the d electron distribution of the catalysts. The electron information can be derived from metal L$_3$-edge XANES spectra. Specifically, in Fig. 4a, the peaks for NiCu$_x$ are all shifted to higher energy by 0.40 eV higher than the Ni peak, indicating that Ni was distinctly oxidized due to the introduction of Cu. This is consistent with the previous results. Further, the relative intensity of the Ni L$_3$-edge rises with increasing Cu content, which suggests that the 3d electron donation is enhanced.[23–25] Similarly, the same trend is also found in the Cu L$_3$-edge XANES spectra (Fig. 4b). As depicted in Fig. 4c, we compared the electron donation and CO selectivity. As the Cu content in the NiCu$_x$ increases (the direction indicated by the dashed arrow), the 3d electron donations of Ni and Cu become stronger (the direction indicated by the solid arrow), which means that more obvious 3d electron transfer occurs in both metals. According to the previous XPS analysis, an increase in Cu content in NiCu$_x$ causes more metals centers in higher oxidation states. And these strongly electronegative oxygen atoms may be responsible for promoting the 3d electron transfer of Ni and Cu. The electron transfer from the metals directly affects the electron distribution of the NiCu$_x$, resulting in a decrease in the 3d electron density. This weakens the adsorption of the *COOH intermediate on the catalyst, hinders the formation of *CO, and consequently leads to a decrease in CO selectivity. Therefore, changing the Cu content of the bimetallic NiCu$_x$ redistributes the electronic structure and shows a negative correlation with CO selectivity.
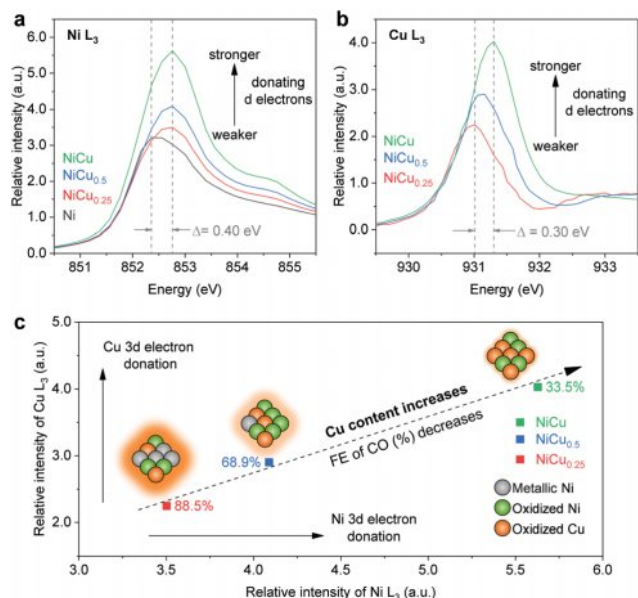
Fig. 4 XANES L$_3$-edge spectra of (a) Ni and (b) Cu. A higher relative intensity corresponds to stronger d electron donation. (c) The electron donation and CO selectivity trend with increasing Cu content in NiCu$_x$. The glow represents the 3d electron density of the molecular model, a stronger glow represents a higher electron density.

In conclusion, we engineered Ni by adding Cu to obtain graphene-encapsulated Ni–Cu bimetallic nanoparticle catalysts for the electrochemical reduction of CO_2 to CO. Compared to the single metal Ni catalyst, the NiCu$_x$ catalysts had significantly higher catalytic performance due to the presence of dual metal active sites. However, increased Cu content led to electron redistribution in the metals, resulting in a decrease in 3d orbital electron density which caused weak adsorption of *COOH by the catalyst. The highest CO selectivity was achieved on the Cu-lean catalyst, NiCu$_{0.25}$, with an FE reaching 88.5% at a moderate potential of −1.0 V vs. RHE.

Conflicts of interest

There are no conflicts to declare.

Notes and references

1 M. Aresta, A. Dibenedetto and A. Angelini, *Chem. Rev.*, 2014, **114**, 1709–1742.
2 S. Nitopi, E. Bertheussen, S. B. Scott, X. Liu, A. K. Engstfeld, S. Horch, B. Seger, I. E. L. Stephens, K. Chan, C. Hahn, J. K. Norskov, T. F. Jaramillo and I. Chorkendorff, *Chem. Rev.*, 2019, **119**, 7610–7672.
3 R. Francke, B. Schille and M. Roemelt, *Chem. Rev.*, 2018, **118**, 4631–4701.
4 W. Sheng, S. Kattel, S. Yao, B. Yan, Z. Liang, C. J. Hawxhurst, Q. Wu and J. G. Chen, *Energy Environ. Sci.*, 2017, **10**, 1180–1185.
5 A. Vasileff, C. Xu, Y. Jiao, Y. Zheng and S.-Z. Qiao, *Chem*, 2018, **4**, 1809–1831.
6 C. Xu, A. Vasileff, D. Wang, B. Jin, Y. Zheng and S.-Z. Qiao, *Nanoscale Horiz.*, 2019, **4**, 1411–1415.
7 L. Zhao, Y. Zhang, L. B. Huang, X. Z. Liu, Q. H. Zhang, C. He, Z. Y. Wu, L. J. Zhang, J. Wu, W. Yang, L. Gu, J. S. Hu and L. J. Wan, *Nat. Commun.*, 2019, **10**, 1278.
8 J.-C. Dupin, D. Gonbeau, P. Vinatier and A. Levasseur, *Phys. Chem. Chem. Phys.*, 2000, **2**, 1319–1324.
9 K. Zhang, J. Ran, B. Zhu, H. Ju, J. Yu, L. Song and S. Z. Qiao, *Small*, 2018, **14**, 1801705.
10 A. Vasileff, X. Zhi, C. Xu, L. Ge, Y. Jiao, Y. Zheng and S.-Z. Qiao, *ACS Catal.*, 2019, **9**, 9411–9417.
11 A. Vasileff, C. Xu, L. Ge, Y. Zheng and S. Z. Qiao, *Chem. Commun.*, 2018, **54**, 13965–13968.
12 Y. Wang, P. Han, X. Lv, L. Zhang and G. Zheng, *Joule*, 2018, **2**, 2551–2582.
13 L. Han, Q. Meng, D. Wang, Y. Zhu, J. Wang, X. Du, E. A. Stach and H. L. Xin, *Nat. Commun.*, 2016, **7**, 13335.
14 Y. Yang, M. Luo, W. Zhang, Y. Sun, X. Chen and S. Guo, *Chem*, 2018, **4**, 2054–2083.
15 E. T. Saw, U. Oemar, X. R. Tan, Y. Du, A. Borgna, K. Hidajat and S. Kawi, *J. Catal.*, 2014, **314**, 32–46.
16 M. Dunwell, W. Luc, Y. Yan, F. Jiao and B. Xu, *ACS Catal.*, 2018, **8**, 8121–8129.
17 M. Ma, B. J. Trzesniewski, J. Xie and W. A. Smith, *Angew. Chem., Int. Ed.*, 2016, **55**, 9748–9752.
18 B. L. Mojet, S. D. Ebbesen and L. Lefferts, *Chem. Soc. Rev.*, 2010, **39**, 4643–4655.
19 S. Zhu, T. Li, W.-B. Cai and M. Shao, *ACS Energy Lett.*, 2019, **4**, 682–689.
20 M. C. Figueiredo, I. Ledezma-Yanez and M. T. M. Koper, *ACS Catal.*, 2016, **6**, 2382–2392.
21 F. Cavalca, R. Ferragut, S. Aghion, A. Eilert, O. Diaz-Morales, C. Liu, A. L. Koh, T. W. Hansen, L. G. M. Pettersson and A. Nilsson, *J. Phys. Chem. C*, 2017, **121**, 25003–25009.
22 X. Zhu, Q. Guo, Y. Sun, S. Chen, J. Q. Wang, M. Wu, W. Fu, Y. Tang, X. Duan, D. Chen and Y. Wan, *Nat. Commun.*, 2019, **10**, 1428.
23 P. De Luna, R. Quintero-Bermudez, C.-T. Dinh, M. B. Ross, O. S. Bushuyev, P. Todorović, T. Regier, S. O. Kelley, P. Yang and E. H. Sargent, *Nat. Catal.*, 2018, **1**, 103–110.
24 Y. Jeon, J. Chen and M. Croft, *Phys. Rev. B: Condens. Matter Mater. Phys.*, 1994, **50**, 6555–6563.
25 D. H. Pearson, C. C. Ahn and B. Fultz, *Phys. Rev. B: Condens. Matter Mater. Phys.*, 1993, **47**, 8471–8478.

Electronic Supplementary Information

Graphene-encapsulated nickel-copper bimetallic nanoparticle catalysts for electrochemical reduction of CO$_2$ to CO

Chaochen Xu,[a] Anthony Vasileff,[a] Bo Jin,[a] Dan Wang,[b] Haolan Xu,[c] Yao Zheng*[a], and Shi-Zhang Qiao*[a]

[a] Centre for Materials in Energy and Catalysis, School of Chemical Engineering and Advanced Materials, The University of Adelaide, Adelaide, SA 5005, Australia
[b] Institute of Process Engineering, Chinese Academy of Sciences, Beijing, 100190, China
[c] Future Industries Institute, University of South Australia, SA 5095, Australia

* Email: s.qiao@adelaide.edu.au, yao.zheng01@adelaide.edu.au

Part I: Experimental Section

Chemicals

Nickel(II) nitrate hexahydrate ($Ni(NO_3)_2 \cdot 6H_2O$), copper(II) nitrate hemi-pentahydrate ($Cu(NO_3)_2 \cdot 2.5H_2O$), ethylenediaminetetraacetic acid (EDTA), *N,N*-dimethylformamide (DMF), trimethylamine (TMA), potassium bicarbonate ($KHCO_3$), dimethyl sulfoxide (DMSO), phenol, and deuterium oxide (D_2O) were purchased from Sigma-Aldrich and were used without further purification. Deionized water (DI water, 18 MΩ·cm) was from a Milli-Q water purifier. A 0.05 wt.% Nafion solution was diluted from LIQUion™ Solutions (LQ-1115 - 1100 EW at 15 wt.%). Ultra-high purity Ar (99.999%), N_2 (99.999%), and laser grade CO_2 (99.995%) were supplied from BOC Gas.

Synthesis Method

NiCu bimetallic nanoparticles were prepared using a modified method.[1] 0.6 g of EDTA and 1.0 mL of TMA were dissolved in 30 mL DMF and formed EDTA solution. The bimetallic salt solution was prepared by dissolution of specific ratios of nickel(II) and copper(II) nitrate salts in 20 mL DMF. For example, 1.4 g of the Ni salt and 0.3 g of the Cu salt were used for the preparation of $NiCu_{0.25}$ salt solution. For $NiCu_{0.5}$ and NiCu salt solution, 1.2 and 0.9 g of the Ni salt and 0.5 and 0.7 g of the Cu salt were used, respectively. The bimetallic salt solution was then added dropwise to the EDTA solution under vigorous stirring. A clear gelatinous precipitate was received after washing with DMF three times by centrifugation (6000 rpm). The washed precipitate was dried in a vacuum oven at 80°C overnight. The fully dried resultant was transferred to a tube furnace and was annealed at 550°C with a heating rate of 10°C·min^{-1} for 1 h under Ar atmosphere. Once cooled to room temperature, the received black powder was washed with DI water three times and was dried in a vacuum oven at 60°C overnight again. For comparison, single Ni or Cu nanoparticles were synthesized using the same method by adding 1.7 g of the Ni salt or 1.4 g of the Cu salt only.

Material Characterization

Scanning electron microscopy (SEM) images and energy dispersive spectroscopy (EDS) spectra were acquired with FEI Quanta 450. Transmission electron microscopy (TEM) images and selected area electron diffraction (SAED) patterns were taken using Philips CM200. High-angle annular dark-field scanning transmission electron microscopy (HAADF-STEM) images and EDS spectra were acquired with FEI Titan Themis 80-200. X-ray powder diffraction

(XRD) patterns were recorded on a Rigaku X-Ray Diffractometer (Cu Kα, λ = 1.5406 Å). X-ray photoelectron spectroscopy (XPS) measurements were performed on Kratos AXIS Ultra (mono Al Kα), and all spectra were calibrated to the C-C peak at 284.8 eV. X-ray absorption spectra were collected from the soft X-ray spectroscopy (sXAS) and X-ray absorption spectroscopy (XAS) beamlines at the Australian synchrotron. All spectra were calibrated by corresponding reference standards of metal foils (Cu K-edge at 8978.9 eV, Ni L_3-edge at 853.0 eV, and Cu L_3-edge at 934.3 eV). The position of the absorption edge was determined from the first derivatives of the spectrum. X-ray absorption near edge structure (XANES) and extended X-ray absorption fine structure (EXAFS) data processing was conducted in Athena. Raman spectra were collected using a Raman spectroscopy (HORIBA LabRAM HR Evolution) configured by an MPLN50x objective lens (Olympus) and a 633-nm laser (CVI Melles Griot).

Electrochemical Measurements

The experiments were performed on an electrochemical workstation (CH Instruments 760E) using a three-electrode H-cell separated by a proton exchange membrane (Nafion 117). A glassy carbon electrode (⌀ 5 mm), Ag/AgCl (3.5 M KCl), and RuO_2-coated titanium mesh served as the working, reference, and counter electrodes, respectively. To prepare a catalyst ink, 4 mg of catalyst was ultrasonically dispersed in 2 mL of 0.05 wt.% Nafion aqueous solution. Then, 40 µL of the ink was dropped onto the surface of the glassy carbon and dried in air, resulting in a catalyst loading of 0.4 mg·cm^{-2}. The electrochemical measurements including cyclic voltammetry (CV), linear scan voltammetry (LSV), and chronoamperometry *i-t* curve (*i-t*) were carried out in CO_2-saturated 0.1 M $KHCO_3$ electrolyte (pH = 6.8) under a stirring rate of 100 rpm. All *iR*-corrected potentials were converted to the reversible hydrogen electrode (RHE) at 20°C:

$$E \ (V \ vs. \ RHE) = E \ (V \ vs. \ Ag/AgCl) + 0.059 \times pH + 0.205$$

where *pH* is measured using a pH meter.

For the analysis of electrochemical kinetics, Tafel slopes were derived from the Tafel equation:

$$\eta = b \ lg \ (j_{CO} / j_0)$$

where η [V] is an overpotential between the applied potential to the standard CO_2/CO reduction potential ($E_{CO2/CO}$ = -0.11 V *vs.* RHE); *b* is the Tafel slope [mV·dec^{-1}]; j_{co} is the partial current density of CO; j_0 is the exchange current density of CO [mA·cm^{-2}].

Product Evaluation

Briefly, 100 µL of headspace gas in the cathode compartment was manually injected into gas chromatography (GC, Agilent 7890B configured with TCD and Methanizer/FID) for gas product quantification *via* a syringe; The liquid products were determined using nuclear magnetic resonance spectroscopy (NMR, Agilent 500/600 MHz ^{1}H NMR) and were quantified with internal standards (DMSO and phenol in D_2O).[2] No detectable liquid products were found in this work. Faradaic efficiency of a certain product was calculated by:

$$FE_i = n_i\, e\, F\, /\, Q_t \times 100\%$$

where n_i is the total amount of a certain product i [mol]; e is the number of electrons transferred for the product i formation, which equals to two for both CO and H_2; F is the Faradaic constant [$C \cdot mol^{-1}$]; Q_t is the total amount of passed charge [C].

***In-situ* Raman Spectroscopy Measurements**

The same catalyst inks used for electrochemical measurements were also used for *in-situ* Raman spectroscopy measurements. 40 µL of catalyst ink was uniformly deposited on a 5 mm × 4 mm screen-printed working electrode (Pine Research Instrumentation, RRPE1002C). The electrode was then transferred to a vacuum oven and was dried at 60°C. The fully dried electrode was connected to the 760E electrochemical workstation *via* a cell grip and USB connector and was then attached on a microscope slide at the sample stage. 100 µL of CO_2-saturated 0.1M $KHCO_3$ electrolyte was dropwise added on the electrode. A coverslip was then placed on the top of the electrode. *In-situ* Raman spectra were collected using a Raman spectroscopy (HORIBA LabRAM HR Evolution) configured by an MPLN50x objective lens (Olympus), 1800 l/mm grating, and a 633-nm Raman laser. Baseline correction was applied in all *in-situ* Raman spectra. All applied potentials were converted to RHE at 20°C:
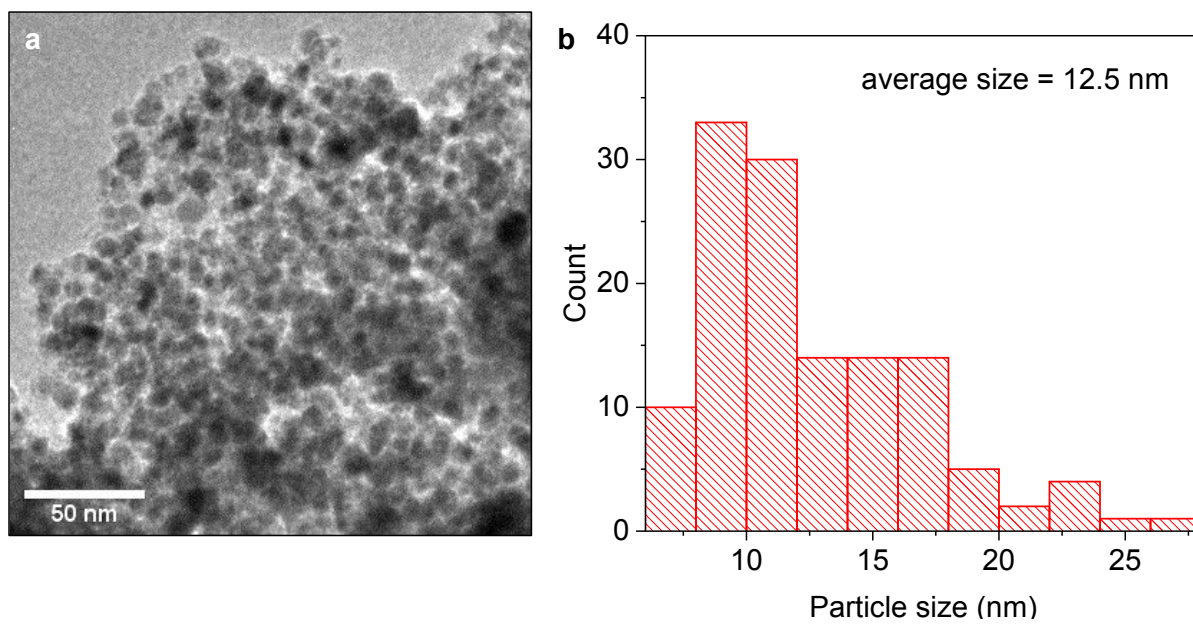
$$E\ (V\ vs.\ RHE) = E\ (V\ vs.\ Ag/AgCl) + 0.059 \times pH + 0.527$$
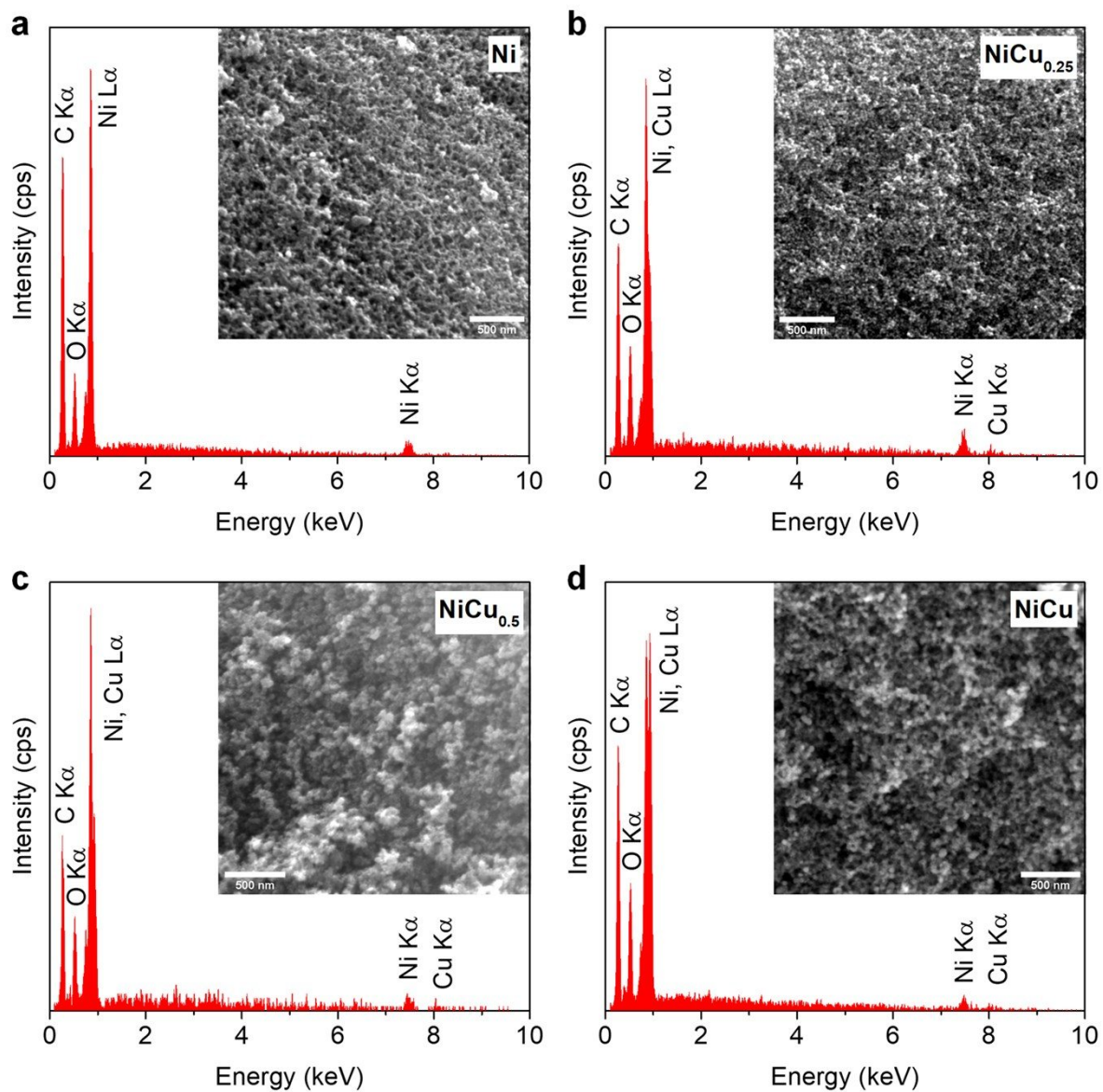
where *pH* is measured using a pH meter.

Part II: Supplementary Results
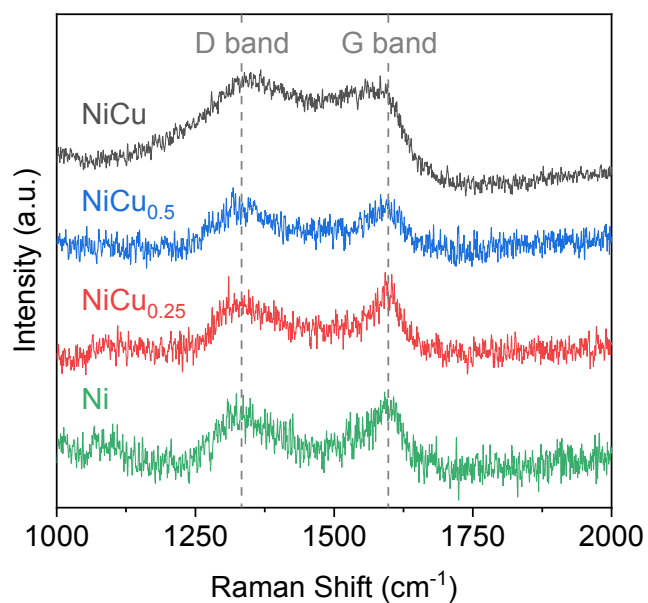
Fig. S1 Raman spectroscopy spectra. The dash lines are assigned to the D- (~1350 cm^{-1}) and G- (~1580 cm^{-1}) band peaks.
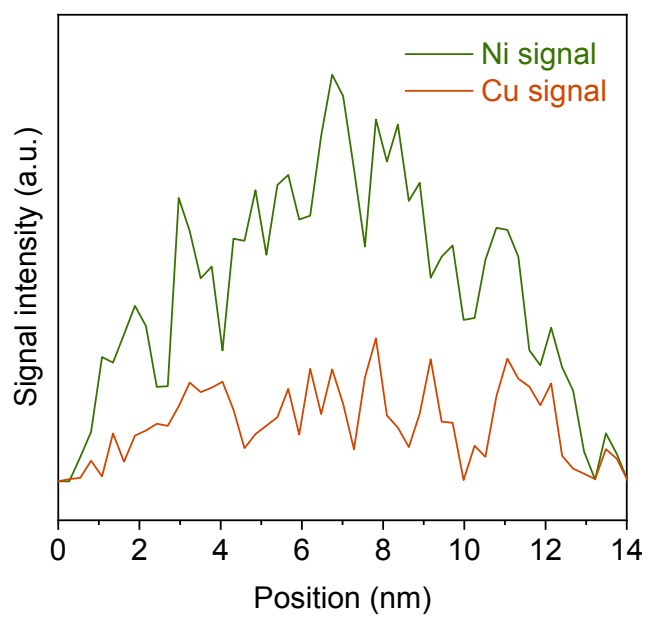

Fig. S2 (a) TEM image of NiCu$_{0.25}$ and (b) its corresponding particle size distribution.

Fig. S3 SEM images (inset) and corresponding EDS elemental analysis of (a) Ni, (b) NiCu$_{0.25}$, (c) NiCu$_{0.5}$, and (d) NiCu (scale bars = 500 nm).
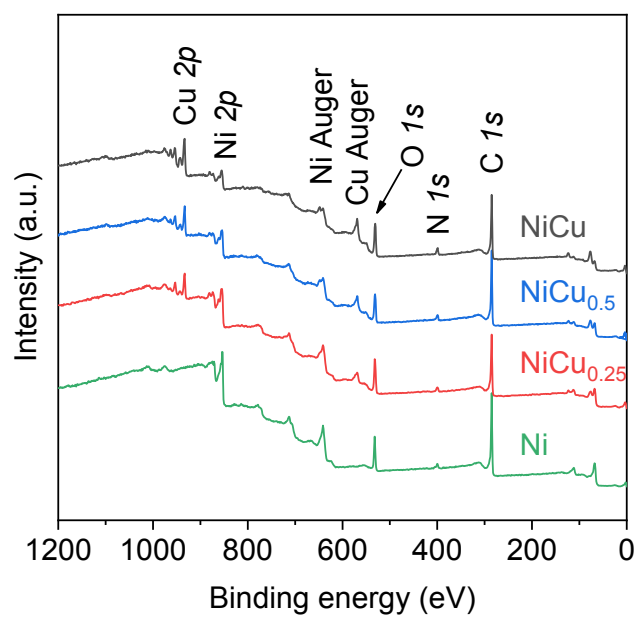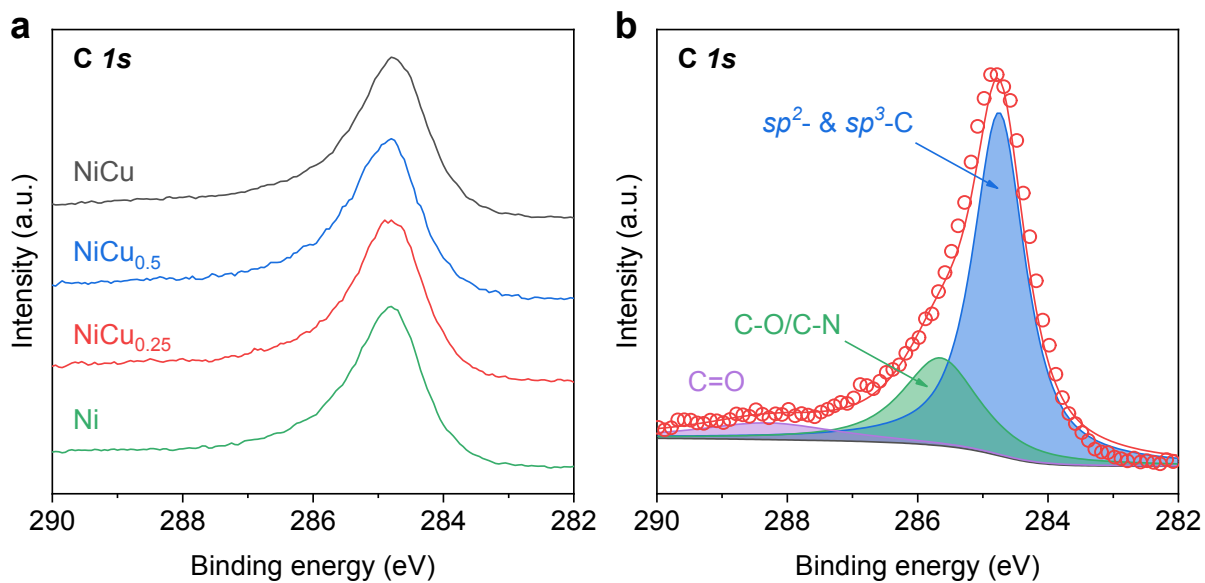
Fig. S4 EDS line scan of $NiCu_{0.25}$ along the arrowed direction in Fig. 1(b).

Fig. S5 HAADF-STEM images of Ni-Cu bimetallic nanoparticle catalysts.

Fig. S6 XPS survey spectra with distinct signals of C, N, O, Ni, and Cu.

Fig. S7 High-resolution XPS spectra of (a) C 1s and (b) the deconvoluted spectrum of NiCu$_{0.25}$.
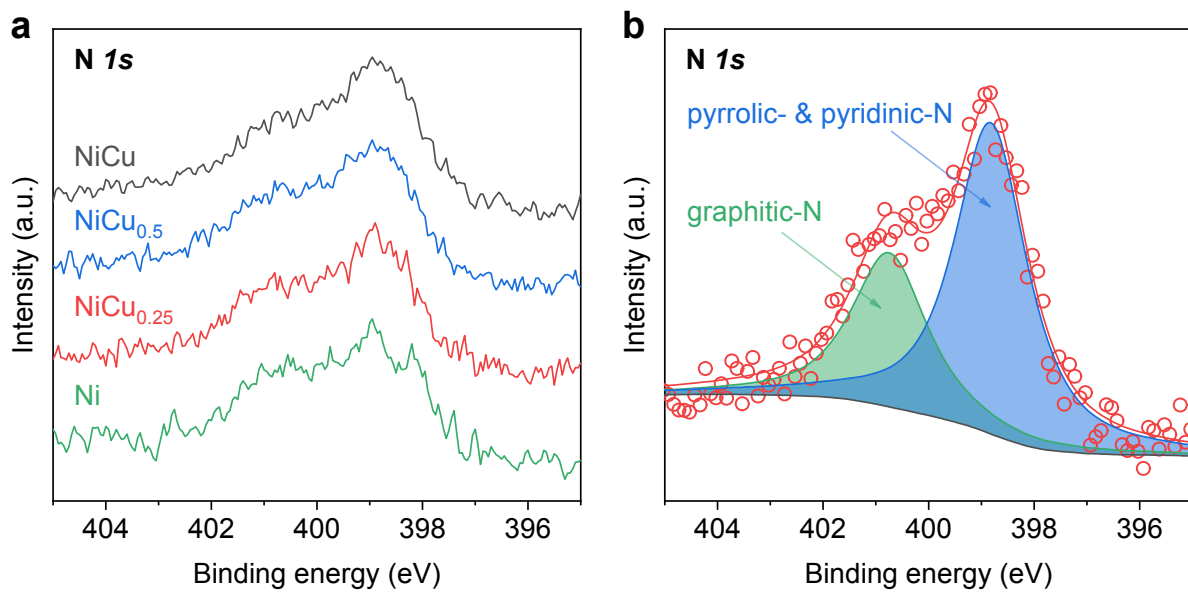
Fig. S8 High-resolution XPS spectra of (a) N 1s and (b) the deconvoluted spectrum of NiCu$_{0.25}$.
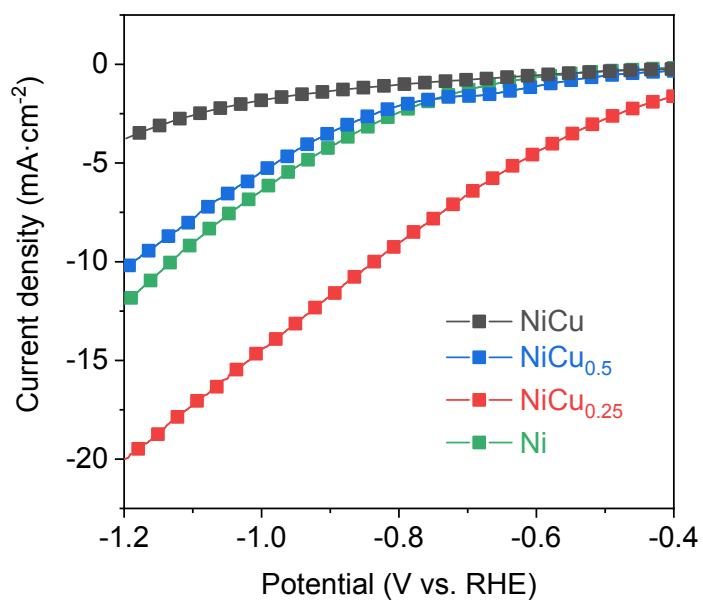
Fig. S9 LSV polarization curves in CO$_2$-saturated 0.1 M KHCO$_3$ electrolyte.
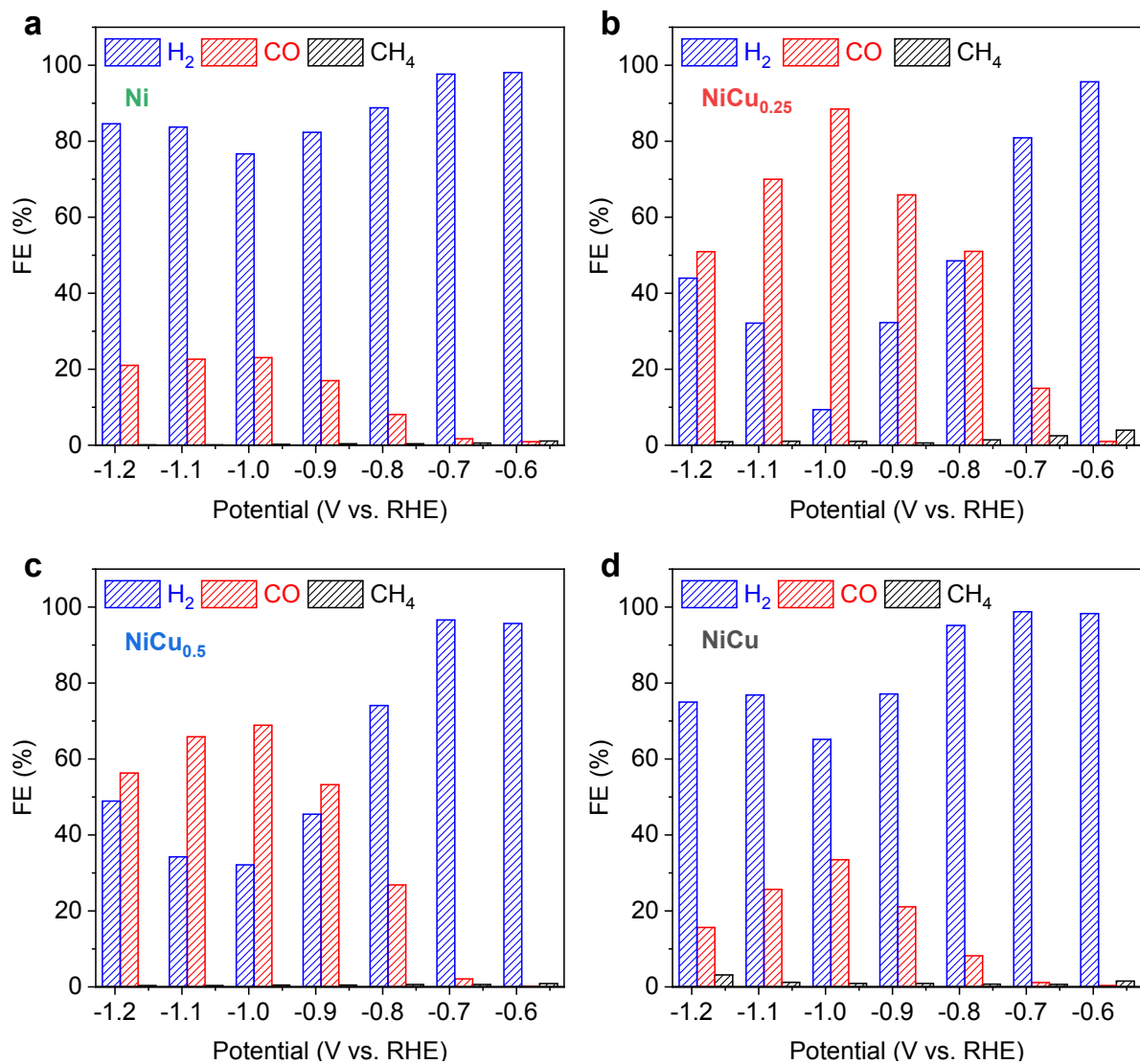
Fig. S10 Measured FE distributions of CO_2 electroreduction on (a) Ni, (b) $NiCu_{0.25}$, (c) $NiCu_{0.5}$, and (d) NiCu in CO_2-saturated 0.1 M $KHCO_3$ electrolyte.
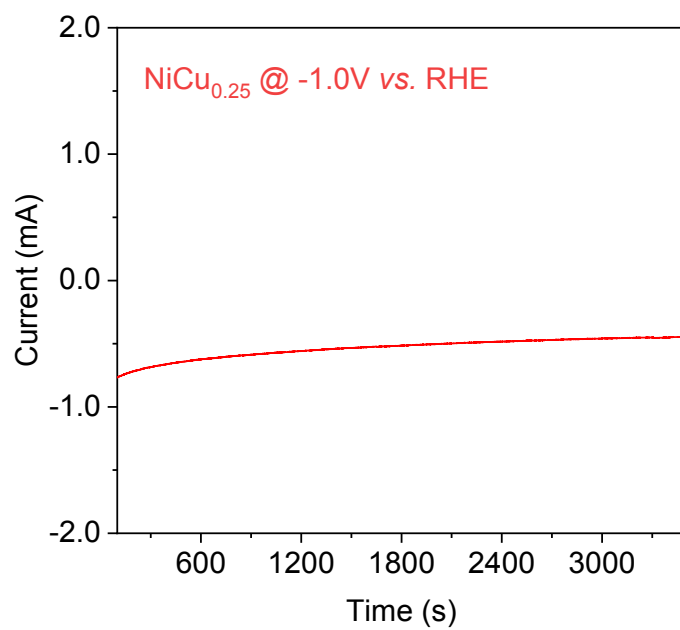
Fig. S11 Current-time dependence of $NiCu_{0.25}$ for CO_2 electroreduction in CO_2-saturated 0.1 M $KHCO_3$ electrolyte at -1.0 V *vs.* RHE.
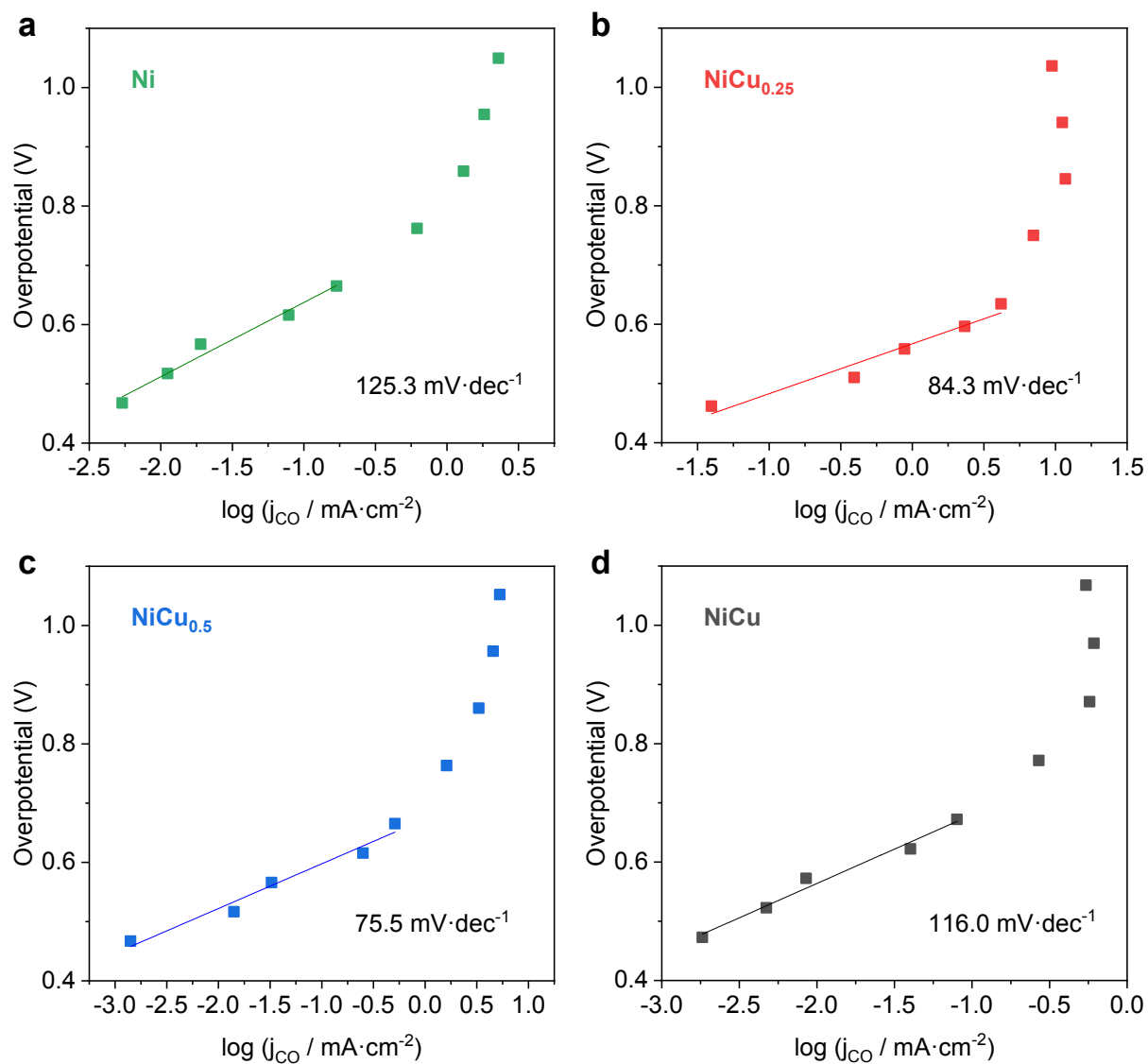
Fig. S12 Tafel plots for CO evolution on (a) Ni, (b) $NiCu_{0.25}$, (c) $NiCu_{0.5}$, and (d) NiCu in CO_2-saturated 0.1 M $KHCO_3$ electrolyte.
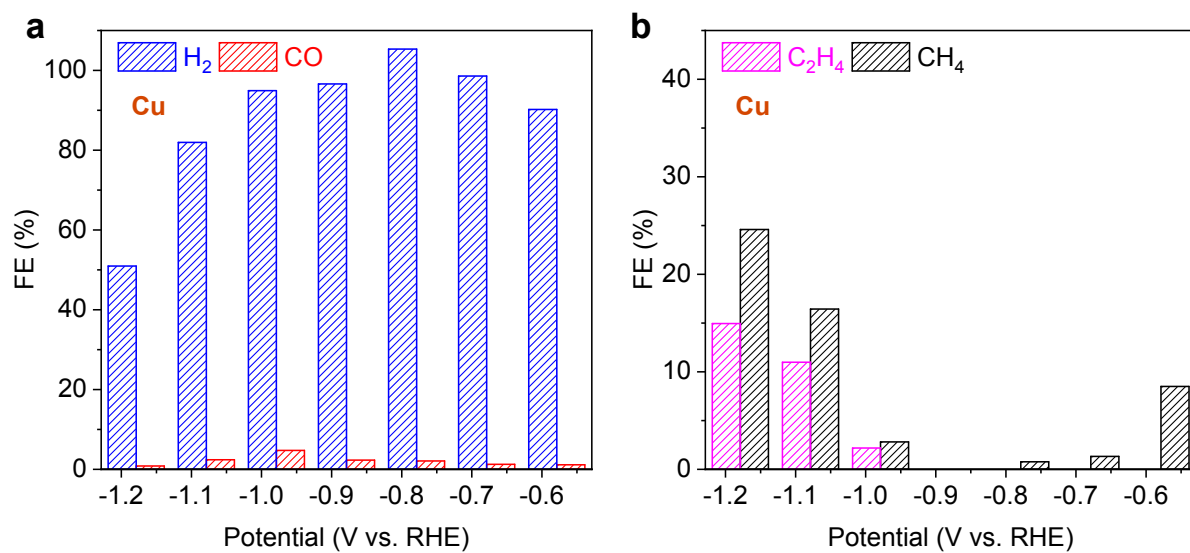
Fig. S13 Measured FEs toward (a) H_2, CO, and (b) hydrocarbons on the Cu catalyst.

Table S1. Theoretical and STEM-EDS measured atomic ratios of Cu-to-Ni.

Sample	Atomic ratios of Cu-to-Ni	
	Theoretical	*Measured*
NiCu	1.00	0.95
NiCu0.5	0.50	0.46
NiCu0.25	0.25	0.24
Ni	0.00	N/A

Table S2. Surface chemical composition measured by XPS

Signals	Atomic%			
	NiCu	*NiCu$_{0.5}$*	*NiCu$_{0.25}$*	*Ni*
C 1s	62.84	66.41	63.02	69.78
N 1s	5.5	4.82	4.17	3.93
O 1s	18.32	15.81	17.95	14.37
Ni 2p	5.5	7.67	10.61	10.52
Cu 2p	7.84	5.29	4.25	N/A

Part III: References

1.   K. Zhang, J. Ran, B. Zhu, H. Ju, J. Yu, L. Song and S. Z. Qiao, *Small*, 2018, **14**, 1801705.

2.   K. P. Kuhl, E. R. Cave, D. N. Abram and T. F. Jaramillo, *Energy Environ. Sci.*, 2012, **5**, 7050-7059.

Chapter 4

Synergistic Catalysis Between Atomically Dispersed Fe and a Pyrrolic-N-C Framework for CO_2 Electroreduction

Herein, we successfully design and synthesize atomically dispersed iron catalysts immobilized within N-doped carbon nanosheets (Fe-SA). Iron nanoparticles on N-doped carbon nanosheets (Fe-NP) and N-doped carbon nanosheets (NS) are also prepared via a similar synthetic method and serve as controls. The optimal Fe-SA-900 sample (annealed at 900°C) shows a high Faradaic efficiency (FE) of *ca.* 90% under a low potential of -0.58 V vs. RHE (reversible hydrogen electrode) for CO_2 reduction toward CO. This superior performance is attributed to the synergistic effect in the Fe-pyrrolic-N-C framework. Specifically, the adjacent pyrrolic-N-C sites serve as one active site which can activate CO_2 molecules while the coordinated Fe centers serve as another active site that can generate protons (via water dissociation) for further CO_2 reduction.

This Chapter is presented as a research paper by Chaochen Xu, Anthony Vasileff, Dan Wang, Bo Jin, Yao Zheng, and Shi-Zhang Qiao: Synergistic catalysis between atomically dispersed Fe and a pyrrolic-N-C framework for CO_2 electroreduction.

Statement of Authorship

Title of Paper	Synergistic Catalysis between Atomically Dispersed Fe and a Pyrrolic-N-C Framework for CO$_2$ Electroreduction
Publication Status	☑ Published ☐ Accepted for Publication ☐ Submitted for Publication ☐ Unpublished and Unsubmitted work written in manuscript style
Publication Details	Chaochen Xu, Anthony Vasileff, Dan Wang, Bo Jin, Yao Zheng, Shi-Zhang Qiao. *Nanoscale Horizons*, 2019, 4, 1411-1415.

Principal Author

Name of Principal Author (Candidate)	Chaochen Xu
Contribution to the Paper	Proposed ideas, performed experiments, carried out data processing and interpretation, wrote the manuscript.
Overall percentage (%)	70
Certification:	This paper reports on original research I conducted during the period of my Higher Degree by Research candidature and is not subject to any obligations or contractual agreements with a third party that would constrain its inclusion in this thesis. I am the primary author of this paper.
Signature	Date 22 July 2020

Co-Author Contributions

By signing the Statement of Authorship, each author certifies that:

    i.   the candidate's stated contribution to the publication is accurate (as detailed above);

    ii.   permission is granted for the candidate in include the publication in the thesis; and

    iii.   the sum of all co-author contributions is equal to 100% less the candidate's stated contribution.

Name of Co-Author	Anthony Vasileff
Contribution to the Paper	Assisted in experiments and revised the manuscript.
Signature	Date 22 July 2020

Name of Co-Author	Dan Wang
Contribution to the Paper	Supervised the research project and revised the manuscript.
Signature	Date 22/07/2020

Name of Co-Author	Bo Jin
Contribution to the Paper	Supervised the research project and revised the manuscript.
Signature		Date	22/07/2020

Name of Co-Author	Ya
Contribution to the Paper	Discussed experimental results and findings, supervised the research project, and revised the manuscript.
Signature		Date	22/07/2020

Name of Co-Author	Shi-Zhang Qiao
Contribution to the Paper	Discussed experimental results and findings, supervised research project and revised the manuscript.
Signature		Date	22/07/2020

COMMUNICATION

Check for updates

Synergistic catalysis between atomically dispersed Fe and a pyrrolic-N-C framework for CO_2 electroreduction†

Chaochen Xu, [ID] [a] Anthony Vasileff, [ID] [a] Dan Wang, [ID] [b] Bo Jin, [a] Yao Zheng [ID] *[a] and Shi-Zhang Qiao [ID] *[a]

Atomically dispersed Fe immobilized within N-doped carbon nanosheets (Fe-SA) is successfully synthesized. The optimal Fe-SA catalyst achieves a high faradaic efficiency of *ca.* 90% for CO_2 electroreduction toward CO at a low overpotential of 0.47 V. A series of controlled tests show that there is a synergistic effect between the Fe centers and the pyrrolic-N-C framework which facilitates catalytic activity. Specifically, pyrrolic-N-C sites with high local electron density increase the initial CO_2 adsorption while positively charged Fe enhances the water dissociation to provide a proton source for further CO_2 reduction.

New concepts

Single atom metal catalysts within a framework support present as an ideal platform for multi-step electron transfer processes like the electrocatalytic CO_2 reduction reaction (CRR) because of the possibility for synergistic effects between two electroactive sites. Currently, the contribution of the metal atoms as active sites has been well-studied while the role of the supporting substrate in the catalytic process is scarcely reported. Herein, using atomically dispersed Fe immobilized within N-doped carbon nanosheets as a model, we carefully investigated the synergistic effect between the metal atom and its anchoring framework sites for efficient CRR. A series of controlled tests show that there is a synergistic effect between the Fe centers and the pyrrolic-N-C framework which facilitates catalytic activity.

The electrochemical CO_2 reduction reaction (CRR) is a promising technology for CO_2 conversion toward carbonaceous products. Desirable catalyst properties for the CRR are high activity, selectivity, and robustness.[1–5] However, a major hurdle for current CRR electrocatalysts is the inability to efficiently cleave the C=O bond in order to form specific intermediates for further multi-step proton-assisted electron-transfer processes.[6–10] This leads to a high overpotential and/or a low selectivity toward a specific product, consequently impeding the large scale applications of this CO_2 conversion technology.

Recently, single atom catalysts (SACs) have been explored by material science fields,[2,11–14] offering new opportunities for electrocatalysis. Ideal SACs refer to metals that are uniformly distributed within a framework and chemically coordinated with specific species to form a new functional group. Atom-level utilization of metal catalysts provides a unique property that may trigger reactions through different pathways, resulting in enhanced performances. For instance, atomically dispersed 3d-transition metal catalysts trapped within N-doped carbon

nanosheets have recently been highlighted as promising candidates for electrocatalytic applications, such as hydrogen- and oxygen-involving reactions and the CRR.[11,15–18]

A typical structure of SACs involves metal atoms that are anchored to the N sites of a N-containing carbon (N-C) framework.[11,12,19] The interaction between the metal and N-C, denoted as a metal–N-C domain site, has been widely reported as the possible active site for facilitating the selective reduction of CO_2 to CO.[20–28] More interestingly, for a multi-step reaction, *e.g.*, CRR, this metal–non-metal interaction provides two active sites (*i.e.*, one metal site; one N-C site). In principle, they can work synergistically to break the inherent adsorption energy scaling relation of different reaction intermediates, leading to an enhanced selectivity towards a specific product.[4,24,29,30] However, most research has focused on the role of the metal center itself or the metal–N-C domain; the function of the N-C framework and resultant synergistic effect is poorly known. Additionally, different from carbon-based metal-free materials, the effect of various N species (*e.g.* pyridinic-N, pyrrolic-N, and graphitic-N) in metal–N-C sites is scarcely reported in SAC studies. For example, most of the experimental and computational studies claim that the metal atoms are typically trapped at pyridinic-N-C sites.[2,11,12,31–33] On the other hand, some metal complexes with similar π conjugated systems with metal–pyrrolic-N-C sites,

[a] Centre for Materials in Energy and Catalysis, School of Chemical Engineering and Advanced Materials, The University of Adelaide, Adelaide, SA 5005, Australia. E-mail: s.qiao@adelaide.edu.au, yao.zheng01@adelaide.edu.au

[b] Institute of Process Engineering, Chinese Academy of Sciences, Beijing, 100190, China

† Electronic supplementary information (ESI) available. See DOI: 10.1039/c9nh00361d

such as heme, chlorophyll, and metal phthalocyanines, commonly exist and possess good stability. In fact, pyrrolic- and pyridinic-N-C have distinct electron structures. Compared to pyridinic-N, the unhybridized p_z orbital in pyrrolic-N has a pair of electrons that contributes to increasing the electron density on the N-C sites.

Herein, to utilize this discussed synergistic effect and clarify the role of pyridinic/pyrrolic-N-C in catalysis, we successfully design and synthesize atomically dispersed iron catalysts immobilized within N-doped carbon nanosheets (Fe-SA). Iron nanoparticles on N-doped carbon nanosheets (Fe-NP) and N-doped carbon nanosheets (NS) are also prepared *via* a similar synthetic method and serve as controls. The optimal Fe-SA-900 sample (annealed at 900 °C) shows a high faradaic efficiency (FE) of *ca.* 90% under a low potential of −0.58 V *vs.* RHE (reversible hydrogen electrode) for CO_2 reduction toward CO. This superior performance is attributed to the synergistic effect in the Fe–pyrrolic-N-C framework. Specifically, the adjacent pyrrolic-N-C sites serve as one active site which can activate CO_2 molecules while the coordinated Fe centers serve as another active site which can generate protons (*via* water dissociation) for further CO_2 reduction.

Fe-SA-900 was prepared by introducing Fe into a N-C framework *via* a facile thermal pyrolysis process (see the ESI† for Experimental details). Fe-NP-900 and NS-900 were prepared using the same method but with 10-fold Fe salt and no Fe salt added, respectively. Scanning electron microscopy (SEM) and high-resolution transmission electron microscopy (HRTEM) clearly confirm that ultrathin carbon nanosheets in Fe-SA-900 were successfully synthesized, and no visible particle phase was observed (Fig. S1a and b, ESI†). For further confirmation, Raman spectra display distinct D-band (1350 cm^{-1}) and G-band (1580 cm^{-1}) signals which correspond to the vibrational mode of sp^2 and disordered sp^2 carbon atoms within the nanosheet, respectively (Fig. S1c, ESI†).[34] To identify atomic-level dispersed Fe, aberration-corrected high-angle annular dark-field scanning transmission electron microscopy (HAADF-STEM) imaging was applied. As seen in Fig. 1a, bright spots distributed in the carbon substrate are distinguishable from the carbon substrate. This indicates the presence of Fe atoms owing to the *Z*-contrast sensitivity for heavy elements. In contrast, Fe aggregated to form nanoparticles in Fe-NP-900 while the absence of Fe was observed for NS-900 (Fig. 1b and c). Energy-dispersive X-ray spectroscopy (EDS) results further confirmed the presence of Fe in Fe-SA-900 and Fe-NP-900 and its absence in NS-900 (Fig. S2, ESI†). X-ray diffraction (XRD) patterns exhibit a broad peak from 20° to 30° (intense crystalline peaks at $2\theta = 24.5°$) for each sample in Fig. 1d. This represents the (002) plane of hexagonal carbon as evidenced by the transmission electron microscopy (TEM) image and selected area electron diffraction (SAED) pattern (Fig. S1d, ESI†).[35] The XRD pattern of Fe-NP-900 shows peaks related to Fe$_3$C (PDF #35-0772) as Fe aggregation likely formed Fe carbide nanoparticles. No such peaks were observed for Fe-SA-900, indicating that Fe is atomically dispersed rather than aggregated.

X-ray photoelectron spectroscopy (XPS) survey spectra display distinct signals of C 1s, N 1s, and O 1s from all samples (Fig. 2a). The element quantification results show that Fe-SA-900 contains
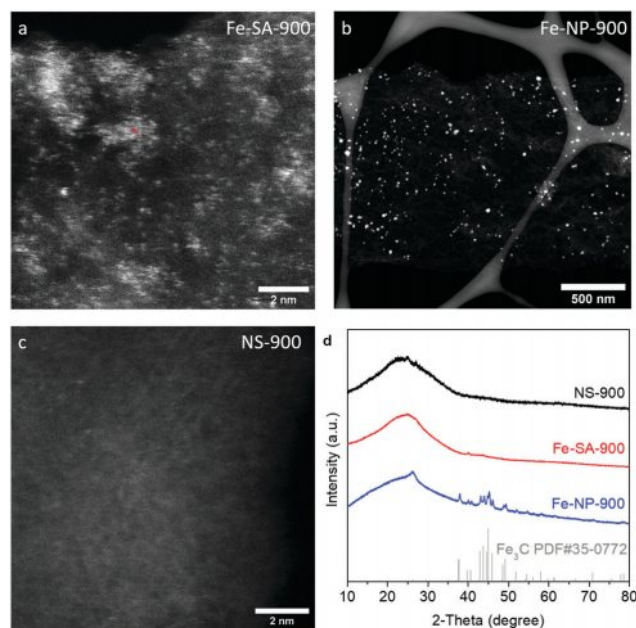

Fig. 1 HAADF-STEM images of (a) Fe-SA-900, (b) Fe-NP-900, and (c) NS-900. (d) XRD patterns of NS-900, Fe-SA-900, and Fe-NP-900.
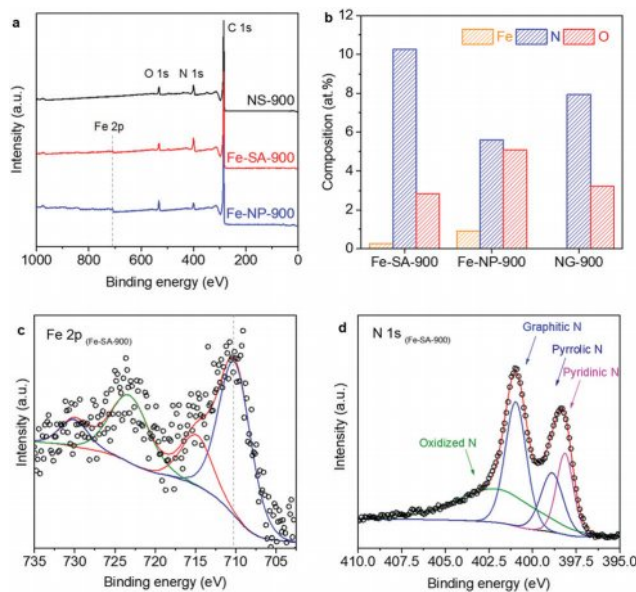
Fig. 2 (a) XPS survey spectra of NS-900, Fe-SA-900, and Fe-NP-900. (b) XPS-based quantification of elemental compositions for all samples. (c) High-resolution Fe 2p spectra of Fe-SA-900. (d) Deconvoluted high-resolution N 1s spectra of Fe-SA-900.

a trace amount of Fe at only 0.27 at% compared to 0.90 at% in Fe-NP-900 (Fig. 2b, see Table S1 (ESI†) for full elemental compositions). To investigate the chemical state of Fe, high-resolution XPS measurements were studied. In the Fe 2p region, the binding energy of the Fe 2p$_{3/2}$ peak is located at 710.4 eV in Fe-SA-900, which is more positive than that of metallic Fe at 706.6 eV (Fig. 2c).[36] This suggests that Fe exists in an oxidation state greater than zero in Fe-SA-900 where Fe atoms are likely

coordinated *via* covalent bonds at N sites.[2,11,12,31,32,37] A shoulder peak appears at a binding energy of 707.9 eV in Fe-NP-900 (Fig. S3, ESI†). This confirms that Fe aggregation leads to the formation of Fe compounds (*e.g.* Fe$_3$C) in Fe-NP-900, which agrees with the XRD pattern of Fe-NP-900 in Fig. 1d. In the N 1s region, the signals are typically deconvoluted into four major N species: graphitic, pyridinic, pyrrolic, and oxidized N (Fig. 1d and Fig. S4, ESI†).[38] In brief, graphitic N refers to a N atom that substitutes a carbon in the carbon framework, coordinating three carbon atoms. Pyrrolic and pyridinic N are assigned to N atoms located at the edge of five- and six-membered carbon rings, respectively.

To explore the effects of atomic-level Fe dispersion on CRR activity, the electrochemical performances of the materials were evaluated in a CO_2-saturated 0.1 M KHCO$_3$ electrolyte (Fig. S5 and S6, ESI†). The generated products identified by gas chromatography (GC) were hydrogen, CO, and methane. No liquid products were detected by nuclear magnetic resonance spectroscopy (NMR) results. In Fig. 3a, a clear selectivity trend for CO can be seen with reduction potential increasing on Fe-SA-900. In the moderate reduction region, the FE of CO increases and approaches 89.8%. Meanwhile, the competitive hydrogen evolution reaction (HER) is effectively suppressed in this region. Similarly, Fe-NP-900 exhibits a similar trend but the HER rate is significantly greater (Fig. S7a, ESI†). NS-900 displays much lower CO_2 reduction activity and instead significant HER activity is observed across all potentials (Fig. S7b, ESI†). Fig. 3b indicates that the FEs of CO formation for the Fe containing catalysts reach maxima as the reduction potential is decreased from −0.38 to −0.58 V *vs.* RHE. According to the measured Tafel slopes of *ca.* 136 mV dec^{-1} for CO formation on Fe-SA-900 and Fe-NP-900 in Fig. 3c, the rate-determining step (RDS) for CO_2 reduction toward

CO is identical on these two Fe containing catalysts, *i.e.*, the CO_2 molecule adsorbs at the active site with a rate limiting electron transfer to form the *CO_2^- intermediate.

Fig. 3d clearly demonstrates the selectivity trend across the samples. (i) The Fe containing catalysts have enhanced performances for CO formation. Therefore, Fe atoms are likely involved in the active sites for CO_2 reduction. However, (ii) the catalytic activity for CO generation on the Fe-rich catalyst (Fe-NP) is inferior to that of the Fe-lean catalyst (Fe-SA). This finding suggests that Fe is not the only active component which determines catalytic activity and selectivity for CO on Fe-SA-900. Instead, it may be attributed to dual active sites rather than single active sites. (iii) The Fe-rich catalyst shows much higher HER activity than that of the Fe-lean catalyst. From this evidence, we hypothesize that it is likely the N-C sites that are the secondary active sites.

To identify the second active sites in the Fe-based samples, Fe-SA and Fe-NP were also synthesized at 700 °C and 800 °C. Changing the annealing temperature results in various levels of both overall N content and specific N species (Table S1 and Fig. S8, ESI†). The three catalysts contained the same Fe content but the ratio of pyrrolic-to-pyridinic-N (N_{pyr}/N_{pyd}) increased with annealing temperature. Raman spectroscopy showed that the degree of graphitization hardly changes with annealing temperature, thus it is not likely to be an influencing factor here (Fig. S9, ESI†). Importantly, as shown in Fig. 4a, there is a clear trend showing that the FE toward CO is correlated with the value of N_{pyr}/N_{pyd}. Specifically, Fe-SA-900 has the largest N_{pyr}/N_{pyd} of 0.96 and the highest FE toward CO among the Fe-SA samples. However, no obvious relationship between N_{pyr}/N_{pyd} and CO selectivity was observed for the Fe-NP samples (Fig. 4b). This further confirms that the atomically dispersed Fe coordinated to pyrrolic-N-C sites can synergistically promote CO_2 reduction.

Towards the reaction mechanism, from the previous analysis of Tafel slopes (Fig. 3c), the first electron transfer step (CO_2 + e$^-$ + * = *CO_2^-) is likely the RDS of the entire catalytic process. Therefore, improving the adsorption of CO_2 on the active sites can facilitate the reaction kinetics and enhance activity.[23,24,26] Also, it should be noted that the protons participating in CO_2 reduction can also affect the reaction rate, *e.g.* insufficient protons lead to hindering the following proton-assisted reduction steps (*e.g.*, *CO_2^- + H$^+$ = *COOH, *COOH + H$^+$ + e$^-$ = *CO + H$_2$O, *etc.*).[39,40] From the zero-order dependency of CO generation on [HCO$_3^-$] in the electrolyte (Fig. 4c), it is shown that the protons for consequent hydrogenation steps are provided from water dissociation instead of HCO$_3^-$ ionization.[41,42] Thus, optimization of water dissociation can also facilitate CO_2 reduction. At this stage, we identify that CO_2 adsorption and water dissociation are key processes for optimization of catalysts. From Fig. 3d, Fe-NP-900 contains a high Fe content that leads to obvious competition from the HER against CO_2 reduction. This implies that Fe as the sole active site plays a role in facilitating water dissociation. The other active site is indicated in Fig. 4a. Given their identical Fe content, the significant increase in performance across the Fe-SA samples derives from the increase in N_{pyr}/N_{pyd}. It supports that the N-C sites adjacent to the Fe atom contribute to CO_2 adsorption.
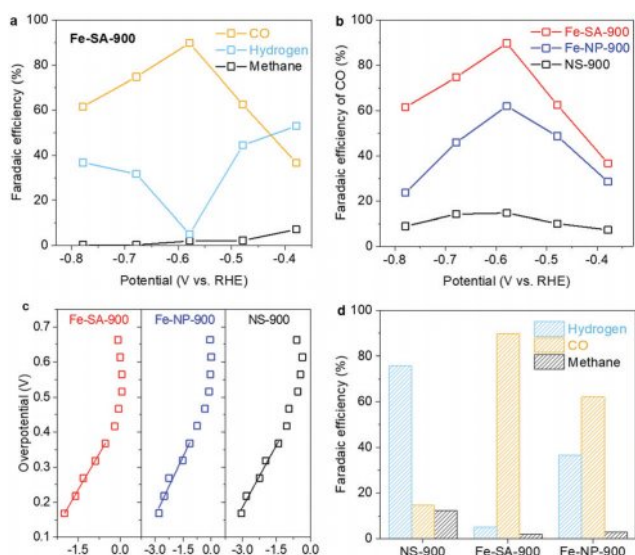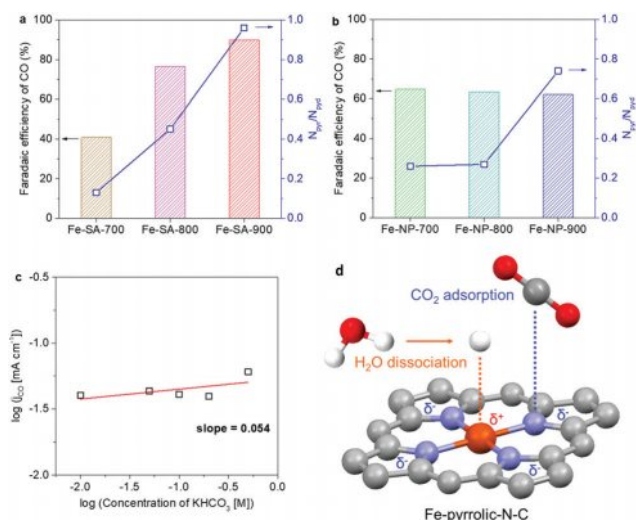

Fig. 3 (a) The measured FEs for CO_2 reduction on Fe-SA-900. (b) The measured FEs of CO on Fe-SA-900, Fe-NP-900, and NS-900. (c) Tafel plots for CO generation on Fe-SA-900, Fe-NP-900, and NS-900. (d) The distribution of FEs for CO_2 reduction on NS-900, Fe-SA-900, and Fe-NP-900 at a constant applied potential of −0.58 V *vs.* RHE.

Fig. 4 The measured FEs of CO on (a) Fe-SA samples and (b) Fe-NP samples with the corresponding ratios of pyrrolic-to-pyridinic-N species. (c) Rate dependency on [HCO$_3^-$] for CO on Fe-SA-900 at -0.38 V *vs.* RHE. (d) Scheme of synergetic catalysis between the Fe atom and pyrrolic-N-C sites. At the metal site, the positively charged (δ^+) Fe atom further enhances water dissociation to form protons for CO$_2$ reduction. While, at the N-C sites, the pyrrolic N contributes a pair of p$_z$ electrons toward π bonds, resulting in high electron density (δ^-) at N-C sites that improves CO$_2$ adsorption.

At the atomic level, the pyrrolic N has a pair of electrons in the unhybridized p$_z$ orbital that leads to increased electron density on the N-C sites. In contrast, the lone pair of electrons from pyridinic N form bonds and do not participate in the π system on N-C sites. Therefore, pyrrolic N induces greater electron density at the N-C sites, which favors CO$_2$ adsorption and electron transfer. This can be also reflected by the more negatively charged N-C sites resulting in positively charged Fe. From the Fe 2p spectra, the binding energy of the Fe 2p$_{3/2}$ peak shifts to higher energy as the annealing temperature is increased (Fig. S10 and S11, ESI†), indicating that the oxidation state of Fe increases. This confirms that more positively charged Fe is achieved in a pyrrolic-N-rich structure, which has been widely reported in facilitating water dissociation for proton generation.[43,44]

To summarize, we successfully obtained Fe-SA-900 using a simple pyrolysis method. The atomically dispersed Fe coordinated to the pyrrolic-N-C framework sites synergistically enhanced CO$_2$ reduction to CO. As one of the active sites, the Fe promotes water dissociation to form sufficient protons for CO$_2$ reduction. Furthermore, the Fe atom is also affected by the local electron structure of adjacent N-C sites. Consequently, the Fe exists in a positively charged state which favors water dissociation. The pyrrolic-N-C site acts as the other active site which synergistically promotes CO$_2$ reduction. Pyrrolic-N-C sites provide regions of higher electron density that facilitate CO$_2$ adsorption and electron transfer, which activates the first reaction step. Through a combination of atomically dispersed Fe and pyrrolic-N-C framework sites (Fig. 4d), a near 90% FE toward CO is achieved on Fe-SA-900 at a low overpotential of 0.47 V (*i.e.* -0.58 V *vs.* RHE). The effect of

pyrrolic-N-C sites in metal–N-C catalysts could be extended to further study CO$_2$ reduction toward products like methane and C$_2$ products.

Conflicts of interest

There are no conflicts to declare.

Acknowledgements

Notes and references

1 Z. Y. Sun, T. Ma, H. C. Tao, Q. Fan and B. X. Han, *Chem*, 2017, **3**, 560–587.
2 C. Zhu, S. Fu, Q. Shi, D. Du and Y. Lin, *Angew. Chem., Int. Ed.*, 2017, **56**, 13944–13960.
3 R. Francke, B. Schille and M. Roemelt, *Chem. Rev.*, 2018, **118**, 4631–4701.
4 A. Vasileff, C. Xu, Y. Jiao, Y. Zheng and S.-Z. Qiao, *Chem*, 2018, **4**, 1809–1831.
5 T. Zheng, K. Jiang and H. Wang, *Adv. Mater.*, 2018, **30**, 1802066.
6 L. Zhang, Z. J. Zhao and J. Gong, *Angew. Chem., Int. Ed.*, 2017, **56**, 11326–11353.
7 Y. Wang, J. Liu, Y. Wang, A. M. Al-Enizi and G. Zheng, *Small*, 2017, **13**, 1701809.
8 J. L. Liu, C. X. Guo, A. Vasileff and S. Z. Qiao, *Small Methods*, 2017, **1**, 1600006.
9 D. D. Zhu, J. L. Liu and S. Z. Qiao, *Adv. Mater.*, 2016, **28**, 3423–3452.
10 Y. Zheng, A. Vasileff, X. Zhou, Y. Jiao, M. Jaroniec and S. Z. Qiao, *J. Am. Chem. Soc.*, 2019, **141**, 7646–7659.
11 Y. J. Chen, S. F. Ji, C. Chen, Q. Peng, D. S. Wang and Y. D. Li, *Joule*, 2018, **2**, 1242–1264.
12 Y. Wang, J. Mao, X. Meng, L. Yu, D. Deng and X. Bao, *Chem. Rev.*, 2019, **119**, 1806–1854.
13 A. Han, B. Wang, A. Kumar, Y. Qin, J. Jin, X. Wang, C. Yang, B. Dong, Y. Jia, J. Liu and X. Sun, *Small Methods*, 2019, 1800471.
14 B.-W. Zhang, Y.-X. Wang, S.-L. Chou, H.-K. Liu and S.-X. Dou, *Small Methods*, 2019, 1800497.
15 T. T. Zheng, K. Jiang, N. Ta, Y. F. Hu, J. Zeng, J. Y. Liu and H. T. Wang, *Joule*, 2019, **3**, 265–278.
16 Y. Chen, S. Ji, Y. Wang, J. Dong, W. Chen, Z. Li, R. Shen, L. Zheng, Z. Zhuang, D. Wang and Y. Li, *Angew. Chem., Int. Ed.*, 2017, **56**, 6937–6941.

17 P. Yin, T. Yao, Y. Wu, L. Zheng, Y. Lin, W. Liu, H. Ju, J. Zhu, X. Hong, Z. Deng, G. Zhou, S. Wei and Y. Li, *Angew. Chem., Int. Ed.*, 2016, **55**, 10800–10805.

18 H. J. Qiu, Y. Ito, W. Cong, Y. Tan, P. Liu, A. Hirata, T. Fujita, Z. Tang and M. Chen, *Angew. Chem., Int. Ed.*, 2015, **54**, 14031–14035.

19 L. Zhao, Y. Zhang, L. B. Huang, X. Z. Liu, Q. H. Zhang, C. He, Z. Y. Wu, L. J. Zhang, J. Wu, W. Yang, L. Gu, J. S. Hu and L. J. Wan, *Nat. Commun.*, 2019, **10**, 1278.

20 Z. Zhang, J. Xiao, X. J. Chen, S. Yu, L. Yu, R. Si, Y. Wang, S. Wang, X. Meng, Y. Wang, Z. Q. Tian and D. Deng, *Angew. Chem., Int. Ed.*, 2018, **57**, 16339–16342.

21 L. Zhang, F. Mao, L. R. Zheng, H. F. Wang, X. H. Yang and H. G. Yang, *ACS Catal.*, 2018, **8**, 11035–11041.

22 A. S. Varela, N. Ranjbar Sahraie, J. Steinberg, W. Ju, H. S. Oh and P. Strasser, *Angew. Chem., Int. Ed.*, 2015, **54**, 10758–10762.

23 A. Vasileff, Y. Zheng and S. Z. Qiao, *Adv. Energy Mater.*, 2017, **7**, 1700759.

24 Y. Jiao, Y. Zheng, P. Chen, M. Jaroniec and S. Z. Qiao, *J. Am. Chem. Soc.*, 2017, **139**, 18093–18100.

25 X. Li, W. Bi, M. Chen, Y. Sun, H. Ju, W. Yan, J. Zhu, X. Wu, W. Chu, C. Wu and Y. Xie, *J. Am. Chem. Soc.*, 2017, **139**, 14889–14892.

26 X. Wang, Z. Chen, X. Zhao, T. Yao, W. Chen, R. You, C. Zhao, G. Wu, J. Wang, W. Huang, J. Yang, X. Hong, S. Wei, Y. Wu and Y. Li, *Angew. Chem., Int. Ed.*, 2018, **57**, 1944–1948.

27 C. H. Zhang, S. Z. Yang, J. J. Wu, M. J. Liu, S. Yazdi, M. Q. Ren, J. W. Sha, J. Zhong, K. Q. Nie, A. S. Jalilov, Z. Y. Li, H. M. Li, B. I. Yakobson, Q. Wu, E. L. Ringe, H. Xu, P. M. Ajayan and J. M. Tour, *Adv. Energy Mater.*, 2018, **8**, 1703487.

28 W. Ren, X. Tan, W. Yang, C. Jia, S. Xu, K. Wang, S. C. Smith and C. Zhao, *Angew. Chem., Int. Ed.*, 2019, **58**, 6972–6976.

29 M. Zhu, J. Chen, L. Huang, R. Ye, J. Xu and Y. F. Han, *Angew. Chem., Int. Ed.*, 2019, **58**, 6595–6599.

30 W. Zhong, R. Sa, L. Li, Y. He, L. Li, J. Bi, Z. Zhuang, Y. Yu and Z. Zou, *J. Am. Chem. Soc.*, 2019, **141**, 7615–7621.

31 W. Bi, X. Li, R. You, M. Chen, R. Yuan, W. Huang, X. Wu, W. Chu, C. Wu and Y. Xie, *Adv. Mater.*, 2018, **30**, 1706617.

32 Y. Cheng, S. Zhao, B. Johannessen, J. P. Veder, M. Saunders, M. R. Rowles, M. Cheng, C. Liu, M. F. Chisholm, R. De Marco, H. M. Cheng, S. Z. Yang and S. P. Jiang, *Adv. Mater.*, 2018, **30**, 1706287.

33 W. Ju, A. Bagger, G. P. Hao, A. S. Varela, I. Sinev, V. Bon, B. Roldan Cuenya, S. Kaskel, J. Rossmeisl and P. Strasser, *Nat. Commun.*, 2017, **8**, 944.

34 M. Liu, R. Zhang and W. Chen, *Chem. Rev.*, 2014, **114**, 5117–5160.

35 Y. Zheng, J. Liu, J. Liang, M. Jaroniec and S. Z. Qiao, *Energy Environ. Sci.*, 2012, **5**, 6717–6731.

36 P. L. Tan, *J. Catal.*, 2016, **338**, 21–29.

37 H. Fei, J. Dong, C. Wan, Z. Zhao, X. Xu, Z. Lin, Y. Wang, H. Liu, K. Zang, J. Luo, S. Zhao, W. Hu, W. Yan, I. Shakir, Y. Huang and X. Duan, *Adv. Mater.*, 2018, **30**, 1802146.

38 Y. Zheng and S. Z. Qiao, *Nat. Chem.*, 2018, **10**, 900–902.

39 M. Dunwell, W. Luc, Y. S. Yan, F. Jiao and B. J. Xu, *ACS Catal.*, 2018, **8**, 8121–8129.

40 A. Wuttig, Y. Yoon, J. Ryu and Y. Surendranath, *J. Am. Chem. Soc.*, 2017, **139**, 17109–17113.

41 W. Luo, J. Zhang, M. Li and A. Züttel, *ACS Catal.*, 2019, **9**, 3783–3791.

42 M. Ma, B. J. Trzesniewski, J. Xie and W. A. Smith, *Angew. Chem., Int. Ed.*, 2016, **55**, 9748–9752.

43 H. Y. Jin, X. Liu, Y. Jiao, A. Vasileff, Y. Zheng and S. Z. Qiao, *Nano Energy*, 2018, **53**, 690–697.

44 J. Staszak-Jirkovsky, C. D. Malliakas, P. P. Lopes, N. Danilovic, S. S. Kota, K. C. Chang, B. Genorio, D. Strmcnik, V. R. Stamenkovic, M. G. Kanatzidis and N. M. Markovic, *Nat. Mater.*, 2016, **15**, 197–203.

Electronic Supplementary Information

Synergistic catalysis between atomically dispersed Fe and a pyrrolic-N-C framework for CO$_2$ electroreduction

Chaochen Xu,[a] Anthony Vasileff,[a] Dan Wang,[b] Bo Jin,[a] Yao Zheng[*a] and Shi-Zhang Qiao[*a]

[a] Centre for Materials in Energy and Catalysis, School of Chemical Engineering and Advanced Materials, The University of Adelaide, Adelaide, SA 5005, Australia

[b] Institute of Process Engineering, Chinese Academy of Sciences, Beijing, 100190, China.

* Email: s.qiao@adelaide.edu.au; yao.zheng01@adelaide.edu.au

Part I: Experimental Section

Chemicals. Dicyandiamide, glucose, and iron (III) chloride hexahydrate were purchased from Sigma-Aldrich and used without further purification. N_2 (99.999%) and CO_2 (99.995%) were supplied from BOC Gas.

Synthesis. Fe-SA samples were prepared using a modified method.[1] 2.0 g of dicyandiamide and 0.1 g of glucose were dissolved in 100 mL deionized water, followed by the dropwise addition of 1.0 mL of fresh 0.01 M iron (III) chloride solution. The solution was then mixed well and dried in a rotary vacuum evaporator. The resultant precursor was placed in a tube furnace and annealed at 700, 800, and 900°C for 2 h under N_2 atmosphere, respectively (heating rate of 5°C·min^{-1}). Once cooled to room temperature, the received powder was washed with deionized water several times and dried at 60°C overnight. For comparison, Fe-NP samples were prepared using the same method but 10.0 mL of the iron salt solution was added instead; NS samples were prepared using the same method but without the addition of the iron salt solution.

Material characterization. SEM images were taken using an FEI Quanta 450. TEM images and SAED patterns were acquired with a Philips CM200. HAADF-STEM images and EDS spectra were acquired with an FEI Titan Themis 80-200. XRD patterns were recorded on a Rigaku X-Ray Diffractometer (Cu Kα). XPS measurements were performed on a Kratos AXIS Ultra (mono Al Kα). Raman spectra were collected using a HORIBA Scientific Raman Spectroscopy (Laser excitation at 633 nm).

CO_2 electroreduction measurements. Experiments were performed on an electrochemical workstation (CH Instruments 760E) using a three-electrode H-cell separated by proton exchange membrane (Nafion 117). A glassy carbon electrode (⌀ 5 mm), Ag/AgCl (3.5 M KCl), and RuO_2 coated titanium mesh served as the working, reference, and counter electrodes, respectively. To prepare the catalyst ink, 4 mg of catalyst was ultrasonically dispersed in 2 mL of 0.05 wt.% Nafion aqueous solution. Then, 40 μL of the ink was dropped onto the surface of the glassy carbon and dried in air (catalyst loading of 0.4 mg·cm^{-2}). CO_2 electroreduction was carried out in CO_2-saturated 0.1 M $KHCO_3$ aqueous electrolyte. All *iR*-corrected potentials were converted to RHE at 25°C: *E (vs. RHE) = E (vs. Ag/AgCl) + 0.059 × pH + 0.205*, where pH is measured using a pH meter. For analysis of electrochemical kinetics, Tafel slopes were derived from the Tafel equation: $\eta = b \lg (j_{CO} / j_0)$, where η [V] is the overpotential between the applied potential to the standard CO_2/CO reduction potential

(-0.11 V *vs.* RHE); b is the Tafel slope [mV·dec^{-1}]; j_{co} is the CO partial current density and j_0 is the CO exchange current density [mA·cm^{-2}].

Reduction products were quantified using the same procedures as previous work.[2] Briefly, 100 μL of headspace gas in the cathode compartment was manually injected into a GC (Agilent 7890B configured with TCD and Methanizer/FID) for gas product quantification; liquid products were determined using NMR (Agilent 500/600 MHz ^{1}H NMR) and quantified with internal standards (DMSO and phenol in D_2O).[3] No liquid products were detected in this work. Faradaic efficiency of a certain product was calculated: *FE$_i$ = n$_i$eF / Q$_t$ × 100%*, where n_i is the total amount of a certain product i [mol]; e is the number of electrons transferred for product i formation, which is 2 for both CO and hydrogen; F is the Faradaic constant [C·mol^{-1}]; and Q_t is the total amount of passed charge [C].

Part II: Supplementary Results
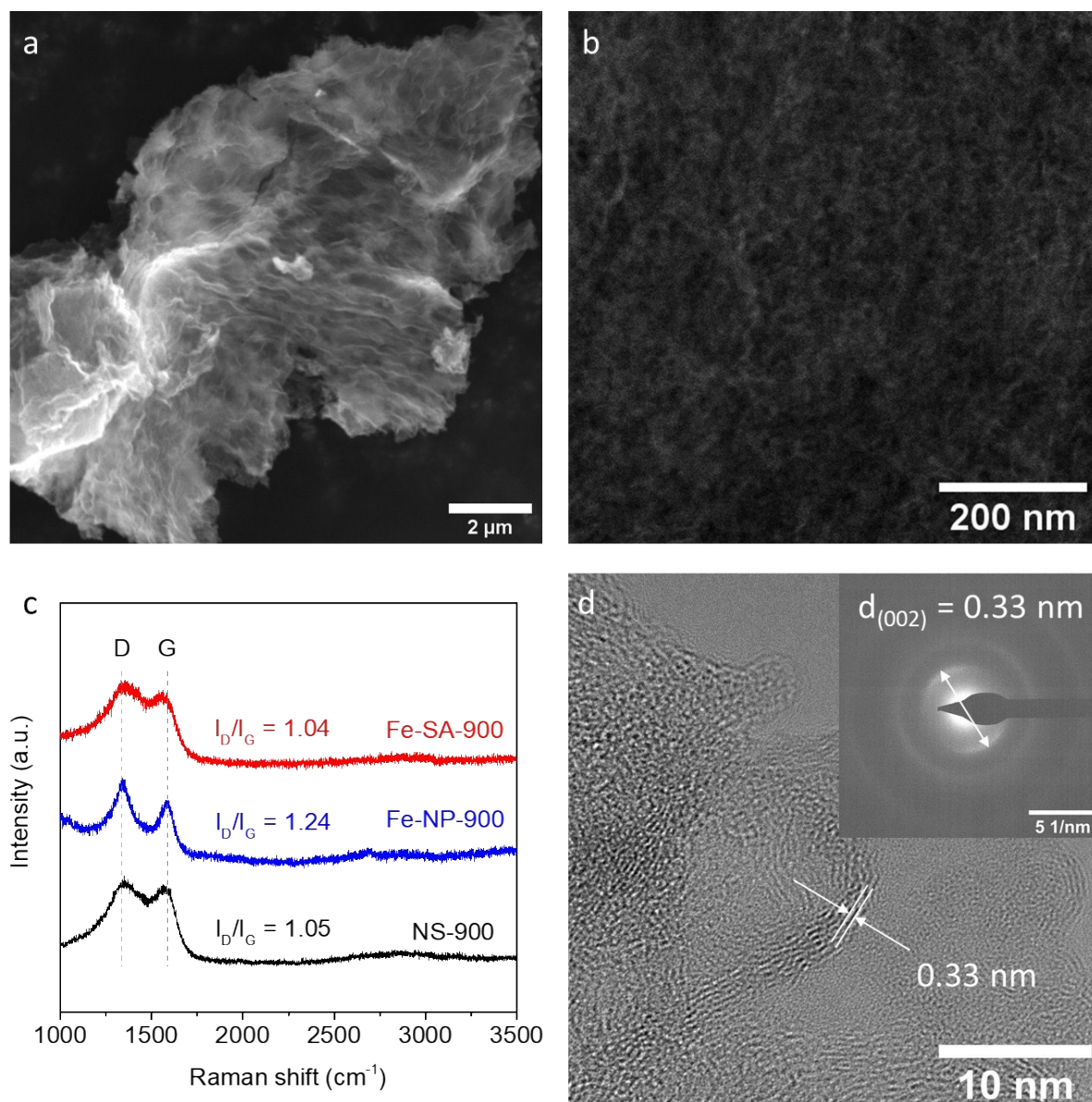
Figure S1. Morphology characterization. (a) SEM image of Fe-SA-900 with some wrinkles. (b) HRTEM image of Fe-SA-900. (c) Raman spectra with D-to-G band intensity ratios for Fe-SA-900, Fe-NP-900, and NS-900. D band (~1350 cm^{-1}) and G band (~1580 cm^{-1}) are typical peaks assigned to carbon nanosheets.[4] No sharp 2D peak (~2700 cm^{-1}) due to the stacking of carbon nanosheets was observed. (d) TEM image of Fe-SA-900 with a marked interplanar distance of 0.33 nm and inset of SAED pattern, which corresponds to the inter lattice spacing of the (002) plane in a hexagonal carbon structure.
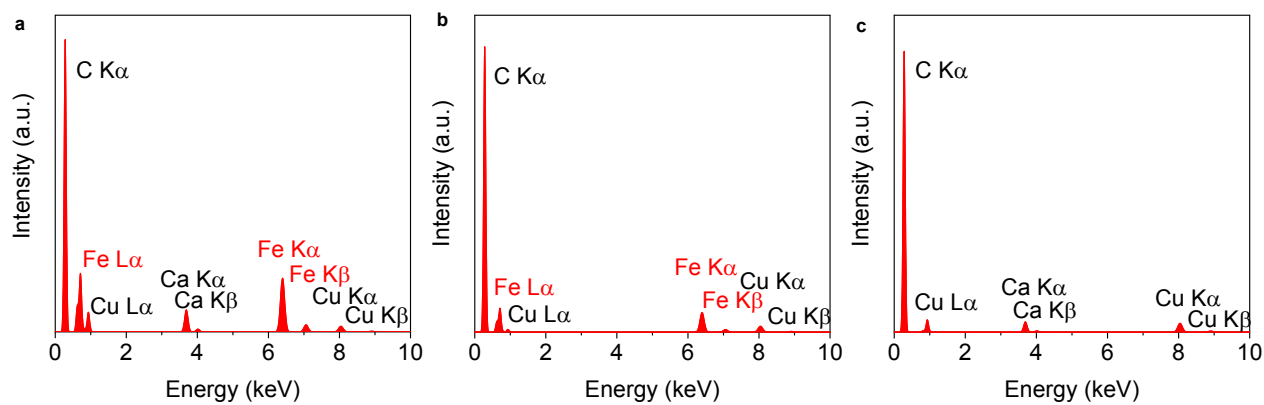
Figure S2. Corresponding EDS spectra of (a) Fe-SA-900, (b) Fe-NP-900, and (c) NS-900.
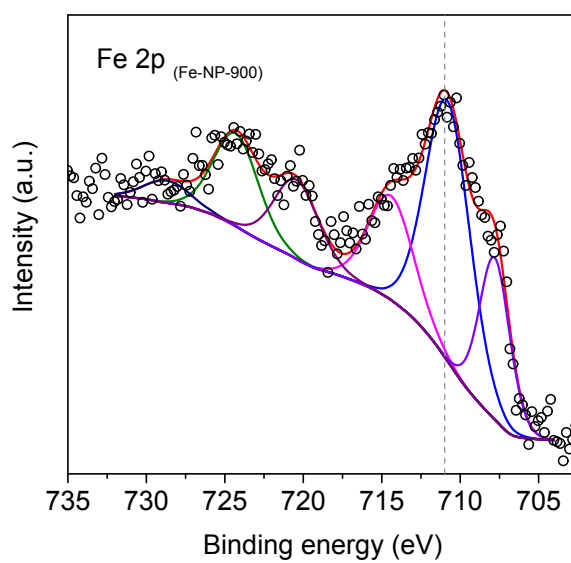
Figure S3. High-resolution XPS Fe 2p spectra of Fe-NP-900.
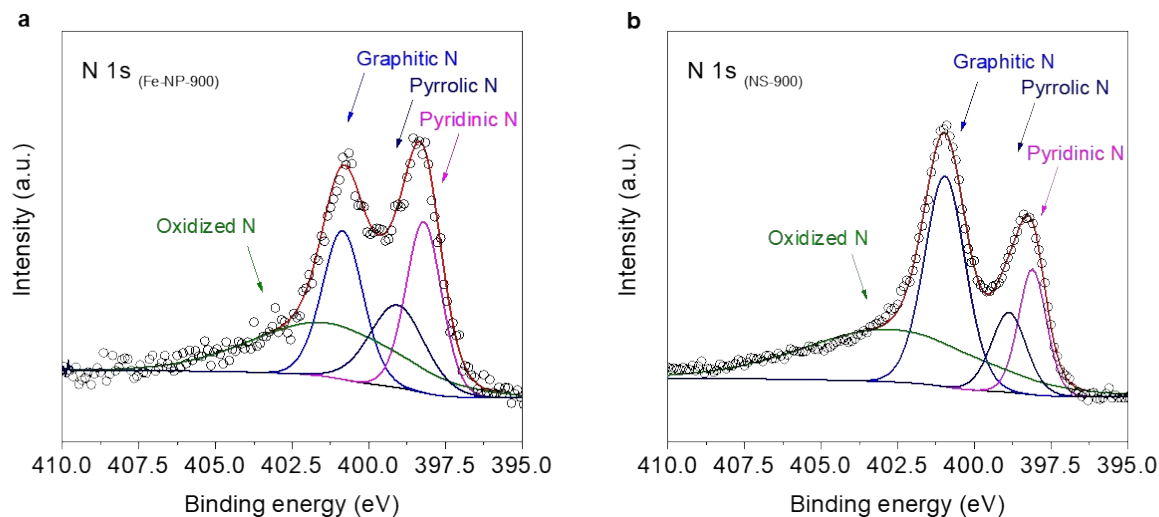
Figure S4. High-resolution XPS N 1s spectra for (a) Fe-NP-900 and (b) NS-900. The deconvoluted peaks are attributed to graphitic, pyrrolic, pyridinic, and oxidized N species.[5]
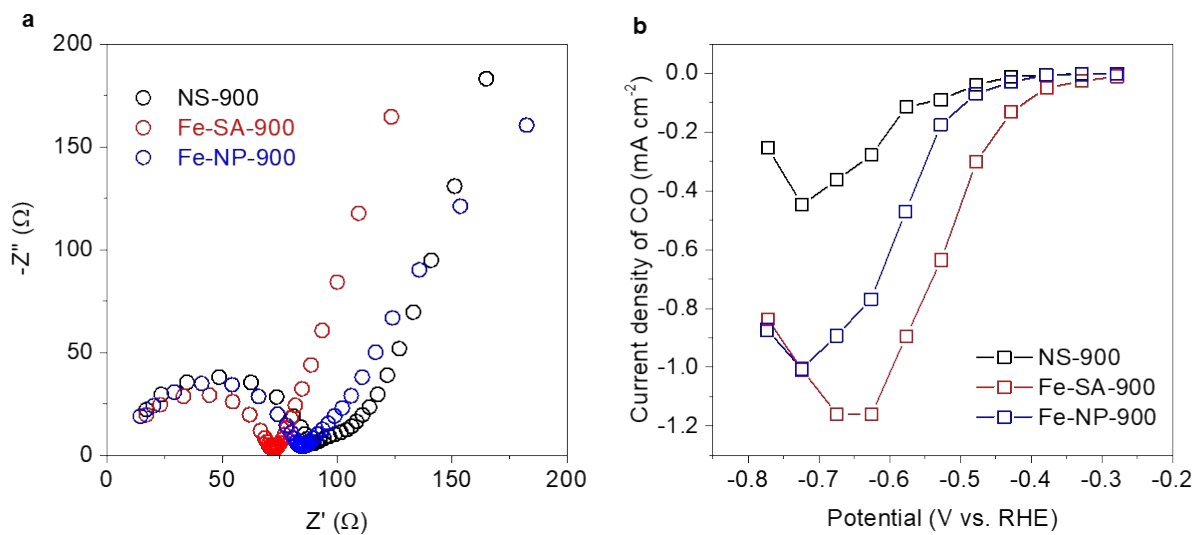
Figure S5. (a) Nyquist diagrams and (b) Polarization plots for CO generation on NS-900, Fe-NP-900, and Fe-SA-900.
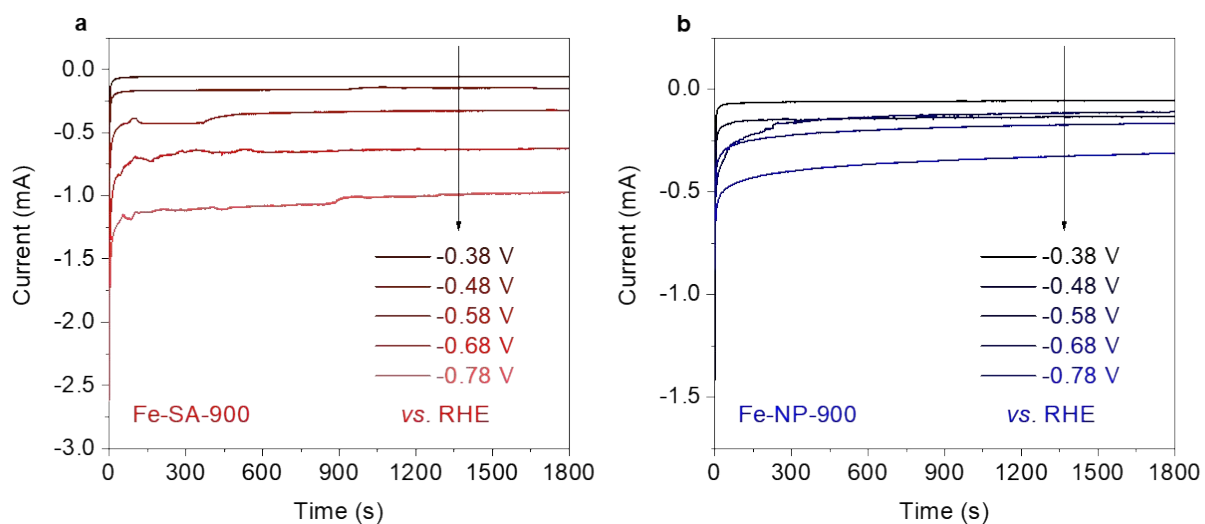
Figure S6. Amperometric *i-t* curves of (a) Fe-SA-900 and (b) Fe-NP-900 during CO_2 reduction.
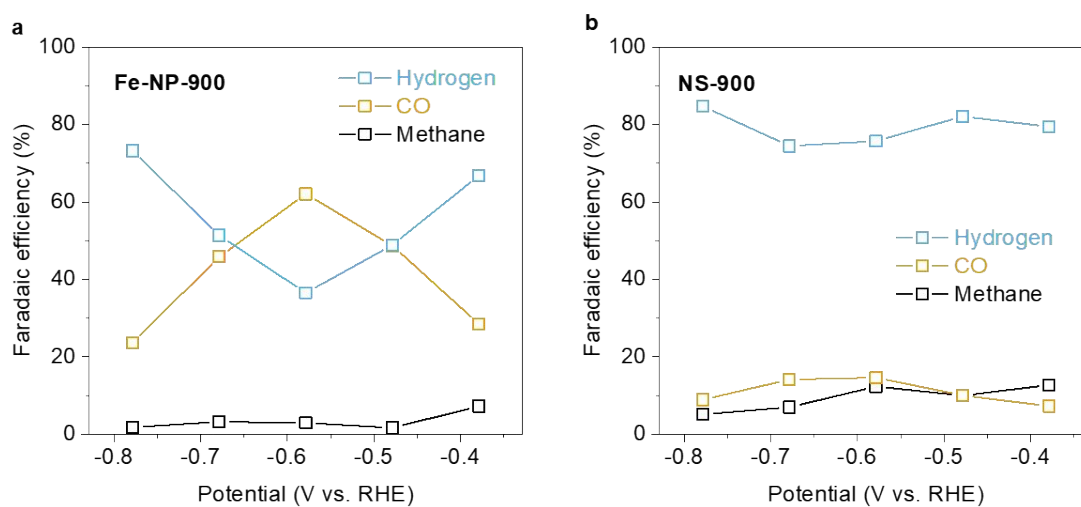
Figure S7. Measured FEs of CO_2 reduction on (a) Fe-NP-900 and (b) NS-900.
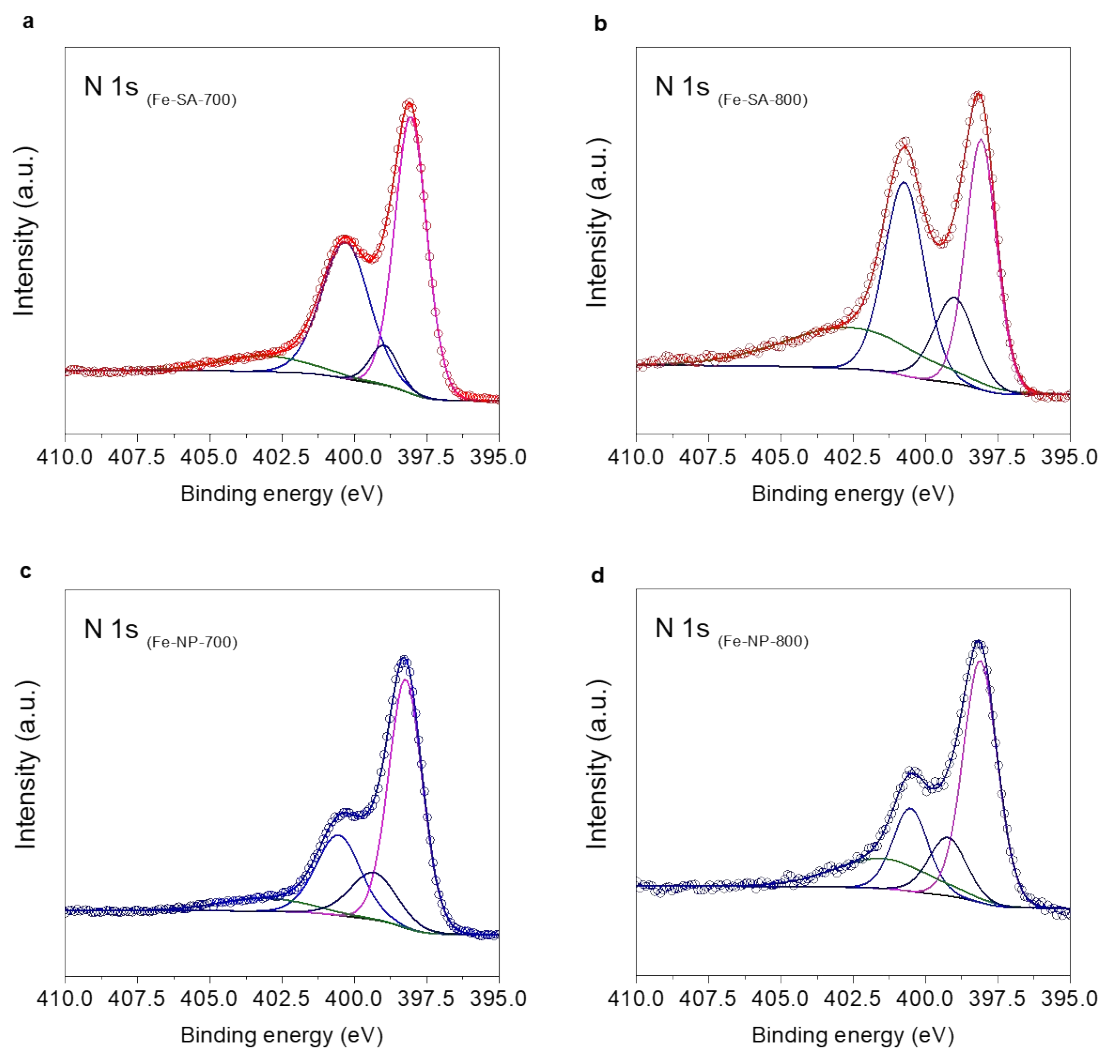
Figure S8. High-resolution XPS N1s spectra for (a) Fe-SA-700, (b) Fe-SA-800, (c) Fe-NP-700, and (d) Fe-NP-800.
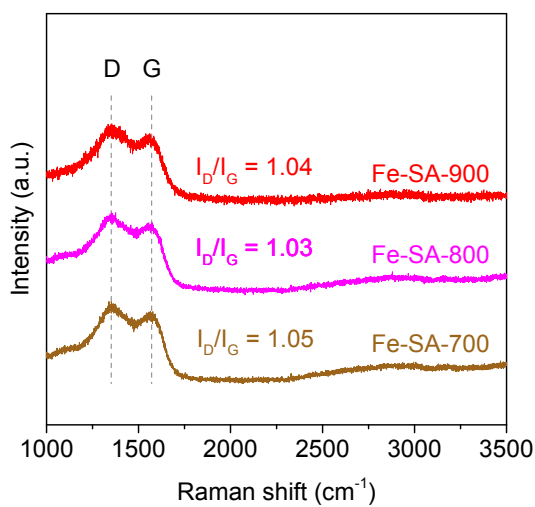
Figure S9. Raman spectra with D-to-G band intensity ratios for Fe-SA-900, Fe-SA-800, and Fe-SA-700.
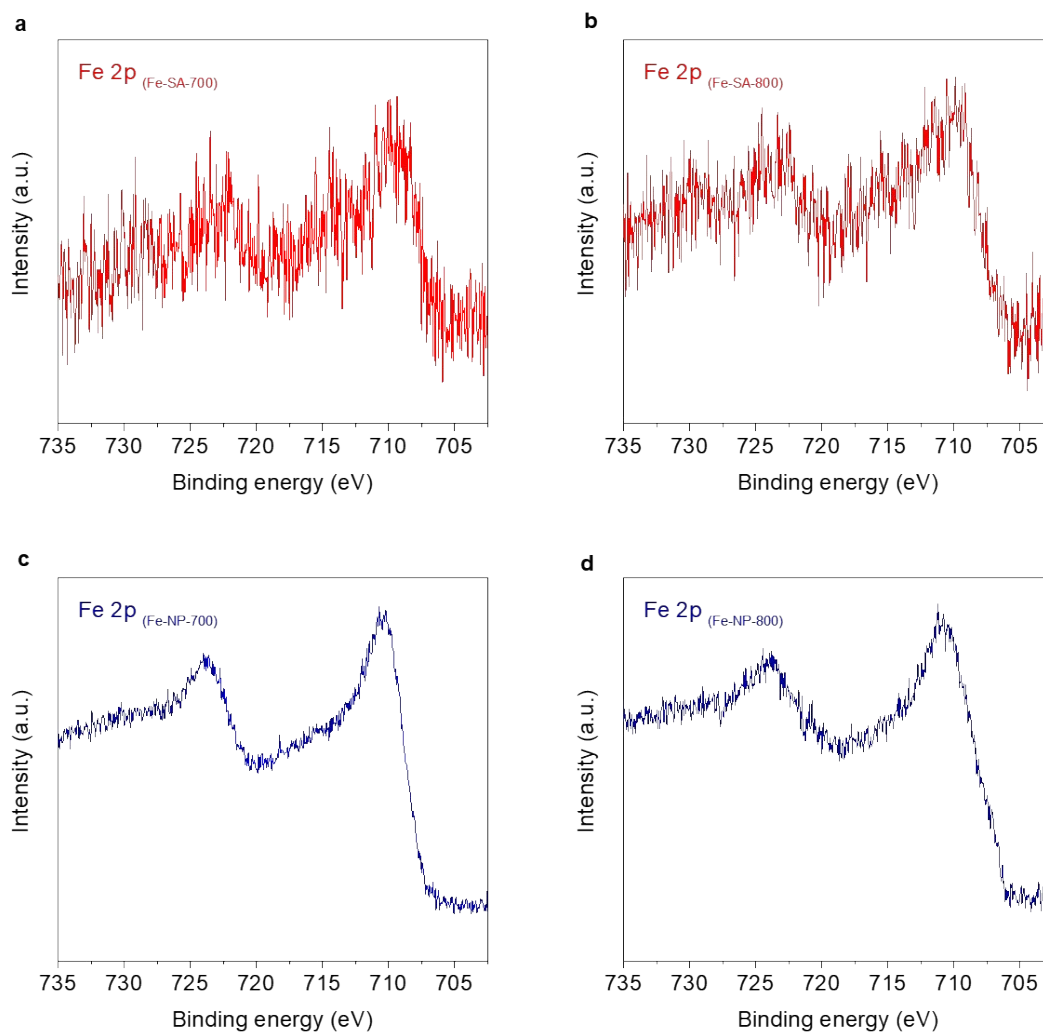
Figure S10. Deconvoluted high-resolution XPS N 1s spectra for (a) Fe-SA-700, (b) Fe-SA-800, (c) Fe-NP-700, and (d) Fe-NP-800.
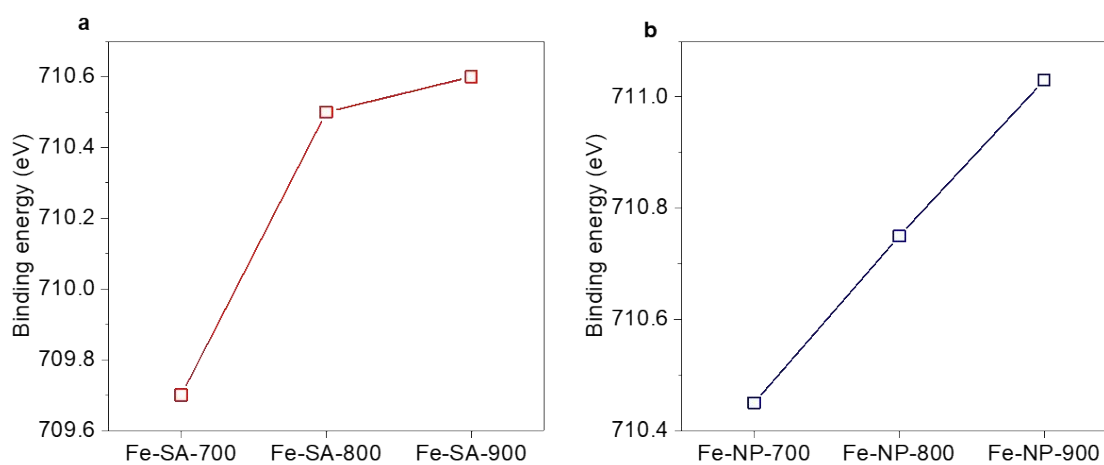
Figure S11. Fe $2p_{3/2}$ binding energy peak position for (a) Fe-SA and (b) Fe-NP group catalysts.

Table S1. XPS quantification of elemental composition and N species in at.%.

	Annealing T [°C]	Fe	C	O	N	N_g	N_{pyr}	N_{pyd}	N_{pyr}/N_{pyd}
	900	0.27	86.64	2.83	10.26	3.37	1.69	1.76	0.96
Fe-SA Group	800	0.28	80.11	2.93	16.67	5.26	2.37	5.27	0.45
	700	0.28	65.39	2.96	31.38	11.44	1.95	15.48	0.13
	900	0.90	88.42	5.08	5.60	1.37	1.03	1.38	0.74
Fe-NP Group	800	1.84	77.87	9.87	10.42	1.86	1.41	5.31	0.27
	700	1.88	75.24	4.98	17.91	4.16	2.58	9.82	0.26
NS Group	900	-	88.83	3.23	7.94	2.84	0.92	1.15	0.80

References

1.   D. B. Liu, C. Q. Wu, S. M. Chen, S. Q. Ding, Y. F. Xie, C. D. Wang, T. Wang, Y. A. Haleem, Z. U. Rehman, Y. Sang, Q. Liu, X. S. Zheng, Y. Wang, B. H. Ge, H. X. Xu and L. Song, *Nano Research*, 2018, **11**, 2217-2228.

2.   A. Vasileff, C. Xu, L. Ge, Y. Zheng and S. Z. Qiao, *Chem. Commun.*, 2018, **54**, 13965-13968.

3.   K. P. Kuhl, E. R. Cave, D. N. Abram and T. F. Jaramillo, *Energy Environ. Sci*, 2012, **5**, 7050-7059.

4.   M. Liu, R. Zhang and W. Chen, *Chem. Rev.*, 2014, **114**, 5117-5160.

5.   Y. Zheng and S. Z. Qiao, *Nat. Chem.*, 2018, **10**, 900-902.

Chapter 5

Highly Selective Two-Electron Electrocatalytic CO$_2$ Reduction on Single-Atom Cu Catalysts

Herein, we successfully synthesized a single-atom Cu catalyst embedded in N-doped graphene (Cu-N$_4$-NG) by a two-step pyrolysis method. Synchrotron-based X-ray absorption characterization identifies a Cu-N$_4$ structure whereby the Cu atom is coordinated by four adjacent N atoms within the two-dimensional graphene substrate. Compared to the conventional bulk Cu catalyst which exhibited relatively low selectivity for the CRR, the electrochemical evaluation showed that Cu-N$_4$-NG achieved a notably higher Faradaic Efficiency (FE$_{CO}$) of 80.6 % at -1.0 V vs. RHE. The kinetics results indicate that the Cu-N$_4$ moiety facilitates CO$_2$ adsorption, and the graphene substrate played a role in facilitating water dissociation, which provides protons for the CRR. The results given by density functional theory (DFT) calculations further confirm that the CRR was favored on Cu-N$_4$-NG due to its lower thermodynamic barrier than the competing hydrogen evolution reaction (HER).

This Chapter is presented as a research paper by Chaochen Xu, Xing Zhi, Anthony Vasileff, Dan Wang, Bo Jin, Yan Jiao, Yao Zheng, and Shi-Zhang Qiao: Highly selective two-electron electrocatalytic CO$_2$ reduction on single-atom Cu catalysts.

Statement of Authorship

Title of Paper	Highly Selective Two-Electron Electrocatalytic CO_2 Reduction on Single-Atom Cu Catalysts
Publication Status	☑ Published ☐ Accepted for Publication ☐ Submitted for Publication ☐ Unpublished and Unsubmitted work written in manuscript style
Publication Details	Chaochen Xu, Xing Zhi, Anthony Vasileff, Dan Wang, Bo Jin, Yan Jiao, Yao Zheng, Shi-Zhang. Qiao. *Small Structures*, 2020.

Principal Author

Name of Principal Author (Candidate)	Chaochen Xu
Contribution to the Paper	Proposed ideas, performed experiments, carried out data processing and interpretation, wrote the manuscript.
Overall percentage (%)	60
Certification:	This paper reports on original research I conducted during the period of my Higher Degree by Research candidature and is not subject to any obligations or contractual agreements with a third party that would constrain its inclusion in this thesis. I am the primary author of this paper.
Signature		Date	

Co-Author Contributions

By signing the Statement of Authorship, each author certifies that:

i.   the candidate's stated contribution to the publication is accurate (as detailed above);

ii. permission is granted for the candidate in include the publication in the thesis; and

iii. the sum of all co-author contributions is equal to 100% less the candidate's stated contribution.

Name of Co-Author	Xing Zhi
Contribution to the Paper	Performed DFT calculation, carried out DFT data processing and interpretation, wrote the DFT section in the manuscript.
Signature		Date	

Name of Co-Author	Anthony Vasileff
Contribution to the Paper	Assisted in experiments and revised the manuscript.
Signature		Date	

Name of Co-Author	Dan Wang
Contribution to the Paper	Supervised the research project and revised the manuscript.
Signature		Date	

Name of Co-Author	Bo Jin
Contribution to the Paper	Supervised the research project and revised the manuscript.
Signature		Date	

Name of Co-Author	Yan Jiao
Contribution to the Paper	Discussed DFT calculation results and findings; supervised the research project and revised the manuscript.
Signature		Date	

Name of Co-Author	Yao Zheng
Contribution to the Paper	Discussed experimental results and findings, supervised the research project, and revised the manuscript.
Signature		Date	

Name of Co-Author	Shi-Zhang Qiao
Contribution to the Paper	Discussed experimental results and findings, supervised research project and revised the manuscript.
Signature		Date	

Highly Selective Two-Electron Electrocatalytic CO$_2$ Reduction on Single-Atom Cu Catalysts

Chaochen Xu, Xing Zhi, Anthony Vasileff, Dan Wang, Bo Jin, Yan Jiao, Yao Zheng,* and Shi-Zhang Qiao*

Cu-based electrocatalysts with high catalytic selectivity for the CO$_2$ reduction reaction present a significant technological challenge. Herein, a catalyst comprised of Cu single atoms in a nitrogen-doped graphene matrix (Cu–N$_4$–NG) is developed for highly selective electrocatalytic reduction of CO$_2$ to CO. The single-atom structure and coordination environment of Cu–N$_4$–NG are identified by synchrotron-based characterization. Compared to a conventional bulk Cu catalyst, Cu–N$_4$–NG achieves a Faradaic efficiency of 80.6% toward CO under a moderate applied potential of -1.0 V versus reversible hydrogen electrode (RHE). Kinetic experiments show that 1) the Cu–N$_4$ moiety favors the CO$_2$ activation step and 2) the moiety-anchoring graphene facilitates water dissociation, which supplies protons for CO$_2$ reduction. Moreover, density functional theory (DFT) calculations reveal that CO$_2$ reduction is less hindered thermodynamically on Cu–N$_4$–NG compared to the competing hydrogen evolution reaction (HER) due to their limiting potential differences. Therefore, the highest CO selectivity is observed on Cu–N$_4$–NG over the bulk Cu catalyst due to more favorable kinetics and thermodynamics.

1. Introduction

The electrocatalytic CO$_2$ reduction reaction (CRR) is considered a promising solution for future energy by using renewable energy to convert CO$_2$ to useful chemical feedstocks such as CO, hydrocarbons, and alcohols. To become a feasible prospect, highly selective catalysts are required and have driven the extensive search for suitable materials.[1] In this regard, fundamental studies in the field aim to screen promising electrocatalysts that can be used for highly selective CO$_2$ reduction. So far, Cu has been widely reported as a unique metal with adequate efficiency because of its moderate adsorption of reactive intermediates

and ability to facilitate C—C coupling to longer chain products.[2] Metallic Cu, oxide-derived Cu, and Cu bimetallic alloys have been extensively investigated as electrocatalysts for the CRR and have shown various levels of catalytic performance.[3–5] However, these studies commonly report two noted issues that still await to be addressed: 1) low catalytic selectivity and 2) low atom-utilization efficiency in catalysts. To be specific, Cu is inert to the CRR at potentials lower than -1.0 V versus reversible hydrogen electrode (RHE).[6,7] Further, at high overpotentials (>1.5 V), the competing hydrogen evolution reaction (HER) becomes dominant, resulting in low CRR selectivity. Even under a relatively narrow potential window, Cu facilitates multiple CRR pathways, which eventually results in obtaining a variety of products (from C$_1$ to C$_3$).[2–7] This leads to both low catalytic efficiency for a specific product and the need for product separation. In terms of atom utilization, due to the unexposed Cu atoms that cannot directly participate in the catalytic reaction, it is necessary to increase the utilization efficiency of the Cu atoms in catalysts to improve the turnover frequency to industrial levels.

Compared to bulk metal counterparts, single-atom catalysts with completely exposed active atoms can effectively increase the number of active sites and exhibit high catalytic performance.[8–14] Moreover, single-atom catalysts are diverse in the scope given the metal center can be regulated by various surrounding ligands such as different synthetic conditions.[15] The electronic structures of single-atom catalysts can be engineered to optimize the activation energy of a reaction and alter the reaction pathway, leading to changes in activity and selectivity.[16–19] In particular, single-atom 3d transition metal (mainly Fe, Co, Ni) catalysts have achieved highly selective electroreduction of CO$_2$ to CO.[18–21] However, the most well-known 3d metal for the CRR, Cu, has rarely been reported in its single-atom form. This is likely because bulk Cu and its derivatives are expected to produce highly reduced products instead of C$_1$ products such as CO.[22–24] However, the study of single-atom Cu catalysts for the CRR is essential for understanding the catalytic mechanism as the active site is more easily identified in a single-atom catalyst.

Herein, we successfully synthesized a single-atom Cu catalyst embedded in N-doped graphene (Cu–N$_4$–NG) by a two-step pyrolysis method. Synchrotron-based X-ray absorption

C. Xu, X. Zhi, Dr. A. Vasileff, Prof. B. Jin, Dr. Y. Jiao, Dr. Y. Zheng, Prof. S.-Z. Qiao
Centre for Materials in Energy and Catalysis
School of Chemical Engineering and Advanced Materials
The University of Adelaide
Adelaide, SA 5005, Australia
E-mail: s.qiao@adelaide.edu.au; yao.zheng01@adelaide.edu.au

Prof. D. Wang
Institute of Process Engineering
Chinese Academy of Sciences
Beijing 100190, China

ⓘ The ORCID identification number(s) for the author(s) of this article can be found under https://doi.org/10.1002/sstr.202000058.

**ADVANCED
SCIENCE NEWS**
www.advancedsciencenews.com

**small
structures**
www.small-structures.com

characterization identifies a Cu–N_4 structure whereby the Cu atom is coordinated by four adjacent N atoms within the 2D graphene substrate. Compared to the conventional bulk Cu catalyst, which exhibited relatively low selectivity for the CRR, the electrochemical evaluation showed that Cu–N_4–NG achieved a notably higher CO Faradaic efficiency (FE) of 80.6% at −1.0 V versus RHE. The kinetics results indicate that the Cu–N_4 moiety facilitates CO_2 adsorption, and the graphene substrate plays a role in facilitating water dissociation and generation of protons for the CRR. The results given by density functional theory (DFT) calculations further confirm that the CRR was favored on Cu–N_4–NG due to its lower thermodynamic barrier than the competing HER.

2. Results and Discussion

The aberration-corrected high-angle annular dark-field scanning transmission electron microscopy (HAADF-STEM) image of the catalyst clearly shows Cu single atoms supported by ultrathin carbon layers with no apparent bulk particles observed (**Figure 1**a). The Raman spectra confirm that the carbon layer is composed of functionalized graphene, evidenced by the distinct *D*- and

G-band peaks corresponding to A_{1g} and E_{2g} vibrational modes of carbon (Figure S1, Supporting Information). Given the *Z*-contrast is strongly sensitive to heavy elements, the galaxy-like image generated shows how the Cu atoms were ubiquitously distributed throughout the graphene substrate. The line profile across four representative bright spots, shown in Figure 1b, indicates that the Cu was atomically dispersed with a size of 1–2 Å. The STEM image–derived pseudo-colored figure also confirms that the dispersed Cu atoms were observed at the sub-nanoscale (Figure S2, Supporting Information). The energy-dispersive X-ray spectroscopy (EDS) mapping and elemental analysis shown in Figure S3, Supporting Information, are consistent with the STEM images. To avoid Cu agglomeration in Cu–N_4–NG, a low amount of Cu was deliberately used in the synthesis process.[25] The Cu content in Cu–N_4–NG was measured by inductively coupled plasma mass spectrometry (ICP-MS) and was found to be 4.7 wt% or ≈0.93 at% (Figure S4, Supporting Information). The X-ray diffraction (XRD) pattern indicates the absence of crystalline Cu particles in Cu–N_4–NG (Figure 1c). As a control, N-doped graphene-supported Cu particles (Cu/NG) were prepared and characterized. The XRD pattern of Cu/NG shows distinct peaks that can be indexed to metallic Cu (PDF#70-3038). This indicates that Cu aggregation occurred
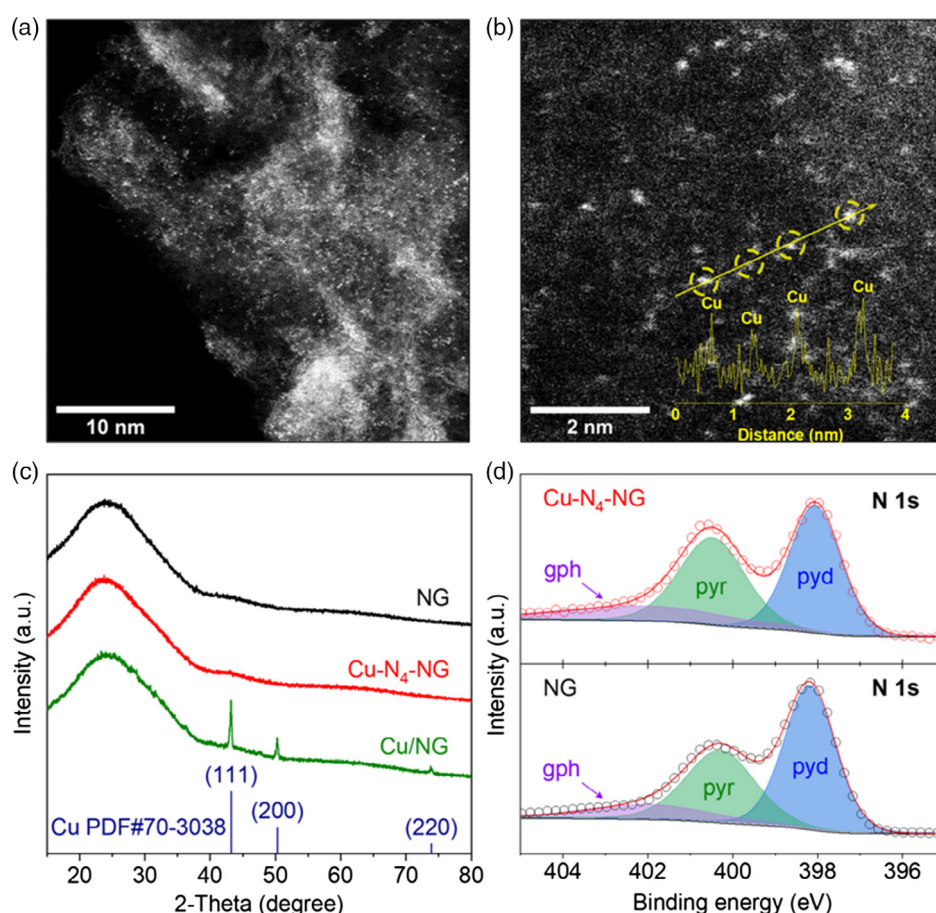

Figure 1. a) HAADF-STEM image of Cu–N_4–NG. b) HAADF-STEM image of Cu–N_4–NG at high magnification with a line profile (inset) along the arrow direction and through circled Cu atoms. c) Powder XRD patterns of different samples. d) The high-resolution N 1s XPS spectra of different samples.

**ADVANCED
SCIENCE NEWS**
www.advancedsciencenews.com

**small
structures**
www.small-structures.com

and led to the formation of heterogeneous Cu particles, which was further supported by scanning electron microscopy (SEM) imaging and EDS (Figure S5, S6, Supporting Information).

On both N-doped graphene (NG) and Cu–N₄–NG samples, the high-resolution X-ray photoelectron spectroscopy (XPS) spectra clearly identified signals from C, N, and O. The high-resolution

C 1s and O 1s spectra confirm the presence of N-doped graphene and the absence of Cu carbides and oxides in Cu–N₄–NG (Figure S7, S8, Supporting Information).[26,27] Moreover, the C 1s spectra of Cu–N₄–NG show a weaker C—N peak at 285.9 eV than that of NG, which is likely because the N atoms in Cu–N₄–NG partially participate in coordination with the Cu
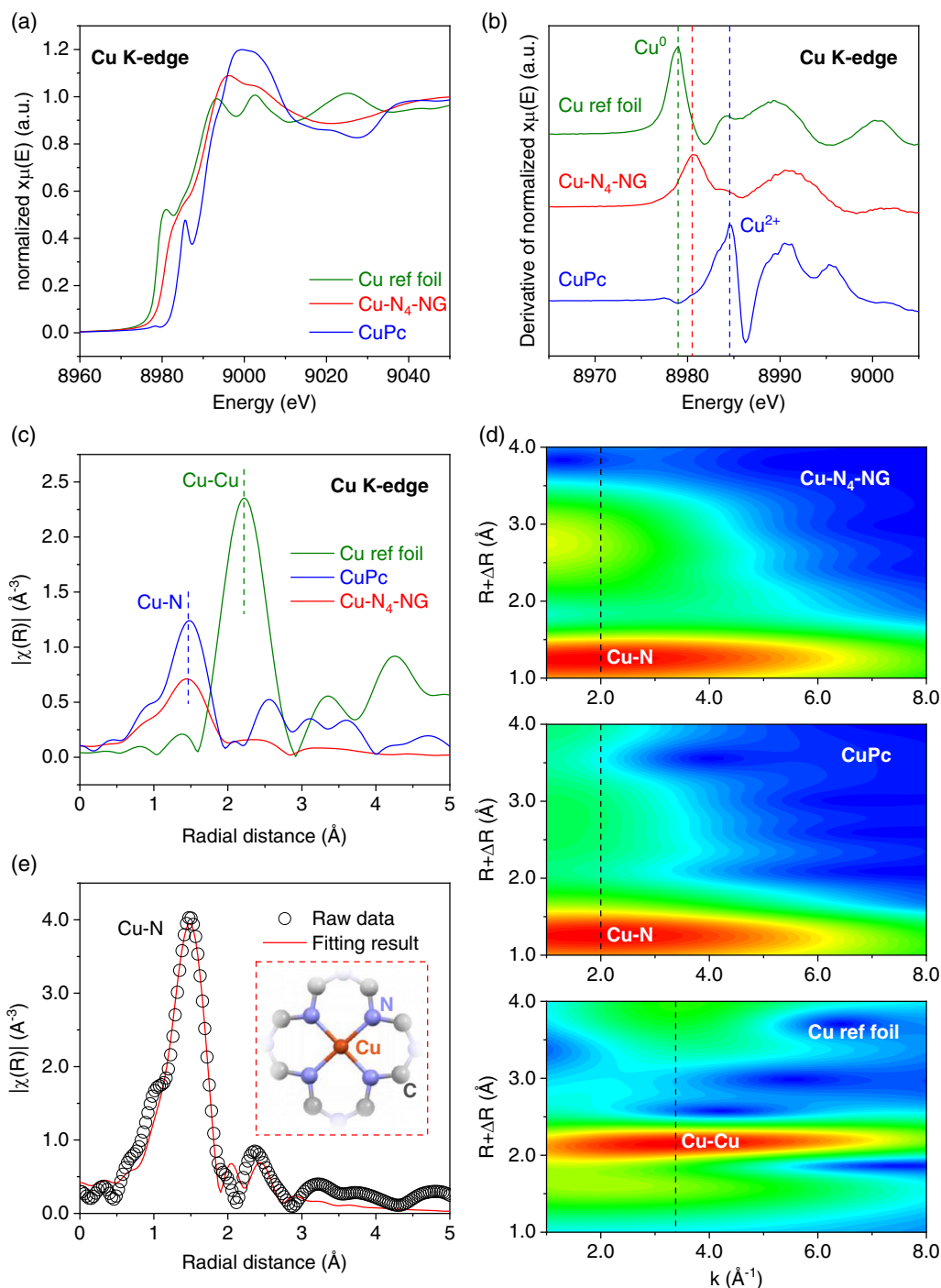
**Figure 2.** a) Cu K-edge XANES spectra and b) the first derivatives of the normalized Cu K-edge XANES spectra of different samples. c) Cu K-edge EXAFS spectra in R-space and d) wavelet transform analysis of Cu K-edge EXAFS oscillations of different samples. e) Experimental fitting of EXAFS data for Cu–N₄–NG with the fitting result shown as a solid line. The inset is the experimental model used for the fitting.

**ADVANCED
SCIENCE NEWS**

www.advancedsciencenews.com

**small
structures**

www.small-structures.com

atoms instead of only with C atoms.[26] From Figure 1d, the N 1s spectra can be deconvoluted and assigned to pyridinic- (N_{pyd}), pyrrolic- (N_{pyr}), and graphitic-N (N_{gph}) species at 398.1, 400.4, and 402.0 eV, respectively.[8] The N_{pyr}/N_{pyd} ratio is slightly higher in Cu–N_4–NG (0.87) compared to NG (0.67), indicating that more active pyrrolic-N sites were formed with the addition of Cu. This can possibly provide synergistic effects between the Cu atoms and pyrrolic N moieties to facilitate CO_2 electroreduction.[28]

To further confirm the coordination environment of Cu in Cu–N_4–NG, the synchrotron-based Cu K-edge X-ray absorption near-edge structure (XANES) and extended X-ray absorption fine structure (EXAFS) were investigated (**Figure 2**a). From the first derivatives of the XANES spectra (Figure 2b), the absorption edge of Cu–N_4–NG appears between that of metallic Cu(0) in the Cu reference foil (8978.9 eV) and Cu(II) in the copper(II) phthalocyanine reference (CuPc, 8984.4 eV), which confirms that Cu in Cu–N_4–NG is predominantly in an intermediate oxidation state ($Cu^{\delta+}$, $\delta = 0$–2). This indicates the presence of chemical bonds between the Cu atoms and their neighboring ligands.[29] The first-shell Cu coordination information was derived from the R-space EXAFS spectra (Figure 2c). The dominant peak of Cu–N_4–NG and CuPc appears at the same radial distance

(1.48 Å), and there are no significant Cu–Cu peaks (2.21 Å) in Cu–N_4–NG, which is consistent with the XRD findings. Specifically, the contour plots of the wavelet transform of the EXAFS spectra show that two center positions with the same k value of 2.0 Å^{-1} were observed in Cu–N_4–NG and the CuPc standard, indicating that the first-shell metal ligand of Cu–N_4–NG is predominantly assigned to Cu–N rather than Cu–C and/or Cu–O (Figure 2d).[29,30] This result implies that the Cu coordination environment of Cu–N_4–NG is similar to that of CuPc, i.e. the Cu–N structure. In Figure 2e, the Cu–N_4 structure shows a good fit to the EXAFS spectrum, where the measured dominant peak represents the first-shell coordination. Therefore, the X-ray absorption spectroscopy results demonstrate that the Cu atoms in Cu–N_4–NG were anchored to the N sites within the N-graphene substrate, and formed Cu–N_4 moieties.

The CRR performance measurements were conducted in CO_2-saturated 0.1 M $KHCO_3$ electrolyte which was continuously bubbled with CO_2 in the cathode chamber (Figure S9, Supporting Information). As shown in **Figure 3**a, a low onset potential for CO of ≈−0.4 V versus RHE was observed on Cu–N_4–NG. With a negatively increasing potential, the observed FE for CO rose to a maximum of 80.6% at an applied potential of −1.0 V versus RHE, while the HER was dramatically suppressed,
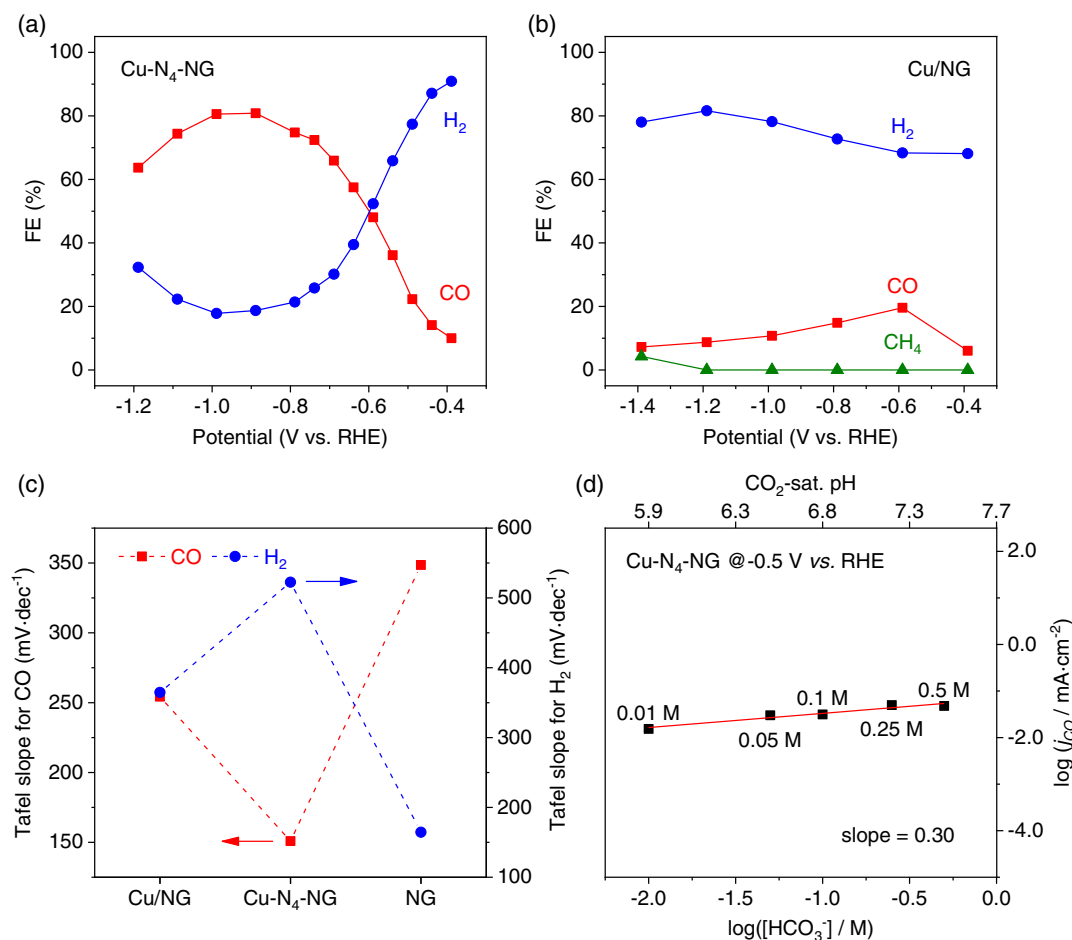
**Figure 3.** Measured FEs on a) Cu–N_4–NG and b) Cu/NG. c) Tafel slopes for CO and H_2 evolution on Cu/NG, Cu–N_4–NG, and NG. d) Rate dependencies on [HCO_3^-] for Cu–N_4–NG at a near onset potential of −0.5 V versus RHE.

ADVANCED
SCIENCE NEWS

www.advancedsciencenews.com

small
structures

www.small-structures.com

indicating that the CRR was much more favored than the HER on Cu–N_4–NG. On the other hand, high FEs toward CO were not obtained on Cu/NG and NG, and the HER was undoubtedly the dominant reaction for these catalyst systems (Figure 3b and S10, Supporting Information). From a comparison of measured FEs under stable operation at −1.0 V versus RHE (Figure S11, Supporting Information), it is clear that Cu–N_4–NG favors the reduction of CO2 to CO, whereas the other catalysts favor the HER (Figure S12, Supporting Information).

Kinetic Tafel studies were performed to understand the electrocatalytic mechanism of CO_2 reduction on Cu–N_4–NG (Figure S13, Supporting Information). In Figure 3c, the Tafel slope for CO evolution on Cu–N_4–NG is ≈150.9 mV dec^{-1}, which can be attributed to a rate-determining step (RDS) related to the first electron transfer, i.e., CO_2 activation with proton-coupled electron transfer (PCET).[31] To discover the source of protons, the experiments were conducted with various concentrations of $KHCO_3$ electrolyte solutions at the near-onset potential of −0.5 V versus RHE. The results demonstrate an approximate zero-order dependency on [HCO_3^-] and/or [H^+] according to a near-zero slope shown in Figure 3d. This suggests that the protons that participated in the PCET step were mainly generated from water dissociation rather than directly from the bicarbonate and/or hydronium ions in the electrolyte, i.e., $* + CO_2 + H_2O + e^- = *COOH + OH^-$.[31,32] The *COOH

species is a key intermediate for CO_2 reduction, and it can be further reduced to CO (*COOH reduction: $*COOH + H_2O + e^- = *CO + H_2O + OH^-$; *CO desorption: $*CO = * + CO$). Further reaction beyond the CO, i.e., C–C coupling, was not observed on Cu–N_4–NG. This is likely due to the lack of adjacent Cu atoms where adsorbed *CO in close vicinity can couple together to form more reduced products. Compared to Cu–N_4–NG, the *COOH formation steps on Cu/NG and NG were kinetically more hindered, with Tafel slopes of 254.3 and 348.6 mV dec^{-1}, respectively. Furthermore, NG exhibited a Tafel slope of 164.5 mV dec^{-1} for the HER, as shown in Figure 3d, indicating that the Volmer step is the dominant RDS for water dissociation on the N-graphene ($* + H_2O + e^- = *H + OH^-$).[33] However, Cu/NG and Cu–N_4–NG, which showed larger Tafel slopes, were kinetically sluggish in this first step of H_2 formation. It implies that N-graphene can promote water dissociation to provide protons. Therefore, the kinetics results suggest that the presence of Cu–N_4 moieties in Cu–N_4–NG plays a key role in facilitating the CO_2 activation step, while the graphene substrate is responsible for generating protons via catalytic water dissociation.

Unlike the HER process, the CRR is a reaction involving multiple reaction steps and electron transfers. Consequently, its kinetic analysis can be affected by the coverage of the various intermediate adsorbates, resulting in a deviation from theoretical
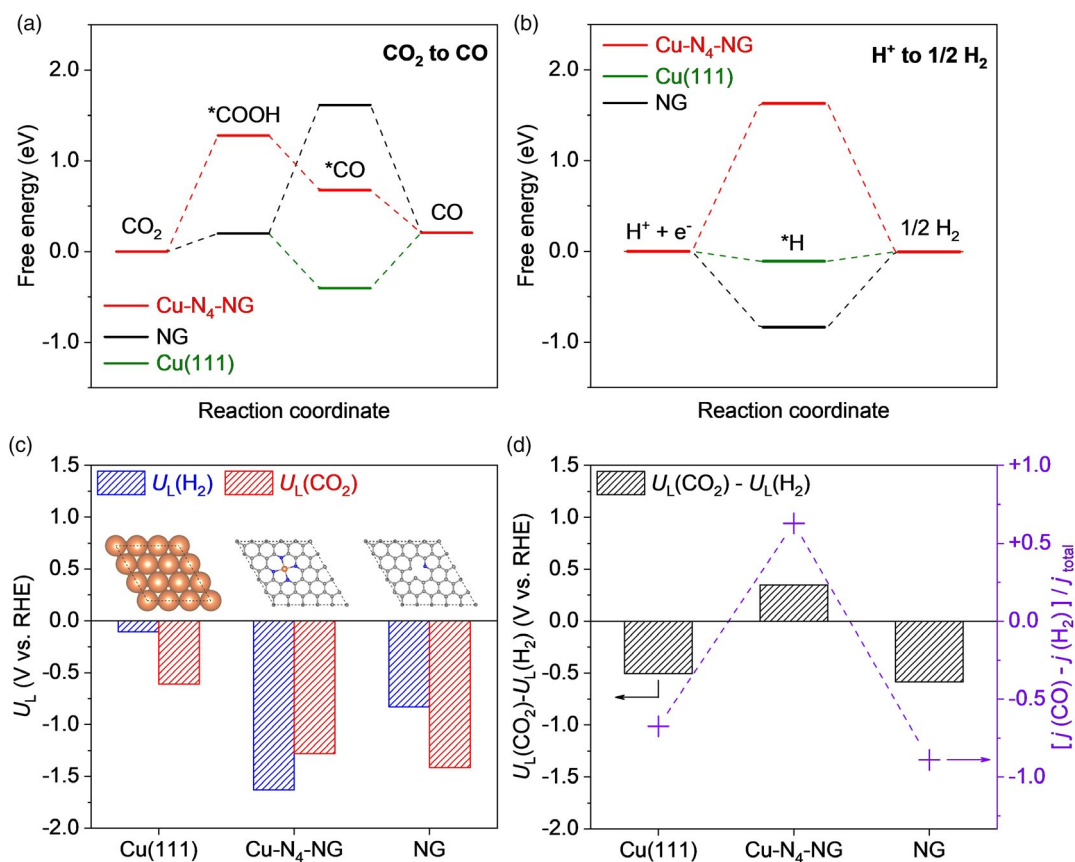
Figure 4. Free energy diagrams of a) CO_2 electroreduction to CO and b) H_2 evolution on Cu–N_4–NG, NG, and Cu (111). c) Calculated limiting potentials for CO_2 reduction, H_2 evolution, and d) their differences between CO and H_2 partial current densities (+) at −1.0 versus RHE on Cu(111), Cu–N_4–NG, and NG.

**ADVANCED
SCIENCE NEWS**

www.advancedsciencenews.com

**small
structures**

www.small-structures.com

results.[33] Therefore, the CRR performance of different catalysts studied was further investigated by theoretical DFT calculations. As reported in previous studies, the electrochemical reduction of CO_2 to CO generally occurs through two adsorbed intermediates: *COOH and *CO. The free energy diagrams for CO_2 electroreduction to CO on Cu–N_4–NG, NG, and Cu(111) surfaces are compared (**Figure 4**a). The data for Cu(111) refer to our previous study and are used to represent Cu/NG as Cu(111) is the dominant phase in this material (Figure 1c).[34] The potential-limiting step for Cu–N_4–NG is the protonation of CO_2 to *COOH (1.28 eV), while NG shows the highest free energy change for the *COOH hydrogenation step to *CO (1.62 eV). Overall, the limiting potential of CO_2 reduction to CO for Cu–N_4–NG is lower than that for NG, indicating a thermodynamic preference for CO evolution on Cu–N_4–NG. Meanwhile, the reaction energies of H_2 evolution are also compared (Figure 4b). For Cu–N_4–NG, the free energy change of *H formation is uphill with 1.63 eV. In contrast, NG exhibits strong adsorption of *H with a downhill free energy change. It is noteworthy that the Cu(111) surface shows a near-zero free energy change for *H formation, suggesting that the HER thermodynamics are favorable on Cu(111). In addition, more spontaneous *H formation and strong adsorption of *H were observed on NG, which are consistent with the kinetic results that N-graphene facilitates water dissociation to provide protons for coupling with the CO_2 reduction step.

According to the computational hydrogen electrode (CHE) model, the least negative potential at which all elementary steps of a reaction pathway become downhill in free energy is referred to as the limiting potential (U_L) (Figure 4c).[35,36] Previous DFT studies have suggested that the difference between the limiting potentials for the CRR and HER (i.e., $U_L(CO_2)-U_L(H_2)$) can be applied as a reasonable descriptor for CRR selectivity.[37] It is suggested that the more positive the value of $U_L(CO_2)-U_L(H_2)$, the higher is the activity toward the CRR over the HER. The $U_L(CO_2)-U_L(H_2)$ values across the models are plotted in Figure 4d and show a similar trend with the experimental differences between partial current densities for the CRR and HER (i.e., $[j(CO)-j(H_2)]/j_{total}$). To be specific, Cu–N_4–NG shows the most positive $U_L(CO_2)-U_L(H_2)$, suggesting it has the highest preference for the CRR compared to NG and bulk Cu. This agrees well with the experimental results whereby Cu–N_4–NG exhibits the most positive value for $[j(CO) - j(H_2)]/j_{total}$.

3. Conclusion

In conclusion, Cu–N_4–NG was prepared using a facile method and showed selective electroreduction of CO_2 to CO compared to NG and Cu/NG control samples. Material characterization and CRR kinetics study of Cu–N_4–NG demonstrate that 1) the single Cu atoms are predominantly coordinated by four adjacent N atoms and enhance the CO_2 activation step and 2) the homogeneous graphene substrate, where the Cu–N_4 moieties are embedded, promotes water dissociation for the supply and participation of protons in the CRR process. Further, the thermodynamic results from DFT calculations suggest that the trend of the differences between the calculated CRR and HER limiting potentials is consistent with the experimental trend of the differences between CO and H_2 partial current densities. Combining the

advantages of more favorable kinetics and thermodynamics, Cu–N_4–NG achieved the highest CO selectivity compared with Cu-based single-atom catalysts that have been reported so far, reaching an FE of 80.6% at a low potential of -1.0 V versus RHE (Table S1, Supporting Information). This study demonstrates how sub-nanoscale engineering of Cu electrocatalysts can be used to improve CRR selectivity and provides a well-defined model to further explore the reaction mechanism.

Supporting Information

Supporting Information is available from the Wiley Online Library or from the author.

Conflict of Interest

The authors declare no conflict of interest.

[1] C. Chen, J. F. Khosrowabadi Kotyk, S. W. Sheehan, *Chem* **2018**, *4*, 2571.

[2] S. Nitopi, E. Bertheussen, S. B. Scott, X. Liu, A. K. Engstfeld, S. Horch, B. Seger, I. E. L. Stephens, K. Chan, C. Hahn, J. K. Norskov, T. F. Jaramillo, I. Chorkendorff, *Chem. Rev.* **2019**, *119*, 7610.

[3] D. Gao, R. M. Arán-Ais, H. S. Jeon, B. Roldan Cuenya, *Nat. Catal.* **2019**, *2*, 198.

[4] Y. Zheng, A. Vasileff, X. Zhou, Y. Jiao, M. Jaroniec, S. Z. Qiao, *J. Am. Chem. Soc.* **2019**, *141*, 7646.

[5] A. Vasileff, C. Xu, Y. Jiao, Y. Zheng, S.-Z. Qiao, *Chem* **2018**, *4*, 1809.

[6] Y. Hori, A. Murata, R. Takahashi, *J. Chem. Soc., Faraday Trans. 1* **1989**, *85*, 2309.

[7] K. P. Kuhl, E. R. Cave, D. N. Abram, T. F. Jaramillo, *Energy Environ. Sci.* **2012**, *5*, 7050.

[8] Y. Wang, J. Mao, X. Meng, L. Yu, D. Deng, X. Bao, *Chem. Rev.* **2019**, *119*, 1806.

[9] C. Zhu, S. Fu, Q. Shi, D. Du, Y. Lin, *Angew. Chem. Int. Ed.* **2017**, *56*, 13944.

[10] Y. Chen, S. Ji, C. Chen, Q. Peng, D. Wang, Y. Li, *Joule* **2018**, *2*, 1242.

ADVANCED
SCIENCE NEWS

www.advancedsciencenews.com

small
structures

www.small-structures.com

[11] A. Wang, J. Li, T. Zhang, *Nat. Rev. Chem.* **2018**, *2*, 65.

[12] H. Fei, J. Dong, Y. Feng, C. S. Allen, C. Wan, B. Volosskiy, M. Li, Z. Zhao, Y. Wang, H. Sun, P. An, W. Chen, Z. Guo, C. Lee, D. Chen, I. Shakir, M. Liu, T. Hu, Y. Li, A. I. Kirkland, X. Duan, Y. Huang, *Nat. Catal.* **2018**, *1*, 63.

[13] B. W. Zhang, Y. X. Wang, S. L. Chou, H. K. Liu, S. X. Dou, *Small Methods* **2019**, *3*, 1800497.

[14] J. Wu, L. Xiong, B. Zhao, M. Liu, L. Huang, *Small Methods* **2019**, *4*, 1900540.

[15] T. Sun, Y. Li, T. Cui, L. Xu, Y. G. Wang, W. Chen, P. Zhang, T. Zheng, X. Fu, S. Zhang, Z. Zhang, D. Wang, Y. Li, *Nano Lett.* **2020**, *20*, 6206.

[16] Z. Sun, T. Ma, H. Tao, Q. Fan, B. Han, *Chem* **2017**, *3*, 560.

[17] A. S. Varela, W. Ju, P. Strasser, *Adv. Energy Mater.* **2018**, *8*, 1703614.

[18] L. Wang, W. Chen, D. Zhang, Y. Du, R. Amal, S. Qiao, J. Wu, Z. Yin, *Chem. Soc. Rev.* **2019**, *48*, 5310.

[19] W. Ju, A. Bagger, G. P. Hao, A. S. Varela, I. Sinev, V. Bon, B. Roldan Cuenya, S. Kaskel, J. Rossmeisl, P. Strasser, *Nat. Commun.* **2017**, *8*, 944.

[20] C. Ding, C. Feng, Y. Mei, F. Liu, H. Wang, M. Dupuis, C. Li, *Appl. Catal. B* **2020**, *268*, 118391.

[21] Y. Cheng, S. Zhao, B. Johannessen, J. P. Veder, M. Saunders, M. R. Rowles, M. Cheng, C. Liu, M. F. Chisholm, R. De Marco, H. M. Cheng, S. Z. Yang, S. P. Jiang, *Adv. Mater.* **2018**, *30*, 1706287.

[22] H. Yang, Y. Wu, G. Li, Q. Lin, Q. Hu, Q. Zhang, J. Liu, C. He, *J. Am. Chem. Soc.* **2019**, *141*, 12717.

[23] D. Karapinar, N. T. Huan, N. Ranjbar Sahraie, J. Li, D. Wakerley, N. Touati, S. Zanna, D. Taverna, L. H. Galvao Tizei, A. Zitolo, F. Jaouen, V. Mougel, M. Fontecave, *Angew. Chem. Int. Ed.* **2019**, *58*, 15098.

[24] Y. Jiao, Y. Zheng, P. Chen, M. Jaroniec, S. Z. Qiao, *J. Am. Chem. Soc.* **2017**, *139*, 18093.

[25] J. Wu, H. Zhou, Q. Li, M. Chen, J. Wan, N. Zhang, L. Xiong, S. Li, B. Y. Xia, G. Feng, M. Liu, L. Huang, *Adv. Energy Mater.* **2019**, *9*, 1900149.

[26] M. C. Ortega-Liebana, N. X. Chung, R. Limpens, L. Gomez, J. L. Hueso, J. Santamaria, T. Gregorkiewicz, *Carbon* **2017**, *117*, 437.

[27] X. Rong, H. J. Wang, X. L. Lu, R. Si, T. B. Lu, *Angew. Chem., Int. Ed.* **2020**, *59*, 1961.

[28] C. Xu, A. Vasileff, D. Wang, B. Jin, Y. Zheng, S.-Z. Qiao, *Nanoscale Horiz.* **2019**, *4*, 1411.

[29] Y. Qu, Z. Li, W. Chen, Y. Lin, T. Yuan, Z. Yang, C. Zhao, J. Wang, C. Zhao, X. Wang, F. Zhou, Z. Zhuang, Y. Wu, Y. Li, *Nat. Catal.* **2018**, *1*, 781.

[30] C. Xu, A. Vasileff, B. Jin, D. Wang, H. Xu, Y. Zheng, S.-Z. Qiao, *Chem. Commun.* **2020**, *56*, 11275.

[31] M. Dunwell, W. Luc, Y. Yan, F. Jiao, B. Xu, *ACS Catal.* **2018**, *8*, 8121.

[32] M. Ma, B. J. Trzesniewski, J. Xie, W. A. Smith, *Angew. Chem., Int. Ed.* **2016**, *55*, 9748.

[33] T. Shinagawa, A. T. Garcia-Esparza, K. Takanabe, *Sci. Rep.* **2015**, *5*, 13801.

[34] X. Zhi, Y. Jiao, Y. Zheng, A. Vasileff, S.-Z. Qiao, *Nano Energy* **2020**, *71*, 104601.

[35] A. A. Peterson, F. Abild-Pedersen, F. Studt, J. Rossmeisl, J. K. Norskov, *Energy Environ. Sci.* **2010**, *3*, 1311.

[36] A. A. Peterson, J. K. Norskov, *J. Phys. Chem. Lett* **2012**, *3*, 251.

[37] C. Shi, H. A. Hansen, A. C. Lausche, J. K. Norskov, *Phys. Chem. Chem. Phys.* **2014**, *16*, 4720.

2000058 (7 of 7)

Supporting Information

Highly Selective Two-Electron Electrocatalytic CO₂ Reduction on Single-Atom Cu Catalysts

Chaochen Xu,† Xing Zhi,† Anthony Vasileff, Dan Wang, Bo Jin, Yan Jiao, Yao Zheng*, and Shi-Zhang Qiao*

Chemicals

Copper(II) chloride dihydrate ($CuCl_2 \cdot 2H_2O$), dicyandiamide (Dicy), glucose, copper(II) phthalocyanine (CuPc, $C_{32}H_{16}CuN_8$), copper(I) oxide (Cu_2O), potassium bicarbonate ($KHCO_3$), dimethyl sulfoxide (DMSO), phenol, deuterium oxide (D_2O), hydrochloric acid (37%), and nitric acid (65%) were purchased from Sigma-Aldrich and used without further purification. Deionized water (DI water, 18 MΩ·cm) was from a Milli-Q water purifier. A 0.05 wt.% Nafion solution was diluted from LIQUion™ Solutions (LQ-1115 - 1100 EW at 15 wt.%). Liquid N_2, ultra-high purity Ar and N_2 (99.999%), and laser grade CO_2 (99.995%) were supplied from BOC Gas.

Synthesis Method

$Cu-N_4-NG$ was prepared using a modified method.[1] In detail, 2.0 g of dicyandiamide and 0.1 g of glucose were dissolved in 50 mL deionized water, followed by the dropwise addition of 1 mL of fresh 0.01 M copper(II) chloride solution. After 2 h vigorous stirring, the solution was immediately frozen by liquid N_2 at 77.15 K and was then transferred to a freeze dryer for water removal. Once completely dried, the received powder was placed into a lidded crucible in a tube furnace under Ar atmosphere. The powder was firstly annealed at 550°C for 1h with a heating rate of 5°C min^{-1}. The temperature was then raised to 900°C at a heating rate of 3°C min^{-1} and held for another hour. This step is for the decomposition of $g-C_3N_4$ and liberates $Cu-N_x$ moieties into the graphene lattices. Once cooled to room temperature, the resultant was washed with deionized water and centrifugated at 10,000 rpm for three times. The washed resultant was dried in an oven under vacuum at 60°C overnight. For comparison, NG was prepared using the same method but without the addition of the Cu(II) solution; Cu/NG was prepared using the same method but 20 mL of the Cu(II) solution was added instead.

Material Characterization

The scanning electron microscopy (SEM) images and energy-dispersive X-ray spectroscopy (EDS) spectra were acquired with FEI Quanta 450. The aberration-corrected high-angle annular

2

dark-field scanning transmission electron microscopy (HAADF-STEM) images and EDS data were acquired with FEI Titan Themis 80-200. The inductively coupled plasma mass spectrometry (ICP-MS) measurements were performed using Agilent 8900x ICP-QQQ-MS. The X-ray diffraction (XRD) patterns were recorded on Rigaku X-Ray Diffractometer (Cu Kα, $\lambda = 1.5406$ Å). The X-ray photoelectron spectroscopy (XPS) measurements were performed on Kratos AXIS Ultra (mono Al Kα), and XPS spectra were calibrated to the C-C peak at 284.8 eV. The X-ray absorption spectroscopy (XAS) spectra were collected from 1.9 T Wiggler XAS beamline using liquid nitrogen cooled Si (111) crystal at Hutch B experimental station at the Australian synchrotron. Cu-N$_4$-NG was measured in fluorescence mode, while CuPc was measured in transmission mode. All spectra for investigation of the X-ray absorption near edge structure (XANES) and extended X-ray absorption fine structure (EXAFS) were calibrated by the reference standards of copper foil (Cu K-edge at 8978.9 eV). The position of adsorption edge was determined from the first maximum of the first derivatives of the spectrum. The XAS data processing was done using Athena and Artemis. The crystallographic information file of copper phthalocyanine (CIF #2103883) was used for EXAFS fitting with an R-factor of 0.0110. The continuous Cauchy wavelet transform (WT) analysis of EXAFS spectra was performed on MATLAB. The Raman spectra were collected using HORIBA LabRAM HR Evolution Raman Spectroscopy with Olympus MPLN50x objective lens and 532 nm DPSS laser (Laser Quantum, mpc3000). The Fourier-transform infrared spectroscopy (FTIR) spectra were recorded using Nicolet 6700 FTIR spectrometer.

Electrochemical Measurements

The experiments were performed on an electrochemical workstation (CH Instruments 760E) using a three-electrode H-cell separated by a proton exchange membrane (Nafion 117). A glassy carbon electrode (1.0 cm × 1.0 cm), Ag/AgCl (3.5 м KCl), and RuO$_2$-coated titanium mesh served as the working, reference, and counter electrodes, respectively. To prepare a catalyst ink, 8 mg of catalyst was ultrasonically dispersed in 2 mL of 0.05 wt.% Nafion aqueous solution.

Then, 100 μL of the ink was dropwise added onto the surface of the glassy carbon and dried in air (catalyst loading of 0.4 mg·cm^{-2}). The electrochemical measurements, cyclic voltammetry (CV), linear scan voltammetry (LSV), and chronoamperometric curve (*i-t*) were carried out in 0.1 M KHCO$_3$ aqueous electrolyte (*pH* = 6.8) with continuously bubbled CO$_2$ with a flow rate of 10 sccm. All *iR*-corrected potentials were converted to the reversible hydrogen electrode (RHE) scale at 20°C according to the Nernst equation:

$$E \ (\ V \ vs. \ RHE\ ) = E \ (\ V \ vs. \ Ag/AgCl\ ) + 0.059 \times pH + 0.205$$

where *pH* is measured using a pH meter. The measured *pH* values are shown below (Table 1).

Table 1. The measured *pH* values of KHCO$_3$ solutions

KHCO$_3$ solution [M]	lg ([HCO$_3^-$] / M)	CO$_2$-sat. *pH*@20°C
0.01	-2.0	5.89
0.05	-1.3	6.49
0.10	-1.0	6.79
0.25	-0.6	7.22
0.50	-0.3	7.40

For electrochemical kinetic analysis, Tafel slopes were derived from the Tafel equation:

$$\eta = b \ lg \ (\ j_{CO} \ / \ j_0 \ )$$

where η [V] is the overpotential between the applied potential to the standard CO$_2$/CO reduction potential ($E_{CO2/CO}$ = -0.11 V *vs.* RHE); *b* is the Tafel slope [mV·dec^{-1}]; j_{co} is the partial current density for CO; j_0 is the exchange current density for CO [mA·cm^{-2}].

Product Quantification

The reduction products were quantified using similar procedures as previous works. Briefly, the headspace gas in the cathode compartment was automatically injected into gas chromatography (GC, Agilent 7890B configured with TCD and Methanizer/FID) for gas product quantification; The liquid products were determined using a nuclear magnetic resonance (NMR, Agilent 500/600 MHz ^{1}H NMR) and quantified with internal standards

(DMSO and phenol in D_2O). No notable liquid products were found in this work. The Faradaic efficiency for a certain product was calculated:

$$FE_i = n_i \, e \, F / Q_t \times 100\%$$

where n_i is the total amount of a certain product i [mol]; e is the number of electrons transferred for the product i formation, which equals to two for both CO and H_2; F is the Faradaic constant [C·mol^{-1}]; Q_t is the total amount of passed charge [C].

DFT Theoretical Calculation

All calculations were carried out using density functional theory (DFT) with the Perdew-Burke-Ernzerhof (PBE) exchange-correlation functional in the VASP code.[2-4] The ionic cores were described by the projector-augmented wave (PAW) method. The cut-off energy for plane wave expansion was set to be 500 eV. During geometry optimization, the force convergence on each atom was set to be smaller than 0.02 eV·Å^{-1}. A 0.2 eV width of Gaussian smearing and a (5 × 5 × 1) Monkhorst-Pack k-point grid were applied. The DFT-D2 method of Grimme was employed in all calculations to address van der Waals (vdW) interactions between atoms.

The Cu-N$_4$-NG and NG models were based on a 5 × 5 graphene supercell with 20 Å of vacuum space. For the Cu-N$_4$-NG model, a single copper atom was bonded to four pyridinic-N atoms. For the NG model, one single-pyridinic N was doped. The computational hydrogen electrode (CHE) model was employed for free energies calculations.[5, 6] In this model, the free energy of a proton-electron pair at 0 V *vs.* RHE is by definition equal to half of the free energy of gaseous hydrogen at 101325 Pa. The free energies of intermediates were obtained by $G = E + ZPE - TS$. The zero-point energy (ZPE) and entropy correction (TS) were calculated from vibration analysis by standard methods. The solvation effects were included for *COOH and *CO by stabilizing 0.25 eV and 0.1 eV, respectively.[6, 7]
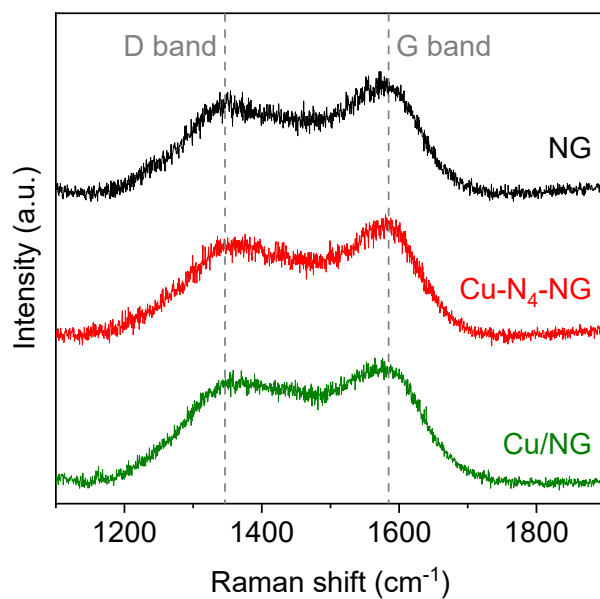
Figure S1. Raman spectra of NG, Cu-N4-NG, and Cu/NG. The dashed lines are assigned to D- and G-band peaks, which were observed at ~1350 cm^{-1} and ~1580 cm^{-1}, respectively.
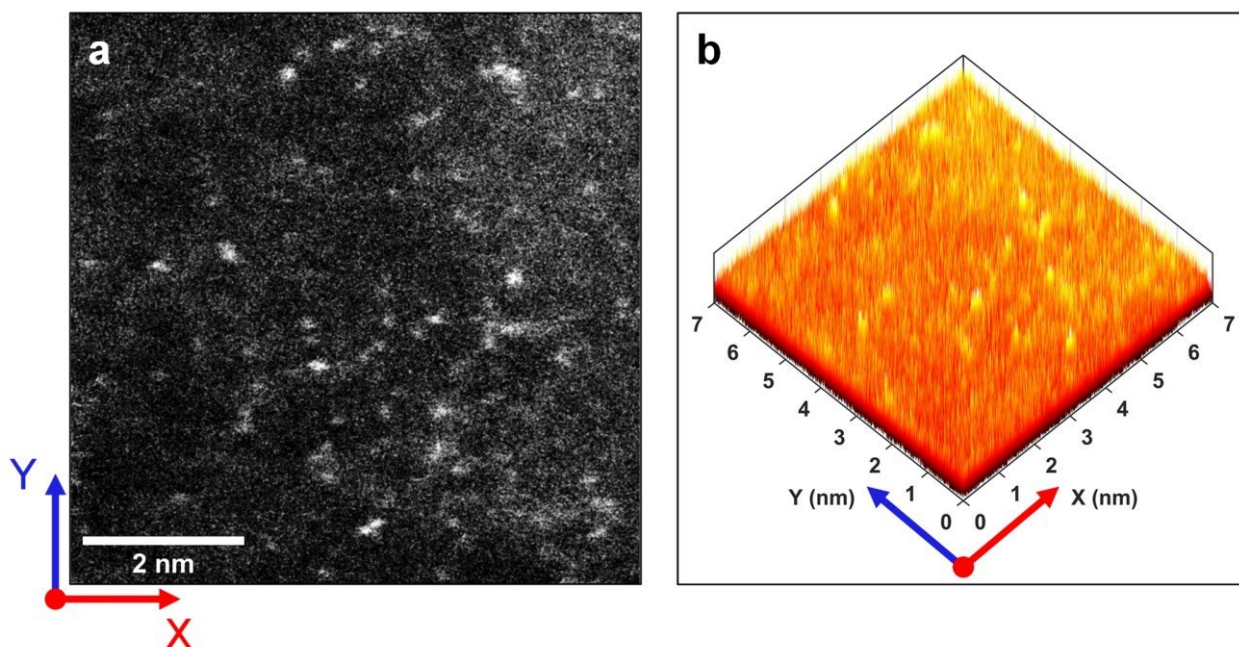
Figure S2. HAADF-STEM image of **(a)** Cu-N4-NG and **(b)** its corresponding pseudo-colored plot for illustration of the atomically dispersed Cu atoms.
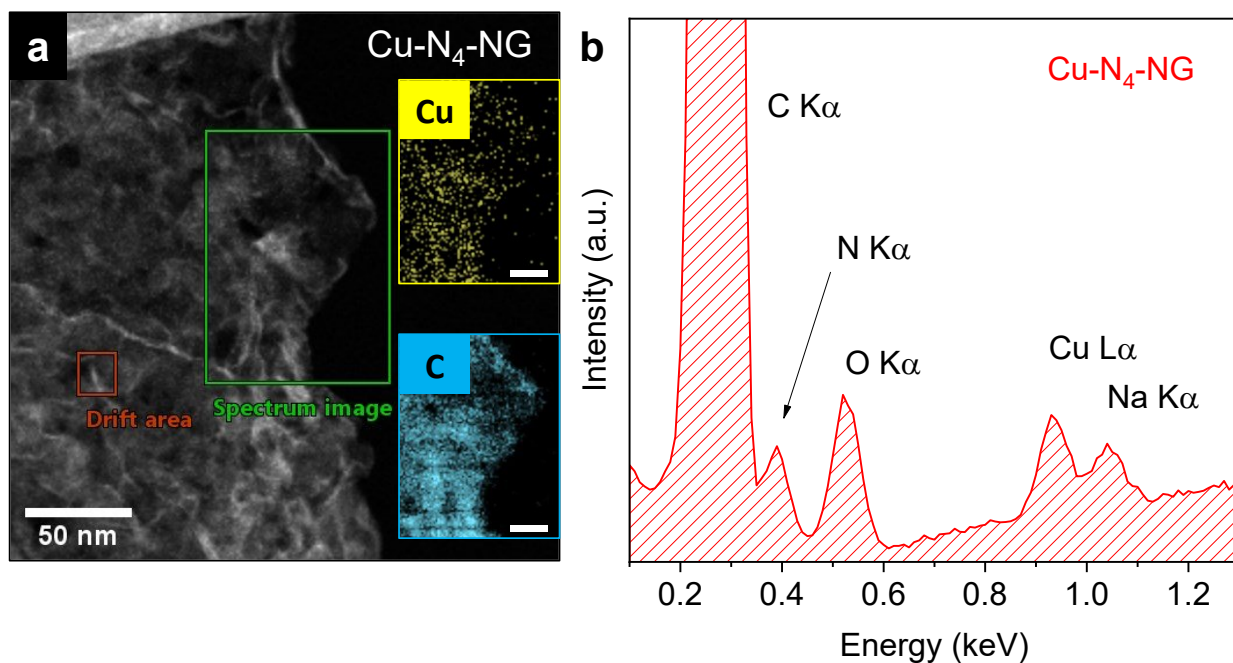
Figure S3. (a) HAADF-STEM image of Cu-N$_4$-NG and its corresponding EDS mappings in the selected area (insets: 20 nm scale bars). **(b)** STEM-EDS elemental analysis of Cu-N$_4$-NG.
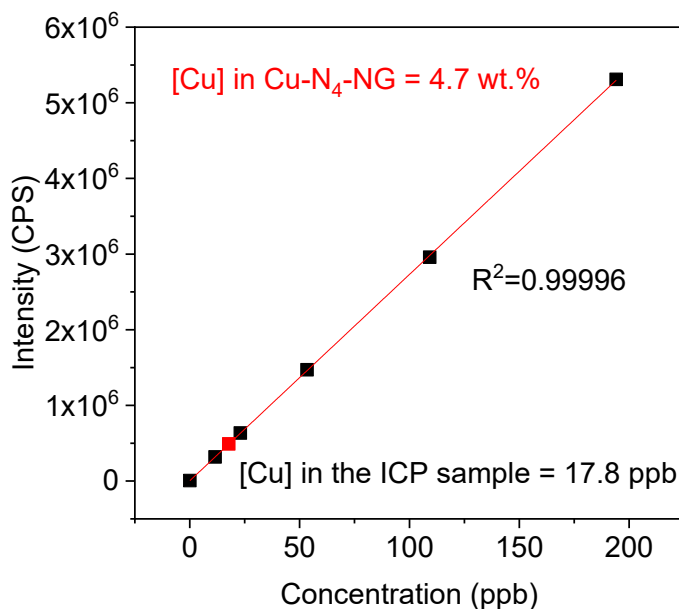
Figure S4. ICP-MS measurements for Cu-N$_4$-NG (the red mark) and the standard Cu calibration solution (the black marks).
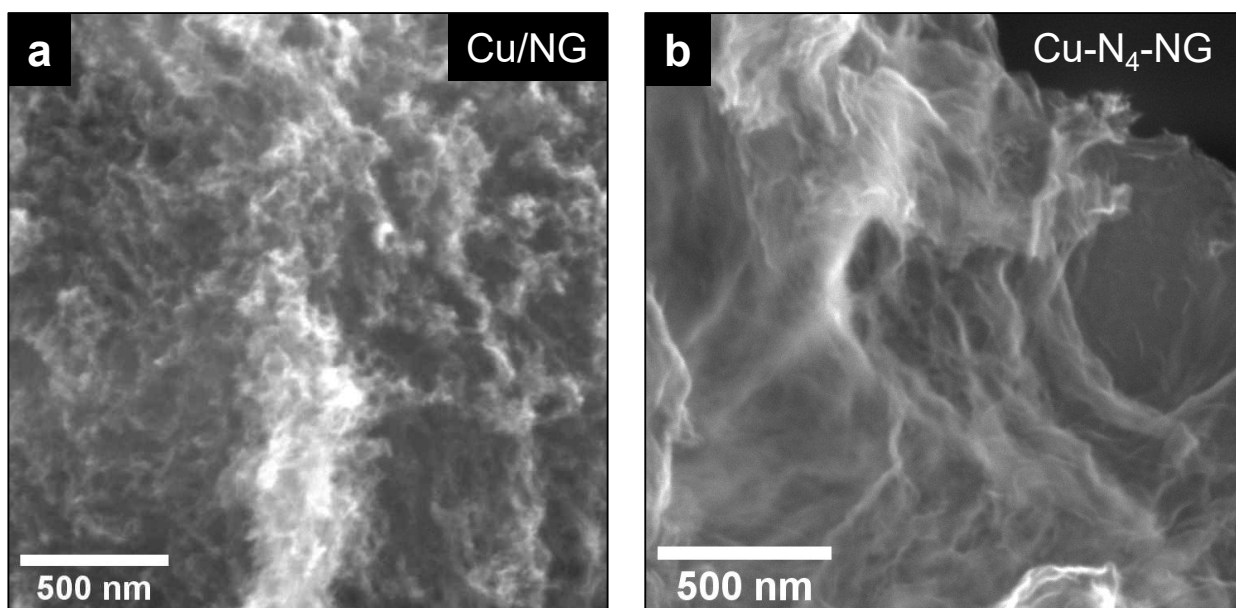
Figure S5. SEM images of **(a)** Cu/NG and **(b)** Cu-N₄-NG.
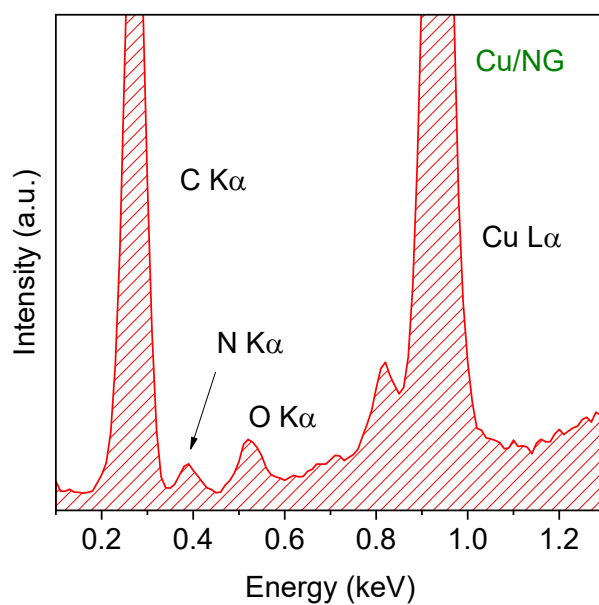
Figure S6. SEM-EDS elemental analysis of Cu/NG.
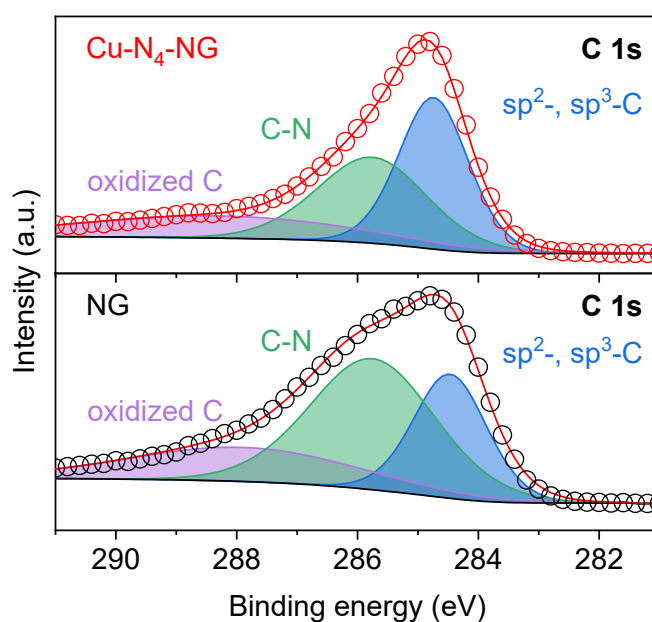
Figure S7. High-resolution C 1s XPS spectra of Cu-N4-NG and NG. The deconvoluted C 1s spectra can be assigned to the sp^2- and sp^3-C (284.2 eV), C-N (285.9 eV), and oxidized C (288.5 eV).
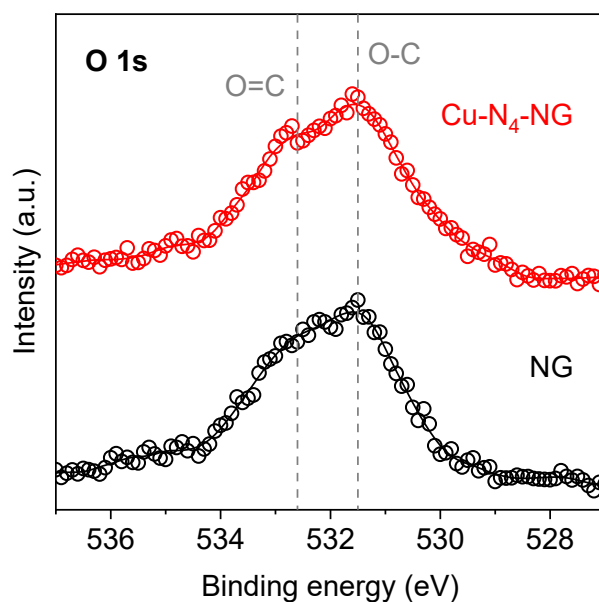
Figure S8. High-resolution O 1s XPS spectra of Cu-N4-NG and NG. The weak signals of O 1s spectra can be assigned to the O-C at 531.5 eV and the O=C at 532.6 eV.
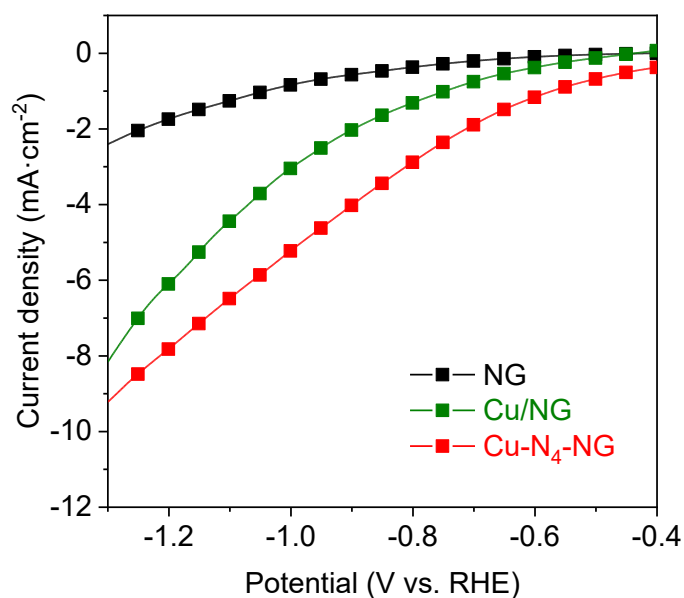
Figure S9. LSV polarization curves of NG, Cu/NG, and Cu-N4-NG for CO_2 electroreduction in CO_2-saturated 0.1 M $KHCO_3$ electrolyte.
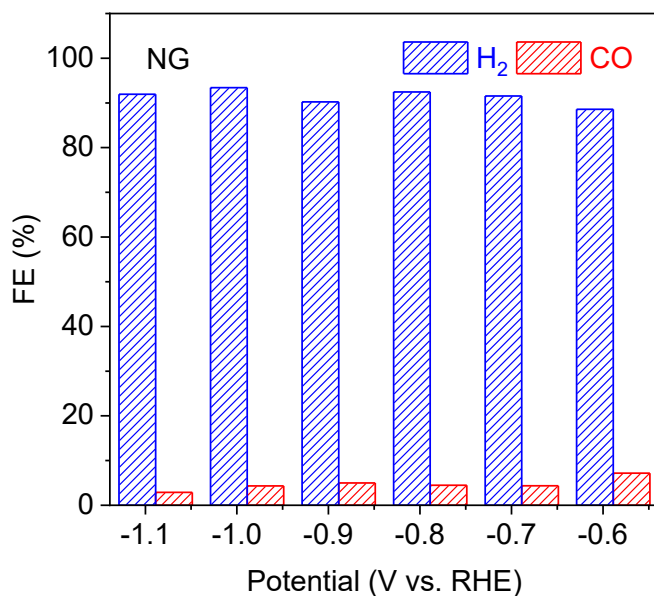
Figure S10. Measured FEs of CO_2 electroreduction on NG.
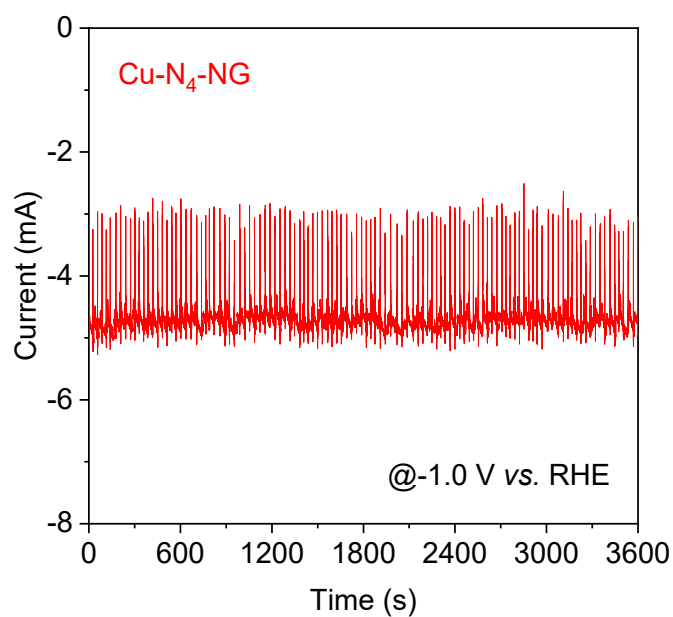
Figure S11. Chronoamperometric *i-t* curve of Cu-N$_4$-NG operated at -1.0 V *vs.* RHE. The fluctuation was caused by bubbles periodically coming off from the working electrode surface.
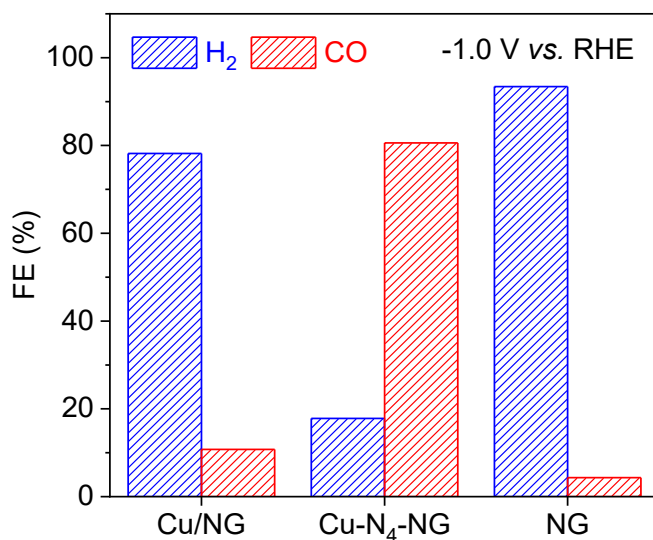
Figure S12. Comparison of measured FEs on Cu/NG, Cu-N$_4$-NG, and NG at a potential of -1.0 V *vs.* RHE.
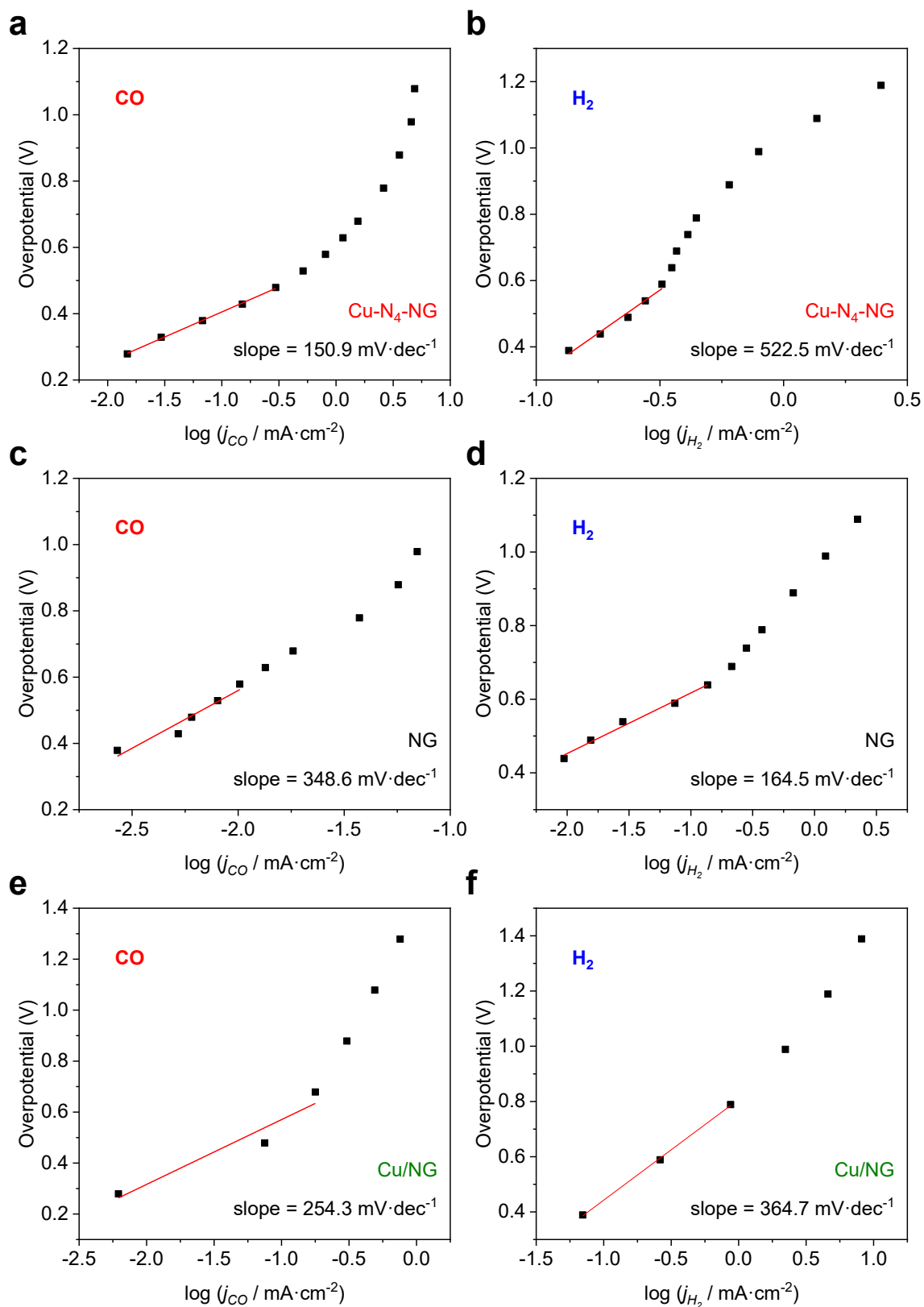
Figure S13. Tafel plots for CO and H₂ evolution on **(a, b)** Cu-N₄-NG, **(c, d)** NG, and **(e, f)** Cu/NG in CO₂-saturated 0.1 M KHCO₃ electrolyte.

Table S1. Recently reported single-atom Cu catalysts for the electrocatalytic CO_2 reduction reaction.

Catalyst	FE for CO (%)	$KHCO_3$/ M	Potential (V *vs.* RHE)	Ref.
Cu-N$_4$-NG	80.6	0.1	-1.0	**This work**
Cu-N$_x$	30	0.1	-0.76	[8]
Cu-NG	10	0.5	-0.62	[9]
Cu-N-C	28	0.1	-0.8	[10]
Cu-C$_3$N$_4$	36	0.1	-1.1	[11]
CuSAs/TCNFs	CH$_3$OH: 44 CO: 56	0.1	-0.9	[12]
Cu-N$_2$/GN	81	0.1	-0.5	[13]
Cu-N-C-900	CH$_4$: 38.6	0.1	-1.6	[14]
Cu$_{0.5}$NC	67.5	0.1 ($NaHCO_3$)	-0.6	[15]

References

[1]   C. Xu, A. Vasileff, D. Wang, B. Jin, Y. Zheng, S.-Z. Qiao, *Nanoscale Horiz.* **2019**, *4*, 1411-1415.

[2]   G. Kresse, J. Furthmuller, *Phys. Rev. B* **1996**, *54*, 11169-11186.

[3]   J. P. Perdew, K. Burke, M. Ernzerhof, *Phys. Rev. Lett.* **1996**, *77*, 3865-3868.

[4]   G. Kresse, D. Joubert, *Phys. Rev. B* **1999**, *59*, 1758-1775.

[5]   J. K. Nørskov, J. Rossmeisl, A. Logadottir, L. Lindqvist, J. R. Kitchin, T. Bligaard, H. Jónsson, *J. Phys. Chem. B* **2004**, *108*, 17886-17892.

[6]   A. A. Peterson, F. Abild-Pedersen, F. Studt, J. Rossmeisl, J. K. Norskov, *Energy Environ. Sci.* **2010**, *3*, 1311-1315.

[7]   W. J. Durand, A. A. Peterson, F. Studt, F. Abild-Pedersen, J. K. Norskov, *Surf. Sci.* **2011**, *605*, 1354-1359.

[8]   W. Ju, A. Bagger, G. P. Hao, A. S. Varela, I. Sinev, V. Bon, B. Roldan Cuenya, S. Kaskel, J. Rossmeisl, P. Strasser, *Nat. Commun.* **2017**, *8*, 944.

[9]   K. Jiang, S. Siahrostami, T. Zheng, Y. Hu, S. Hwang, E. Stavitski, Y. Peng, J. Dynes, M. Gangisetty, D. Su, K. Attenkofer, H. Wang, *Energy Environ. Sci.* **2018**, *11*, 893-903.

[10]   L. Takele Menisa, P. Cheng, C. Long, X. Qiu, Y. Zheng, J. Han, Y. Zhang, Y. Gao, Z. Tang, *Nanoscale* **2020**, *12*, 16617-16626.

[11]   Y. Jiao, Y. Zheng, P. Chen, M. Jaroniec, S. Z. Qiao, *J. Am. Chem. Soc.* **2017**, *139*, 18093-18100.

[12]   H. Yang, Y. Wu, G. Li, Q. Lin, Q. Hu, Q. Zhang, J. Liu, C. He, *J. Am. Chem. Soc.* **2019**, *141*, 12717-12723.

[13]   W. Zheng, J. Yang, H. Chen, Y. Hou, Q. Wang, M. Gu, F. He, Y. Xia, Z. Xia, Z. Li, B. Yang, L. Lei, C. Yuan, Q. He, M. Qiu, X. Feng, *Adv. Funct. Mater.* **2019**, *30*, 1907658.

[14]   A. Guan, Z. Chen, Y. Quan, C. Peng, Z. Wang, T.-K. Sham, C. Yang, Y. Ji, L. Qian, X. Xu, G. Zheng, *ACS Energy Lett.* **2020**, *5*, 1044-1053.

[15]   D. Karapinar, N. T. Huan, N. Ranjbar Sahraie, J. Li, D. Wakerley, N. Touati, S. Zanna, D. Taverna, L. H. Galvao Tizei, A. Zitolo, F. Jaouen, V. Mougel, M. Fontecave, *Angew. Chem. Int. Ed.* **2019**, *58*, 15098-15103.

Chapter 6

Graphene-Supported 3d-Block Metallophthalocyanines as Synergistic Catalysts for Electrochemical CO$_2$ Reduction

Herein, we fabricated metal phthalocyanine (MPc, M = Fe, Co, Ni) electrodes for the CRR measurements. Their morphological information and chemical structure were confirmed through material characterization and the catalysts were tested for the CRR in CO_2-saturated 0.1 M $KHCO_3$ electrolyte. Compared to the pristine MPc, high selectivity for CO evolution was significantly improved on graphene-supported MPc (MPc/NG). The maximum of Faradaic efficiency toward CO was received on CoPc/NG under a moderate potential, which was almost 100% CO_2 conversion to CO. To understand the impacts of CoPc and NG on CO selectivity, a series of CoPc-to-NG ratio controlled CoPc/NG were prepared for further investigations. The results indicated that the differences in the amount of CoPc and NG in CoPc/NG have a negative correlation with CO selectivity. A synergistic effect was uncovered that CoPc acted as an important role in CO_2 activation, NG served as a bridge for electron transfer to π-π stacked CoPc.

This Chapter is presented as a research paper by Chaochen Xu, Anthony Vasileff, Dan Wang, Bo Jin, Yao Zheng, and Shi-Zhang Qiao: Graphene-supported 3d-block metallophthalocyanines as synergistic catalysts for electrochemical CO_2 reduction.

Statement of Authorship

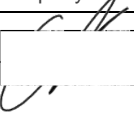| Title of Paper	Graphene-Supported 3d-Block Metallophthalocyanines as Synergistic Catalysts for Electrochemical CO₂ Reduction
Publication Status	☐ Published ☐ Accepted for Publication ☐ Submitted for Publication ☑ Unpublished and Unsubmitted work written in manuscript style
Publication Details	Chaochen Xu, Anthony Vasileff, Dan Wang, Bo Jin, Yao Zheng, Shi-Zhang Qiao. 2020. This paper will be submitted to *Chemical Communications*.
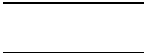
Principal Author

Name of Principal Author (Candidate)	Chaochen Xu		
Contribution to the Paper	Proposed ideas, performed experiments; carried out data processing and interpretation, wrote the manuscript.		
Overall percentage (%)	70		
Certification:	This paper reports on original research I conducted during the period of my Higher Degree by Research candidature and is not subject to any obligations or contractual agreements with a third party that would constrain its inclusion in this thesis. I am the primary author of this paper.		
Signature		Date	31 Aug 2020

Co-Author Contributions

By signing the Statement of Authorship, each author certifies that:

    i.   the candidate's stated contribution to the publication is accurate (as detailed above);

    ii.   permission is granted for the candidate in include the publication in the thesis; and

    iii.   the sum of all co-author contributions is equal to 100% less the candidate's stated contribution.

Name of Co-Author	Anthony Vasileff		
Contribution to the Paper	Assisted in experiments and revised the manuscript.		
Signature		Date	31 Aug 2020

Name of Co-Author	Dan Wang		
Contribution to the Paper	Supervised the research project and revised the manuscript.		
Signature		Date	31/08/2020

Name of Co-Author	Bo Jin
Contribution to the Paper	Supervised the research project and revised the manuscript.
Signature			Date	31/08/2020

Name of Co-Author	Yao Zheng
Contribution to the Paper	Discussed experimental results and findings, supervised the research project, and revised the manuscript.
Signature			Date	31/08/2020

Name of Co-Author	Shi-Zhang Qiao
Contribution to the Paper	Discussed experimental results and findings, supervised research project and revised the manuscript.
Signature			Date	31/08/2020

Name of Co-Author

Bo Jin

Contribution to the Paper

Supervised the research project and revised the manuscript.

COMMUNICATION

Graphene-supported 3d-block metallophthalocyanines as synergistic catalysts for electrochemical CO$_2$ reduction

Chaochen Xu,[a] Anthony Vasileff,[a] Dan Wang,[b] Bo Jin,[a] Yao Zheng*[a] and Shi-Zhang Qiao*[a]

The highest Faradaic efficiency of CO was achieved on cobalt phthalocyanine/N-doped graphene (CoPc/NG) at a moderate potential, which is almost 100% CO$_2$ conversion to CO. Further investigations showed a synergistic effect between the Cobalt phthalocyanine and graphene for electrochemical CO$_2$ reduction to CO.

The electrochemical CO$_2$ reduction reaction (CRR) is a carbon cycling technology driven by sustainable energy sources such as solar and wind.[1, 2] CO$_2$ can be converted into high value-added feedstocks through the CRR applications. Although this process is thermodynamically feasible, its kinetic problem has not been resolved, which results in a sluggish reaction rate and relatively low selectivity. A well-developed electrocatalyst can lower the activation energy and facilitate CO$_2$ conversion, which makes the CRR happens efficiently.

Recently, graphene-supported single-atom transition metals have been widely studied as electrocatalysts for the CRR.[3-5] The single-atom metal catalyst is known for its extraordinary catalytic performance and high atomic utilization., For the CRR applications, the commonly reported transition metals in the single-atom catalysts are Fe, Co, and Ni.[4-6] These 3d-block transition metals have a similar electron configuration that is $3d^x4s^2$ (x = 6 ~ 8). Specifically, highly selective CO$_2$ reduction to CO has been achieved on these catalysts under a low applied potential. However, there is a defect found in these single-atom catalysts for the CRR, that is, the distribution of metal atoms is disordered.[6-8] Microscopy imaging confirmed that the metal atoms are randomly dispersed within the catalysts.[4] This leads to the existence of local enrichment or deficiency of the metal atoms throughout the catalysts. Besides, the chemical structure of these catalysts, *e.g.* metal

coordination number, is determined by X-ray absorption spectroscopy (XAS) which is a weak long-range order characterization, leading to uncertainty of structure analysis.[9] By this, these catalysts should be considered as atomically dispersed metal catalysts instead of single-atom catalysts. A single-atom catalyst should be strictly defined as a catalyst that is uniformly distributed metal atom moieties with a precise chemical structure. [5, 10]

The reported structure of single-atom catalysts normally has a metal-N-C framework (M-N-C, M = Fe, Co, Ni), *i.e.* a transition metal atom is trapped by its neighboring N atoms in the carbon framework.[3-5] Coincidentally, this is similar to the structure of macrocyclic metal phthalocyanines (MPc, M = Fe, Co, Ni). As shown in Fig. 1a, the metal atom in MPc is coordinated to its adjacent four pyrrolic N atoms (M-N$_4$) contributing to isoindole units. The azomethinic N atom acts as a linkage of two adjacent isoindole units.[11] Due to the existence of M-N bonds throughout MPc, the R-space result derived from the extended X-ray absorption fine structure (EXAFS) spectra of MPc is used a as reference to identify whether the existence of M-N structure in the single-atom catalysts. MPc are important ingredients used for the dye industry because of their vivid colors and chemical stability. However, there are few detailed reports of using MPc as electrocatalysts for the CRR.[7, 12-18] The catalytic performance and underlying mechanism of MPc catalysts are still unclear. Therefore, a series of experiments are required to investigate whether MPc can replace the previously reported single-atom catalysts for efficiently electrocatalytic CO$_2$ reduction.

Herein, we fabricated two types of MPc electrodes for the CRR measurements: the one consisted in MPc (M = Fe, Co, Ni), the other comprised of graphene-supported MPc (MPc/NG). And N-doped graphene (NG) was prepared and served as a blank. Their morphological information and chemical structure were confirmed through material characterization. The catalysts were tested for the CRR in the CO$_2$-saturated 0.1 M KHCO$_3$ electrolyte. Compared to the pristine MPc, high selectivity for CO evolution was significantly improved on MPc/NG. Specifically, a maximum of Faradaic efficiency toward

a. *Centre for Materials in Energy and Catalysis, School of Chemical Engineering and Advanced Materials, The University of Adelaide, Adelaide, SA 5005, Australia. Email: s.qiao@adelaide.edu.au, yao.zheng01@adelaide.edu.au*
b. *Institute of Process Engineering, Chinese Academy of Sciences, Beijing, 100190, China.*

CO was received on CoPc/NG under a moderate potential, which was almost 100% CO_2 conversion to CO. Kinetic studies were carried out and suggested that CO_2 reduction on MPc was hindered at the first reaction step. To understand the impacts of CoPc and NG on CO selectivity, a series of CoPc-to-NG ratio controlled CoPc/NG catalysts were prepared for further investigations. The experimental results indicated that the amount difference between CoPc and NG in CoPc/NG has a negative correlation with CO selectivity. A synergistic effect was uncovered that CoPc acts as an important role in CO_2 activation, NG serves as a bridge for electron transfer to π–π stacked CoPc.

As can be seen in Fig. 1b, the scanning electron microscopy (SEM) image clearly shows randomly distributed needle-like CoPc with a length of ~40 μm. Similar morphology with slightly different dimensions was also observed in both FePc and NiPc images (Fig. S1). The aberration-corrected high-angle annular dark-field scanning transmission electron microscopy (HAADF-STEM) image is consistent with the SEM image of CoPc (Fig. S2a). Corresponding energy-dispersive X-ray spectroscopy (EDS) mapping was used for elemental identification. In Fig. 1c, the distinct signals of C, N, and Co were detected from the selected area of CoPc, which was also confirmed in the EDS spectrum of CoPc (Fig. S2b). Similar EDS spectra were found in FePc and NiPc and confirmed the presence of elements Fe and Ni (Fig. S3). The crystal structure of CoPc was identified in the selected area electron diffraction (SAED) pattern. The SAED image indicates the crystalline nature of CoPc, shown in Fig. 1d. This pattern was measured and given characteristic spacings of 0.47 and 0.63 nm for the (10$\bar{4}$) and the (200) lattice planes in CoPc. To be specific, the X-ray diffraction (XRD) patterns of MPc exhibited a high similarity, the main phase is well-indexed to the (100) and ($\bar{1}$02)

planes (Fig. 2a). The CIF-simulated XRD pattern is consistent with the measured pattern (Fig. S4). This further confirmed that MPc have a similar crystal structure, it is probably because of their similar chemical structure.

Fourier-transform infrared spectroscopy (FTIR) was used for understanding the chemical structure of MPc. The recorded spectra are shown in Fig. 2b. All characteristic peaks of MPc in FTIR spectra were marked in dashed lines. These indicated peaks can be assigned to the standard identification of MPc (Table S1).[19] Specifically, the dominant peaks of both C-H bending and ring bending appeared at ~730 and ~760 cm^{-1} in all spectra, revealing the existence of a typical macrocyclic structure in MPc. Apart from this infrared characterization, Raman spectra were also measured for the determination of the structural details. The positions of significant peaks were highlighted in Fig. 2c. In the low-frequency region, the peaks at ~593 and ~684 cm^{-1} are ascribed to bending vibration from the macrocycle, while the peak appeared at ~1530 cm^{-1} is attributed to C-N-C stretching vibration from the pyrrole group.[20] Therefore, the combined FTIR study with the Raman result supports the presence of the same chemical structure in MPc, which agrees with the illustrated structure shown in Fig. 1a.

XPS measurements were carried out for investigation of the chemical environments of MPc. The XPS survey spectra exhibit distinct signals of C 1s and N 1s (Fig. S5). Due to a low mass loading of MPc was used for the measurement, there were no obvious metal peaks found, the EDS spectra identified the existence of metals in MPc instead (Fig. S2b, S3). In the high-resolution C 1s spectra, only two carbonaceous species were observed, which are the peaks of C-C and C-N located at 284.8
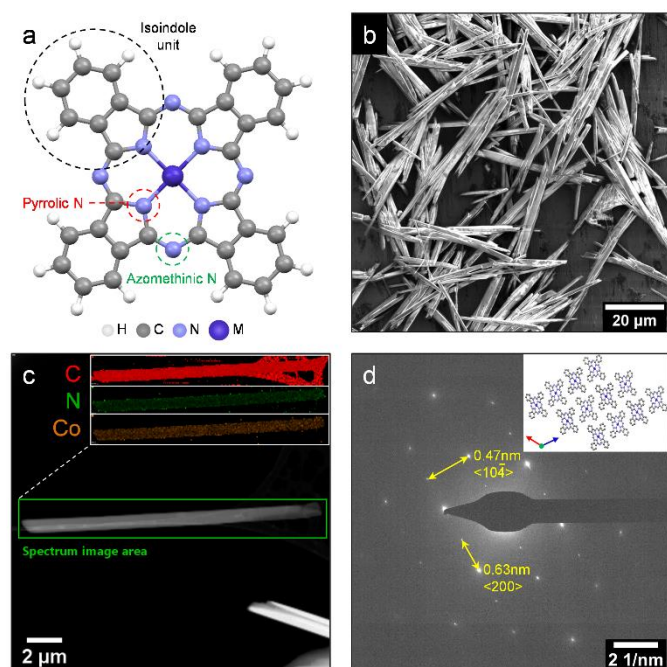
Fig. 1 (a) Scheme of the chemical structure of MPc. (b) SEM image of CoPc. Scale bar: 20 μm. (c) HAADF-STEM image of CoPc with its corresponding EDS mappings. Scale bar: 2 μm. The rod sat on a lacey carbon support film. (d) SAED pattern of CoPc. The inset suggests an illustration for CoPc crystalline.
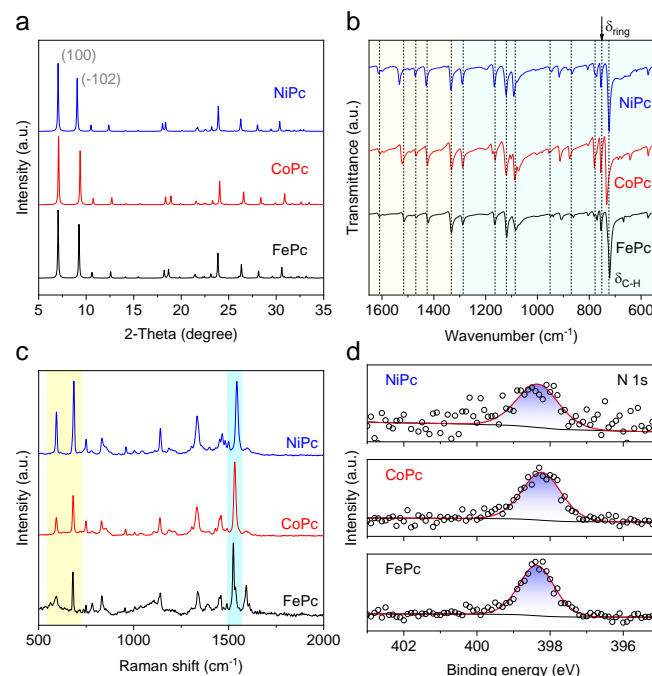
Fig. 2 (a) XRD patterns of MPc. (b) FTIR spectra of MPc. The characteristic peaks were indicated in the dashed lines. The light yellow and the light cyan regions refer to stretching and bending vibration zones, respectively. (c) Raman spectra of MPc. The dominant peaks were highlighted. (d) High-resolution XPS N 1s spectra for FePc, CoPc, and NiPc.

and 286.0 eV, respectively (Fig. S6).[21] This result is the same as the stated carbon structure in MPc (Fig. 1a). For the scan for metal 2p, there were no peaks detected in the corresponding spectra because of a low concentration of metal in the MPc sample (Fig. S7). From Fig. 2d, the N 1s spectra illustrate that the N atoms in MPc predominantly exist in the same chemical environment, which can be assigned to a peak of C-N appeared at 398.6 eV.[22]

To investigate how changes of the metal center in MPc affect their catalytic activity for CO_2 reduction, MPc electrodes were well-prepared and tested for the CRR in CO_2-saturated 0.1 M $KHCO_3$ aqueous solution (electrochemical data were given in Fig. S8). The gas products were identified and quantified by online gas chromatography, and only H_2 and CO were detected. There were no liquid products notably detected from the nuclear magnetic resonance spectroscopy results. To explore the intrinsic catalytic activity of MPc, the pristine MPc was firstly used for the CRR tests. As can be seen in Fig. 3a, the measured FEs of CO on pure FePc and CoPc were no apparent responses with the increase of reduction potential until -1.2 V $vs.$ RHE, and the maxima of FEs were received at -1.4 V $vs.$ RHE, which were 43.5% and 24.6%, respectively. While the FE trend is slightly different on NiPc. To be specific, CO (FE of 42.0%) was firstly observed at a low potential of -0.6 V $vs.$ RHE. Then, as the potential increased, the FE of CO monotonously decreases below 10%. Thus, the results received on pure MPc showed that MPc could barely facilitate the CRR by themselves because their macrocyclic structure leads to a poor conductivity like a semiconductor.[11] By this, the electron transfer between CO_2 and catalytic sites was significantly hindered in the electrochemical process, resulting in low selectivity. To address this issue, NG was introduced to assist with MPc for the improvement of electron transfer via strong π–π interaction.[14]
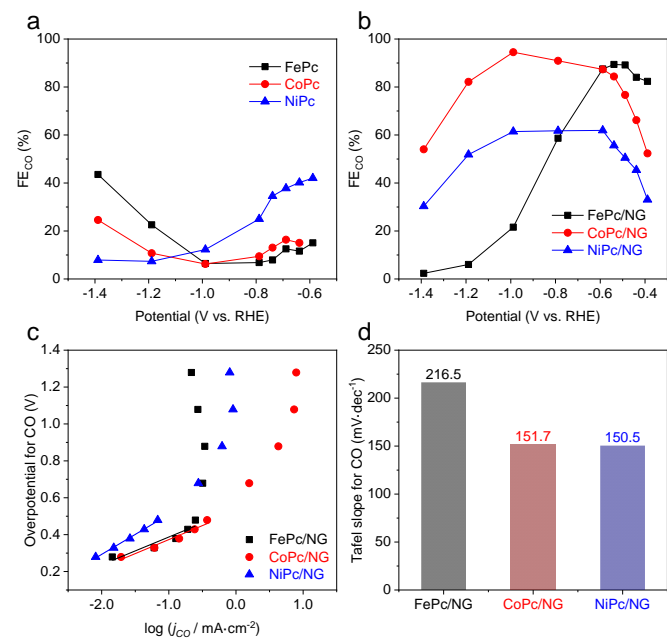
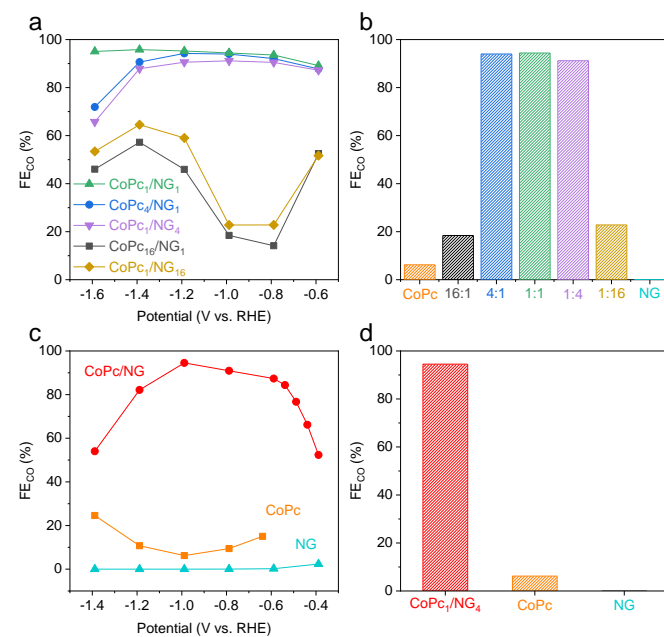The experiments were conducted on FePc/NG, CoPc/NG, and NiPc/NG (MPc-to-NG weight ratio = 1:4). As the results are shown in Fig. 3b, high FEs of CO (over 80%) were obtained on FePc/NG under a low potential range (-0.4 ~ -0.6 V $vs.$ RHE), however, the FEs rapidly dropped as more negative potential applied. Compared to FePc/NG group, CoPc/NG and NiPc/NG showed the same catalytic trend but different activities. In detail, high FEs of CO were received in a moderate potential range (-0.6 ~ -1.0 V $vs.$ RHE), which reached over 90% on CoPc/NG and near 60% on NiPc/NG at -1.0 V $vs.$ RHE. The catalytic result of NG was given in Fig. S9. It shows that NG was inert in the catalytic process of CRR, which implies that a synergistic effect exists between MPc and NG framework for enhancement of the catalytic activity. According to the previous reported CRR pathways, kinetic studies for MPc/NG were carried out and revealed that the rate-determining step of CO_2 activation, $i.e.$ * + CO_2 + H^+ + e^- = *COOH, is less hindered on CoPc/NG and NiPc/NG because their Tafel slopes were clearly smaller than FePc/NG, which are 151.7 and 150.5 mV·dec^{-1} (Fig. 3c, d). [23, 24]

To further understand the role of NG in MPc/NG on changing CO selectivity, the participant in this study was CoPc/NG where the highest FE of CO was observed. In detail, various CoPc/NG samples with controlled ratios were prepared for the CRR tests ($CoPc_x/NG_y$ was simply denoted as x:y). In Fig. 4a, an extremely good catalytic performance was found on $CoPc_1/NG_1$. The overall FE of CO was over 90%, and the highest FE of 95.8% was observed at -1.4 V $vs.$ RHE. As increasing either CoPc or NG amount in CoPc/NG, $CoPc_4/NG_1$ and $CoPc_1/NG_4$ exhibited the same trend and catalytic performance in the whole potential range. Interestingly, $CoPc_{16}/NG_1$ and $CoPc_1/NG_{16}$ also displayed the same trend, but the catalytic selectivity was notably insufficient, which is below 60%. It is

Fig. 3 Measured FEs of CO on (a) pristine MPc and (b) MPc/NG. (c) Tafel plots for CO evolution on FePc/NG, CoPc/NG, and NiPc/NG and (d) a comparison of their Tafel slopes for CO evolution.

Fig. 4 (a) Measured FEs of CO on CoPc/NG with various weight ratios and (b) their comparison at -1.0 V $vs.$ RHE. (c) Measured FEs of CO on CoPc/NG, CoPc, and NG and (d) their FE comparison at -1.0 V $vs.$ RHE.

clear to see that the addition of NG facilitated the CO_2 reduction process on CoPc, and the catalytic selectivity was further affected by the CoPc-to-NG ratios (Fig. 4b). According to the electrochemical results, there was a synergistic effect between CoPc and NG. To be more specific, pure CoPc without NG addition exhibited an inferior conductivity, which caused impeded electron transfer for the CRR, leading to low selectivity. As increasing the amount of addition of NG in CoPc/NG, the extensive π delocalization led to CoPc attached with NG through π–π stacking due to CoPc have a ring structure consisting of 18 π electrons.[14] The electron was rapidly conveyed through the π linkage from the electrode to the catalyst and was then transferred to the catalytic sites to engage in CO_2 reduction. So, a relatively high FE of CO was received on the CoPc/NG. However, excessive NG in CoPc/NG cannot remain a high selectivity of the CRR. NG is considered to be a candidate for electrocatalytic hydrogen evolution reaction. A large amount of NG in CoPc/NG overwhelmed the reaction preference to the CRR instead of hydrogen evolution. The result of CoPc/NG can be seen in Fig. 4c, d. Neither CoPc nor NG appeared alone received a significantly high FE of CO. The optimal ratio was $CoPc_1/NG_4$ because of its catalytic activity as high as $CoPc_1/NG_1$ and $CoPc_4/NG_1$ but less CoPc used.

In conclusion, we prepared pure MPc and MPc/NG for the CRR investigations. The catalytic selectivity for CO was significantly improved, compared to the MPc without NG introduction. We also found that the amount difference between CoPc and NG showed a negative correlation with CO selectivity as the existence of a synergistic effect. Furthermore, the highest FE of CO was received on CoPc/NG, which is almost 100% conversion of CO_2 to CO. Also, the H_2 evolution was simultaneously suppressed. Therefore, the MPc-based catalysts can be extended the selection for highly selective electrocatalytic CO_2 reduction to CO. Besides, the high-purity CO product received on CoPc/NG can be used as a feed gas for the electrocatalytic CO reduction reaction to obtain C2 products like ethanol and ethylene.

Conflicts of interest

There are no conflicts to declare.

Notes and references

1. C. Chen, J. F. Khosrowabadi Kotyk and S. W. Sheehan, *Chem*, 2018, **4**, 2571-2586.

2. S. Nitopi, E. Bertheussen, S. B. Scott, X. Liu, A. K. Engstfeld, S. Horch, B. Seger, I. E. L. Stephens, K. Chan, C. Hahn, J. K. Norskov, T. F. Jaramillo and I. Chorkendorff, *Chem. Rev.*, 2019, **119**, 7610-7672.

3. C. Zhu, S. Fu, Q. Shi, D. Du and Y. Lin, *Angew. Chem. Int. Ed.*, 2017, **56**, 13944-13960.

4. Y. Chen, S. Ji, C. Chen, Q. Peng, D. Wang and Y. Li, *Joule*, 2018, **2**, 1242-1264.

5. Y. Wang, J. Mao, X. Meng, L. Yu, D. Deng and X. Bao, *Chem. Rev.*, 2019, **119**, 1806-1854.

6. L. Wang, W. Chen, D. Zhang, Y. Du, R. Amal, S. Qiao, J. Wu and Z. Yin, *Chem. Soc. Rev.*, 2019, **48**, 5310-5349.

7. L. Gong, D. Zhang, C. Y. Lin, Y. Zhu, Y. Shen, J. Zhang, X. Han, L. Zhang and Z. Xia, *Adv. Energy Mater.*, 2019, **9**, 1902625.

8. A. Wang, J. Li and T. Zhang, *Nat. Rev. Chem.*, 2018, **2**, 65-81.

9. F. Lin, Y. Liu, X. Yu, L. Cheng, A. Singer, O. G. Shpyrko, H. L. Xin, N. Tamura, C. Tian, T. C. Weng, X. Q. Yang, Y. S. Meng, D. Nordlund, W. Yang and M. M. Doeff, *Chem. Rev.*, 2017, **117**, 13123-13186.

10. B. Lu, Q. Liu and S. Chen, *ACS Catal.*, 2020, **10**, 7584-7618.

11. A. B. Sorokin, *Chem. Rev.*, 2013, **113**, 8152-8191.

12. Z. Zhang, J. Xiao, X. J. Chen, S. Yu, L. Yu, R. Si, Y. Wang, S. Wang, X. Meng, Y. Wang, Z. Q. Tian and D. Deng, *Angew. Chem. Int. Ed.*, 2018, **57**, 16339-16342.

13. L. Sun, V. Reddu, A. C. Fisher and X. Wang, *Energy Environ. Sci.*, 2020, **13**, 374-403.

14. X. Zhang, Z. Wu, X. Zhang, L. Li, Y. Li, H. Xu, X. Li, X. Yu, Z. Zhang, Y. Liang and H. Wang, *Nat. Commun.*, 2017, **8**, 14675.

15. N. Furuya and S. Koide, *Electrochim. Acta*, 1991, **36**, 1309-1313.

16. N. Furuya and K. Matsui, *J. Electroanal. Chem. Interf. Electrochem.*, 1989, **271**, 181-191.

17. Y. Xia, S. Kashtanov, P. Yu, L.-Y. Chang, K. Feng, J. Zhong, J. Guo and X. Sun, *Nano Energy*, 2020, **67**, 104163.

18. S. Ren, D. Joulie, D. Salvatore, K. Torbensen, M. Wang, M. Robert and C. P. Berlinguette, *Science*, 2019, **365**, 367-369.

19. S. F. Pop and R. M. Ion, *J. Optoelectron. Adv. M.*, 2010, **12**, 1976-1980.

20. D. D. Klyamer, T. V. Basova, P. O. Krasnov and A. S. Sukhikh, *J. Mol. Struct.*, 2019, **1189**, 73-80.

21. M. C. Ortega-Liebana, N. X. Chung, R. Limpens, L. Gomez, J. L. Hueso, J. Santamaria and T. Gregorkiewicz, *Carbon*, 2017, **117**, 437-446.

22. C. Xu, A. Vasileff, D. Wang, B. Jin, Y. Zheng and S.-Z. Qiao, *Nanoscale Horiz.*, 2019, **4**, 1411-1415.

23. M. Dunwell, W. Luc, Y. Yan, F. Jiao and B. Xu, *ACS Catal.*, 2018, **8**, 8121-8129.

24. Z. Sun, T. Ma, H. Tao, Q. Fan and B. Han, *Chem*, 2017, **3**, 560-587.

Graphene-supported 3d-block metallophthalocyanines as synergistic catalysts for electrochemical CO₂ reduction

Chaochen Xu,[a] Anthony Vasileff,[a] Dan Wang,[b] Bo Jin,[a] Yao Zheng*[a], and Shi-Zhang Qiao*[a]

[a] Centre for Materials in Energy and Catalysis, School of Chemical Engineering and Advanced Materials, The University of Adelaide, Adelaide, SA 5005, Australia

[b] Institute of Process Engineering, Chinese Academy of Sciences, Beijing, 100190, China

* Email: s.qiao@adelaide.edu.au, yao.zheng01@adelaide.edu.au

Part I: Experimental Section

Chemicals

Iron(II) phthalocyanine (FePc), Cobalt(II) phthalocyanine (CoPc), Nickel(II) phthalocyanine (NiPc), dicyandiamide (Dicy), potassium bicarbonate ($KHCO_3$), dimethyl sulfoxide (DMSO), phenol, and deuterium oxide (D_2O) were purchased from Sigma-Aldrich and used without further purification. Deionized water (DI water, 18 MΩ·cm) was from a Milli-Q water purifier. A 0.05 wt.% Nafion solution was diluted from LIQUion™ Solutions (LQ-1115 - 1100 EW at 15 wt.%). Ultra-high purity Ar (99.999%), N_2 (99.999%), and laser grade CO_2 (99.995%) were supplied from BOC Gas.

Synthesis Method

N-doped graphene (NG) was prepared by a modified method.[1] Briefly, 5.0 g of dicyandiamide and 0.25 g of glucose were dissolved in 100 mL deionized water. After 1 h vigorous stirring, the solution was dried in a rotary vacuum evaporator. Once completely dried, the received powder was transferred into a crucible placed in a tube furnace under Ar atmosphere. The powder was annealed at 900°C for 2 h with a heating rate of 3°C·min^{-1}. Once cooled to room temperature, the powder was washed with deionized water and centrifugated at 10,000 rpm for three times. The washed resultant was transferred to a vacuum oven at 60°C overnight.

Material Characterization

Scanning electron microscopy (SEM) images and energy-dispersive X-ray spectroscopy (EDS) spectra were acquired with FEI Quanta 450. Transmission electron microscopy (TEM) images and selected area electron diffraction (SAED) patterns were taken using Philips CM200. Aberration-corrected high-angle annular dark-field scanning transmission electron microscopy (HAADF-STEM) images and EDS spectra were acquired with FEI Titan Themis 80-200. X-ray diffraction (XRD) patterns were recorded on a Rigaku X-Ray Diffractometer (Cu Kα, λ = 1.5406 Å). X-ray photoelectron spectroscopy (XPS) measurements were performed on Kratos AXIS Ultra (mono Al Kα), and the XPS spectra were calibrated to the C-C peak at 284.8 eV. Raman spectra were collected using a HORIBA LabRAM HR Evolution Raman Spectroscopy with an Olympus MPLN50x objective lens and a 633-nm laser (CVI Melles Griot). Fourier-transform infrared spectroscopy (FTIR) spectra were recorded using a Nicolet 6700 FT-IR spectrometer.

Electrochemical Measurements

The experiments were performed on an electrochemical workstation (CH Instruments 760E) using a three-electrode H-cell separated by a proton exchange membrane (Nafion 117). A glassy carbon electrode (1.0 cm × 1.0 cm), Ag/AgCl (3.5 M KCl), and RuO_2-coated titanium mesh served as the working, reference, and counter electrodes, respectively. To prepare a catalyst ink, 8 mg of a metal phthalocyanine catalyst (with the specific weight of NG) was ultrasonically dispersed in 2 mL of 0.05 wt.% Nafion aqueous solution. 100 μL of the ink was dropwise added onto the surface of a glassy carbon electrode and was then dried in air (catalyst loading of 0.4 mg·cm^{-2}). The electrochemical measurements including cyclic voltammetry (CV), linear scan voltammetry (LSV), and chronoamperometric curve (*i-t*) were carried out in 0.1 M $KHCO_3$ aqueous electrolyte (pH = 6.8) with continuously bubbled CO_2 (flow rate of 10 sccm). All *iR*-corrected potentials were converted to the reversible hydrogen electrode (RHE) scale at 20°C according to the Nernst equation:

$$E \ (\ V \ vs. \ RHE \ ) = E \ (\ V \ vs. \ Ag/AgCl \ ) + 0.059 \times pH + 0.205$$

where *pH* is measured by a pH meter.

For the analysis of electrochemical kinetics, Tafel slopes were derived from the Tafel equation:

$$\eta = b \ lg \ (\ j_{co} \ / \ j_0 \ )$$

where η [V] is the overpotential between the applied potential to the standard CO_2/CO reduction potential ($E_{CO2/CO}$ = -0.11 V *vs.* RHE); *b* is the Tafel slope [mV·dec^{-1}]; j_{co} is the partial current density for CO; j_0 is the exchange current density for CO [mA·cm^{-2}].

Product Analysis

The reduction products were quantified using similar procedures as previous works.[1-3] Briefly, the headspace gas in the cathode compartment was automatically injected into gas chromatography (GC, Agilent 7890B configured with TCD and Methanizer/FID) for gas product quantification; The liquid products were determined using a nuclear magnetic resonance (NMR, Agilent 500/600 MHz ^{1}H NMR) and quantified with internal standards (DMSO and phenol in D_2O). No notable liquid products were found in this work. The Faradaic efficiency of a certain product was calculated:

$$FE_i = n_i \ e \ F \ / \ Q_t \times 100\%$$

where n_i is the total amount of a certain product i [mol]; e is the number of electrons transferred for the product i formation, which equals to two for both CO and H_2; F is the Faradaic constant [$C \cdot mol^{-1}$]; Q_t is the total amount of passed charge [C].

Part II: Supplementary Results

Fig. S1 SEM images of (a) FePc and (b) NiPc.
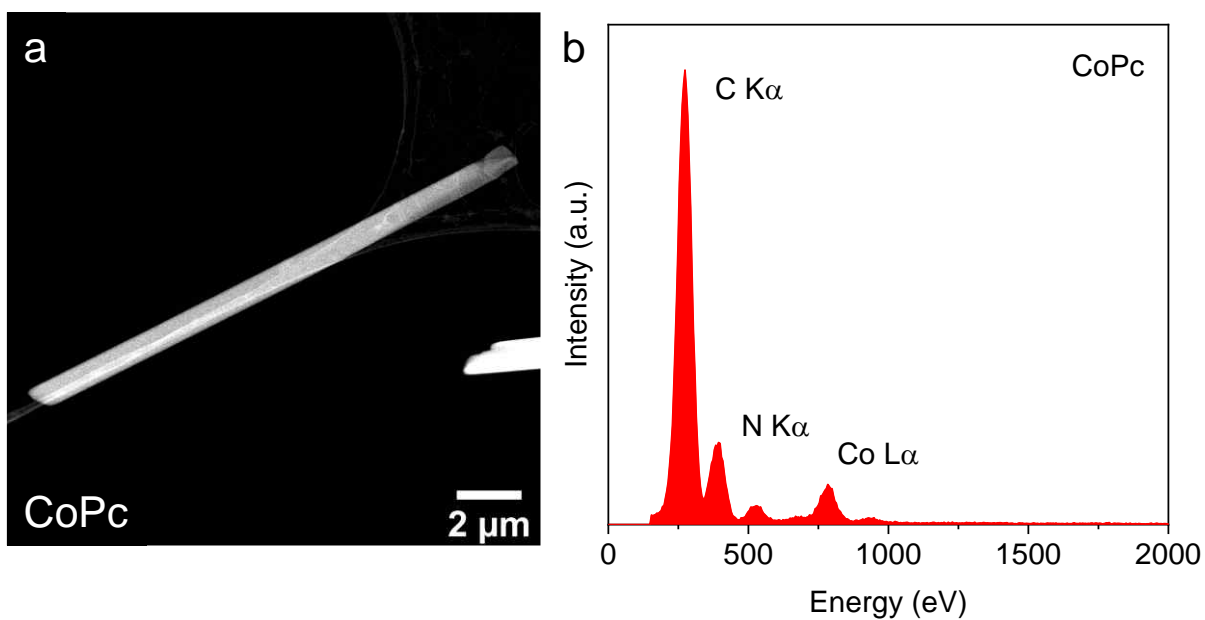
Fig. S2 (a) HAADF-STEM image of CoPc and (b) its corresponding EDS elemental analysis.
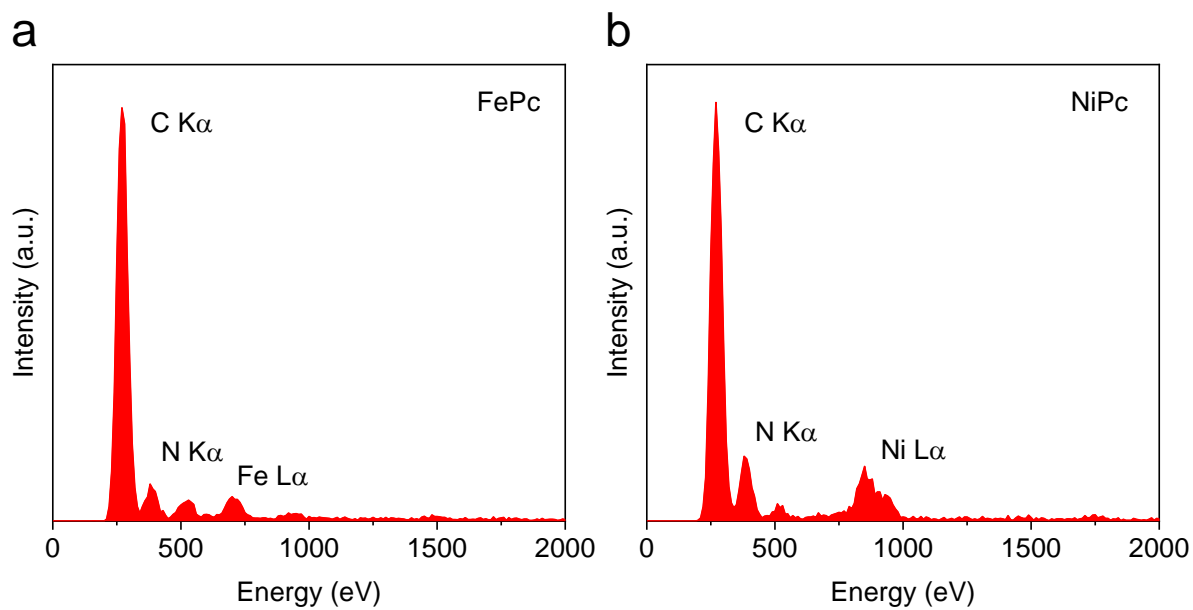
Fig. S3 EDS spectra of (a) FePc and (b) NiPc.
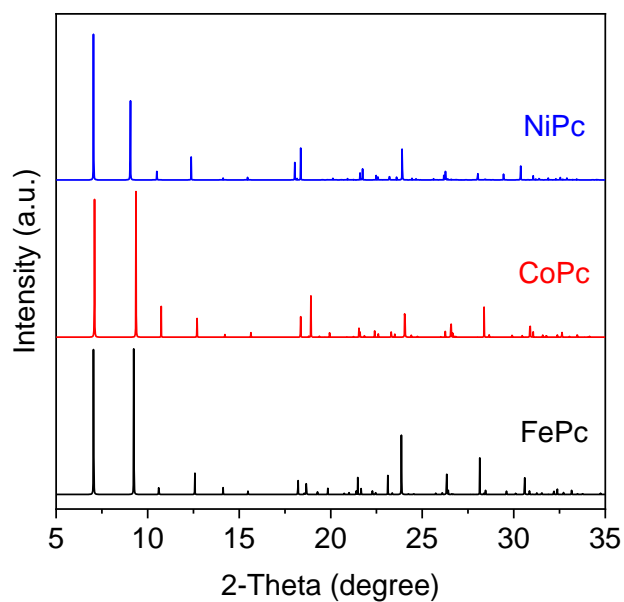
Fig. S4 Simulated XRD patterns for FePc (CIF#4334302), CoPc (CIF#2100746), and NiPc (CIF#4001864).
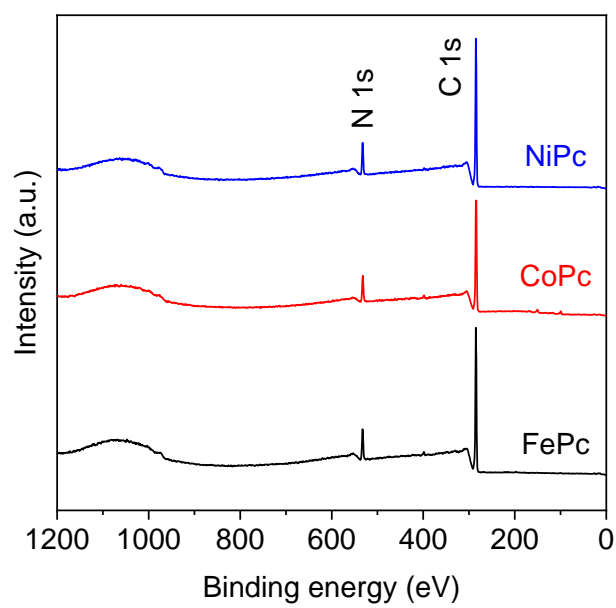
Fig. S5 XPS survey spectra with distinct signals of C 1s and N 1s.
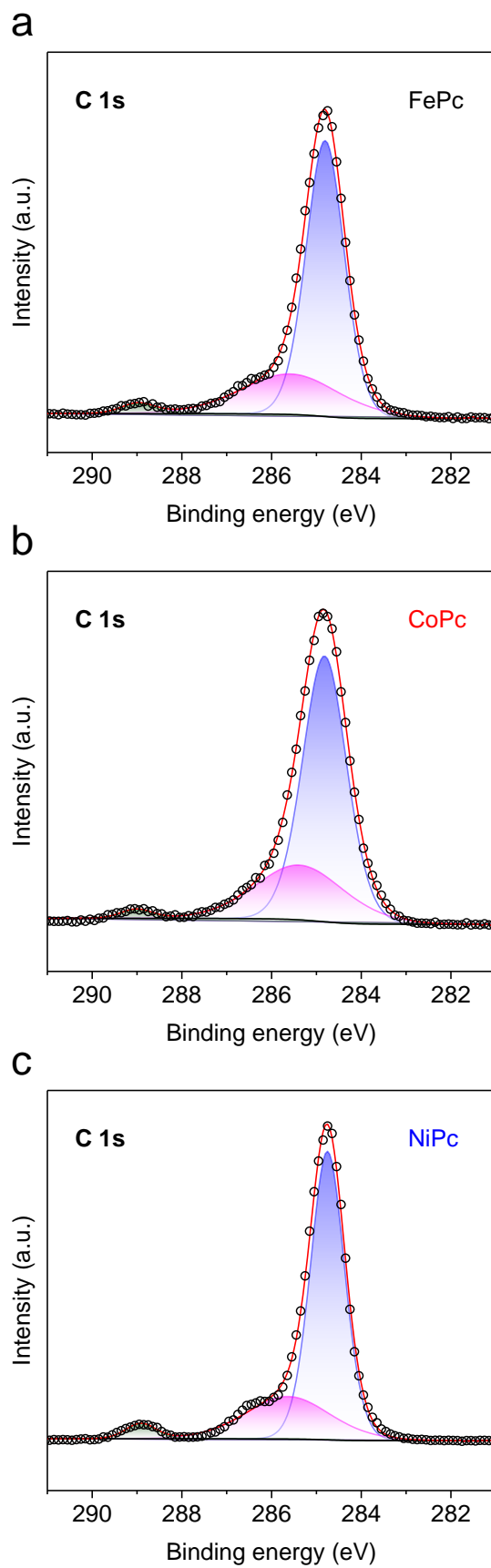
Fig. S6 High-resolution XPS C 1s spectra for (a) FePc, (b) CoPc, and (c) NiPc.[4]
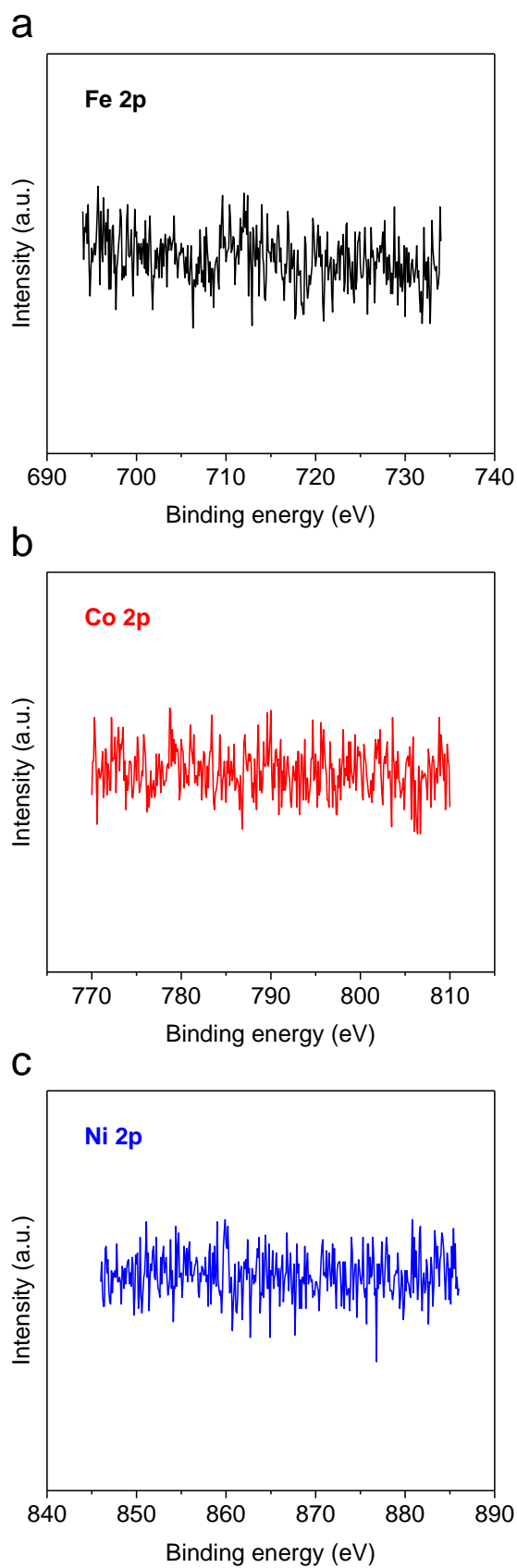
Fig. S7 High-resolution XPS metal (Fe, Co, Ni) 2p spectra for (a) FePc, (b) CoPc, and (c) NiPc, respectively. The metal signals were hardly observed because the well-dispersed samples for XPS measurements were obtained by dilution, which results in low concentration to the metals and is barely detected.
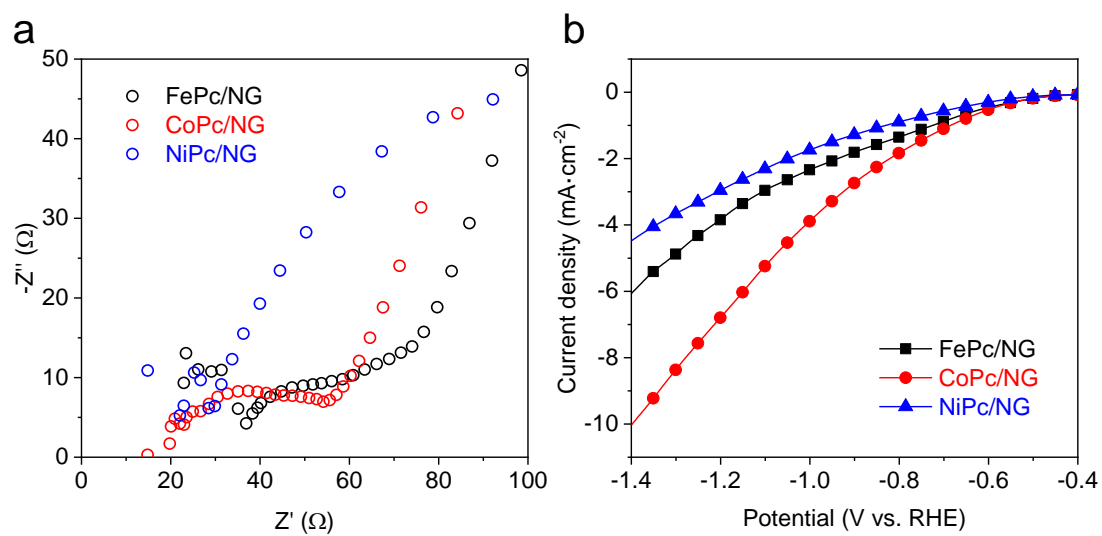
Fig. S8 (a) Electrochemical impedance spectroscopy measurements and (b) LSV polarization curves on FePc/NG, CoPc/NG, and NiPc/NG.
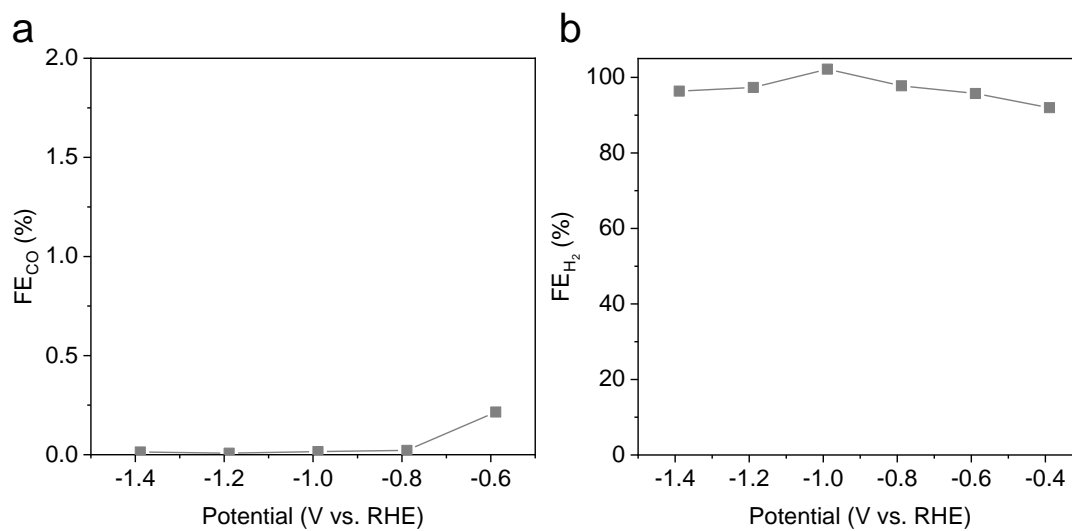
Fig. S9 Measured FEs for (a) CO and (b) H_2 on NG.

Table. S1 Identification of FTIR spectra for FePc, CoPc, and NiPc.[5]

Identification		Wavenumber [cm^{-1}]		
		FePc	**CoPc**	**NiPc**
δ (bending)	C-H$_{out\text{-}of\text{-}plane}$	721.2	732.8	723.2
	Pc rings	754.0	756.0	756.0
	C-H$_{out\text{-}of\text{-}plane}$	771.4	781.0	771.4
	Isoindole	862.0	875.5	867.8
	Benzene	948.8	954.6	946.9
	C-H$_{in\text{-}plane}$	1091.5	1087.7	1083.8
	Isoindole	1118.5	1120.4	1120.4
	C-H$_{in\text{-}plane+isoindole}$	1164.8	1162.9	1166.7
	C-H$_{in\text{-}plane}$	1288.2	1288.2	1290.1
ν (stretching)	Pyrrole	1332.6	1332.6	1334.5
	Isoindole	1421.2	1425.1	1429.0
	Isoindole	1467.6	1467.6	1471.4
	-N=	1515.8	1521.6	1533.1
	C=C	1610.3	1608.4	1614.1

Part III: References

1. C. Xu, A. Vasileff, D. Wang, B. Jin, Y. Zheng and S.-Z. Qiao, *Nanoscale Horiz.*, 2019, **4**, 1411-1415.

2. A. Vasileff, C. Xu, L. Ge, Y. Zheng and S. Z. Qiao, *Chem. Commun.*, 2018, **54**, 13965-13968.

3. A. Vasileff, X. Zhi, C. Xu, L. Ge, Y. Jiao, Y. Zheng and S.-Z. Qiao, *ACS Catal.*, 2019, **9**, 9411-9417.

4. M. C. Ortega-Liebana, N. X. Chung, R. Limpens, L. Gomez, J. L. Hueso, J. Santamaria and T. Gregorkiewicz, *Carbon*, 2017, **117**, 437-446.

5. S. F. Pop and R. M. Ion, *J. Optoelectron. Adv. M.*, 2010, **12**, 1976-1980.

Chapter 7

Conclusions and Perspectives

7.1 Conclusions

This Thesis has demonstrated the development of transition metal-based electro-catalysts for highly selective CO_2 reduction. The well-designed catalysts were synthesized by controllable methods and were investigated through fundamental characterization, advanced synchrotron-based techniques, and *in situ* Raman spectroscopy. The electrochemical evaluation and product quantification were also conducted for understanding the catalytic performance of CO_2 reduction. Combined the experimental and computational results provided a series of new insights into the CRR on transition metal-based materials. To be specific:

In **Chapter 2**, we summarized recently reported studies for the CRR by using the sub-nanoscale 3d-block transition metal-based catalysts (metals = Mn, Fe, Co, Ni, Cu, Zn). Also, this review paper proposed suggestions and prospects of the future development of single-atom 3d-block transition metal as electrocatalysts for the CRR.

In **Chapter 3**, we engineered and alloyed Ni with Cu to obtain ultrasmall graphene-encapsulated Ni-Cu bimetallic catalysts. We then comprehensively investigated the catalytic activity and selectivity of these catalysts for the CRR. A series of control tests and the advanced characterization involving synchrotron-based and *in situ* techniques showed that the well-engineered Ni-Cu catalyst facilitated CO_2 reduction to CO. The highlights include: (i) The Ni-Cu catalyst exhibited significant activity and selectivity for the CRR than the single metal Ni catalyst. The Cu-lean catalyst ($NiCu_{0.25}$) showed the highest Faradaic efficiency towards CO (*ca.* 90%) at a moderate potential of -1.0 V vs. RHE. (ii) By analyzing the results from *in situ* Raman spectroscopy and synchrotron-based soft X-ray absorption spectroscopy, we observed the effects of electron transfer and redistribution in the Ni-Cu alloys. Specifically, changing the Cu content in the Ni-Cu alloys causes charge redistribution, which leads to a negative correlation between the Cu content and CO selectivity.

In **Chapter 4**, we synthesized atomically dispersed Fe immobilized within

N-doped carbon nanosheets as a model, we carefully investigated the synergistic effect between the metal atom and its anchoring framework sites for efficient CRR. A series of controlled tests show that there is a synergistic effect between the Fe centers and the pyrrolic-N-C framework which facilitates catalytic activity. The highlights include: (i) High FE was received on the atomically dispersed Fe catalyst, which reaches 90% at a low potential of -0.58 V vs. RHE. (ii) We found that there is a synergistic effect at two active sites. The water dissociation occurs at the metal site; While CO_2 adsorption occurs at the N-C sites. For the first time, we revealed the important function of the pyrrolic-N-C framework in single-atom catalysis. (iii) The origin of synergistic effect was uncovered that 1) Pyrrolic N contributes to π electrons that lead to negatively charged pyrrolic-N-C sites favoring CO_2 adsorption; 2) Due to the more negatively charged N-C sites in pyrrolic-N-rich catalysts, Fe sites exist in a positively charged state that enhances water dissociation kinetics to provide sufficient protons for the reduction of CO_2.

In **Chapter 5**, we prepared the single-atom Cu catalyst embedded in N-doped graphene (Cu-N_4-NG) and then comprehensively investigated its chemical structure and catalytic performance. A series of experiments and density functional theory (DFT) calculations showed that the Cu-N_4-NG enhances the selective electroreduction of CO_2 to CO. The highlights include: (i) FE towards CO (80.6%) was achieved on the Cu-N_4-NG at a moderate potential -1.0 V vs. RHE. (ii) The experimental results provided a kinetic understanding of the catalytic contribution in Cu-N_4-NG. The Cu-N_4 moiety in Cu-N_4-NG facilitates the CO_2 activation step which forms the *COOH intermediate; The graphene substrate, where the single-atom Cu was embedded, provides a place for electrocatalytic water dissociation, which supplies the protons for participation in *COOH formation. Through this structure, the CRR was favored over hydrogen evolution. (iii) Also, the computational results gave a thermodynamic understanding of the reaction preference on Cu-N_4-NG. The DFT calculations showed a trend between the differences in limiting potentials of CO_2 reduction and the H_2 evolution, which

is consistent with the trend between the differences in current selectivity for CO and H_2 observed in the experiments. The most positive difference in limiting potentials was found for Cu-N_4-NG, indicating that the occurrence of the CRR is favored over H_2 evolution.

In **Chapter 6**, we prepared graphene-supported 3d transition metal phthalocyanines (MPc/NG, M = Fe, Co, Ni) as ideal single-atom electrocatalysts for the CRR. A series of controlled experiments demonstrated that there is an existence of synergistic interaction between the metal phthalocyanine molecule and the graphene substrate, which results in a high FE for CO. (i) The remarkable catalytic performance was received on CoPc/NG, the FE for CO was almost 100% at a mild potential of -1.0 vs. RHE. (ii) Changing the metal type of MPc significantly affected the catalytic selectivity. The experimental results indicated that the rank of measured FEs toward CO on the catalysts is CoPc/NG > NiPc/NG > FePc/NG. Moreover, the amount difference between CoPc and NG in CoPc/NG was negatively correlated with the CO selectivity. The optimal weight ratio of CoPc-to-NG was given to 1:4.

7.2 Perspectives

Although considerable achievement has been made in the development of 3d transition metal electrocatalysts for highly selective CO_2 reduction, further studies are still required to carry out for understanding catalytic mechanisms and optimizing catalytic activity. The following viewpoint should be taken into consideration in future research.

Controllable synthesis. The fabrication of catalyst plays an important role in the development of the CRR process. Accurately controllable synthesis is the prerequisite to receiving the catalyst with high catalytic activity and selectivity. At present, the nanoscale and sub-nanoscale synthesis still need to be improved. To be specific, the morphology of the received catalysts is not identical, which

may affect the surface area and the number of exposed active sites, resulting in low catalytic performance. For example, in the single-atom metal catalyst, the metal atoms are randomly dispersed in carbon framework, which leads to local enrichment of single atoms, while other regions lack the single-atom metal sites, which may result in inferior catalytic performance; The chemical structure of the obtained catalysts is not uniform, which makes it difficult to determine the effective active centers and further affects understanding the catalytic mechanism.

Advanced characterization. (i) Advanced microscopy characterization can better understand and analyze the fine structure of catalysts. For example, High-angle annular dark-field scanning transmission electron microscopy (HAADF-STEM) imaging is employed to observe and analyze catalysts at nanoscale and sub-nanoscale, obtaining high-resolution morphological details. In this Thesis, all developed catalysts were characterized by HAAD-STEM imaging. Using an atomic force microscope (AFM) is welcomed, which can acquire atomic and molecular level images for understanding the ultrafine structure details, thereby obtaining information that cannot be technically detected by HAADF-STEM. (ii) *In situ* characterization is also considered as a very important real-time measurement. For example, *in situ* Raman characterization involved in Chapter 3 is to record the characteristic peaks of intermediates on the active sites during the CRR, these peaks reveal the possible reaction pathways and help to propose an appropriate catalytic mechanism. *In situ* Fourier-transform infrared spectroscopy (FTIR) is a similar real-time characterization that can be combined with *in situ* Raman technique to obtain all the vibration modes contributed by intermediates during the CRR process. In addition, *in situ* X-ray absorption spectroscopy (XAS) is different from the former two techniques. The formers highlight the chemical states of the intermediates on active sites, while the latter measures the changes in the catalyst itself, such as changes in the oxidation states and coordination environments. Therefore, these advanced characterizations can help to better understand the CRR process on the 3d transition metal catalyst.

Computational support. Density functional theory (DFT) calculation is an alternative way to explain and predict the catalytic CRR process. The active center of atomically dispersed transition metal catalysts is relatively easy to be determined by theoretical calculation. And the modeling for the single-atom metal is not complicated compared to the bulk material. The computational DFT results can help understand the outcomes which may difficult to be interpreted experimentally. Importantly, DFT calculation offers a prediction of catalytic performance, which proposes a reasonable design for catalyst synthesis. This helps save research and development costs and effectively achieve the high catalytic activity. With the introduction of high-end techniques, it is believed that a comprehensive understanding of the catalytic mechanism of the CO_2 reduction reaction on 3d transition metal catalysts will be achieved.

Appendix A

Supplementary Literature Review: Surface and Interface Engineering in Copper-Based Bimetallic Materials for Selective CO_2 Electroreduction

Statement of Authorship

Title of Paper	Surface and Interface Engineering in Copper-Based Bi-Metallic Materials for Selective CO$_2$ Electroreduction
Publication Status	☑ Published ☐ Accepted for Publication ☐ Submitted for Publication ☐ Unpublished and Unsubmitted work written in manuscript style
Publication Details	A. Vasileff, C.C. Xu, Y. Jiao, Y. Zheng, S.Z. Qiao, Surface and interface Engineering in Copper-based Bi-metallic Materials for Selective CO$_2$ Electroreduction, Chem, 2018, 4, 1809-1832

Principal Author

Name of Principal Author (Candidate)	Anthony Vasileff		
Contribution to the Paper	Devised the idea of the paper with supervisors, gathered the bulk of the information and wrote the bulk of the paper		
Overall percentage (%)	70		
Certification:	This paper reports on original research I conducted during the period of my Higher Degree by Research candidature and is not subject to any obligations or contractual agreements with a third party that would constrain its inclusion in this thesis. I am the primary author of this paper.		
Signature		Date	05/02/2020

Co-Author Contributions

By signing the Statement of Authorship, each author certifies that:

     i.   the candidate's stated contribution to the publication is accurate (as detailed above);

     ii.   permission is granted for the candidate in include the publication in the thesis; and

     iii.   the sum of all co-author contributions is equal to 100% less the candidate's stated contribution.

Name of Co-Author	Chaochen Xu		
Contribution to the Paper	10% Gathered information and helped to write some sections of the paper		
Signature		Date	05/02/2020

Name of Co-Author	Yan Jiao			
Contribution to the Paper	4% Provided specialist guidance and helped to write certain sections of the paper related to her field.			
Signature			Date	05/02/2020

Name of Co-Author	Yao Zheng			
Contribution to the Paper	8% Provided guidance and supervision from conception through to submission and helped to revise the paper.			
Signature			Date	05/02/2020

Name of Co-Author	Shizhang Qiao			
Contribution to the Paper	8% Provided guidance and supervision from conception through to submission and helped to revise the paper.			
Signature			Date	05/02/2020

4% Provided specialist guidance and helped to write certain sections of the paper related to her field.

Review

Surface and Interface Engineering in Copper-Based Bimetallic Materials for Selective CO$_2$ Electroreduction

Anthony Vasileff,[1,2] Chaochen Xu,[1,2] Yan Jiao,[1] Yao Zheng,[1,*] and Shi-Zhang Qiao[1,*]

The electrochemical CO$_2$ reduction reaction (CO$_2$RR) can couple carbon-capture storage with renewable energy to convert CO$_2$ into chemical feedstocks. For this process, copper is the only metal known to catalyze the CO$_2$RR to hydrocarbons with adequate efficiency, but it suffers from poor selectivity. Copper bimetallic materials have recently shown an improvement in CO$_2$RR selectivity compared with that of copper, such that the secondary metal is likely to play an important role in altering inherent adsorption energetics. This review explores the fundamental role of the secondary metal with a focus on how oxygen (O) and hydrogen (H) affinity affect selectivity in bimetallic electrocatalysts. Here, we identify four metal groups categorized by O and H affinities to determine their CO$_2$RR selectivity trends. By considering experimental and computational studies, we link the effects of extrinsic chemical composition and physical structure to intrinsic intermediate adsorption and reaction pathway selection. After this, we summarize some general trends and propose design strategies for future electrocatalysts.

The Bigger Picture

Global consumption of fossil fuels is driving anthropogenic climate change and depleting reserves. To stem these environmental problems and secure future energy commodities, the electrochemical CO$_2$ reduction reaction (CO$_2$RR) presents an ideal solution because it can couple carbon-capture storage technology with renewable energy to convert atmospheric CO$_2$ into useful chemical feedstocks. Efficient catalysts are required to drive this process with adequate energy efficiency and product selectivity. In this review, we discuss how surface and interfacial engineering can be used as a strategy for designing copper alloy and bimetallic materials for selective CO$_2$ reduction to CO or hydrocarbons and alcohols.

INTRODUCTION

The world currently relies on fossil fuels for energy production and its chemical industries. However, the burning of fossil fuels releases significant carbon dioxide (CO$_2$) emissions into the atmosphere, which is considered the primary driver for anthropogenic climate change. CO$_2$ is a highly stable molecule and is generally inert in most conditions. However, under appropriate cathodic reduction potentials and the assistance of protons in solution, CO$_2$ can be electrochemically activated and converted via the CO$_2$ reduction reaction (CO$_2$RR) to reduced products. The CO$_2$RR is an elegant route to sustainable fuel and chemicals production when coupled with carbon-capture storage technology and renewable energy sources such as solar radiation. However, this process is kinetically sluggish because of the multiple electron transfer steps and high energy barriers involved. Therefore, efficient electrocatalysts are required to reduce the reaction overpotential and facilitate the kinetics to accomplish commercially significant rates. To date, a wide range of electrocatalysts for the CO$_2$RR have been reported, and reduction products are highly catalyst specific.[1–6] Copper (Cu) is a unique metal because it is the only metal that can form deep reduction products (i.e., hydrocarbons and alcohols) with acceptable activity and efficiency during the CO$_2$RR.[7] However, the selectivity of Cu toward a certain product is typically poor, generating many reduction products concurrently, which range from two-electron (2e$^-$) transfer products (e.g., CO and HCOOH) to eight-electron (8e$^-$) transfer products (e.g., CH$_4$) and above.[8–10] On the microscopic level, the origin of copper's poor selectivity is its moderate binding energy of most reaction intermediates.[6,11,12] Additionally, considering the Sabatier

principle, improving the selectivity of copper is not a simple task given that the adsorption energies of different intermediates scale with one another.[11] Thus, it is extremely difficult to optimize the binding of a specific intermediate without affecting another.

For various heterogeneous catalytic processes, it has been found that the relative metal oxygen (O) and hydrogen (H) affinities play important roles in a catalyst's activity and selectivity by influencing the binding strength of specific reaction intermediates on their surface.[13,14] Toward the electrocatalytic CO_2RR, for metals with higher O affinity but lower H affinity than Cu (such as In, Sn, Hg, and Pb), the *COOH intermediate formed after the first reaction step is weakly bound. Therefore, the primary CO_2 reduction product on these surfaces is HCOOH. Evidence even suggests that the reaction may proceed through an O-bound *OCHO intermediate on these metals.[15] However, metals with lower O and H affinities than Cu (such as Zn, Ag, and Au) can bind *COOH stronger than *CO. Therefore, CO is desorbed as the main product with the formation of *COOH as the potential determining step (PDS).[16] Other metals with both higher O affinity and H affinity than Cu (including Co, Ni, Fe, Ir, and Pt) tend to favor the competitive hydrogen evolution reaction (HER), although small amounts of hydrocarbons and alcohols have been detected on these metal surfaces.[14,17–20]

The grouping of CO_2RR products based on a catalyst's O and H affinities leads to the idea that by alloying with specific O-binding or H-binding sites, Cu-based alloys can be engineered to have one or two active sites with tuned binding energies for key reaction intermediates. As a precedent, introducing a secondary metal to tune the activity of Pt is well documented, particularly for the oxygen reduction reaction (ORR) in fuel cells.[21–23] For the ORR, many Pt alloys show significantly improved activity and stability compared with those of pure Pt.[24,25] Although many factors (strain, ligand effect, etc.) can contribute to altering the electronic structure (i.e., d-band center) of a material, it is likely that they all function to weaken the adsorption of O-bound species on the surface. Accordingly, targeting the key reaction intermediates in this way may also be useful for CO_2RR pathway selection. To be specific, metals with high O affinity are favorable for C-O bond cleavage, whereas metals with high H affinity favor proton transfer and provide protons or hydroxyl groups for hydrogenation.[19] However, considering that the HER is generally highly competitive on metal surfaces, it is necessary to understand how these secondary metal sites affect Cu to be able to predict activity and selectivity. Furthermore, the electronic structure and morphology are almost always different in the bimetallic material compared with copper. This inevitably modifies intermediate binding and is therefore another necessary consideration when evaluating Cu bimetallic catalysts.

In this review, we first briefly provide some background to the CO_2RR process and the fundamental principles that govern the selectivity of copper catalysts. We then introduce the concept of interfacial engineering of copper-based catalysts and review current examples of Cu bimetallic electrocatalysts. Each example is categorized into sections on the basis of the O and H affinities of the secondary metal, and we highlight the effects from the introduced O- and H-binding sites on the selectivity of the Cu bimetallic system. The effects of the secondary metal on the chemical composition, electronic structure, geometry, morphology, and electrocatalytic activity of these bimetallic catalysts are then linked to their intermediate binding energetics. This is done with the aim of interpreting any trends in CO_2RR selectivity that might result from modification of the Cu interface with another metal. To further this, we discuss

[1]School of Chemical Engineering, University of Adelaide, Adelaide, SA 5005, Australia

[2]These authors contributed equally

*Correspondence:
yao.zheng01@adelaide.edu.au (Y.Z.),
s.qiao@adelaide.edu.au (S.-Z.Q.)

Chem

some key examples that combine experimental and computational studies in this field. Finally, we propose some general trends on the basis of these metal groups with strategies for the future design of Cu bimetallic electrocatalysts.
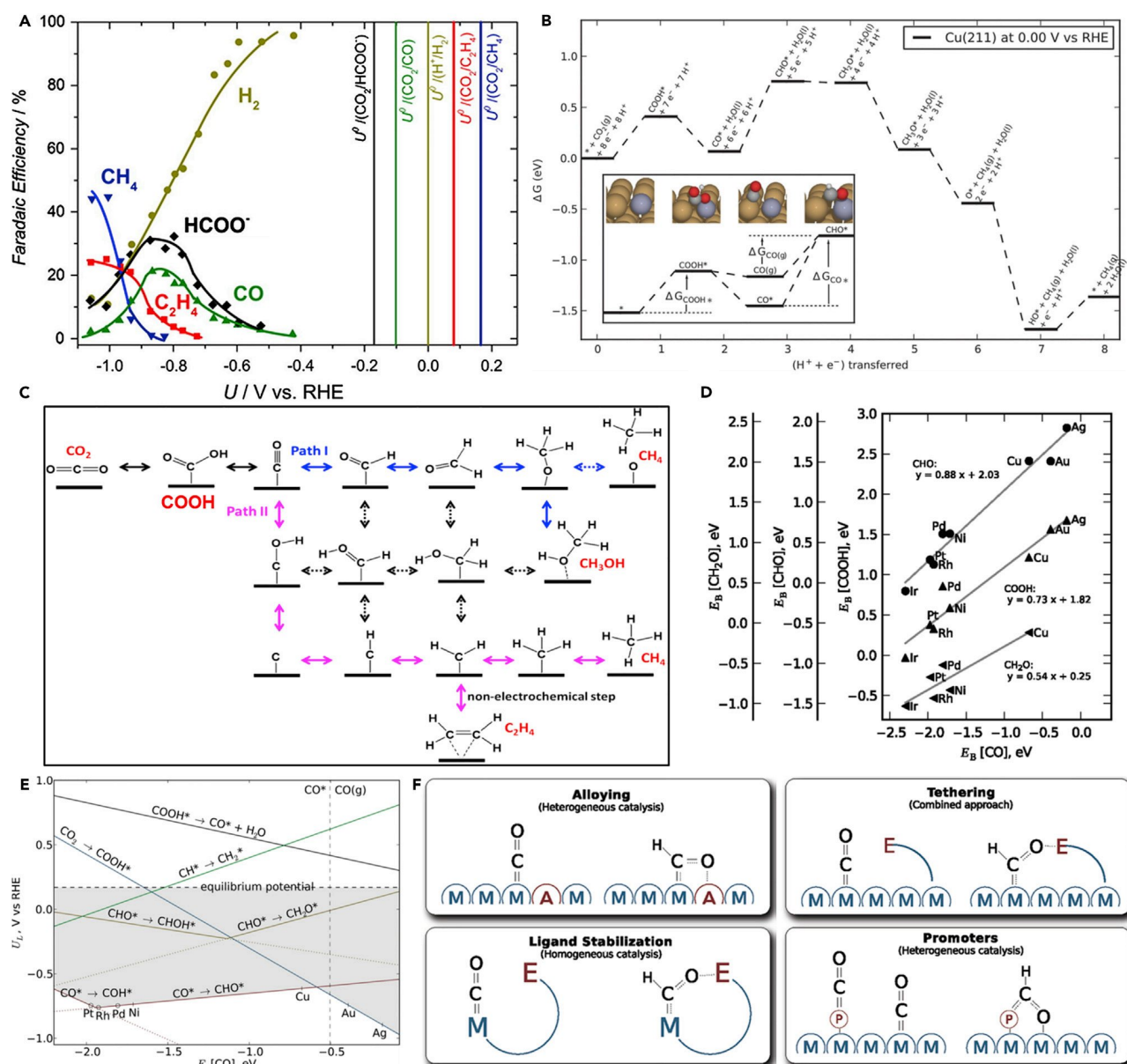
FUNDAMENTAL UNDERSTANDING OF THE CO$_2$RR

CO$_2$RR Reaction Mechanism on Cu

Cu has been widely studied as an electrocatalyst for the CO$_2$RR because of its ability to produce hydrocarbons and alcohols at modest overpotentials.[8,17,26–28] Electrocatalytic CO$_2$RR on Cu proceeds via multiple electron-proton coupled transfer steps to adsorbed intermediates through multiple pathways. Therefore, it is very non-selective and produces a range of products concurrently. Pioneering work by Hori and co-workers found that on Cu electrodes, generally 2e$^-$ products (H$_2$, CO, HCOOH) are formed at lower overpotentials, whereas higher e$^-$ products (CH$_4$: 8e$^-$ and C$_2$H$_4$: 6e$^-$) are formed at higher overpotentials (Figure 1A).[17,27,29,30] However, the specific mechanism of the CO$_2$RR on Cu is surface and condition sensitive,[31,32] and a comprehensive understanding is still lacking. As shown in Figure 1B, the most widely accepted reaction pathway to CH$_4$ proceeds via the hydrogenation of adsorbed *CO to the *CHO intermediate, which is identified as the PDS.[33,34] Further hydrogenation to *CH$_2$O and *CH$_3$O then leads to CH$_4$ production with the remaining reaction steps being exergonic. Additionally, the hydrogenation of the methyl end of *CH$_3$O is more readily achieved with solvated protons to produce CH$_4$ than with hydrogen addition at the oxygen end via co-adsorbed *H to produce CH$_3$OH. Besides the thermodynamic analysis, the role of kinetics for the reactions on Cu surfaces has also been considered.[35] It was found that CH$_4$ production through the CHO* intermediate faced a 1.21-eV kinetic barrier at a potential of −1.15 V versus reversible hydrogen electrode (RHE), whereas CH$_3$OH only needed to overcome 0.15 eV at this potential. Therefore, to explain why CH$_4$ is predominantly produced experimentally it was proposed that *CO reduction to the *COH intermediate is favored over CHO* (Figure 1C).[36] This *COH intermediate then undergoes further reduction to *C and is then hydrogenated by co-adsorbed *H, as has been proposed previously.[10] This pathway also explains the experimentally observed concurrent production of CH$_4$ and C$_2$H$_4$ as a result of the identification of a common intermediate (*CH$_2$). After considering the kinetic aspects, some other studies support the route through the *CHO intermediate to *CH$_2$ via *CHOH, mainly because of the sluggish kinetics involved in the hydrogenation of *CH$_3$O at the methyl end and other experimental observations.[28,37]

Scaling Relationships

An inherent challenge of the CO$_2$RR is that the binding of intermediates follows conventional scaling relationships on the basis of the formation of similar surface-adsorbate bonds among different intermediates (e.g., *COOH, *CO, and *COH all involve C-bound intermediates). Given this, the adsorption energy of a certain intermediate cannot be optimally tuned without affecting another.[11,38,39] For example, Figure 1D shows the calculated scaling relationships between various C-bound intermediates in the reaction pathway to CH$_4$. As previously discussed, the hydrogenation of *CO to *CHO is considered the PDS of this process because it has the highest free-energy change (0.74 eV); the magnitude of this energy change predominantly originates from the weak *CHO binding relative to *CO binding.[39] To reduce this, the surface would have to bind *CHO stronger than *CO. However, this is difficult to realize because of the constraint imposed by conventional scaling relationships.[11] Experimentally, the large overpotentials and poor turnover frequencies for CO$_2$ reduction to CO on Au and Ag electrodes can also be attributed to the similar weak adsorption of *COOH caused by the linear scaling between *COOH and *CO.[40]

Figure 1. Fundamental Understanding of the CO₂RR on Cu Surfaces

(A) Product distribution expressed as FE as a function of the potential on a polycrystalline Cu electrode. The vertical lines represent the reversible potentials for various products. Adapted from Jovanov et al.[30]

(B) Proposed reaction pathways for the reduction of CO_2 to CH_4 on Cu(211) surface through the *CHO intermediate. Adapted from Hansen et al.[33] with permission of the Royal Society of Chemistry.

(C) The reaction pathway (path II) of the CO₂RR through the *COH intermediate to CH_4, CH_3OH, and C_2H_4. Path I reflects the reaction presented in (B). Adapted from Nie et al.[36]

(D–F) Scaling relationships for C-bound intermediates relevant to the CO₂RR pathway on a range of metal surfaces (D), limiting potentials (U_L) for elementary proton-transfer steps of the mechanism in (B) (E), and suggested decoupling strategies to break these scaling relationships (F). Adapted with permission from Peterson and Norskov.[11] Copyright 2012 American Chemical Society.

Regarding Cu, the fundamental reason for its ability to produce products other than CO at reasonable overpotentials is that it binds *CO neither too weakly nor too strongly (Figure 1B). Therefore, *CO formed on the surface does not desorb immediately (adsorption not too weak), and does not poison the surface (adsorption not

too strong). Furthermore, from Figure 1E it can also be seen that out of all transition metals, Cu has relatively moderate binding of most C-bound intermediate species.[11] As a result, Cu is at the top of the "volcano" plot for the calculated limiting potentials of the two reaction steps which present the largest free-energy barriers (i.e., proton-electron coupled steps: CO_2 to *COOH and *CO to *CHO).[11,37] However, having moderate-level binding of the various surface adsorbates in the pathway also leads to poor selectivity for a particular final product. Therefore, by breaking the above scaling relationships, it is possible to optimize the adsorption energy of a particular intermediate(s) not only for a reduction in overpotential but also for enhanced selectivity. Some useful strategies that focus on tuning the intrinsic electronic parameters underlying the scaling relationships, such as alloying with strong O-binding metals, ligand stabilization, tethering, and addition of promoters, have been proposed (Figure 1F).[11] Ultimately, the aim of these strategies is to strengthen the binding energy of *CHO (i.e., more negative) relative to that of *CO for improved selectivity to deep reduction products.

IMPROVING SELECTIVITY BY INTERFACIAL ENGINEERING

Classification

Various strategies have been employed to enhance the activity of Cu catalysts, and these mainly involve exploiting nanostructuring techniques and morphological control.[9,41–44] However, these approaches generally reduce the overall overpotential for the CO_2RR, improving its selectivity over the HER, and a distinct reduction pathway is not always achieved.[9] With regard to metal catalysts, by coupling two (or more) metal species in alloy or bimetallic materials, the catalyst interface can be engineered to contain multiple sites that contribute to binding of key intermediates in the pathway.[39,45] As a result, designing catalysts on the basis of this principle could lead to conventional scaling relationships being broken in order to tune the selectivity for the reduction of CO_2. Cu is a logical model since it is the only metal catalyst that can promote the CO_2RR toward various hydrocarbon products at non-negligible faradic efficiency (FE).[46] Recently, it has been suggested that alloying Cu, as a form of interfacial engineering, can tune the adjacent chemical environment around the Cu atoms. Therefore, by employing alloys and bimetallic materials, it is possible to tune the binding strength of targeted intermediates on the catalyst surface and enhance the reaction kinetics and selectivity.

In general, the changes to intermediate binding energy, and consequently the reaction pathway, highly depend on the nature of the secondary metal. Herein, we classify the secondary metals on the basis of two factors: H affinity and O affinity; high H affinity describes a metal that binds hydrogen more strongly than Cu, whereas high O affinity describes a metal that binds oxygen more strongly than Cu. The choice of these two descriptors is based on the following considerations. Given that the hydrogenation of *CO is the PDS for deep reduction of CO_2, a secondary site with strong H or O affinity can facilitate the adsorption of *CHO species with alternative configurations (Figure 2A). As a result, the inherent scaling relationship of *CO and *CHO/*COH can be broken. Additionally, the adsorption strength of O-bound reaction intermediates (e.g., *CH_2O and *CH_3O), which appear in the latter half of the CO_2RR pathway, directly relates to the selectivity of hydrocarbon and alcohol products.[47] For determining H and O affinities, a scatterplot presented in Figure 2B provides the trend of H adsorption energy (ΔE_H) against O adsorption energy (ΔE_O) for various metal surfaces. These trends have been extensively used as activity descriptors for the HER and ORR, respectively.[48,49] It can clearly be seen that the metals located to the top left (e.g., Ag and Au) have weaker ΔE_H and ΔE_O than Cu. These
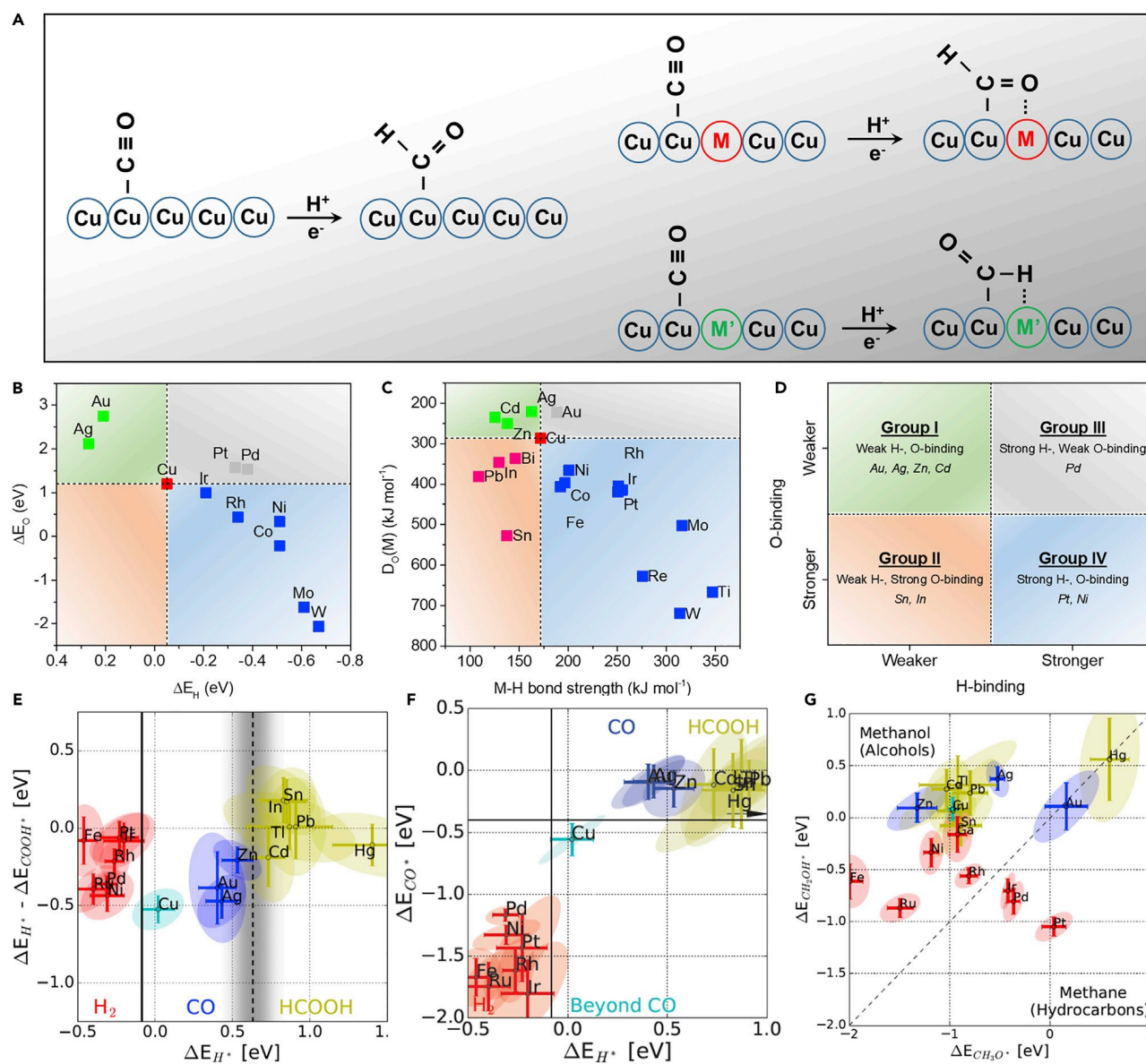
Figure 2. Grouping of Various Metals in Relation to Copper Based on Various Descriptors

(A) Schematic illustration of *CHO adsorption on pure Cu and Cu-M alloy surfaces. M indicates a site with strong O affinity, and M' indicates a site with strong H affinity.

(B) The oxygen adsorption energy plotted as a function of the hydrogen adsorption energy over different metals. Data of ΔE_O and ΔE_H are from Norskov et al.[48]

(C) The intermediate M-H bond strength plotted as a function of the bond dissociation enthalpy of metal oxides. M-H bond strength data are from Trasatti,[50] and $D_O(M)$ data are from Kepp.[51]

(D) Grouping of various metals in relation to copper alloys based on O and H affinities from previous studies.

(E–G) The experimental product classification of H_2, CO, and HCOOH by the ΔE_{H^*} descriptor (E); the binding energies of intermediates ΔE_{CO^*} and ΔE_{H^*}, which categorize metal catalysts into three distinct groups (F); and the DFT energy relation between ΔE_{CH2OH^*} and ΔE_{CH3O^*} descriptors as a measure of CH_3OH or CH_4 production from carbon-oxygen compounds (G). Adapted with permission from Bagger et al.[6] Copyright 2017 Wiley-VCH Verlag GmbH & Co. KGaA.

metals therefore have to overcome a higher energy to bind hydrogen or oxygen. The metals to the bottom right of Cu (e.g., Ir and Rh) show stronger H and O affinities. The metals located to the top right of Cu (e.g., Pt and Pd) show stronger H affinity

but weaker O affinity. Importantly, these trends can be presented in other forms of H- and O-binding strength. A similar scatterplot shown in Figure 2C provides the trend of the hydrogen-metal bond strength against the enthalpy of bond dissociation of metal oxides as an alternative form. Specifically, for determining H affinity, the strength of the metal-hydrogen (M-H) bond was experimentally measured on various metal surfaces; a greater M-H bond strength favors hydrogen binding.[50] Similarly, a quantitative scale of O affinity has been calculated by applying the enthalpy of bond dissociation for M-O as a descriptor, denoted as $D_O(M)$; metals with $D_O(M)$ values greater than $D_O(Cu)$ signify greater metal-oxygen bond strength (stronger O affinity), and vice versa.[51] As a result, four metal groups are identified depending on their H and O affinity relative to that of Cu (Figure 2D). On the basis of this classification, our goal here is to comprehensively review recent Cu-based alloy (Cu-M) electrocatalysts for the CO_2RR and to evaluate any apparent selectivity trends that may be useful in the rational design of future electrocatalysts.

It should be noted that others have also found that the adsorption energetics of specific reaction intermediates can be applied to classify a wide range of single metals for the CO_2RR. For example, the binding energies of *COOH and *H were calculated as the descriptors to explain the trend of $2e^-$ CO and HCOOH generation for the CO_2RR, whereas binding energies of *CO and *H were applied as the descriptors to predict activity toward deep reduction products.[6] Specifically, as shown in Figure 2E, the metals can be separated into three groups when only ΔE_H is considered as the descriptor: metals with stronger hydrogen affinity than Cu (i.e., within the hydrogen underpotential deposition, H_{upd}, zone) mainly form H_2, metals with moderate H adsorption energy at the CO_2 reduction potential mainly form CO, and metals with weaker H adsorption at the CO_2 reduction potential form HCOOH.[6] Additionally, binding energies of *CO and *H separate Cu from all other metals, as shown in Figure 2F. In this plot, Cu is the only metal in the bottom-right zone possessing relatively weaker *H binding and stronger *CO binding along with the ability to reduce CO_2 to hydrocarbon products or partly reduced alcohol products. It was also found that the C-bound (*CH_2OH) and the O-bound (*CH_3O) intermediates can distinguish hydrocarbon or alcohol formation (Figure 2G). Therefore, four intermediates—ΔE_{H*}, ΔE_{CO*}, ΔE_{COOH*}, and ΔE_{CH3O*}—can be used to explain product groups and selectivity distributions for the CO_2RR on most pure metal surfaces. To predict the products selectivity of Cu-based bimetallic materials, herein we use metal categories based on the O and H affinities of the secondary metal.

Group 1: Weak H Binding and Weak O Binding

Gold (Au)

Au is a d-block metal with both weak hydrogen and oxygen adsorption and has been the most common group 1 metal alloyed with Cu for the CO_2RR. Experimentally it was shown that increased Au content favored CO production, and the pathway to CH_4 was suppressed.[52] Mechanistically, the desorption of CO on Cu sites was promoted because of the lower activation energy for CO desorption caused by Au alloying. In another example, it was found that both the composition and nanostructure of Cu-Au nanoparticles affected the catalytic performance, such that CH_3OH and C_2H_5OH were selectively produced.[53] The optimal $Cu_{63.9}Au_{36.1}$ composition exhibited an FE of 28% for alcohols (including 15.9% for CH_3OH), which is 19 times higher than that of pure Cu. This study claimed that *CO is a significant intermediate for CO_2 reduction toward hydrocarbons and alcohols, whereby binding of *CO was likely optimized in this Cu-Au system. As a comprehensive investigation into the effect of the Cu-Au stoichiometric ratio in bimetallic catalysts,[46] electrochemical results showed that alloys with increased Cu content obtained various reduction
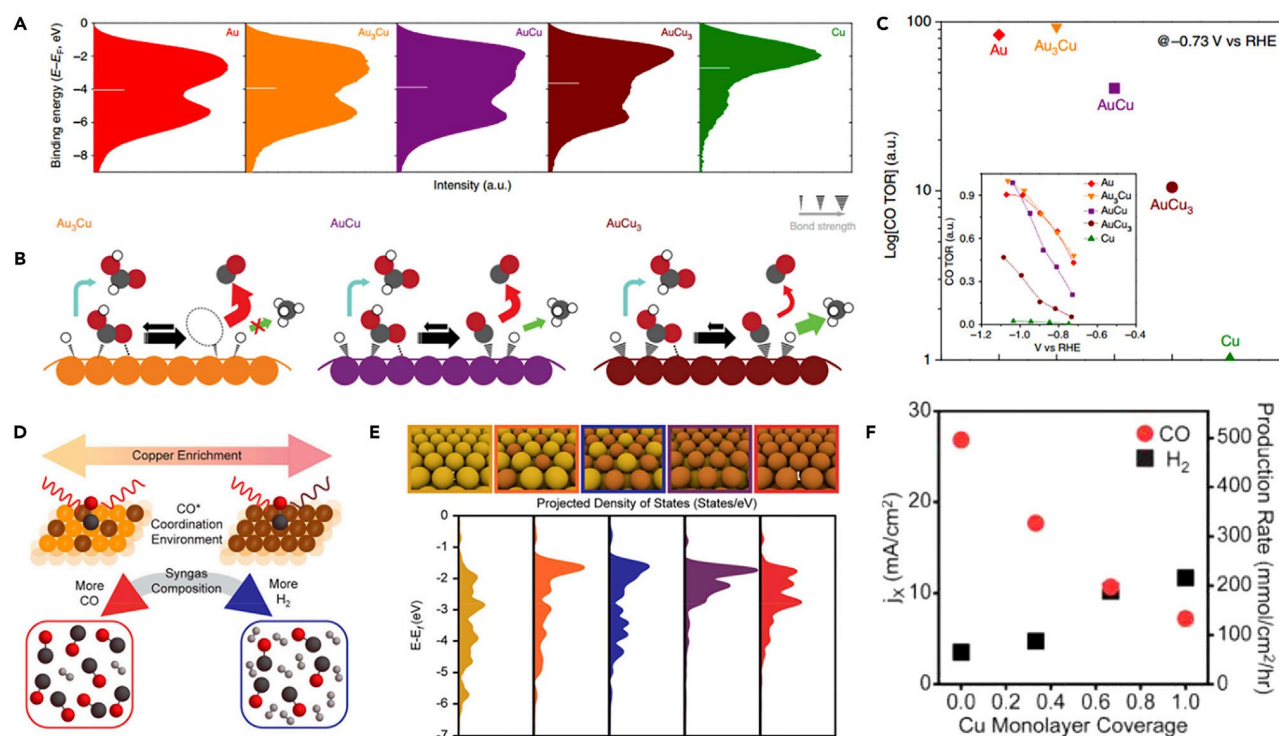
Figure 3. Characterization and Performance of Cu-Au Catalysts for the CO$_2$RR

(A–C) Surface valence-band photoemission spectra of Au-Cu bimetallic nanoparticles (the white bars indicate the d-band centers) (A); proposed mechanism for the CO$_2$RR on the surface of Au-Cu bimetallic nanoparticles (gray, red, and white atoms represent C, O, and H, respectively) (B); and CO generation rate on various alloy electrocatalysts at a certain overpotential (inset shows relative CO generation rate as a function of the applied potential) (C). Adapted by permission from Springer Customer Service Centre GmbH: Springer Nature, *Nature Communications*, Kim et al.[46] copyright 2014.

(D–F) Scheme depicting the relationship between the Cu-enriched Au surface, *in situ* characterization of CO* coordination, and syngas composition (D); calculated d-band electronic states for increasingly Cu-enriched Au surfaces (E); and partial current densities (left axis) and production rates (right axis) for CO and H$_2$ as a function of Cu monolayer deposition on Au (F). Adapted with permission from Ross et al.[55] Copyright 2017 American Chemical Society.

products, whereas increased Au content simultaneously improved CO formation and suppressed other pathways. It was indicated that Cu-Au alloys favored CO production because of their synergistic electronic and geometric effects. Specifically, density functional theory (DFT) calculations demonstrated that the d-band center shifts downwards from pure Cu to pure Au (Figure 3A). As a result, the binding strength for *COOH and *CO should decrease as the Au content increases, and the formation of CO in Cu-Au systems should exhibit a monotonic tendency (Figure 3B). However, *COOH binding was found to be relatively unaffected as a result of an observed geometric effect that stabilized *COOH intermediates. This explains their experimental observations whereby the highest FE toward CO was obtained on Au$_3$Cu alloy (Figure 3C), and provides a better understanding of the effects of electronic structure and geometric modification in bimetallic materials. Additionally, it was found that increasing the degree of atomic ordering in Cu-Au alloys can tune the selectivity of CO$_2$ reduction toward CO with a high FE of ~80%, which is due to the stabilization *COOH intermediates on compressively strained Au sites.[54]

Ross et al. used underpotential deposition (UPD) to construct another type of Cu-Au alloy by depositing a single layer of Cu with different coverages (1/3, 2/3, and 1).[55] They found that less Cu coverage increased CO production, whereas increased Cu coverage promoted H$_2$ evolution. Employing *in situ* Raman microscopy, they used

Chem

CellPress REVIEWS

the vibration of the C-O bond (ν_{C-O}) in *CO species as a descriptor to understand the effects of the Cu/Au ratio on the *CO adsorption strength. It was found that with greater Cu coverage, ν_{C-O} experienced a red shift, which was associated with bond lengthening attributable to greater interaction with the metal (Figure 3D). DFT calculations showed that the projected density of states (DOS) moved further away from the Fermi level on increasingly Au-dominant surfaces, favoring CO production (Figure 3E). On the other hand, Cu enrichment provided a greater improvement to *H adsorption than *CO. Therefore, the degree of Cu enrichment can affect the relative activity of the HER to the CO_2RR, which can realize controllable syngas production (Figure 3F). Similarly, in an Au-Cu core-shell (Au@Cu) system, experimental results indicated that seven to eight layers of Cu resulted in a better selectivity for C_2H_4, whereas CH_4 production slightly increased for 14 or more Cu layers.[56] This was explained by the calculated DFT results, which showed that *COH intermediates were favored over *CHO on terraces; however, *CHO was slightly favored as *CO coverage increased.[57] Therefore, both structural and electronic effects that change the binding of *CO have a significant impact on selectivity and product distribution on the Au@Cu catalysts. In another study, Cu-Au core-shell nanostructures (Cu@Au) also exhibited enhanced current density over polycrystalline Cu and achieved a greater FE toward CO.[58]

Silver (Ag)

Ag is another group 1 metal that has been coupled with Cu for CO_2 reduction. In the Ag-Cu core-shell nanoparticle (Ag@Cu) system, samples with low Cu coverage showed high conversion of CO_2 toward CO, while Cu-dominant nanoparticles had greater selectivity for hydrocarbons.[59] As with the Au@Cu material, both electronic effect and geometric effects were important factors involved in the catalytic activity of the Ag@Cu system. Specifically regarding the electronic effect, the binding energy of *CO on Ag active sites was weaker than that on Cu. Therefore, desorption of CO was facilitated when the coverage of Cu was low. For the geometric effect, the binding strength of intermediates was tuned by changing the local atomic arrangement at the active sites. Additionally, for electrodeposited Cu-Ag alloys, it was found that Cu segregation caused Cu enrichment on the catalyst surface.[60] As a result, the $Ag_{57}Cu_{43}$ alloy achieved 2.2-fold higher mass-normalized activity than the Ag_{100} catalyst. In another study, electrodeposited nanocoral Cu-Ag bimetallic catalysts exhibited only 30% FE toward hydrogen and around 70% for total C_1–C_3 products by a solar-driven electrochemical cell.[61] In this system it appears that Cu contributed the dominant binding effect, as overall product selectivity was poor. However, the Cu-Ag electrode was more active toward producing alcohols and oxygenates compared with pure Cu. Cu-Ag bimetallic catalysts have also been prepared by melting mixtures of Cu and Ag powders with specific atomic ratios.[62] When the Cu content was low, it was found that the Cu was dissolved in the Ag phase and segregated on the surface during the CO_2RR. These Ag-dominant catalysts produced CO as the major product on the surface although the Cu sites formed the reactive sites. On the other hand, the Cu-dominant catalysts suppressed the HER by about 75% without affecting the ability to produce deep reduction products from CO. On the atomic level, it is believed that compressive strain on Cu introduced by neighboring Ag causes a shift in the valence band DOS, therefore causing weaker binding of *H and *O relative to *CO.

Zinc (Zn)

Cu-Zn bimetallic catalysts were also found to be selective toward CO_2 reduction to alcohols, in which Cu_4Zn achieved the highest FE of 29.1%.[63] The authors indicated that CO_2 is reduced to *CO on either Cu or Zn active sites in the first step, and is

Chem 4, 1809–1831, August 9, 2018 1817

further reduced to *CHO or *CH$_x$ (x = 1–3) on the Cu sites. However, because of the weak adsorption of *CO on the Zn sites, desorbed CO may diffuse and spill over on the Cu sites, whereby the *CO can insert between Cu sites and *CH$_2$ intermediates to form *COCH$_2$, which is then reduced further to produce C$_2$H$_5$OH.

Cadmium (Cd)

Hori investigated *in situ* Cd-electrodeposited Cu electrodes under different Cd coverages.[64] At a constant current density, Cd electrodeposition occurred along with the HER and CO$_2$RR. Therefore, as Cd deposition increased with time, a trend in product selectivity could be observed. The results showed that the FE toward CO increases with increasing Cd coverage, whereas the FE toward other gas products decreases significantly. However, the FE toward CO reaches a maximum, and with further increase in Cd coverage the production of HCOOH is favored.

Group 2: Weak H Binding and Strong O Binding

Tin (Sn)

Sn is identified as a group 2 metal with higher O affinity and weaker H affinity than Cu.[51] Because of its weak H adsorption, Sn metal is relatively inactive toward the HER and Sn electrodes have been found to mainly produce HCOO$^-$.[7,65] This suggests that on Sn, the CO$_2$RR overwhelmingly proceeds via the *COOH intermediate or, as has been suggested, through the bidentate *OCHO intermediate.[15] In the Cu-Sn bimetallic system, theoretically *CO intermediates are unaffected by O-binding sites (e.g., Sn) as they tend to bind in end-on configurations, where the O atom contributes little to the chemisorption. However, O atoms contribute more in the *COOH intermediate to overall adsorbate stabilization and its binding energy is likely increased when O-binding sites are present.[39] Furthermore, O-binding sites likely play an even greater role if the CO$_2$RR proceeds via the *OCHO intermediate, as the two oxygens bond to the surface in a bidentate configuration.[15] Cu-Sn bimetallic materials for selective CO$_2$ reduction have only been demonstrated experimentally in a few cases, and it seems that Sn limits the usual CO$_2$RR pathway on Cu to 2e$^-$ reduction products.[66] For example, it was found that while maintaining an onset potential similar to that of a Cu sheet electrode, a Cu-Sn material was significantly more selective to CO production with an FE of 90% at −0.6 V versus RHE (Figure 4A).[67] In comparison, the Cu sheet achieved a wide range of products (CO, HCOOH, and H$_2$) under the same conditions (Figure 4B). A noted consequence of coupling Sn with Cu was that the bimetallic material exhibited approximately one-third less catalytic current density compared with the Cu sheet electrode (Figure 4C). However, when considering the improved selectivity for the CO$_2$RR over the HER on the Cu-Sn material, this difference becomes less significant.

Core-shell Cu-SnO$_2$ nanoparticles achieved a maximum FE of 93% toward CO at −0.7 V versus RHE for samples with a 0.8-nm thick SnO$_2$ shell (Figure 4D).[68] In this study, the thickness of the Sn shell was found to have a marked effect on product selectivity. When the shell thickness was increased to 1.8 nm, negligible CO was produced within this range, and instead HCOOH was produced in preference along with increased HER at more positive potentials (Figure 4E). This sample exhibited a trend similar to that in Sn foil, indicating that for increased shell thickness the Sn characteristics dominated the electrocatalytic pathway. DFT calculations found that the 0.8-nm thick SnO$_2$ shell could induce a large compressive strain on the surface (∼10%), and Cu atoms simultaneously diffuse out on the SnO$_2$ shell. As a result, differing from the 1.8-nm thick SnO$_2$ shell model on which HCOOH production is energetically more favorable, the overpotential for CO production is less negative than that for HCOOH production on the model where both compression and Cu
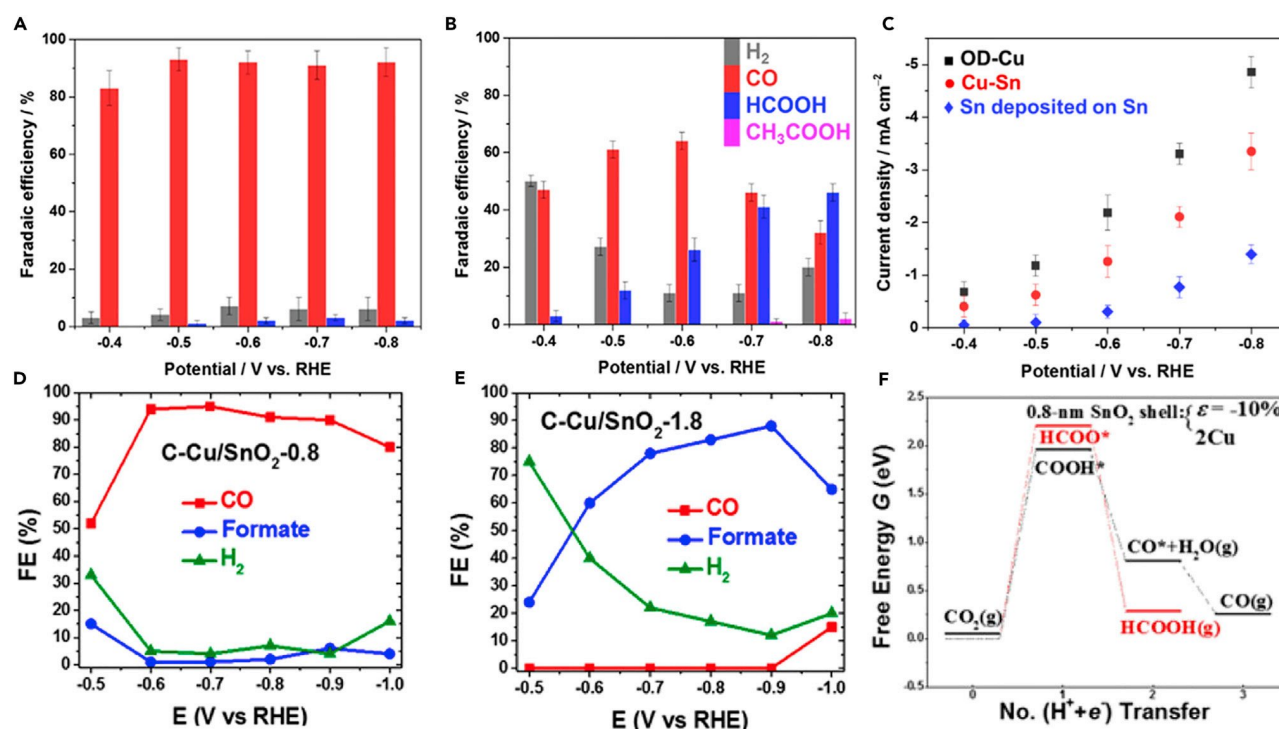
Figure 4. Characterization and Performance of Cu-Sn Catalysts for the CO$_2$RR

(A–C) FE analysis of (A) Cu-Sn and (B) Cu catalyst at different applied potentials and (C) overall current density of different electrocatalysts. Adapted with permission from Sarfraz et al.[67] Copyright 2016 American Chemical Society.

(D–F) Potential-dependent FEs on different electrodes (D and E) and free-energy diagrams of two reaction pathways on a 0.8-nm SnO$_2$ shell with two Cu atoms on the surface and 10% uniaxial compression (F). The red and black lines represent the path of HCOOH and CO generation, respectively. Adapted with permission from Li et al.[68] Copyright 2017 American Chemical Society.

doping are present (Figure 4F). Other studies also report the effect of the deposited Sn thickness in Cu-Sn systems, in which the thicker Sn layers favor HCOOH production but thinner layers favor CO production.[66,69] A mechanistic study on SnO$_2$-coated CuO nanoparticles found that the binding strength of *H and *CO is significantly lower than that of unmodified CuO nanoparticles.[69] As a result, firstly CO will be more easily desorbed from the surface upon formation, and subsequent hydrogenation will be more difficult because of the dilution of adsorbed *H intermediates. Secondly, the weak *H adsorption will limit the HER and increase the selectivity for the CO$_2$RR. Given that CO is the main product formed on Cu-Sn materials, this view gives a good overall explanation of the underlying mechanism.

Indium (In)

Similarly to Sn, when In was alloyed with Cu the resultant Cu-In electrocatalysts were reported to be highly selective and stable toward CO at low overpotential, reaching FEs of around 90% for CO formation.[45,70] It was found that the presence of In increases the energy barrier to H adsorption but stabilizes the *COOH intermediate by 0.1 eV.[70] As with Sn, binding of *CO was relatively unchanged and the relative increase in stability of *COOH is likely responsible for the observed activity for CO production.

Group 3: Strong H Binding and Weak O Binding
Palladium (Pd)

Pd is identified as a group 3 metal and has been used extensively in the field of gas-phase heterogeneous catalysis.[71,72] Pd has little to no barrier toward H$_2$ adsorption

and readily forms the metal hydride (PdH_x),[73,74] which makes it a good candidate for catalyzing hydrogenation reactions. As dispersion of Pd atoms on Cu surfaces has been shown to significantly reduce the barrier to hydrogen adsorption, Pd-Cu alloy nanoparticles were employed as heterogeneous catalysts in the hydrogenation of CO_2.[75,76] It was proposed that the stronger binding of *H possibly facilitates this process and affects selectivity toward *COH/*CHO in the CO_2RR.[36] However, pure Pd mainly produces CO during the CO_2RR and only produces small amounts of CH_4, likely because hydride formation inhibits *CO binding.[11] For the Cu-Pd system, alloy composition and intermetallic arrangement were found to have significant effects on activity and selectivity. For example, it was found that Cu-Pd nanoparticles with regular intermetallic arrangements exhibited selective CO_2RR toward CO.[77,78] DFT calculations showed that on an ordered Pd-terminated Pd-Cu (111) surface, binding of *COOH was stronger than Pd (111), and *CO adsorption was significantly weakened. Interestingly, Pd is the active site in this system and the observed effects are the result of neighboring Cu atoms with higher O affinity. Another study explains that the electronic effect of charge transfer from Pd to Cu causes the weaker adsorption of *CO in the Cu-Pd system.[79]

According to d-band theory, a negative shift in the DOS away from the Fermi level normally results in weaker binding of adsorbates on a catalyst surfaces.[80] However, this does not encompass an example of phase-separated Cu-Pd nanoparticles.[81] Therefore, a comprehensive view of intermediate binding is required for catalyst design strategies beyond the d-band center theory. Expanding upon the above example, Cu-Pd bimetallic nanoparticles with various atomic mixing patterns (ordered, disordered, and phase separated) exhibited very different selectivities toward C1 and C2 products (Figures 5A–5C).[81] Specifically, for ordered Cu-Pd nanoparticles the FE toward C1 products (primarily CO) reached approximately 80%. However, for nanoparticles with distinct Cu and Pd phases (phase separated), C2 products (primarily C_2H_4) were selectively produced at an FE of >60%. The underlying reason for this may be that in the phase-separated system, the binding of *CO is less affected when the two sites are segregated. Therefore, Cu sites can facilitate C–C coupling, and co-adsorbed H on Pd sites can facilitate further reduction and hydrogenation of *CO.[75] More importantly, as mentioned above, phase-separated Cu-Pd had the lowest lying d-band center (shown in Figure 5D), and Cu nanoparticles had the highest. This would suggest that the former has the weakest binding and that the latter has the strongest binding of *CO. However, given the experimental results showing that the phase-separated Cu-Pd and Cu nanoparticles have similar catalytic selectivity and activity, geometric and structural effects probably played a more important role than electronic effects in determining catalytic performance among the various Cu-Pd samples.

Cu-Pd nanoparticles have also been applied as photocatalysts for selective CO_2 reduction to CH_4.[82] Nanoparticles with relatively low Cu concentration (Cu/Pd ratio of 1:7) achieved a selectivity toward CH_4 of 96% and effectively suppressed the HER (Figure 5E). The low concentration of Cu in this material was an important factor as it increased the number of isolated Cu atoms in the Pd lattice and, hence, the number of neighboring Cu-Pd sites. On this configuration, as shown in Figure 5F, the CO_2 adsorption energy was maximized at −0.46 eV, which is significantly stronger than on sites with adjacent Cu-Cu atoms (−0.31 eV).[82] Additionally, the Pd atoms had a significant electronic effect on the isolated Cu, causing an increase in their d-band centers and, hence, catalytic activity of the Cu active sites toward multi-electron pathways.
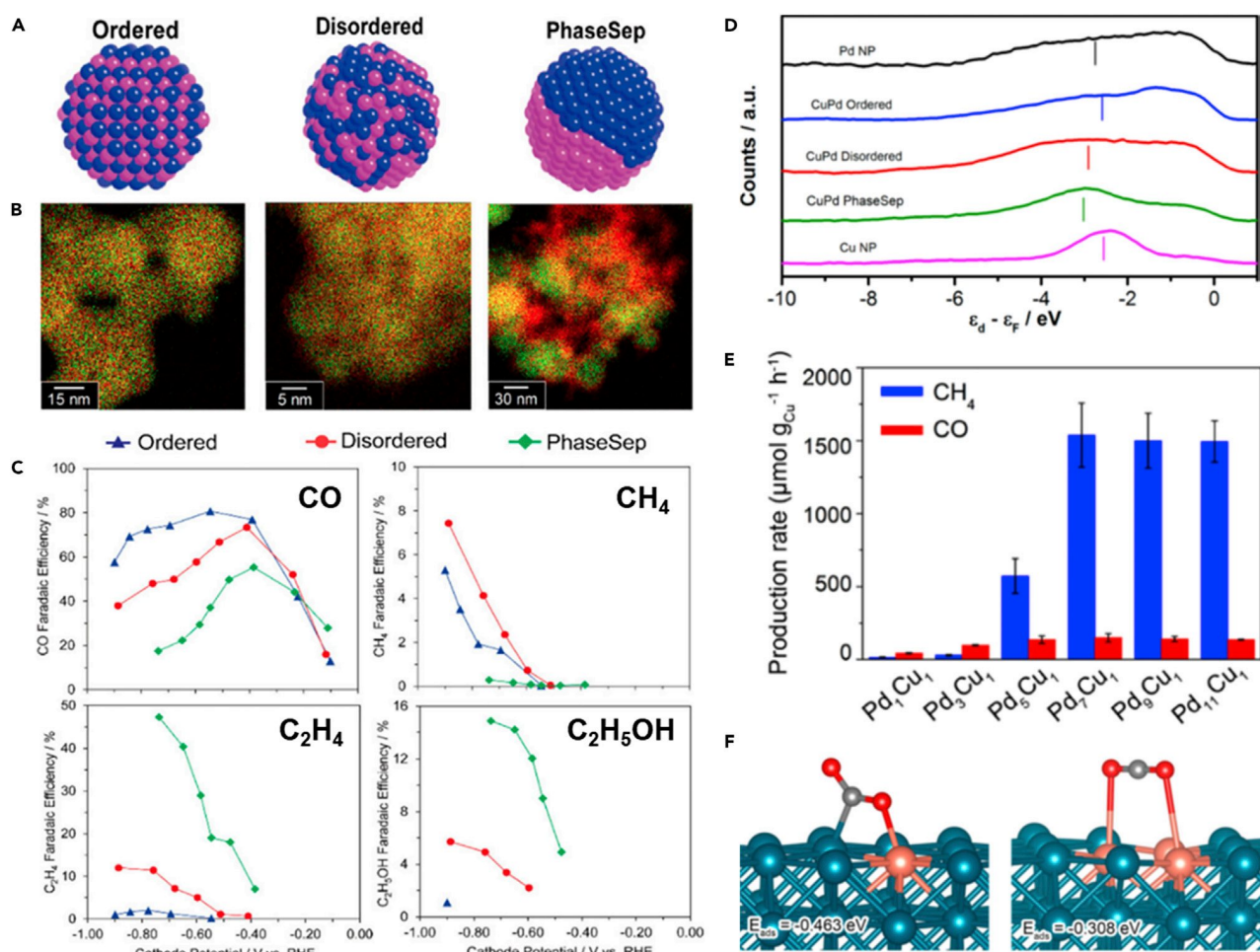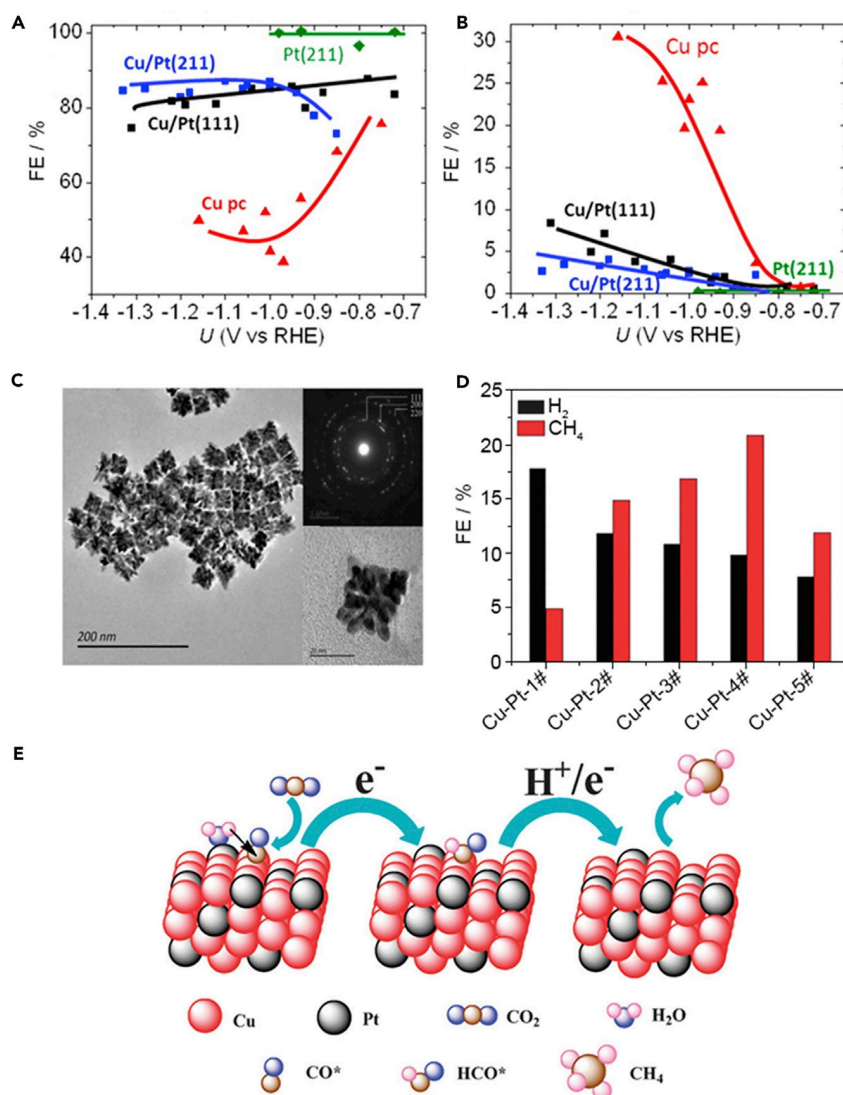
Figure 5. Characterization and Performance of Cu-Pd Catalysts for the CO₂RR

(A–D) Cu-Pd nanoalloys with different atomic mixing patterns (A); combined elemental maps of Cu (red) and Pd (green) (B); FEs for CO, CH₄, C₂H₄, and C₂H₅OH for bimetallic Cu-Pd catalysts with different mixing patterns (ordered [blue], disordered [red], and phase-separated [green]) (C); and background-corrected surface valence-band photoemission spectra of Cu-Pd nanoalloys relative to the Fermi level (the vertical line indicates the d-band center of each sample in relation to the Fermi level) (D). Adapted with permission from Ma et al.[81] Copyright 2017 American Chemical Society. (E and F) Average production rates of CH₄ and CO normalized by the amount of Cu atoms in the Cu-Pd catalysts 9E) and most favorable configurations and adsorption energies of CO₂ at an isolated Cu atom (Cu-Pd pair shown on the left), and two neighboring Cu atoms (Cu-Cu pair shown on the right) (F). Adapted with permission from Long et al.[82] Copyright 2017 American Chemical Society.

Group 4: Strong H Binding and Strong O Binding

Platinum (Pt)

Few examples of group 4 metals being coupled with Cu for CO₂RR electrocatalysts exist in the literature. This is most likely because of their high activity for the competing HER and poisoning by CO. In one study, Varela et al. fabricated Cu UPD layers on Pt (111) and Pt (211) surfaces to study the strain effect on Cu active sites for the CO₂RR.[83] In this study, hydrogen was the major product obtained on Cu/Pt(111) and Cu/Pt(211) samples, as shown in Figure 6A. However, it should be noted that the presence of *CO alters HER activity on the Cu/Pt interface. Specifically, Pt-containing systems are not likely to be stable and can result in Pt segregation because of the strong interaction between Pt and CO. This phenomenon would in turn promote the HER over the CO₂RR. Furthermore, none of the Cu-Pt catalysts could promote CH₄ production as effectively as polycrystalline Cu (Figure 6B). Therefore, this work suggested that the second metal in a Cu bimetallic catalyst

Figure 6. Characterization and Performance of Cu-Pt Catalysts for the CO₂RR

(A and B) FEs toward (A) H_2 and (B) CH_4 as a function of potential on different surfaces. Adapted with permission from Varela et al.[83] Copyright 2013 American Chemical Society.

(C–E) Low-magnification TEM image (scale bar, 200 nm) of the overall morphology of Cu-Pt (inset shows an FFT and high-magnification TEM image [scale bar, 20 nm] of a single Cu-Pt nanocrystal) (C), the FEs of H_2 and CH_4 on different Cu-Pt materials at −1.6 V (D), and a proposed mechanism illustrating the steps of CO_2 electroreduction and CH_4 formation occurring at the Cu-Pt (3:1) catalyst (E). Adapted from Guo et al.[84] with permission of the Royal Society of Chemistry.

should have a lower affinity for *CO. Another study demonstrated that Cu-Pt nano-crystals with controlled Cu/Pt atomic ratios performed with high FE for CH_4 (>20%; Figure 6C).[84] When the Pt content was high, the HER was dominant. With increased Cu content more adsorbed *CO was generated, thereby improving the production of CH_4. However, further increasing the Cu content subsequently led to a higher density of adsorbed *CO and, thus, lower density of adsorbed *H (Figure 6D). Consequently, the overall performance of the alloy was limited as less co-adsorbed H was available to partake in the reaction. On the basis of experimental results, investigation into the possible mechanism showed that increasing the Cu content

increased the surface coverage of *CO on active sites, and Pt facilitated their protonation to *CHO (Figure 6E). However, when insufficient Pt sites are present, *H generation is suppressed and hinders further reduction of *CO.

THEORETICAL PREDICTION

Pathway to CO Production

In recent years, significant advances in computational modeling have made the screening of potential catalysts for various electrochemical processes much easier, including for the CO_2RR.[14,85] Activity trends for a range of metal catalysts and their alloys have also been formulated with activity descriptors, presenting useful predictors for rational catalyst design.[12,33] These trends generally include descriptors based on the PDS of a reaction; for example, binding strength of the *CO intermediate has obvious influence on the rate of CO production. For precious metals such as Pt, although activation and conversion of CO_2 to CO occurs readily, *CO binding is so strong that desorption is the limiting factor and poisons the surface.[12] In contrast, for Au and Ag, which have very weak binding of *CO, experimental studies have shown that they are some of the most selective metals for CO_2 reduction to CO.[7,11,40,86] Furthermore, alloying Au with Cu (Cu having higher O affinity than Au) has shown to be beneficial for the binding strength of the *COOH intermediate, and hence the activity for CO production can be further increased. For example, compared with Au (111) surfaces, it was found that the free-energy change (ΔG) for *COOH formation (ΔG_{*COOH}) decreases on the alloy configurations (Figure 7A).[87] By constructing the Au nanostructures isolated on the Cu surface (Au-i@Cu), the ΔG_{*COOH} could be further reduced. In such configurations, the nanostructures increase the number of local under-coordinated sites, which have been shown to increase the binding of intermediates.[86,88] Additionally, corner Au sites adjacent to the Cu surface provide a bifunctional effect for the stabilization of the *COOH intermediate, whereby the high O affinity Cu atoms can stabilize the O end of *COOH (Figure 7B). A similar result was determined on A_3B alloy systems where A = Cu, Au, Ag and B = p-group metals.[33] First, it was found that scaling relationships between *COOH, *CO, and *CHO intermediates on the pure metals limit their activity for reduction of CO_2 to *CO and the reduction of *CO to *CHO and onward. Alloying may preferentially increase the interaction of active sites with *COOH or *CHO, resulting in preferential stabilization of these intermediates over *CO (Figure 7C). In this case, the C end of *COOH tends to bind to the A site, whereas the O end has significant interaction with the B site. As a result, the inherent scaling relationship may be broken. Therefore, an important design principle for alloy materials is the coupling of different metal sites that interact with C-bound and O-bound species differently.

Pathways Beyond CO

It is known that the hydrogenation of *CO to *CHO is generally the PDS in the CO_2RR pathway beyond CO. Therefore, destabilization of the *CO intermediate was found to be crucial in reducing the overpotential for the subsequent protonation steps.[32,33] When O-binding sites are created through alloying, *CO may be forced to bind in an unfavorable configuration, and therefore *CHO will be preferentially stabilized. For example, in the Cu-Ni system, C-bound species were generally found to be better stabilized on Ni (211) facets, whereas binding of O-bound intermediates was not changed significantly compared with Cu (211).[90] Therefore, the Cu_3Ni alloy reflected the difference in intermediate binding between the two parent metals. In a follow-up study, the ligand and strain effect on alloys of Cu with Ni and Rh were investigated.[91] In these systems, a significant reduction in overpotential was achieved on a Cu monolayer deposited on an expanded Ni (211) surface, resulting from the effect of expansive strain on the binding of *CO versus *CHO. For Rh overlayers on Cu, the
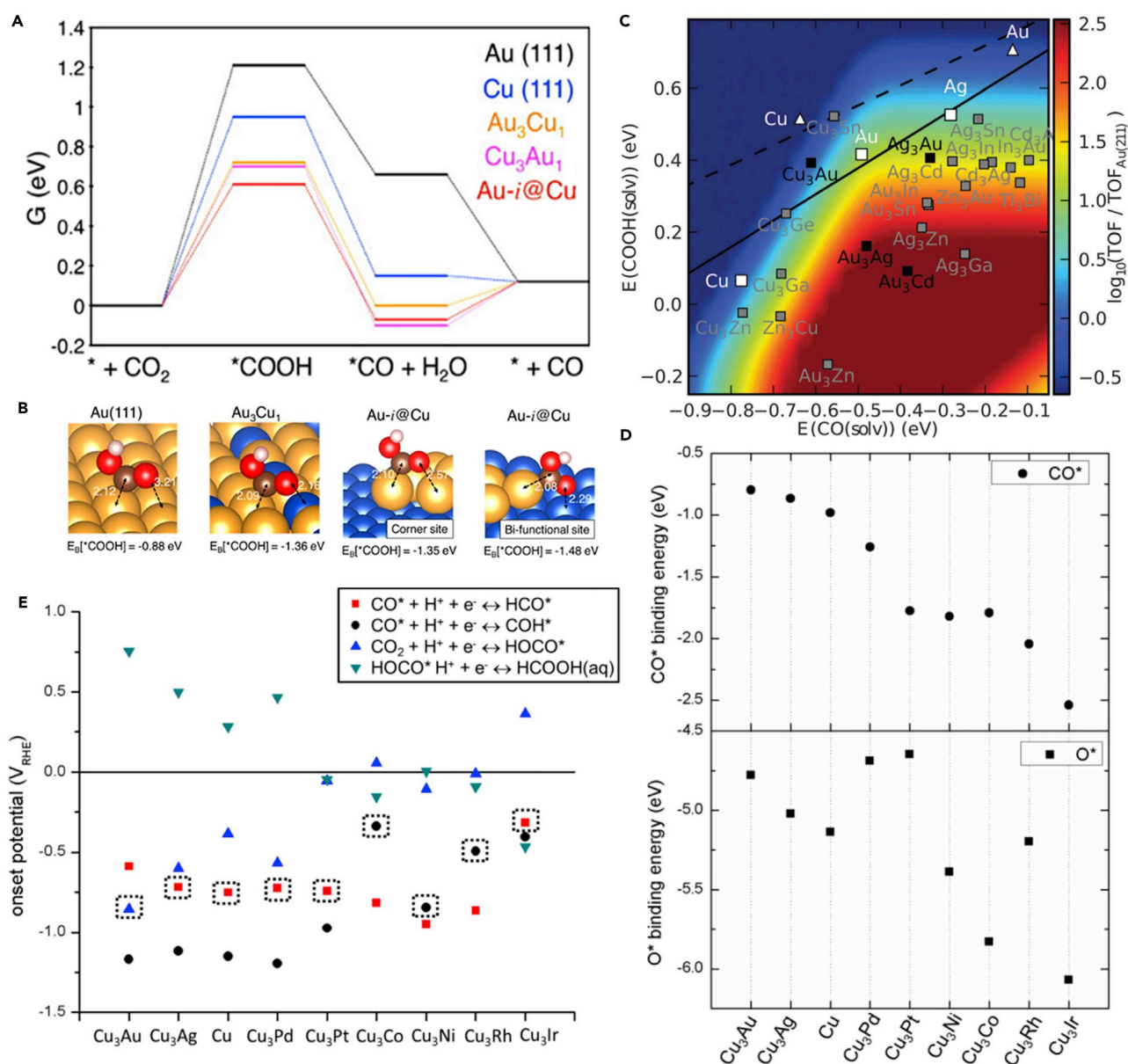
Figure 7. Computational Studies of Various Cu-Based Alloy Catalysts for the CO₂RR

(A and B) Free-energy diagrams for CO generation on various Cu-Au surfaces (A) and binding configurations of *COOH on Au(111), Au₃Cu₁(111), and a corner and bifunctional site of Au-i@Cu (yellow, blue, black, red, and white atoms indicate Au, Cu, C, O, and H, respectively) (B). Adapted with permission from Back et al.[87] Copyright 2016 American Chemical Society.

(C) Breaking the scaling relationship between *COOH and *CO on various alloy surfaces. Color bar indicates CO production on (211) steps normalized to the rate on Au(211). Alloys unstable against corrosion at 0 V versus RHE and pH 7 are shown in gray. Adapted from Hansen et al.[33] with permission of the Royal Society of Chemistry.

(D and E) *CO and *O binding energies on a range of Cu₃M alloy surfaces (D) and onset potentials of the CO₂, *COOH, and *CO protonation steps on a range of Cu₃M alloy surfaces (the dotted squares indicate the calculated limiting potential step) (E). Adapted with permission from Hirunsit et al.[89] Copyright 2015 American Chemical Society.

Cu was found to experience a tensile strain, which also led to a reduction in *CO binding, and consequently a reduction in the overpotential to CH₄ formation was achieved. In a comprehensive study, CO₂ reduction to CH₄ and CH₃OH on a range of Cu₃M (where M = Au, Ag, Pd, Pt, Ni, Co, Rh, and Ir) alloy surfaces was predicted by

DFT modeling.[89] Generally on these alloys, CH_4 generation was found to be more favorable compared with pure Cu, except for Cu_3Pd and Cu_3Pt, which favored a pathway to CH_3OH. Additionally, the protonation of CO* to HCO* or COH* was the PDS on most surfaces. Of note here, binding of *CO, *O, and *H species was analyzed in detail to reveal the inherent trend of the various surfaces. It was found that *CO and *O binding on the alloy surfaces exhibits a general trend similar to that of the pure secondary metal surfaces. For example, alloying Cu with metals that have weaker O* adsorption than Cu (Ag, Au, Pd, and Pt) continue to have relatively weaker O* adsorption, and vice versa, for the metals with stronger *O adsorption (Ni, Co, Rh, and Ir; Figure 7D). This principle is important for the design of Cu-based bimetallic catalysts from both fundamental and functional perspectives. As shown in Figure 7E, the overpotentials on Cu_3Co, Cu_3Rh, and Cu_3Ir surfaces are lower than that on pure Cu, whereas those on Cu_3Ag, Cu_3Pd, and Cu_3Pt surfaces are similar to that on Cu with the same PDS. Additionally, all Cu_3M alloys increased the binding strength of both *CO and *H, except for Au and Ag. Interestingly, these calculations reveal that the activity on Cu-based alloy catalysts does not show a volcano-type relation as was previously found on pure metal catalysts.

GENERAL TRENDS

On the basis of the above examples, it has been shown that by coupling different metals together, the catalyst surface or interface can be engineered to contain multiple sites that contribute to the binding of key reaction intermediates. We posit that the O and H affinities of these secondary sites are significant in this regard, and rational design strategies can be developed by understanding how they affect intermediate binding during the CO_2RR. Despite the effects of the secondary metal sites, different experimental conditions may also affect CO_2RR activity and selectivity, and these considerations have been investigated in recent studies.[92–94] Therefore, a summary of the Cu-based bimetallic catalysts presented in this review along with their reaction conditions are presented in Table 1 for comparison. In our analysis, we found that when group 1 metals (M_1) are the dominant metal in $Cu-M_1$ systems, CO is the major product formed and FE is generally better than that of the parent metals.[46,54,59,62] This is most likely because the higher O affinity of Cu increases *COOH stabilization, whereas the weak *CO-binding ability of M_1 metals assists in CO product desorption. Furthermore, the weak H binding also suppresses the HER, which increases the selectivity toward the CO_2RR overall. For group 2 metals (M_2), the apparent trend shows that the selectivity toward $2e^-$ products is favored in $Cu-M_2$ systems; pathways beyond CO are also most likely suppressed because of weak H binding. When M_2 provides the dominant contribution to the active sites, it is found that HCOOH is the major reduction product.[66,68,69] As the result of an increased number of available O-binding sites, *OCHO may be better stabilized and a pathway to HCOOH through this intermediate may be favored in these systems.[15] However, when M_2 provides a moderate contribution in these systems, CO is generally produced at very high FE.[45,67,68,70] By introducing these O-binding sites next to Cu active sites, it is likely that *COOH is better stabilized than *CO, reducing the barrier to CO formation. Limited studies exist on coupling group 3 metals (M_3; Pd specifically) with Cu, in which the intermetallic arrangement of these materials had a significant impact on the product selectivity. When the metallic arrangement was more regular, CO was the major product and was produced with high FE.[77,81] As with $Cu-M_1$ systems, it is possible that the higher O affinity of the Cu sites increases *COOH stabilization and reduces the barrier to CO formation. For phase-separated Cu-Pd nanoparticles, C2 products were selectively produced

Table 1. Performance Summary of Recent Reports on Cu-M Alloy and Bimetallic Materials

		Catalyst	Electrolyte	Applied Potential	Highlighted Products with FE	Reference
Group 1	Au	Cu@Au	0.5 M KHCO$_3$	−0.65 V versus RHE	CO (∼30%)	Chen et al.[58]
		Au$_{50}$Cu$_{50}$	PBS	−1.9 V versus Ag/AgCl	carbon-containing products (20% ± 5%)	Christophe et al.[52]
		Cu$_{63.9}$Au$_{36.1}$/NCF	0.5 M KHCO$_3$	−1.1 V versus SCE	CH$_3$OH (15.9%), C$_2$H$_5$OH (12%)	Jia et al.[53]
		Au$_3$Cu	0.1 M KHCO$_3$	−0.73 V versus RHE	CO (∼65%), HCOO$^-$ (∼3%)	Kim et al.[46]
		o-AuCu	0.1 M KHCO$_3$	−0.77 V versus RHE	CO (∼80%)	Kim et al.[54]
		Au@Cu1 Au@Cu3	PBS	−0.6 V versus RHE	C$_2$H$_4$ (distribution ∼20%) CH$_4$ (distribution ∼20%)	Monzo et al.[56]
		1/3 Cu UPD Au	0.1 M KHCO$_3$	−0.55 V versus RHE	CO (∼75%)	Ross et al.[55]
		Au$_3$Cu alloy nanocrystals	0.1 M PBS	−1.6 V versus Ag/AgCl	CH$_4$ (∼35%), CO (∼25%), HCOO$^-$ (∼8%)	Zhao et al.[95]
	Ag	Ag@Cu-7 Ag@Cu-20	0.1 M KHCO$_3$	−1.06 V versus RHE	CO (82%) C$_2$H$_4$ (28.6%)	Chang et al.[59]
		Ag$_{57}$Cu$_{43}$	0.5 M KHCO$_3$	−1.5 V versus SCE	CO (∼40%)	Choi et al.[60]
		CuAg surface alloys	0.05 M Cs$_2$CO$_3$		CO dominant (low at % Cu) H$_2$ and C$_2$H$_4$ dominant (high at % Cu)	Clark et al.[62]
		Nanocoral Cu-Ag	0.2 M CsHCO$_3$	−1.0 V versus RHE	C$_2$H$_4$ (20%), H$_2$ (30%–35%)	Gurudayal et al.[61]
	Zn	Oxide-derived Cu$_4$Zn	0.1 M KHCO$_3$	−1.05 V versus RHE	C$_2$H$_5$OH (29.1%), C$_2$H$_4$ (∼10%)	Ren et al.[63]
	Cd	Cu modified with Cd	0.1 M KHCO$_3$	∼−1.66 V versus SHE ∼−1.62 V versus SHE	CO (∼60%) CH$_4$ (∼40%)	Hori et al.[64]
Group 2	Sn	Cu@SnO$_2$-0.8 Cu@SnO$_2$-1.8	0.5 M KHCO$_3$	−0.7 V versus RHE −0.9 V versus RHE	CO (93%) HCOO$^-$ (85%)	Li et al.[68]
		Sn-electrodeposited OD-Cu	0.1 M KHCO$_3$	−0.6 V versus RHE	CO (>∼90%)	Sarfraz et al.[67]
		Cu$_{87}$Sn$_{13}$ Cu$_{55}$Sn$_{45}$	0.1 M KHCO$_3$	−0.99 V versus RHE −1.09 V versus RHE	CO (60%) HCOO$^-$ (89.5%)	Morimoto et al.[66]
	In	Cu-In alloy	0.1 M KHCO$_3$	−0.5 V versus RHE	CO (90%)	Rasul et al.[70]
Group 3	Pd	Pd-decorated Cu	0.5 M KHCO$_3$	−0.96 V versus RHE	CH$_4$ (46%–40%), C$_2$H$_4$ (7–11%)	Weng et al.[96]
		Disordered CuPd	1 M KOH	−0.89 V versus RHE	CH$_4$ (∼7.5%)	Ma et al.[81]
		PhaseSep CuPd	1 M KOH	−0.74 V versus RHE	C2 chemicals (∼65%)	Ma et al.[81]
		CuPd$_3$	1 M KOH	−0.55 V versus RHE	CO (∼90%)	Ma et al.[81]
		Pd$_7$Cu$_3$	0.1 M KHCO$_3$	−0.8 V versus RHE	CO (∼80%)	Li et al.[77]
		Pd$_7$Cu$_3$	0.1 M KHCO$_3$	Bias −1.2 V	CO (∼75%)	Li et al.[78]
		CuPd nanoalloy (Cu$_2$Pd)	0.1 M KHCO$_3$	−1.8 V versus Ag/AgNO$_3$	CH$_4$ (∼51%)	Zhang et al.[97]
		Cu$_2$O-derived Cu with PdCl$_2$	0.1 M KHCO$_3$	−1.0 V versus RHE	C$_2$H$_6$ (30.1%), C$_2$H$_4$ (3.4%)	Chen et al.[98]
Group 4	Pt	Cu-Pt (at. 3:1) nanocrystal	0.5 M KHCO$_3$	−1.6 V versus SCE	CH$_4$ (21%)	Guo et al.[84]
		Cu/Pt(111)	0.1 M KHCO$_3$	−1.3 V versus RHE	CH$_4$ (∼7.5%)	Varela et al.[83]
	Ni	Cu-electrodeposited Ni	0.5 M KHCO$_3$ water/MeOH solution	−1.9 V versus Ag QRE	CH$_4$ (20.2%), C$_2$H$_4$ (7.5%)	Kaneco et al.[99]

QRE, quasi-reference electrode; RHE, reversible hydrogen electrode; SCE, saturated calomel electrode.

because the neighboring Cu sites most likely facilitate C–C coupling, whereas spillover of H from Pd sites facilitates hydrogenation.[75] Fewer examples of group 4 metals (M$_4$) being coupled with Cu exist in the literature. Although M$_4$ metals with high CO affinity should be avoided, it is interesting that these materials can produce hydrocarbons at relatively high FE.

Chem

CellPress
REVIEWS

CONCLUSION AND OUTLOOK

Design and fabrication of selective Cu-based CO_2RR electrocatalysts, especially ones selective for hydrocarbon production, remains a difficult task because of the relatively strong binding of the *CO intermediate during reaction. Surface and interface engineering through coupling Cu with a secondary metal has shown to be a successful initial strategy for reducing the reaction energy barrier to increase its activity. It has also shown to be successful in breaking the scaling relationship that exists between *COOH, *CO, and *CHO/*COH to improve the selectivity of Cu. Here, we have reviewed recent examples of Cu-based alloy and bimetallic materials and how the O and H affinities of the secondary metal affect selectivity. Overall, many examples show that the selectivity for CO/HCOOH and hydrocarbons and alcohols in Cu-M systems can be rationally tuned by modifying O- and/or H-adsorbing sites on the surface. The relationship between an alloy's chemical composition and its CO_2RR activity and selectivity are systematically linked to its intrinsic intermediate binding energies. Along with some general trends, possible design strategies for future CO_2RR electrocatalysts are provided.

The ultimate goal in this field is to design catalysts selective for deep reduction products with high energy density. Therefore, it is crucial that the catalyst design address the inherent scaling between *CO and *CHO intermediates. In some cases, it has been shown that the electronic characteristics of both parent metals are relatively preserved after alloying.[87] For these systems, the binding behavior of the pure metals can be used to predict intermediate binding on the resultant material. Therefore, one such strategy that could be implemented is the limited growth or metal doping of a secondary metal on a Cu surface. This could be achieved by constructing single-metal atom catalysts (SMACs) supported on a Cu substrate. M_3 or M_4 SMAC sites can facilitate hydrogenation of *CO to deeper products while limiting the HER. Additionally, bimetallic dimers of Cu and a secondary metal could exhibit strong interfacial coupling, which could enhance the selectivity for hydrocarbons as has been shown theoretically for M_4 metals.[100] Although Cu-M_3 alloys have shown the best performance toward hydrocarbon production, limited studies exist for these cases. Therefore, more group 3 metals should be identified and studied. Further, ternary alloys with Cu should be explored given that combining specific O-adsorbing and H-adsorbing (i.e., M_2 and M_3) sites next to Cu could also prove beneficial for stabilizing and hydrogenating *CO to deeper products. In all these strategies, greater effort should also be focused on exposing more under-coordinated sites, e.g., steps and corner sites, to maximize the interfacial coupling of different active sites in these materials for optimized binding of intermediates.

To this end, we have provided a general view of the role that O-binding and H-binding sites play at the interface, as well as how they affect the binding of reaction intermediates. Nevertheless, a more profound basis for intermediate energetics is still required. From a theoretical perspective, computational electrochemistry remains the most direct and powerful tool to reveal the microscopic picture of the CO_2RR on different catalyst surfaces. For example, it was identified by computations that the first protonation step (i.e., CO_2 to *COOH) is the step that determines CO_2 activation in the CO_2RR pathway, whereas the second protonation step (i.e., *CO to *COH or *CHO) dominates the selectivity toward different products. Furthermore, electronic structure computation can reveal and direct the subatomic-level and atomic-level tuning of catalyst surfaces. Additionally, the effects of steps, terraces, islands, and single atom morphologies toward the CO_2RR can be visualized directly through computations. However, models used in DFT calculations are normally

constrained to ideal and flat repeating units (this is natural when periodic boundary conditions are adopted). On some catalyst surfaces, it remains a challenge to effectively identify the real active site(s) because of the complexity involved in materials that contain multiple structural features. In some cases, the opposite trend was found to occur on the actual alloy material, whereby instability of the surface can lead to morphological changes during reaction conditions.[30] Therefore, the chemical composition and physical structure stabilities of bimetallic catalysts is a significant consideration and should also be experimentally studied both during and after the CO_2RR process (e.g., surface segregation might be an issue). In the future, more advanced calculations, including high-throughput computation and machine-learning techniques, could be adopted to produce more representative models of these complex catalyst surfaces. Coupled with experimental studies, a route to rational design strategies for CO_2RR electrocatalysts appears possible. The concepts proposed in this review related to O and H affinities are also very general and could be extended to other catalytic processes involving multiple reaction intermediates. Therefore, this general guidance could be adopted for the design of electrocatalysts and heterogeneous catalysts for the ORR, alkaline HER, CO_2 hydrogenation, and so forth.

AUTHOR CONTRIBUTIONS

All authors devised the concept and built the framework of the review. A.V. and C. X. wrote the manuscript and organized the figures. Y.J., Y.Z., and S.-Z.Q. edited and reviewed the manuscript.

REFERENCES AND NOTES

1. Liu, J.L., Guo, C.X., Vasileff, A., and Qiao, S.Z. (2017). Nanostructured 2D materials: prospective catalysts for electrochemical CO_2 reduction. Small Methods 1, 1600006.

2. Wang, Y., Liu, J., Wang, Y., Al-Enizi, A.M., and Zheng, G. (2017). Tuning of CO_2 reduction selectivity on metal electrocatalysts. Small 13, 1701809.

3. Zhang, W., Hu, Y., Ma, L., Zhu, G., Wang, Y., Xue, X., Chen, R., Yang, S., and Jin, Z. (2017). Progress and perspective of electrocatalytic CO_2 reduction for renewable carbonaceous fuels and chemicals. Adv. Sci. 5, 1700275.

4. Zhu, D.D., Liu, J.L., and Qiao, S.Z. (2016). Recent advances in inorganic heterogeneous electrocatalysts for reduction of carbon dioxide. Adv. Mater. 28, 3423–3452.

5. Vasileff, A., Zheng, Y., and Qiao, S.Z. (2017). Carbon solving carbon's problems: recent progress of nanostructured carbon-based catalysts for the electrochemical reduction of CO_2. Adv. Energy Mater. 7, 1700759.

6. Bagger, A., Ju, W., Varela, A.S., Strasser, P., and Rossmeisl, J. (2017). Electrochemical CO_2 reduction: a classification problem. ChemPhysChem 18, 3266–3273.

7. Hori, Y., Wakebe, H., Tsukamoto, T., and Koga, O. (1994). Electrocatalytic process of CO selectivity in electrochemical reduction of CO_2 at metal electrodes in aqueous media. Electrochim. Acta 39, 1833–1839.

8. Kuhl, K.P., Cave, E.R., Abram, D.N., and Jaramillo, T.F. (2012). New insights into the electrochemical reduction of carbon dioxide on metallic copper surfaces. Energy Environ. Sci. 5, 7050–7059.

9. Kim, D., Kley, C.S., Li, Y., and Yang, P. (2017). Copper nanoparticle ensembles for selective electroreduction of CO_2 to C_2-C_3 products. Proc. Natl. Acad. Sci. USA 114, 10560–10565.

10. Hori, Y., Takahashi, R., Yoshinami, Y., and Murata, A. (1997). Electrochemical reduction of CO at a copper electrode. J. Phys. Chem. B 101, 7075–7081.

11. Peterson, A.A., and Norskov, J.K. (2012). Activity descriptors for CO_2 electroreduction to methane on transition-metal catalysts. J. Phys. Chem. Lett. 3, 251–258.

12. Hansen, H.A., Varley, J.B., Peterson, A.A., and Norskov, J.K. (2013). Understanding trends in the electrocatalytic activity of metals and enzymes for CO_2 reduction to CO. J. Phys. Chem. Lett. 4, 388–392.

13. Norskov, J.K., Abild-Pedersen, F., Studt, F., and Bligaard, T. (2011). Density functional theory in surface chemistry and catalysis. Proc. Natl. Acad. Sci. USA 108, 937–943.

14. Greeley, J., Jaramillo, T.F., Bonde, J., Chorkendorff, I.B., and Norskov, J.K. (2006). Computational high-throughput screening of electrocatalytic materials for hydrogen evolution. Nat. Mater. 5, 909–913.

15. Feaster, J.T., Shi, C., Cave, E.R., Hatsukade, T., Abram, D.N., Kuhl, K.P., Hahn, C., Nørskov, J.K., and Jaramillo, T.F. (2017). Understanding selectivity for the electrochemical reduction of carbon dioxide to formic acid and carbon monoxide on metal electrodes. ACS Catal. 7, 4822–4827.

16. Jones, J.P., Prakash, G.K.S., and Olah, G.A. (2014). Electrochemical CO_2 reduction: recent advances and current trends. Isr. J. Chem. 54, 1451–1466.

17. Hori, Y., Kikuchi, K., and Suzuki, S. (1985). Production of CO and CH_4 in electrochemical reduction of CO_2 at metal electrodes in aqueous hydrogen carbonate solution. Chem. Lett. 14, 1695–1698.

18. Hori, Y. (2016). CO_2 reduction using electrochemical approach. In Solar to

Chemical Energy Conversion, M. Sugiyama, K. Fujii, and S. Nakamura, eds. (Springer International Publishing), pp. 191–211.

19. Kuhl, K.P., Hatsukade, T., Cave, E.R., Abram, D.N., Kibsgaard, J., and Jaramillo, T.F. (2014). Electrocatalytic conversion of carbon dioxide to methane and methanol on transition metal surfaces. J. Am. Chem. Soc. *136*, 14107–14113.

20. Zheng, Y., Jiao, Y., Jaroniec, M., and Qiao, S.Z. (2015). Advancing the electrochemistry of the hydrogen-evolution reaction through combining experiment and theory. Angew. Chem. Int. Ed. *54*, 52–65.

21. Lv, H.F., Li, D.G., Strmcnik, D., Paulikas, A.P., Markovic, N.M., and Stamenkovic, V.R. (2016). Recent advances in the design of tailored nanomaterials for efficient oxygen reduction reaction. Nano Energy *29*, 149–165.

22. Nie, Y., Li, L., and Wei, Z. (2015). Recent advancements in Pt and Pt-free catalysts for oxygen reduction reaction. Chem. Soc. Rev. *44*, 2168–2201.

23. Shao, M., Chang, Q., Dodelet, J.P., and Chenitz, R. (2016). Recent advances in electrocatalysts for oxygen reduction reaction. Chem. Rev. *116*, 3594–3657.

24. Huang, X.Q., Zhao, Z.P., Cao, L., Chen, Y., Zhu, E.B., Lin, Z.Y., Li, M.F., Yan, A.M., Zettl, A., Wang, Y.M., et al. (2015). High-performance transition metal-doped Pt_3Ni octahedra for oxygen reduction reaction. Science *348*, 1230–1234.

25. Stamenkovic, V.R., Fowler, B., Mun, B.S., Wang, G., Ross, P.N., Lucas, C.A., and Markovic, N.M. (2007). Improved oxygen reduction activity on $Pt_3Ni(111)$ via increased surface site availability. Science *315*, 493–497.

26. Hori, Y., Takahashi, I., Koga, O., and Hoshi, N. (2002). Selective formation of C2 compounds from electrochemical reduction of CO_2 at a series of copper single crystal electrodes. J. Phys. Chem. B *106*, 15–17.

27. Hori, Y., Kikuchi, K., Murata, A., and Suzuki, S. (1986). Production of methane and ethylene in electrochemical reduction of carbon dioxide at copper electrode in aqueous hydrogen carbonate solution. Chem. Lett. *15*, 897–898.

28. Schouten, K.J.P., Kwon, Y., van der Ham, C.J.M., Qin, Z., and Koper, M.T.M. (2011). A new mechanism for the selectivity to C_1 and C_2 species in the electrochemical reduction of carbon dioxide on copper electrodes. Chem. Sci. *2*, 1902–1909.

29. Hori, Y., Murata, A., and Takahashi, R. (1989). Formation of hydrocarbons in the electrochemical reduction of carbon dioxide at a copper electrode in aqueous solution. J. Chem. Soc. Faraday Trans. 1 *85*, 2309–2326.

30. Jovanov, Z.P., Hansen, H.A., Varela, A.S., Malacrida, P., Peterson, A.A., Norskov, J.K., Stephens, I.E.L., and Chorkendorff, I. (2016). Opportunities and challenges in the electrocatalysis of CO_2 and CO reduction using bifunctional surfaces: a theoretical and experimental study of Au-Cd alloys. J. Catal. *343*, 215–231.

31. Hashiba, H., Sato, H.K., Yotsuhashi, S., Fujii, K., Sugiyama, M., and Nakano, Y. (2017). A broad parameter range for selective methane production with bicarbonate solution in electrochemical CO_2 reduction. Sustain. Energy Fuels *1*, 1734–1739.

32. Durand, W.J., Peterson, A.A., Studt, F., Abild-Pedersen, F., and Norskov, J.K. (2011). Structure effects on the energetics of the electrochemical reduction of CO_2 by copper surfaces. Surf. Sci. *605*, 1354–1359.

33. Hansen, H.A., Shi, C., Lausche, A.C., Peterson, A.A., and Norskov, J.K. (2016). Bifunctional alloys for the electroreduction of CO_2 and CO. Phys. Chem. Chem. Phys. *18*, 9194–9201.

34. Peterson, A.A., Abild-Pedersen, F., Studt, F., Rossmeisl, J., and Norskov, J.K. (2010). How copper catalyzes the electroreduction of carbon dioxide into hydrocarbon fuels. Energy Environ. Sci. *3*, 1311–1315.

35. Nie, X., Esopi, M.R., Janik, M.J., and Asthagiri, A. (2013). Selectivity of CO_2 reduction on copper electrodes: the role of the kinetics of elementary steps. Angew. Chem. Int. Ed. *52*, 2459–2462.

36. Nie, X.W., Luo, W.J., Janik, M.J., and Asthagiri, A. (2014). Reaction mechanisms of CO_2 electrochemical reduction on Cu(111) determined with density functional theory. J. Catal. *312*, 108–122.

37. Ulissi, Z.W., Tang, M.T., Xiao, J.P., Liu, X.Y., Torelli, D.A., Karamad, M., Cummins, K., Hahn, C., Lewis, N.S., Jaramillo, T.F., et al. (2017). Machine-learning methods enable exhaustive searches for active bimetallic facets and reveal active site motifs for CO_2 reduction. ACS Catal. *7*, 6600–6608.

38. Abild-Pedersen, F., Greeley, J., Studt, F., Rossmeisl, J., Munter, T.R., Moses, P.G., Skulason, E., Bligaard, T., and Norskov, J.K. (2007). Scaling properties of adsorption energies for hydrogen-containing molecules on transition-metal surfaces. Phys. Rev. Lett. *99*, 016105.

39. Li, Y.W., and Sun, Q. (2016). Recent advances in breaking scaling relations for effective electrochemical conversion of CO_2. Adv. Energy Mater. *6*, 1600463.

40. Zhu, W., Michalsky, R., Metin, O., Lv, H., Guo, S., Wright, C.J., Sun, X., Peterson, A.A., and Sun, S. (2013). Monodisperse Au nanoparticles for selective electrocatalytic reduction of CO_2 to CO. J. Am. Chem. Soc. *135*, 16833–16836.

41. Dutta, A., Rahaman, M., Luedi, N.C., and Broekmann, P. (2016). Morphology matters: tuning the product distribution of CO_2 electroreduction on oxide-derived Cu foam catalysts. ACS Catal. *6*, 3804–3814.

42. Raciti, D., Livi, K.J., and Wang, C. (2015). Highly dense Cu nanowires for low-overpotential CO_2 reduction. Nano Lett. *15*, 6829–6835.

43. Sen, S., Liu, D., and Palmore, G.T.R. (2014). Electrochemical reduction of CO_2 at copper nanofoams. ACS Catal. *4*, 3091–3095.

44. Wang, Z.L., Li, C.L., and Yamauchi, Y. (2016). Nanostructured nonprecious metal catalysts for electrochemical reduction of carbon dioxide. Nano Today *11*, 373–391.

45. He, J., Dettelbach, K.E., Salvatore, D.A., Li, T., and Berlinguette, C.P. (2017). High-throughput synthesis of mixed-metal electrocatalysts for CO_2 reduction. Angew. Chem. Int. Ed. *56*, 6068–6072.

46. Kim, D., Resasco, J., Yu, Y., Asiri, A.M., and Yang, P. (2014). Synergistic geometric and electronic effects for electrochemical reduction of carbon dioxide using gold-copper bimetallic nanoparticles. Nat. Commun. *5*, 4948.

47. Jiao, Y., Zheng, Y., Chen, P., Jaroniec, M., and Qiao, S.Z. (2017). Molecular scaffolding strategy with synergistic active centers to facilitate electrocatalytic CO_2 reduction to hydrocarbon/alcohol. J. Am. Chem. Soc. *139*, 18093–18100.

48. Norskov, J.K., Bligaard, T., Logadottir, A., Kitchin, J.R., Chen, J.G., Pandelov, S., and Norskov, J.K. (2005). Trends in the exchange current for hydrogen evolution. J. Electrochem. Soc. *152*, J23–J26.

49. Greeley, J., Stephens, I.E.L., Bondarenko, A.S., Johansson, T.P., Hansen, H.A., Jaramillo, T.F., Rossmeisl, J., Chorkendorff, I., and Nørskov, J.K. (2009). Alloys of platinum and early transition metals as oxygen reduction electrocatalysts. Nat. Chem. *1*, 552.

50. Trasatti, S. (1972). Work function, electronegativity, and electrochemical behaviour of metals: III. Electrolytic hydrogen evolution in acid solutions. J. Electroanal. Chem. *39*, 163–184.

51. Kepp, K.P. (2016). A quantitative scale of oxophilicity and thiophilicity. Inorg. Chem. *55*, 9461–9470.

52. Christophe, J., Doneux, T., and Buess-Herman, C. (2012). Electroreduction of carbon dioxide on copper-based electrodes: activity of copper single crystals and copper-gold alloys. Electrocatalysis *3*, 139–146.

53. Jia, F.L., Yu, X.X., and Zhang, L.Z. (2014). Enhanced selectivity for the electrochemical reduction of CO_2 to alcohols in aqueous solution with nanostructured Cu-Au alloy as catalyst. J. Power Sources *252*, 85–89.

54. Kim, D., Xie, C., Becknell, N., Yu, Y., Karamad, M., Chan, K., Crumlin, E.J., Norskov, J.K., and Yang, P. (2017). Electrochemical activation of CO_2 through atomic ordering transformations of AuCu nanoparticles. J. Am. Chem. Soc. *139*, 8329–8336.

55. Ross, M.B., Dinh, C.T., Li, Y., Kim, D., De Luna, P., Sargent, E.H., and Yang, P. (2017). Tunable Cu enrichment enables designer syngas electrosynthesis from CO_2. J. Am. Chem. Soc. *139*, 9359–9363.

56. Monzo, J., Malewski, Y., Kortlever, R., Vidal-Iglesias, F.J., Solla-Gullon, J., Koper, M.T.M., and Rodriguez, P. (2015). Enhanced electrocatalytic activity of Au@Cu core@shell nanoparticles towards CO2 reduction. J. Mater. Chem. A *3*, 23690–23698.

57. Shi, C., Hansen, H.A., Lausche, A.C., and Norskov, J.K. (2014). Trends in electrochemical CO_2 reduction activity for

open and close-packed metal surfaces. Phys. Chem. Chem. Phys. 16, 4720–4727.

58. Chen, K., Zhang, X., Williams, T., Bourgeois, L., and MacFarlane, D.R. (2017). Electrochemical reduction of CO_2 on core-shell Cu/Au nanostructure arrays for syngas production. Electrochim. Acta 239, 84–89.

59. Chang, Z.Y., Huo, S.J., Zhang, W., Fang, J.H., and Wang, H.L. (2017). The tunable and highly selective reduction products on Ag@Cu bimetallic catalysts toward CO_2 electrochemical reduction reaction. J. Phys. Chem. C 121, 11368–11379.

60. Choi, J., Kim, M.J., Ahn, S.H., Choi, I., Jang, J.H., Ham, Y.S., Kim, J.J., and Kim, S.-K. (2016). Electrochemical CO_2 reduction to CO on dendritic Ag-Cu electrocatalysts prepared by electrodeposition. Chem. Eng. J. 299, 37–44.

61. Gurudayal, Bullock, J., Sranko, D.F., Towle, C.M., Lum, Y.W., Hettick, M., Scott, M.C., Javey, A., and Ager, J. (2017). Efficient solar-driven electrochemical CO_2 reduction to hydrocarbons and oxygenates. Energy Environ. Sci. 10, 2222–2230.

62. Clark, E.L., Hahn, C., Jaramillo, T.F., and Bell, A.T. (2017). Electrochemical CO_2 reduction over compressively strained CuAg surface alloys with enhanced multi-carbon oxygenate selectivity. J. Am. Chem. Soc. 139, 15848–15857.

63. Ren, D., Ang, B.S.H., and Yeo, B.S. (2016). Tuning the selectivity of carbon dioxide electroreduction toward ethanol on oxide-derived Cu_xZn catalysts. ACS Catal. 6, 8239–8247.

64. Hori, Y., Murata, A., and Ito, S.-Y. (1990). Enhanced evolution of CO and suppressed formation of hydrocarbons in electroreduction of CO_2 at a copper electrode modified with cadmium. Chem. Lett. 19, 1231–1234.

65. Lv, W., Zhang, R., Gao, P., and Lei, L. (2014). Studies on the faradaic efficiency for electrochemical reduction of carbon dioxide to formate on tin electrode. J. Power Sources 253, 276–281.

66. Morimoto, M., Takatsuji, Y., Yamasaki, R., Hashimoto, H., Nakata, I., Sakakura, T., and Haruyama, T. (2017). Electrodeposited Cu-Sn alloy for electrochemical CO_2 reduction to $CO/HCOO^-$. Electrocatalysis 8, 1–10.

67. Sarfraz, S., Garcia-Esparza, A.T., Jedidi, A., Cavallo, L., and Takanabe, K. (2016). Cu-Sn bimetallic catalyst for selective aqueous electroreduction of CO_2 to CO. ACS Catal. 6, 2842–2851.

68. Li, Q., Fu, J., Zhu, W., Chen, Z., Shen, B., Wu, L., Xi, Z., Wang, T., Lu, G., Zhu, J.J., and Sun, S. (2017). Tuning Sn-catalysis for electrochemical reduction of CO_2 to CO via the core/shell Cu/SnO_2 structure. J. Am. Chem. Soc. 139, 4290–4293.

69. Schreier, M., Heroguel, F., Steier, L., Ahmad, S., Luterbacher, J.S., Mayer, M.T., Luo, J.S., and Gratzel, M. (2017). Solar conversion of CO_2 to CO using Earth-abundant electrocatalysts prepared by atomic layer modification of CuO. Nat. Energy 2, 17087.

70. Rasul, S., Anjum, D.H., Jedidi, A., Minenkov, Y., Cavallo, L., and Takanabe, K. (2015). A highly selective copper-indium bimetallic electrocatalyst for the electrochemical reduction of aqueous CO_2 to CO. Angew. Chem. Int. Ed. 54, 2146–2150.

71. Martin, R., and Buchwald, S.L. (2008). Palladium-catalyzed Suzuki-Miyaura cross-coupling reactions employing dialkylbiaryl phosphine ligands. Acc. Chem. Res. 41, 1461–1473.

72. Suh, D.J., Park, T.J., and Ihm, S.K. (1992). Characteristics of carbon-supported palladium catalysts for liquid-phase hydrogenation of nitroaromatics. Ind. Eng. Chem. Res. 31, 1849–1856.

73. Conrad, H., Ertl, G., and Latta, E.E. (1974). Adsorption of hydrogen on palladium single-crystal surfaces. Surf. Sci. 41, 435–446.

74. Jewell, L.L., and Davis, B.H. (2006). Review of absorption and adsorption in the hydrogen-palladium system. Appl. Catal. A 310, 1–15.

75. Kyriakou, G., Boucher, M.B., Jewell, A.D., Lewis, E.A., Lawton, T.J., Baber, A.E., Tierney, H.L., Flytzani-Stephanopoulos, M., and Sykes, E.C.H. (2012). Isolated metal atom geometries as a strategy for selective heterogeneous hydrogenations. Science 335, 1209–1212.

76. Bai, S., Shao, Q., Wang, P., Dai, Q., Wang, X., and Huang, X. (2017). Highly active and selective hydrogenation of CO_2 to ethanol by ordered Pd-Cu nanoparticles. J. Am. Chem. Soc. 139, 6827–6830.

77. Li, M., Wang, J.J., Li, P., Chang, K., Li, C.L., Wang, T., Jiang, B., Zhang, H.B., Liu, H.M., Yamauchi, Y., et al. (2016). Mesoporous palladium-copper bimetallic electrodes for selective electrocatalytic reduction of aqueous CO_2 to CO. J. Mater. Chem. A 4, 4776–4782.

78. Li, M., Li, P., Chang, K., Liu, H., Hai, X., Zhang, H., and Ye, J. (2016). Design of a photoelectrochemical device for the selective conversion of aqueous CO_2 to CO: using mesoporous palladium-copper bimetallic cathode and hierarchical ZnO-based nanowire array photoanode. Chem. Commun. 52, 8235–8238.

79. Takashima, T., Suzuki, T., and Irie, H. (2017). Electrochemical carbon dioxide reduction on copper-modified palladium nanoparticles synthesized by underpotential deposition. Electrochim. Acta 229, 415–421.

80. Hammer, B., Morikawa, Y., and Norskov, J.K. (1996). CO chemisorption at metal surfaces and overlayers. Phys. Rev. Lett. 76, 2141–2144.

81. Ma, S., Sadakiyo, M., Heima, M., Luo, R., Haasch, R.T., Gold, J.I., Yamauchi, M., and Kenis, P.J. (2017). Electroreduction of carbon dioxide to hydrocarbons using bimetallic Cu-Pd catalysts with different mixing patterns. J. Am. Chem. Soc. 139, 47–50.

82. Long, R., Li, Y., Liu, Y., Chen, S., Zheng, X., Gao, C., He, C., Chen, N., Qi, Z., Song, L., et al. (2017). Isolation of Cu atoms in Pd lattice: forming highly selective sites for photocatalytic conversion of CO_2 to CH_4. J. Am. Chem. Soc. 139, 4486–4492.

83. Varela, A.S., Schlaup, C., Jovanov, Z.P., Malacrida, P., Horch, S., Stephens, I.E.L., and Chorkendorff, I. (2013). CO_2 electroreduction on well-defined bimetallic surfaces: Cu overlayers on Pt(111) and Pt(211). J. Phys. Chem. C 117, 20500–20508.

84. Guo, X., Zhang, Y., Deng, C., Li, X., Xue, Y., Yan, Y.M., and Sun, K. (2015). Composition dependent activity of Cu-Pt nanocrystals for electrochemical reduction of CO_2. Chem. Commun. 51, 1345–1348.

85. Ko, J., Kim, B.K., and Han, J.W. (2016). Density functional theory study for catalytic activation and dissociation of CO_2 on bimetallic alloy surfaces. J. Phys. Chem. C 120, 3438–3447.

86. Back, S., Yeom, M.S., and Jung, Y. (2015). Active sites of Au and Ag nanoparticle catalysts for CO_2 electroreduction to CO. ACS Catal. 5, 5089–5096.

87. Back, S., Kim, J.H., Kim, Y.T., and Jung, Y. (2016). Bifunctional interface of Au and Cu for improved CO_2 electroreduction. ACS Appl. Mater. Interfaces 8, 23022–23027.

88. Han, B.C., Miranda, C.R., and Ceder, G. (2008). Effect of particle size and surface structure on adsorption of O and OH on platinum nanoparticles: a first-principles study. Phys. Rev. B Condens. Matter Mater. Phys. 77, 075410.

89. Hirunsit, P., Soodsawang, W., and Limtrakul, J. (2015). CO_2 electrochemical reduction to methane and methanol on copper-based alloys: theoretical insight. J. Phys. Chem. C 119, 8238–8249.

90. Adit Maark, T., and Nanda, B.R.K. (2016). CO and CO_2 electrochemical reduction to methane on Cu, Ni, and Cu_3Ni (211) surfaces. J. Phys. Chem. C 120, 8781–8789.

91. Adit Maark, T., and Nanda, B.R.K. (2017). Enhancing CO_2 electroreduction by tailoring strain and ligand effects in bimetallic copper-rhodium and copper-nickel heterostructures. J. Phys. Chem. C 121, 4496–4504.

92. Liu, M., Pang, Y., Zhang, B., De Luna, P., Voznyy, O., Xu, J., Zheng, X., Dinh, C.T., Fan, F., Cao, C., et al. (2016). Enhanced electrocatalytic CO_2 reduction via field-induced reagent concentration. Nature 537, 382–386.

93. Resasco, J., Chen, L.D., Clark, E., Tsai, C., Hahn, C., Jaramillo, T.F., Chan, K., and Bell, A.T. (2017). Promoter effects of alkali metal cations on the electrochemical reduction of carbon dioxide. J. Am. Chem. Soc. 139, 11277–11287.

94. Singh, M.R., Kwon, Y., Lum, Y., Ager, J.W., 3rd, and Bell, A.T. (2016). Hydrolysis of electrolyte cations enhances the electrochemical reduction of CO_2 over Ag and Cu. J. Am. Chem. Soc. 138, 13006–13012.

95. Zhao, W.G., Yang, L.N., Yin, Y.D., and Jin, M.S. (2014). Thermodynamic controlled synthesis of intermetallic Au_3Cu alloy nanocrystals from Cu microparticles. J. Mater. Chem. A 2, 902–906.

96. Weng, Z., Zhang, X., Wu, Y., Huo, S., Jiang, J., Liu, W., He, G., Liang, Y., and Wang, H. (2017). Self-cleaning catalyst electrodes for stabilized

CO$_2$ reduction to hydrocarbons. Angew. Chem. Int. Ed. *56*, 13135–13139.

97. Zhang, S., Kang, P., Bakir, M., Lapides, A.M., Dares, C.J., and Meyer, T.J. (2015). Polymer-supported CuPd nanoalloy as a synergistic catalyst for electrocatalytic reduction of carbon dioxide to methane. Proc. Natl. Acad. Sci. USA *112*, 15809–15814.

98. Chen, C.S., Wan, J.H., and Yeo, B.S. (2015). Electrochemical reduction of carbon dioxide to ethane using nanostructured Cu$_2$O-derived copper catalyst and palladium(II) chloride. J. Phys. Chem. C *119*, 26875–26882.

99. Kaneco, S., Sakaguchi, Y., Katsumata, H., Suzuki, T., and Ohta, K. (2007). Cu-deposited nickel electrode for the electrochemical conversion of CO$_2$ in water/methanol mixture media. Bull. Catal. Soc. India *6*, 74–82.

100. Li, Y.W., Su, H.B., Chan, S.H., and Sun, Q. (2015). CO$_2$ electroreduction performance of transition metal dimers supported on graphene: a theoretical study. ACS Catal. *5*, 6658–6664.

Appendix B

Publication List

Publications included in this Thesis:

1. Anthony Vasileff, **Chaochen Xu**, Yan Jiao, Yao Zheng, and Shi-Zhang Qiao. Surface and interface engineering in copper-based bimetallic materials for selective CO_2 electroreduction. *Chem*, 4(8):1809-1831, 2018.

2. **Chaochen Xu**, Anthony Vasileff, Dan Wang, Bo Jin, Yao Zheng, and Shi-Zhang Qiao. Synergistic catalysis between atomically dispersed Fe and a pyrrolic-N-C framework for CO_2 electroreduction. *Nanoscale Horizons*, 4(6):1411-1415, 2019.

3. **Chaochen Xu**, Anthony Vasileff, Bo Jin, Dan Wang, Haolan Xu, Yao Zheng, and Shi-Zhang Qiao. Graphene-encapsulated nickel-copper bimetallic nanoparticle catalysts for electrochemical reduction of CO_2 to CO. *Chemical Communications*, 56(76):11275-11278, 2020.

4. **Chaochen Xu**, Xing Zhi, Anthony Vasileff, Dan Wang, Bo Jin, Yan Jiao, Yao Zheng, and Shi-Zhang Qiao. Highly selective two-electron electro-catalytic CO_2 reduction on single-atom Cu catalysts. *Small Structures*, 202000058, 2020.

5. **Chaochen Xu**, Anthony Vasileff, Yao Zheng, and Shi-Zhang Qiao. Recent progress of 3d transition metal single-atom catalysts for electrochemical CO_2 reduction. *Advanced Materials Interfaces*, 2020. (Submitted)

6. **Chaochen Xu**, Anthony Vasileff, Dan Wang, Bo Jin, Yao Zheng, and Shi-Zhang Qiao. Graphene-supported 3d-block metallophthalocyanines as synergistic catalysts for electrochemical CO_2 reduction. 2020. (To be submitted)

Other publications during PhD candidature:

1. Tian Wen, Yao Zheng, **Chaochen Xu**, Jian Zhang, Mietek Jaroniec, and Shi-Zhang Qiao. A boron imidazolate framework with mechanochromic and electrocatalytic properties. *Materials Horizons*, 5(6):1151-1155, 2018.

2. Anthony Vasileff, **Chaochen Xu**, Lei Ge, Yao Zheng, and Shi-Zhang Qiao. Bronze alloys with tin surface sites for selective electrochemical reduction of CO_2. *Chemical Communications*, 54(99):13965-13968, 2018.

3. Anthony Vasileff, Xing Zhi, **Chaochen Xu**, Lei Ge, Yan Jiao, Yao Zheng, and Shi-Zhang Qiao. Selectivity control for electrochemical CO_2 reduction by charge redistribution on the surface of copper alloys. *ACS Catalysis*, 9(10):9411-9417, 2019.

4. Xuesi Wang, **Chaochen Xu**, Mietek Jaroniec, Yao Zheng, and Shi-Zhang Qiao. Anomalous hydrogen evolution behavior in high-pH environment induced by locally generated hydronium ions. *Nature Communications*, 10(1):4876, 2019.